MEASUREMENT OF BRUSHLESS DC MOTOR CHARACTERISTICS AND PARAMETERS AND BRUSHLESS DC MOTOR DESIGN

A THESIS SUBMITTED TO
THE GRADUATE SCHOOL OF NATURAL AND APPLIED SCIENCES
OF
MIDDLE EAST TECHNICAL UNIVERSITY

BY

İLKER ŞAHİN

IN PARTIAL FULFILLMENT OF THE REQUIREMENTS
FOR
THE DEGREE OF MASTER OF SCIENCE
IN
ELECTRICAL AND ELECTRONICS ENGINEERING

JANUARY 2010

Approval of the thesis:

MEASUREMENT OF BRUSHLESS DC MOTOR CHARACTERISTICS AND

PARAMETERS AND BRUSHLESS DC MOTOR DESIGN

submitted by **İLKER ŞAHİN** in partial fulfilment of the requirements for the degree of **Master of Science in Electrical and Electronics Engineering Department, Middle East Technical University** by,

Prof. Dr. Canan ÖZGEN
Dean, Graduate School of **Natural and Applied Sciences**   _____

Prof. Dr. İsmet ERKMEN
Head of Department, **Electrical and Electronics Engineering**   _____

Prof. Dr. H. Bülent ERTAN
Supervisor, **Electrical and Electronics Engineering Dept, METU**   _____

Examining Committee Members:

Prof. Dr. Muammer ERMİŞ
Electrical and Electronics Engineering Dept., METU   _____

Prof. Dr. H. Bülent ERTAN
Electrical and Electronics Engineering Dept., METU   _____

Prof. Dr. Kemal LEBLEBİCİOĞLU
Electrical and Electronics Engineering Dept., METU   _____

Prof. Dr. Aydın ERSAK
Electrical and Electronics Engineering Dept., METU   _____

Bülent BİLGİN, M.Sc.
ASELSAN Inc.   _____

Date: 10.12.2009

I hereby declare that all information in this document has been obtained and presented in accordance with academic rules and ethical conduct. I also declare that, as required by these rules and conduct, I have fully cited and referenced all material and results that are not original to this work.

Name, Last Name :

Signature   :

ABSTRACT

MEASUREMENT OF BRUSHLESS DC MOTOR CHARACTERISTICS AND PARAMETERS AND BRUSHLESS DC MOTOR DESIGN

Şahin, İlker

M.Sc., Department of Electrical and Electronics Engineering

Supervisor: Prof. Dr. H. Bülent ERTAN

January 2010, 203 pages

The permanent magnet motors have become essential parts of modern motor drives recently because need for high efficiency and accurate dynamic performance arose in the industry. Some of the advantages they possess over other types of electric motors include higher torque density, higher efficiency due to absence of losses caused by field excitation, almost unity power factor, and almost maintenance free construction. With increasing need for specialized PM motors for different purposes and areas, much effort has also gone to design methodologies.

In this thesis a design model is developed for surface PM motors. This model is used with an available optimization algorithm for the optimized design of a PM motor. Special attention is paid to measurement of parameters of a sample PM motor.

As a result of this study, an effective analytical model with a proven accuracy by measurement results is developed and applied in a design process of a surface PM motor. Parametric and performance results of analytical model and tests have been presented comparatively. A prototype motor has been realized and tested.

Keywords: permanent magnet motors, brushless dc, surface magnet motors, design optimization, measurement of motor parameters, determination of motor parameters

ÖZ

FIRÇASIZ DC MOTOR KARAKTERİSTİĞİ VE PARAMETRE ÖLÇÜMÜ VE FIRÇASIZ DC MOTOR TASARIMI

Şahin, İlker

Yüksek Lisans, Elektrik ve Elektronik Mühendisliği Bölümü

Tez Yöneticisi: Prof. Dr. H. Bülent ERTAN

Ocak 2010, 203 sayfa

Sabit mıknatıslı (SM) motorlar, sanayide ortaya çıkan yüksek verim ve dinamik performans ihtiyaçlarından dolayı, modern motor sürücülerin temel parçalarından biri olmuştur. Diğer motor türlerine nazaran öne çıkan bazı özellikleri daha yüksek moment yoğunluğu, alan akısı uyartımının olmaması sayesinde daha yüksek verim, neredeyse birim güç faktörü ve bakım gerektirmeyen yapısıdır. Değişik amaçlar ve uygulama alanlarına yönelik özel amaçlı SM motorlar için artan ihtiyaç sebebiyle, tasarım yöntemlerine yönelik ayrıca gayret sarf edilmektedir.

Bu tez çalışmasında, SM motorlar için bir tasarım modeli geliştirilmiştir. Halihazırdaki bir optimizasyon algoritması ile bu model, bir SM motorun en iyileştirilmiş tasarımında kullanılmıştır. Model parametrelerin ölçüm yöntemlerine özel çaba harcanmıştır.

Bu tez çalışmasının sonucu olarak, doğruluğu deneysel sonuçlarla kanıtlanmış bir tasarım modeli geliştirilmiş ve bir SM motorun tasarımında kullanılmıştır. Analitik ve deneysel olarak elde edilen model değişkenlerinin değerleri ve motor performans sonuçları karşılaştırmalı olarak sunulmuştur. Prototip bir motor üretilmiş ve test edilmiştir.

Anahtar Kelimeler: sabit mıknatıslı motorlar, fırçasız dc, yüzey mıknatıslı motorlar, tasarım optimizasyonu, motor parametrelerinin ölçülmesi, motor parametrelerinin belirlenmesi

ACKNOWLEDGEMENTS

TABLE OF CONTENTS

ix

LIST OF TABLES

TABLES

LIST OF FIGURES

FIGURES

CHAPTER 1

INTRODUCTION

Electric motors, with a background of more than 100 years, had an impact on the human civilization deeply, replacing human muscle power in industry. Ever since the beginning of the story with induction motors (IM) and synchronous motors (SM), the knowledge and experience in design methodologies and technologies of these kinds of motors are already far advanced. However the development of frequency converters and new materials have emerged new challenges for motor designers.

With the introduction of AlNiCo, the first commercial permanent magnet (PM) motor was introduced in 1950s [12]. However, this new technology had to wait long to be widely accommodated in industrial applications. With the discovery of rare earth magnets in 1970s, permanent magnet motor technology has followed footsteps of developments in magnet materials. In 1980s first in DC motors, followed by synchronous motors, more interest and effort has gone to this new technology.

The permanent magnet (PM) motors have become essential parts of modern motor drives recently, since need for high efficiency and accurate dynamic performance arose. Some of the advantages they possess over other types of electric motors include higher torque density, higher efficiency due to absence of losses caused by field excitation, almost unity power factor, and almost maintenance free construction. PM motors became a first choice in industry because of their adaptability to new sophisticated control systems like direct torque control. Any operating speed range is possible with PM motors, whereas a gearbox is needed for IM and SM which is not preferable in many sectors (such as paper and textile).

Analytical modelling and design of PM machines are comprehensive topics which this study focuses on. The basis of analysis is to predict performance of PM machine. This is crucial in motor design to avoid the design misjudgement before the motor is manufactured. Also in PM motor drive applications, drives mostly depend on the analytical model to apply different voltage or current modulations to operate a motor. Any modulation technique need an accurate motor model to be implemented since estimations and calculations must be done according to mathematical equations derived from the motor model. In recent years, there has been also a great interest to develop schemes for sensorless drive

systems due to additional sensor cost, higher number of connections between motor and controller, noise interference, and reduced robustness introduced by presence of a position sensor [25], [26], [27]. Sensorless drive methods are generally based on the measurement of motor currents, voltages, and motor parameters. Therefore, the accuracy of such methods also depends on the availability of an accurate analytical model for the motor.

On the other hand, it is difficult to take into account some magnetic phenomena such as the effects of magnetic saturation, complex configuration, and eddy currents with just an analytical model of the motor. In every motor design, the knowledge of the field distribution in the air gap is essential for prediction of the developed torque, the induced voltage and for determining the flux densities in specific parts of the motor (teeth, yoke etc.). Numerical techniques have been accepted as practical and accurate method of field computation to aid in the machine design. Finite elements, amongst numerical methods, have appeared as a suitable technique for electrical motor design and performance evaluation in low frequency applications. However it should be noticed that those result in a time consuming process. In order to be computationally simple and at the same time functionally accurate, field and circuit combined analysis is a desirable solution. Although accurate field calculations in electrical machines can be carried out using FE method, numerical methods are in general more time consuming and do not provide closed form solutions. In conclude, regardless of the application of a PM motor or operation of the drive, analytical modelling of a PM motor is crucial. In this study an analytical model and its analysis will be presented to be used in design and optimization of the motor.

With increasing need for specialized PM motors for different purposes and areas, much effort has also gone to design methodologies. PMSM technology and its control have gained some much attention that beside individual works, textbooks on design are published also. One of the first comprehensive textbooks is published by Kenjo [29] and Miller [6]. The basics of PM motors with extends to drives has been carefully stated. Gieras and Wing published a complete handbook (first published in 1996 and revised in 2002) with extensions on analytical and numerical design of PM motor drives, examples of performance calculations and optimization [7]. Hanselman also published a textbook covering all about PM motors from basics to winding diagrams and drives [8].

Throughout published papers and textbooks various classifications are made by authors to classify PM motors [22], [23], [24]. Each approach has its own basis. In this thesis, a classification based on electromechanical structure of the PM motor is defined where it can be summarized as in Figure 1.1. In this classification, mechanical construction of moving parts and magnetic design is considered.
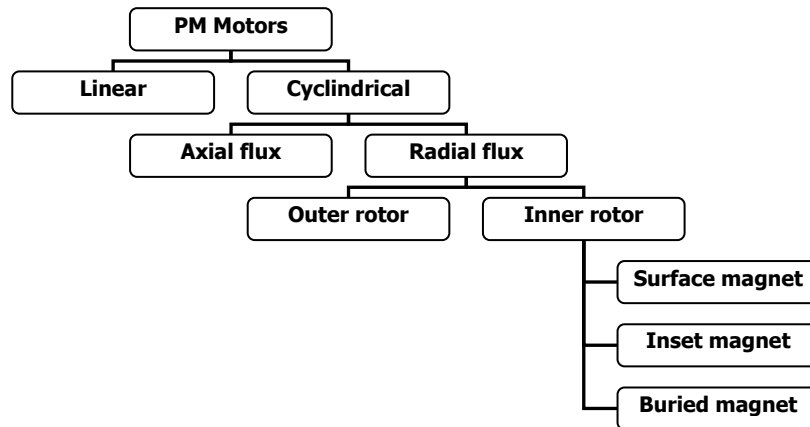
Figure 1.1 Classification of PM motors by Electromechanical Structure

As seen in the figure, first distinction is made according to electromechanical operation of PM motors. Cylindrical PM motors have the conventional rotating motion, with a rotating rotor and stationary stator. On the other hand, linear motors have the movement of "sliding" rather than rotating in their operation where rotor slides on an electronically operated straight path. The path and the sliding rotor facing each other form linear motor structure together.

Since the focus of this work is cylindrical motors, further classifications are done under cylindrical type where the next classification is due to magnetic circuit. Since electro-mechanical energy conversion is done with guiding magnetic flux between moving and stationary parts of the electric motor, they may grouped with respect to magnetic circuit. In axial motors stator and rotor of the motor are flat and facing each other instead of one within the other. Flux transition occurs between the flat faces. Many different designs are available for axial motors (with double stator or double rotor) where they may be called as pancake or hub motor also. Conversely radial flux motors operate in the same manner as conventional electric motors where rotor is inside or outside of the stator.

With magnets as a flux source instead of windings, many structural options arose in electric motors. Unlike conventional motors, rotor may be outside or inside the stator which may enable us to group them as inner or outer rotor motor. There are also constructions with two rotors, both inside and outside a stator, which does not fall into these groups [34].

Depending on the placement of magnets for inner rotor construction, three subgroups may be suggested that are surface, inset and buried magnet PM motors. There are several design options for each type but some of are shown in Figure 1.2 to illustrate. In the

figure "N, S" defines magnetization poles of magnets and "d, q" show direct and quadrature magnetic axis respectively. Each design has its own benefits and drawbacks as summarized in Table 1.1.
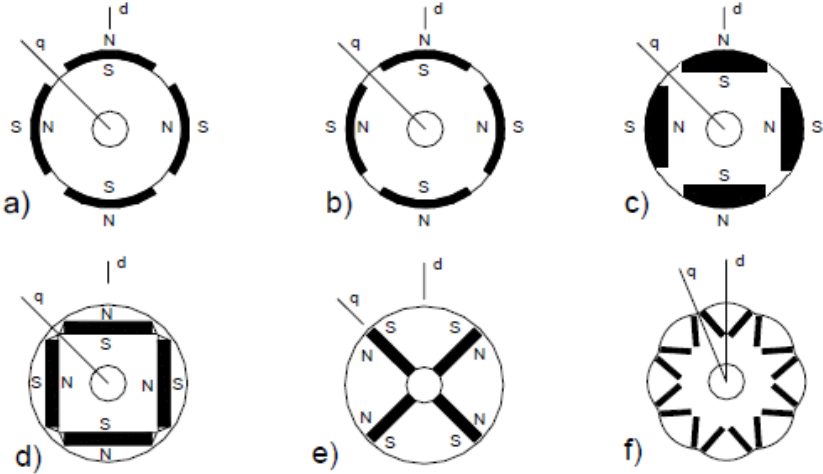
Figure 1.2: Different rotor constructions

(Surface: a, Inset: b-c, Buried: d-e-f)

The simplest and likely the cheapest construction is surface magnet PM motor and they are widely used in industry. Low inertia rotors which are small in diameters can be constructed since airgap flux density is almost same with magnet flux density. The low inertia makes these kind of motor widely preferred where high dynamic performance is needed, e.g. servo applications.

High torque outputs can be achieved with pushing flux densities at limits in the design since there is no other flux source than magnets; risk of saturation is almost eliminated. On the other hand, as the magnets are partially or totally in air, they are exposed to airgap flux harmonics. Since modern rare earth magnets are electrically conductive, those harmonic fluxes will result in eddy currents in the magnets which results in losses and even demagnetization. Also analytical modelling of these motors is simple since magnetic reluctances are easy to calculate and airgap is uniformly cylindrical.

Table 1.1 Different rotor constructions for PM motors

Construction	Benefits	Drawbacks
Surface Magnet	Very simple construction Very low manufacturing costs Low inertia	Weak mechanical strength No flux weakening Exposure to airgap flux harmonics Difficult installation of rotor
Inset Magnet	Simple construction Low flux weakening capability Little resistance to airgap flux harmonics Low inertia	Weak mechanical strength Need for magnet shape design Reduce airgap flux density with stray fluxes Difficult installation of rotor Complex magnet shapes
Buried Magnet	High flux weakening capability Strong mechanical strength Immune to airgap flux harmonics Flux concentration Easy installing of rotor Simple magnet shapes Line start capability	Very complex mechanical construction Expensive manufacturing Increased inertia

Specific attention must be paid to centrifugal forces acting on magnets to avoid deformation of the construction. Magnets may be glued and rotor may me bound with non-magnetic material such as Fiberglas to protect magnets from these forces. Inset magnet rotors are slightly more stable than surface magnet, since magnets are more tightly fastened to the rotor. This time, leakage stray fluxes increase resulting in reduced airgap flux density. Installation of rotor into stator is also problematic with danger of damaging the magnets. Special fixtures should be used for proper installation.

Magnets can also be buried in the rotor in almost any way which gives diverse options for designers (see Figure 1.2). The increase in constructional complexity and manufacturing costs for burying magnets comes with several advantages. The increased flux density with flux concentration methods produces more torque per motor volume. The risk of demagnetization of magnets is prevented with presence of iron path between magnets and airgap. Maybe the most considerable outcome of buried magnets is that sinusoidal airgap flux distribution can be easily achieved resulting in low harmonics, low core losses and low cogging torque.

Buried magnet designs are considered where wide speed operating ranges are needed. Since the field flux is constant in PMSM, one should find a way to oppose the back EMF to inject current into the motor windings without a need for increase in bus voltage of the driver. The solution is lowering the induced back EMF by reducing field flux at airgap with field weakening operation.

The buried magnet PMSM can be modified to adapt line starting by introducing damper windings (or cage) to the rotor. It is possible to apply damper windings to pole shoes or conducting bars between magnets. This modification also protects magnets against demagnetization during transients and accelerates dynamic response to load changes avoiding synchronization loss.

1.1 Permanent Magnets

Dating back to 4000BC, magnets have been used by mankind for thousands of years, first by means of orientation then in many technological inventions where magnetic forces are utilized. The earliest reference to magnetism is found in Chinese literature in a 4th century BC book called *Book of the Devil Valley Master* (鬼谷子): "The lodestone makes iron come or it attracts it." [55].

For PMSM analysis and design, a sound knowledge on magnets is necessary to benefit from them optimally. The magnet is the major component in the magnetic circuit of the motor. Also all the electromagnetic conversion depends on the flux coming out of the magnets.

To have a better understanding, some definitions about magnets have to be presented. There are many parameters and that define the characteristics of the magnet. Some selected ones are remanence, coercivity, permeability, temperature coefficient, Curie temperature.

- The magnet remanence "Br" is the magnetization or flux density remaining in a saturated magnet, measured within a closed magnetic circuit. It is measured in Tesla (T) or Millitesla (mT). In the CGS system, the term is Gauss (G). Nowadays rare earth magnets with 1.5T remanence are available commercially.
- The coercivity "Hc" is the negative magnetic field strength in kA/m (or Oersteds-Oe) which is necessary to bring the remanence Br to zero again. A higher coercivity means better performance of magnet against demagnetizing fields.
- The permeability "μ" can be simply defined as magnetic conductivity. Almost all magnet materials have permeability slightly larger than for air (μ_{air}=1) where it

may exceed a thousand fold for iron. That's why iron is treated as "infinitely permeable" in most magnetic analysis (especially for electric motors).

- The energy product "BH" indicates the stored energy within a magnet. It is measured in kJ/m^3. As the stored energy increases, higher value for energy product is obtained.
- The maximum of energy product "BH_{max}" results from the largest B and H to be drawn inside the demagnetization curve (Figure 1.3). Intrinsic coercive force "$_jHc$" is a measure of the material's inherent ability to resist demagnetisation. It is the demagnetisation force corresponding to zero intrinsic induction in the magnetic material after saturation.
- Coercive force "$_BHc$" is the demagnetising force, measured in Oersteds, necessary to reduce observed induction, B, to zero after the magnet has previously been brought to saturation.
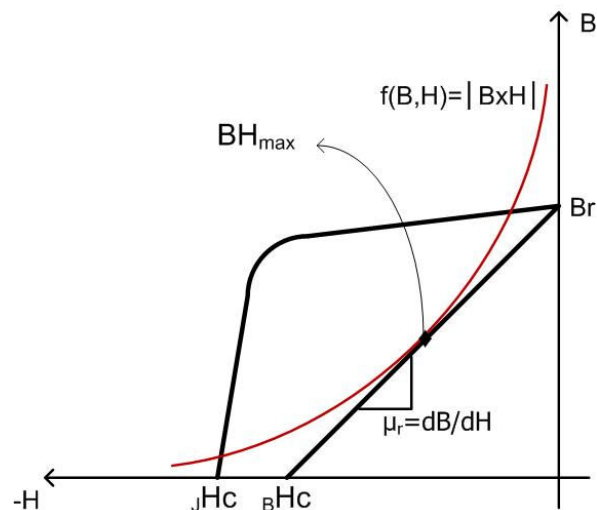
Figure 1.3: Demagnetization curve of a permanent magnet

- The temperature coefficient indicates the reversible decrease of the remanence, based on normal room temperature (20°C) in percent per 1 °C increase in temperature.
- The maximum temperature is only an approximate value as it depends upon the dimensions of a magnet system (L/D-ratio). The given value can only be reached if the product of B and H reach a maximum (see magnetic design).
- If the Curie temperature is reached, every magnetic material loses its magnetism.

Depending on the application of the PM machine, there are many possibilities of magnet material, grade and shape. Three major families of permanent magnet materials (metal, ceramic and rare earth) have been developed in the last century. Revolutionary developments have recently occurred in the old field of permanent magnetism. Rare-earth magnets have raised energy products 4 to 5 multiples and coercivity by an order of magnitude, while leaving their ancestors, hard ferrites, to become an abundant inexpensive magnet material (Figure 1.4). As a consequence, a rapid broadening of magnet uses is now occurring; traditional devices are miniaturized, new applications and design concepts are evolving.
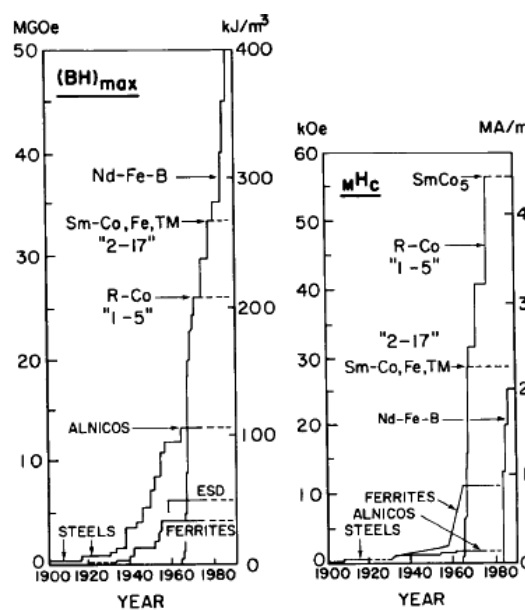
Figure 1.4: Development of permanent magnets in the 20th century [35]

Rare-earth magnets are manufactured from rare earth metals. Those metals (15 elements) form Lanthanides group in periodic table with atomic numbers between 57 and 71. They find application in diverse areas like glass and steel industry, x-ray film manufacturing and magnet industry. Although the name contains "rare", in fact rare earth metals are not rare at all. They make up about 1/7 of all elements occurring naturally [53].

The composition, properties and the method of manufacturing metal (aluminium-nickel-cobalt-iron), ceramic (barium or strontium ferrite) and the three generations of the rare earth (RCo_5, R_2Co_{17} and NdFeB) magnets are different from each other [30]. All have

different magnetization characteristics where this diversity can be visualized on B-H magnetization curves (Figure 1.5).

In the case of most modern magnet materials the remanence and the coercivity decreases on warming. When the temperature drops both values rise. This generally means that there is an improvement in most magnet systems up to - 40°C. SmCo magnets can be used for example in temperature areas below zero, which are necessary for the production of superconductors. The maximum operating temperature also depends on the L/D-ratio; the ratio of the magnet pole area to the magnet thickness. A thin NdFeB magnet disc of 15ø x 2mm e.g. can only be used up to a maximum operating temperature of +70°C, whereas a thicker disc of 15ø x 8mm can achieve +100°C approximately [56].
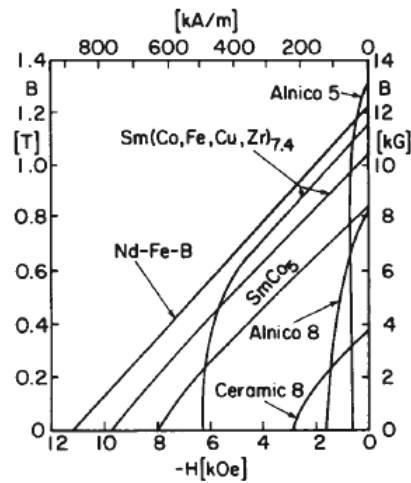
Figure 1.5: B-H demagnetization curves of average commercial magnets [35]

1.2   Conclusion to CHAPTER 1

In this thesis, all the work of parameter measurements, analysis and design are performed on a cylindrical - radial flux - interior rotor – inset magnet motor. This thesis does not propose a new PMSM model, but it uses some of the offered models for the purpose of designing a surface PM motor optimized to meet requirements. Analytical calculations are based on electric circuit as much as magnetic reluctance circuit of the PMSM. It is shown how the electrical and magnetic parameters (such as EMF and inductances) can be estimated analytically. The design and the optimization of a PM motor with analytical

model and then FE analysis is accomplished to conclude the design. Moreover, the designed motor has been prototyped and tested according to defined procedures.

The following chapters contain measurement of parameters of a PMSM, derivation of a steady state motor model and analysis of this model. After successfully building the machine model optimization problem will be defined. Results of the optimization will be validated by experiments performed on the newly designed and manufactured prototype PMSM.

CHAPTER 2

BRUSHLESS DC MOTOR MODEL

In this chapter, an analytical model of a brushless DC (more explicitly a PMSM with inset magnets) has been formed and presented. The proposed method is based on traditional analytical methods for synchronous motors where magnetic and electric circuits are utilized with modification for inset magnet motors.

Modern motor designs utilize finite element method (FEM) that results comprehensive information on magnetic and electric structure taking nonlinearities into account. In the FEM analysis, the motor structure is divided it into several finite elements where magnetic vector potentials are solved in every element with continuity between adjacent ones. The accuracy of the FEM analysis mainly depends on number finite elements. Smaller elements result in higher detail in magnetic data, thus higher accuracy. Once potentials are solved in every element, electromagnetic properties of the motor (i.e. flux densities, electromagnetic torque, losses) can be computed. Depending on the motor configuration, finite element method takes couple hundred to one thousand times longer than lumped analysis to produce the equivalent results. The demand in higher accuracy inevitably results in longer process time even for modern high performance computers. Especially if iteration has to be done in the design, FEM method may not be feasible to perform and optimization by FEM analysis may become unfeasible.

Although FEM enables comprehensive magnetic and electrical analysis, conventional analytical analysis methods may also give out acceptable results for design and analysis of electric machines. This approach has been performed by many researchers. In his work, Wang et all [33] showed that detent torque is the only property which cannot be reasonably predicted by lumped analysis. However, FEM is advised to be useful for improving or confirming the design work by other methods.

Two types of analysis have to be performed; magnetic and electrical. Magnetic analysis gives out flux densities in the motor core and especially in airgap. Electrical circuit analysis is performed to solve phase voltages and currents for any operating condition of the motor so that electromechanical performance of the motor (such as electromagnetic torque output, torque-speed characteristic, rated operating characteristics) can be determined.

11

2.1 Magnetic Circuit Analysis on Open Circuit

There are numerous ways to determine magnetic field distribution within a medium. For simple geometries, magnetic field can be determined with simple analytical equations. For complex structures (i.e. axial flux PMSM) a realistic field analysis can be performed by FEM studies only. However it is possible to approximate field distribution quite reasonably with analytical models. The analytical magnetic motor model offers a fast evaluation tool for performance analysis in steady state. Also it will be shown that optimization of different parameters are much easier and still reliable.

A magnetic circuit is in fact analogous to an electric circuit where Flux - MMF - Reluctance that are present instead of Current – Voltage – Resistance respectively. Magnetic circuits can be solved like an electrical circuit and representations like Thevenin or Norton can be applied to both.

For analytical analysis of magnetic circuit, flux paths and reluctances to each should be defined. In PM machines this task is easy since presence of magnets dictates also the flux paths. The flux just follows the magnetization direction the magnets in the poles and just split into two to adjacent poles.

In the model, the motor is treated as 2D where calculations are performed on cross sectional structure of the machine. In Figure 2.1, each magnet is presented by a Norton equivalent circuit where $\varnothing_o$ is flux source and P_{mo} is internal permeance of magnet. The reluctance seen by airgap flux passing from magnets to stator side is modelled with R_g, R_{th} and R_{bc} represents equivalent reluctances of tooth and back-core path respectively. The leakage fluxes between magnets are modelled with R_{ml} and rotor side reluctance with R_r (Figure 2.1).
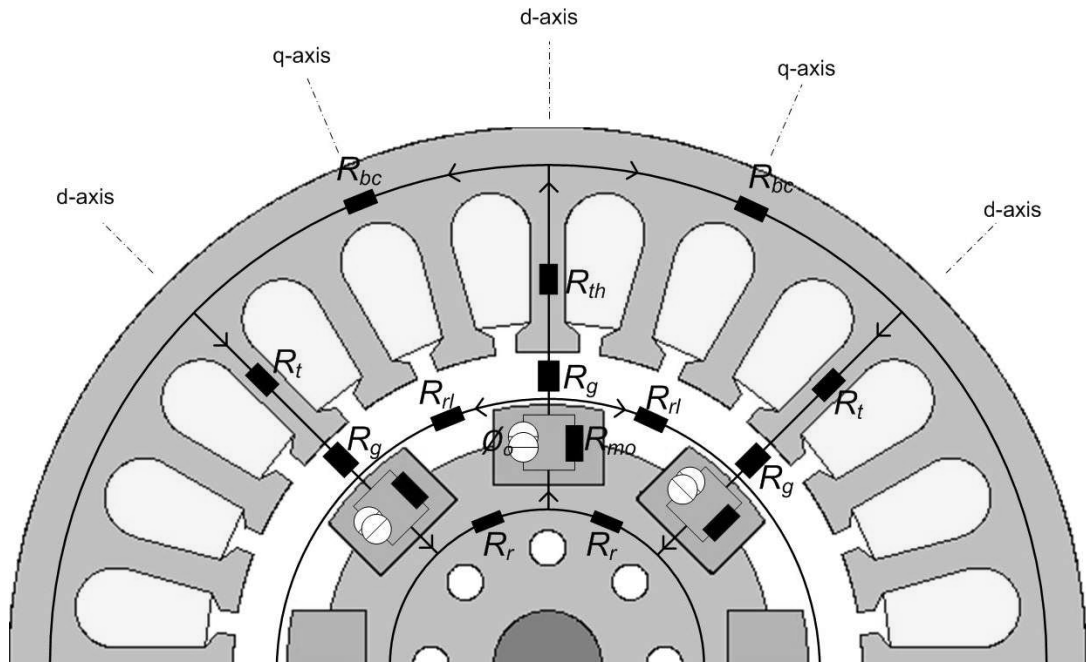
Figure 2.1: 2D modelling of PM motor structure with reluctances

Explanation of parameters in the equivalent magnetic circuit in Figure 2.1 is as follows:

- **$\emptyset_o$**   : Flux generated by magnet
- **R_{mo}**   : Magnet internal reluctance
- **R_{rl}**   : Reluctance of flux path in the rotor between successive poles
- **R_g**   : Equivalent airgap magnetic reluctance
- **R_{th}**   : Reluctance of tooth path
- **R_{bc}**   : Reluctance of stator back core
- **R_r**   : Reluctance of rotor yoke

Considering the motor cross section in Figure 2.1, the motor has 8 poles. The magnet flux leaving the rotor at one magnet surface crosses over to the stator and splits into two equivalent sections. Each flux branch travels in the opposite direction and crosses the airgap toward the next pole to the rotor. The flux travels in a closed path between two adjacent poles (magnets).

In addition to the primary flux path, some magnet flux jumps from one magnet to the next in the airgap without passing to the stator, as illustrated by R_{rl} in Figure 2.2. The flux that follows this path is often called magnet leakage flux [8] or rotor leakage flux [6].

Because the flux paths shown in Figure 2.1 repeat for every pole, it is sufficient to model in one pole to characterize PM motor. It can be noted that stator slot leakage is neglected. The arrows on lines in the figure show direction of flux.

Figure 2.2: Magnetic circuit model for PM motor

$\varnothing_m$: Flux leaving magnet and passing to airgap
$\varnothing_{rl}$: Rotor leakage flux (between magnets)
$\varnothing_g$: Flux at airgap passing from rotor to stator side

As seen in Figure 2.2, the flux leaving the magnets split into leakage and airgap fluxes. The real airgap flux can be determined if those two reluctances are determined. However, rotor leakage paths are difficult to estimate and defining an explicit expression for leakage reluctances is very difficult [6], [7], [8]. Instead an empirical approach for leakage permeance is more convenient for analytical models. For surface and inset magnet motors, leakage flux is typically up to 10% of airgap flux [6], [8] and maybe modelled with a leakage factor multiplying airgap reluctance, so that R_{rl} is a multiple (k_{rl}) of R_g. The rotor leakage factor k_{rl} takes a value of 0 to 0.1. The worst case is considered in this study where leakage term k_{rl} is taken as 0.1 (maximum leakage).

The model in Figure 2.2 can be used to determine mean or rms value flux density in airgap. To get flux distribution more specifically, the airgap area can be divided into finite tubes (like in FE analysis but less elements) and the proposed magnetic circuit can be solved for each region. This approach will result the flux distribution depending on number of regions. Instead of treating the pole as a single area, dividing it into smaller areas

14

(maybe 5 to 10 pieces) and solving the magnetic circuit will give out better and adequate flux distribution knowledge for the designer without need for FE analysis.

2.2 Electric Circuit Analysis

The operating principle of PM motors is similar with conventional synchronous motors such that rotor movement is coupled with the rotating field created by three phase stator windings in the airgap. There is no slip like in induction motors so the rotor is in synchronization with rotating field which is the exact case for PM motors also. Due to this similarity PM motors can be modelled like synchronous motors. To model synchronous machines two kinds of transformation are required. The three-phase winding will be transformed to a two-phase system (which magnetically decouples the rotor and stator windings and also reduces the number of equations per windings from three to two), from a stationary to an arbitrary rotating coordinate system. Performing this transformation will result in constant mutual inductances and the feasibility to take magnetic asymmetry of some machine parts into account for instance the different reactances X_d and X_q of salient pole machines. The transformation also eliminates time-varying inductances by referring the stator and rotor quantities to a fixed or rotating reference frame. The I_d and I_q currents represent the two DC currents flowing in the two equivalent rotor windings (d winding on the same axis with magnets, and q winding in quadratic) producing the same flux as the stator currents (see Appendix).

In electrical machines, core loss arises due to time varying flux density in the core. The varying flux density creates eddy currents and also some energy is lost due to hysteresis in steel core. The flux in the machine core is the magnetizing flux created by windings in conventional IM and SM, where in PM machines this flux is solely due to permanent magnets in normal vector control operation [7]. In PM machines, beside the magnet flux, armature reaction flux also causes some loss in the core. On the other hand those two flux components, permanent magnet flux and armature reaction induces the back EMF voltage seen at machine terminals when the motor is rotating. Therefore, if the core losses are to be parameterized with a resistor then this resistance can be placed in parallel with back EMF seen at q-axis equivalent circuit (Figure 2.3).

The two-axis model of the PM motor can be visualized with two electrical circuits with resistances for copper and core loss, an inductance and a voltage source modelling back EMF. This model is sufficient to accurately model a PMSM operating in linear region (Figure 2.3) as in synchronous motors case.
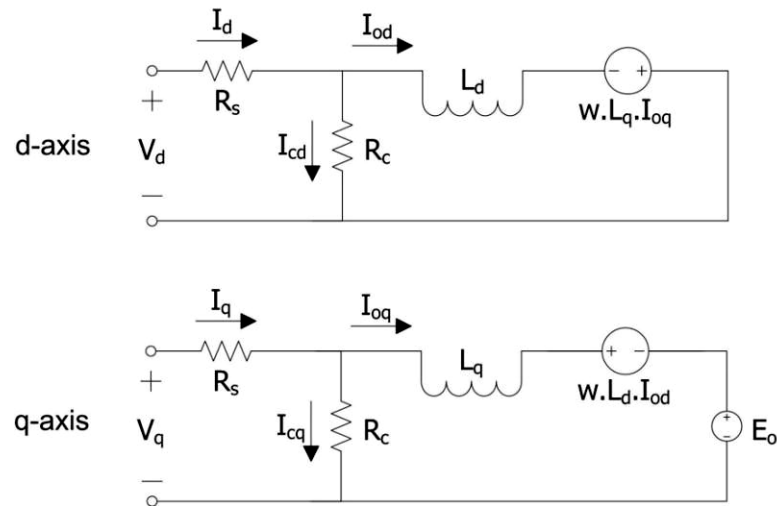
Figure 2.3: Two axes electrical model of PM motor

This two-axis model is based on the following assumptions:

- Rotor and stator winding only excite spatial sinusoidal voltage and current.
- Magnetic materials are isotropic.
- There is no saturation (linear magnetic equations).

The first assumption means that only the fundamental wave of the voltage and current linkages are taken into account and winding factors of harmonics are supposed to be zero. The second assumption declares that the permittivity "ε" and permeability "μ" of the machine steel core are uniform in all directions. The last assumption neglects the magnetic saturations in the motor core.

To fully model polyphase synchronous machines, at least five differential equations are needed, i.e. two for the rotor, two for the stator and one for the rotating masses. However, since there are no windings on the rotor for PM motors the rotor equations are eliminated; leaving only three equations. Two voltage equations are presented in equations (2-1) and (2-2).

$$V_d = R_{ph}I_d + \frac{d\Psi_d}{dt} - \omega.\Psi_q \qquad (2\text{-}1)$$

$$V_q = R_{ph}I_q + \frac{d\Psi_q}{dt} + \omega.\Psi_d \qquad (2\text{-}2)$$

$$\Psi_d = L_dI_d + \Psi_M \qquad (2\text{-}3)$$

16

$$\Psi_q = L_q I_q \tag{2-4}$$

The flux-linkages in equations (2-3) and (2-4) can be pasted directly into the stator voltage equations (2-1) and (2-2).

$$V_d = R_{ph} I_d + L_d \frac{dI_{od}}{dt} - \omega . L_q I_q \tag{2-5}$$

$$V_q = R_{ph} I_q + L_q \frac{d I_{oq}}{dt} + \omega . L_d I_d + \omega . \Psi_M \tag{2-6}$$

The above equations are related to electric circuit defined in Figure 2.3. R_{ph} is per phase resistance, I_d and I_q are d-q axes currents, L_q and L_d axes inductances, ω is electrical speed of shaft in rad$_{/sec}$, Ψ_d and Ψ_q are flux linkages in d-q axes and Ψ_M is magnet flux. The constant rotor flux in the d-axis by the permanent magnets is modelled by an equivalent flux parameter in the equation for the stator flux-linkage in the d-axis. The stator winding is treated as it has no effect on permanent magnet flux. These relations can be visualized by a phase diagram as in Figure 2.4.

Figure 2.4: Phase diagram for PM motor equivalent electrical model

The equations (2-5), (2-6) form total representation of two axes electrical circuit model of the PM motor. The phase voltages and currents can be extracted also if these two equations are solved.

2.3 Induced EMF Voltage on Open Circuit

Theoretically, voltage is induced on a coil if the flux linking the coil is changing in time. The amplitude of the induced voltage is directly related to amount of flux linkage and how the linkage variation occurs in time.

Rotation of rotor with magnets creates a time varying flux linkage in stator windings every time it passes under the coils. The amplitude of the induced voltage E_o is expressed in terms of amplitude of flux linkage and frequency of flux linkage change as in equation (2-7) where flux linkage is represented by "Λ".

$$E_o = \frac{d}{dt}\Lambda \qquad (2\text{-}7)$$

The flux linkage in a coil by magnet can be illustrated as in Figure 2.5.
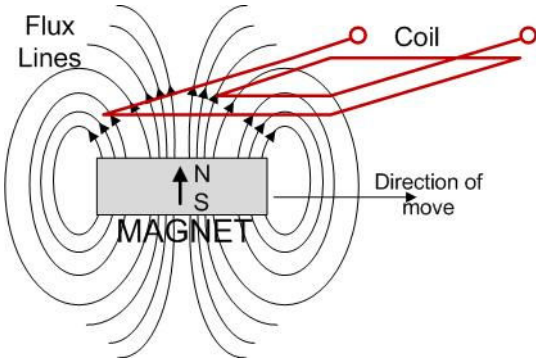
Figure 2.5: Illustration of a magnet linking a coil

As the magnet moves under the coil (see Figure 2.6), number of flux lines (thus flux linkage) varies with time. This variation can be measured as induced voltage between terminals of the coil.
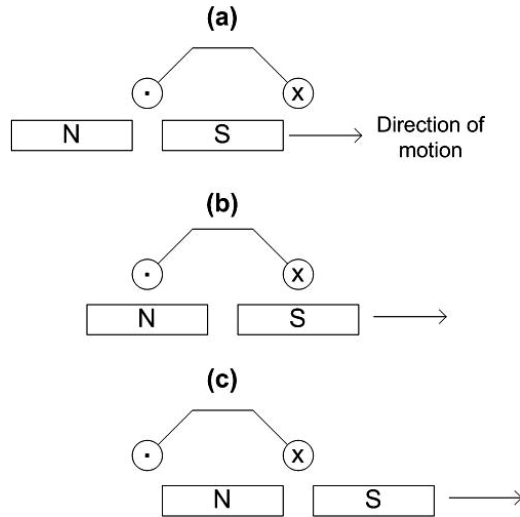
Figure 2.6: Moving magnets under a coil

The variation of flux linkage Λ and induced emf voltage E_o on the coil in Figure 2.6 is illustrated in Figure 2.7.
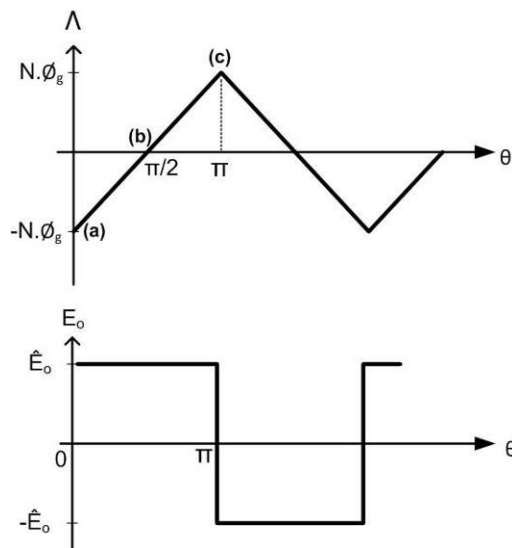
Figure 2.7: Flux linkage and induced EMF voltage on a coil

(Refer to Figure 2.6 for (a), (b), (c) positions)

In the figure "N" represents number of turns in the coil, $\emptyset_g$ is mean or rms value of airgap flux density, $\hat{E}_o$ is peak value of induced emf voltage. The equation (2-7) can be developed to represent the induced emf voltage in terms of airgap flux.

$$E_o = \frac{d}{dt}\Lambda = \frac{d\theta}{dt}\frac{d\Lambda}{dt} = \omega_e\frac{d\Lambda}{dt} \qquad (2\text{-}8)$$

For the flux linkage waveform in Figure 2.7 dΛ/dt term can be written explicitly (equation (2-9)) and amplitude of induced emf voltage can be calculated (equation (2-11)).

$$\frac{d\Lambda}{dt} = \frac{2N\phi_g}{\pi} \qquad (2\text{-}9)$$

$$\omega_e = \frac{p}{2}\omega_m \qquad (2\text{-}10)$$

Integrating equations (2-9), (2-10) and (2-8) results the expression for amplitude of induced EMF voltage (2-11). If induced EMF voltage per phase of a motor is the case, then "N" must be considered as total number of turns per phase of the motor.

$$\hat{E} = p\omega_m\frac{N\phi_g}{\pi} \ (V_{\text{peak}}) \qquad (2\text{-}11)$$

2.4 Steady state operation

In steady-state operation the flux-linkages in the rotating system and the speed are constant. The time varying expressions in voltage equations can be eliminated.

$$d\Psi/dt = 0 \qquad (2\text{-}12)$$

$$d\omega/dt = 0 \qquad (2\text{-}13)$$

At steady state, the dynamic system equations can be simplified. Rewriting equations (2-5), (2-6) gives steady state voltage equations (2-14) and (2-15).

$$V_d = R_{ph}I_d - \omega.L_qI_q \qquad (2\text{-}14)$$

$$V_q = R_{ph}I_q + \omega.L_dI_d + \omega.\Psi_M \qquad (2\text{-}15)$$

For synchronous motors, the steady state electromagnetic torque expression for rotor synchronous frame in two axis d-q model is as in equation (2-16).

$$T_{em} = \frac{3}{2}\frac{p}{2}\left(\Psi_dI_q - \Psi_qI_d\right) \qquad (2\text{-}16)$$

This expression can be edited for PM motor case by equation (2-3) which includes magnet flux term in the equation. Rewriting the equation with editing axis flux terms Ψ_d, Ψ_q results equation (2-17).

$$T_{em} = \frac{3}{2}\frac{p}{2}\left(\left[L_d I_d + \Psi_M\right]I_q - \left[L_q I_q\right]I_d\right) = \frac{3}{2}\frac{p}{2}\left(\Psi_M . I_q + \left[L_d - L_q\right]I_d . I_q\right) \qquad (2\text{-}17)$$

The torque expression in equation (2-17) is formed by two terms. The first term "$\Psi_M.I_q$" represents allignment of the magnet flux with the MMf created by stator windings. The second term is due to saliency of the rotor. The presence of magnets on d-axis increases effective airgap because magnetic permeability of permanent magnets is like air ($\mu_r \sim 1$). This results Ld being smaller than Lq, thus a saliency occurs. Similar to reluctance motors, this saliency produces a torque on the shaft also. However, as seen from the equation, if proper conditions are satisfied for zero I_d current, then this reluctance torque component can be eliminated.

The mechanical response to developed electromagnetic torque can be modeled with equation (2-18).

$$T_{em} = \frac{J}{p/2}\frac{d\omega}{dt} + T_{fw} \qquad (2\text{-}18)$$

In equation (2-18), T_{el} is the developed electromangetic torque, ω is electrical speed in radians per second, p is number of poles, J is mechanical inertia of rotor and T_{fw} is loss torque due to friction and winding losses. Acceleration or deceleration characteristic of a PM motor can be predicted by solving the equation for $d\omega/dt$ term.

2.5 Conclusion to CHAPTER 2

In this chapter analytical model of the PM motor is presented. Solving the magnetic model in Figure 2.2, equivalent two-axis electrical model in Figure 2.3 and torque equations (2-17) and (2-18) results in complete modelling of motor for electromagnetic performance analysis which include torque vs. speed, current vs. speed, induced emf voltage vs. speed.

The parameters defined in the model can be measured directly or calculated with measurements data. Determination of the parameters and integrating to the model will enable the user to simulate the behaviour of the present motor.

CHAPTER 3

MEASUREMENT of PERFORMANCE and PARAMETERS of BRUSHLESS DC MACHINES

Modern high performance drive systems and controllers depend on analytical motor models embedded in the system. Both simulations and controllers need accurate parameters to successfully estimate motor performance. Because of this dependence, several methods for parameters measurement of SM have been presented in the literature during the last century and tests standards are established [1], [2].

Testing and characterization of PM motors are in principle similar to conventional synchronous motors. Performance tests like determination of pull-out torque, starting torque and current have straight forward procedures. Unfortunately, parameter measurement methods for standard SM cannot be applied to the PM synchronous motors (PMSM), because the effect of magnets as a constant source of flux cannot be deactivated where field excitation has to be altered. Due to this fact experimental and operational parameter analysis of PM motors has gained extreme interest, and also intensive activities in design and analysis have appeared. During the last two decades many methods were introduced for PMSM like [13], [14], [15], [16], [17], [18], [19]. In the mentioned studies most authors use special laboratory test setups for their own study, which makes iteration of the proposed method difficult by other researchers. One specific example is determination of the load angle of a PMSM, which is angle between magnetic axis of the rotor and magnetic axis of MMF created by stator winding. This is such a challenging topic that some authors tried to do parameters measurement without dealing with load angle [16]. Despite having so many studies on measurement of PMSM parameters, still there are neither specific test procedures nor standards, which shows that the topic is worth studying.

Although analytical calculations and finite element (FE) methods are friendlier to extract motor parameters, much effort goes to test procedures since exact value of a parameter can be defined by only measuring the relevant parameter directly. Gieras et al [19] states

that "simple analytical equations describing the form factors[i] of the armature field may be adequate for evaluating the synchronous reactance of typical salient-pole synchronous machines with electromagnetic excitation; however they cannot always bring good results in the case of small PM motors". The air gap magnetic field is often difficult to express by analytical equations in case of PMSMs due to intricate rotor structure.

In this chapter, steady state PM motor parameters are defined and extracted through a systematic test procedure. The aim of the work is to develop simple test procedures that can be easily performed in a laboratory environment. Throughout the test, any calculation can be done with a simple hand calculator.

The aim of the experimental measurements must be to offer accurate estimated and validated machine parameters which can be used for validation of the design method and design solution as well as machine operational performance characteristics simulations, so careful study should be performed in order to have an accurate and reliable validation basis.

The parameters to be measured are defined in the previous chapter. The parameters in the proposed motor model will be the focus of the measurements. Those parameters can be listed as follows:

- Armature Resistance (R_s)
- Core Loss Resistance (R_c)
- Inductances (L_d, L_q)
- Induced EMF Voltage (E_o)

Also in this chapter, the electromagnetic performance of the PM motor is evaluated and the analytical model developed in CHAPTER 2 is verified with measurement of the listed parameters and performance of the motor. With this effort, the basis of the design and optimization work is tried to be formed. It should be noted that any measurement method proposed in this chapter is to be done on a Y-connected motor where neutral point cannot be reached. Measurements with respect to machine neutral point are not studied.

---

[i] The form factors of the stator field are defined as the ratios of the first harmonic amplitudes-to-the maximum values of normal components of stator (armature) magnetic flux densities in the d-q axes respectively [19].

3.1 Test Motor and Laboratory Test Setup

3.1.1 Tested Motor

All the test work in this thesis work is going to be performed on a radial flux, inset magnet PM machine. Rated values of the test motor are written on the nameplate as follows:

Table 3.1: Nameplate data of the tested PM motor

Rated Voltage	21 Vdc	Rated Torque	1.47 Nm
Rated Speed	1800 rpm	Rated Current	17 A_{rms}

Dimensional details and some other parameters of the test motor are tabulated in Table 3.2.

Table 3.2: Sample motor data from manufacturer sheet

Stack length	1.5 inch (38 mm)	Continuous stall torque	1.64 Nm
Number of Poles	8	Continuous stall current	19 A_{rms}
Number of slots	27	Peak stall torque	2.9 Nm
Number of coils per phase	9	Peak stall current	35.0 A_{rms}
Number of turns per coil	4	Rated torque	1.47 Nm
Slot fill factor	33.9 %	Rated current	17.0 A_{rms}
Torque constant	0.086 Nm/A_{rms}	EMF constant	0.071 V_{peak}.s/rad
Inductance L_d	0.125 mH	Inductance L_q	0.133 mH
Terminal to terminal resistance	0.136 ohm	Terminal to terminal inductance	0.237 mH

In following Figure 3.1, torque-speed characteristic of the tested machine given by manufacturer is presented. Note that although motor rated current is defined as 17 A_{rms} on the nameplate, torque-speed characteristic is presented for 19 A_{rms} and maximum current 35 A_{rms}. The given graph is not modified by the author of this thesis to keep originality of the manufacturer document.

As presented in Table 3.2, the tested motor has 8 poles and 27 slots with 3 phase winding. Since slots per pole per phase is a fractional value 1.125, it states that stator winding is a

double layer winding. The winding scheme is presented in Table 3.3 where for each coil in-out slot numbers are given.
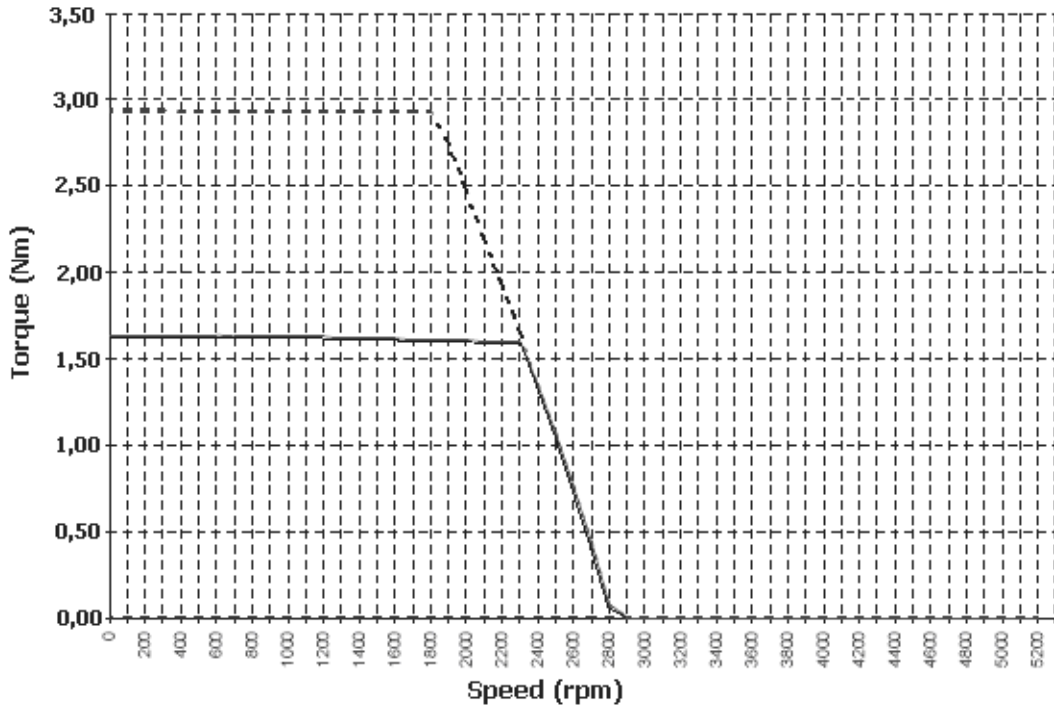
Figure 3.1: Torque vs. Speed characteristic of sample motor by manufacturer

(At 21V bus voltage with vector control drive)
(Dashed line is at max current 35 Arms, straight line is at rated current 19 Arms)

Table 3.3: Test motor winding details

Coil Number	Phase.A		Phase.B		Phase.C	
	IN	OUT	IN	OUT	IN	OUT
1	1	4	19	22	10	13
2	1	25	19	16	10	7
3	7	4	25	22	16	13
4	8	11	26	2	17	20
5	14	11	5	2	23	20
6	14	17	5	8	23	26
7	15	18	6	9	24	27
8	21	18	12	9	3	27
9	21	24	12	15	3	6

As observed in Table 3.3, two conductors of each coil is separated by 3 slots. Since the motor has 27 slots which results in 27/8 slots for each pole, it can concluded that each coil has 8/9 pole pitch.

Moreover, since there are 9 coils for 8 poles, two of the coils form one pole for every phase meaning that one pole has more MMF created by stator winding than other poles.

The tabulated data in Table 3.3 is illustrated in Appendix A.6 as a winding scheme. Two coils coinciding in one pole can be observed in that figure.

3.1.2 Laboratory Test Setup

To perform a comprehensive motor test, all electrical parameters (such as voltage, current, power) must be able to be measured and an auxiliary unit must be available to load the tested machine mechanically. Overall view of the test setup proposed for the tests is illustrated in Figure 3.2.
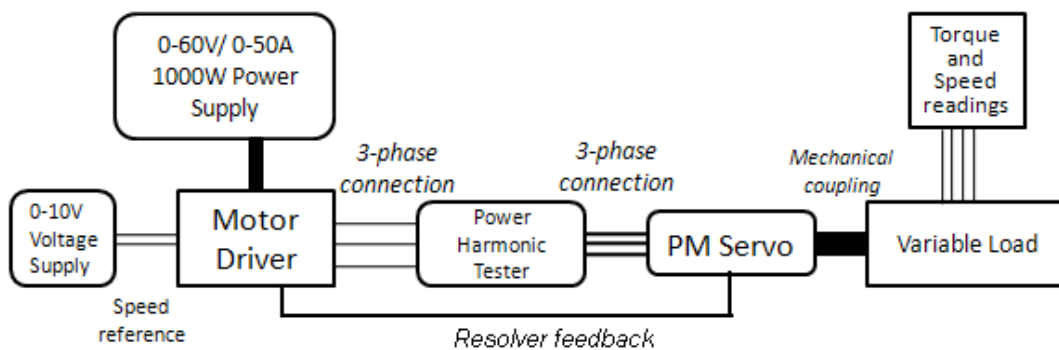
Figure 3.2: Test Setup for Parameter Measurements

The test setup is formed with the following laboratory setup:

   i.   0-60V/0-50A,1000W Power Supply (Agilent 6032A)
   ii.   Oscilloscope (Tektronix TDS3034B)
   iii. Power/Harmonic Tester (Hioki 3194 Motor/Harmonic Hitester)
   iv.   Controlled Variable Load (Lucas-Nülle Magnetic Power Brake SE2662-5R)
   v.   0-10V Voltage Supply
   vi.   Motor Driver
   vii. PM Servo Motor

3.2   Methods for Measurement of Parameters in the Literature

In this section, available standards and previous studies on measurement of parameters of PM machines are presented.

3.2.1 Measurement of Winding Resistance

Procedure of winding resistance measurements of synchronous motors is presented in IEEE Std 1158-1995 [3] in Section 3.3: Resistance measurements which addresses IEEE Std 118-1978 [4]. In reference [4], section 2.1 is dedicated to low value resistance measurements which is the case for the sample motor in this study. It should be noted that most modern motors designed for servo applications have a very low phase resistance value (below 100mΩ).

It is stated that, in low-value resistance measurements, contact resistances may seriously limit accuracy; however their effects can be reduced considerably by using resistor with four terminals. A very useful property of a four-terminal resistor, derivable from the reciprocity theorem, is that the four-terminal resistance is unchanged if the two potential terminals are used as current terminals while the two current terminals are used as potential terminals.

A precise resistance measurement can be performed with a four-wired ohmmeter instead of a four-terminal resistor as stated in the standard where two of the wires are for current injection and others for voltage sensing.
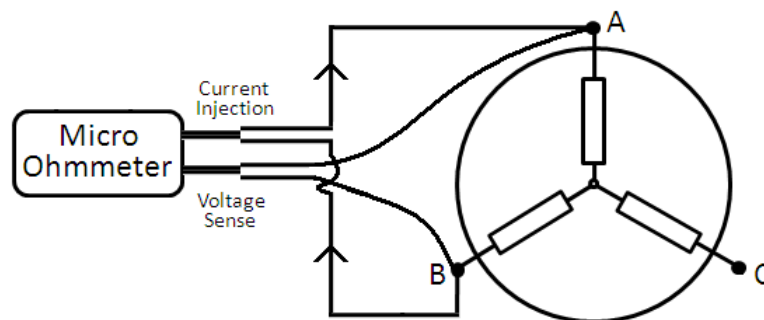
Figure-3.3: Test setup for resistance measurement

The losses appear as heat and increase the machine temperature. The increasing temperature results in increase in the resistance of windings. In this case, the resistance

value measured at room temperature will not be accurate for analytical calculations. For any winding temperature, resistance of the windings at room temperature can be corrected with equation (3-1).

$$R'_{ph} = \frac{234.5 + T}{234.5 + T_o} \times R_{ph}$$

(3-1)

This modified resistance R'_{ph} value may be used instead of resistance at room temperature R_{ph} in analytical performance calculations to get more accurate results in operating conditions.

3.2.2 Measurement of Inductance

Inductance measurement is a special problem for all electrical machines but in PM machines it is an attractive field of theoretical and practical studies. Studies on parameter measurements in the last three decades have investigated measurement of inductance of PM machines and still efforts go to this area.

Although motor performance measurement methods in standards can be easily adapted to PM machines, parameter measurement tests for synchronous and induction machines dealing with reactances (equivalently inductances) are difficult to interpret or even inapplicable to PM machines due to presence of magnets as a constant flux source. That is why standard procedures to measure inductance cannot be applied to PM machines.

Accurate inductance measurement results are important for modern high performance motor drives. Since conventional machines are replaced by PM machines, more work is done to improve the overall electromechanical performance of "drive + motor" systems. Dynamic and steady-state performance analysis and precise control of PM machines depend on accurate equivalent circuit models of the system with correct parameter values.

i. *Measurement of Quadrature-axis synchronous reactance X_q in Standards*

Quadrature axis synchronous reactance X_q is defined in [5] as the ratio of the fundamental component of reactive armature voltage due to the fundamental quadrature-axis component of armature current, to this component of current under steady-state conditions and at rated frequency.

This definition can be clarified on a phase diagram. In Figure 3.4, reactive armature voltage due to quadrature-axis component of armature current is the vector of "$I_q.X_q$" seen on top of the figure. So if amplitudes of "$I_q.X_q$" vector and q-axis armature current "I_q" are extracted, X_q can be determined.
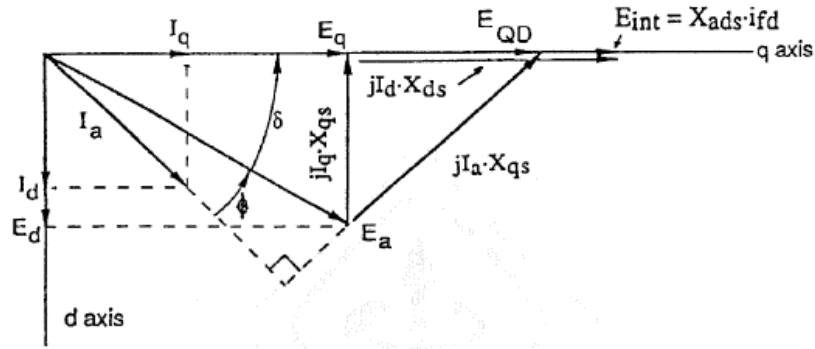
Figure 3.4: Phase diagram for a synchronous machine [3]

The standard [3] proposes four different methods under Section 10.4 to determine X_q. Two of these tests (Sections 10.4.2 and 10.4.3 in [3]) require zero field excitation, so they are not applicable to PM machines. One other method (Section 10.4.4 in [3]) proposes an empirical function of motor dimensions to calculate X_q/X_d ratio and determining X_q from X_d value which is far from being accurate and reliable.

The last method (Section 10.4.5 in [3]) states that load angle determination may be used with voltage and current measurement to determine X_q. This is most applicable where determination of internal load angle is necessary. The definition of internal load angle "δ" is given in IEEE Std 100-1992 as follows: "The angular displacement, at a specified load, of the center-line of a field pole from the axes of the armature MMF pattern."

In section 10.8.2 in [3], various load angle determinations are presented:

      i.   calculation of internal load angle

      ii.   stroboscope technique of measurement,

     iii. electronic measurement of load/phase angle

Among these, the last method of electronic measurement is more applicable in the sense of available laboratory equipment. In this method, internal load angle is measured by comparing the phase difference between a once-per-pole-pair pulse on the shaft and a "squared-off' terminal voltage signal.

ii. Measurement of Direct-axis synchronous reactance X_d in Standards

Direct axis synchronous reactance X_d is defined in [5] as "the quotient of a sustained value of that fundamental alternating current component of armature voltage that is produced by the total direct-axis flux due to direct-axis armature current and the value of the

fundamental alternating-current component of this current, the machine running at rated speed".

The standard [3] proposes one method in Section 10.3 to determine X_d which states that the synchronous impedance X_d in per unit is equal to the ratio of the field current at base armature current, from the short-circuit test, to the field current at base voltage on the air-gap line. Since there is no field excitation in PM machines this method can not be applied.

iii.   *Measurement of X_d and X_q in the Literature*

In this chapter, previous studies in the literature on PM machines inductance measurement presented are investigated. It is evident that it is impossible to cover all the studies, but a selection may be done among them to summarize the proposed methodologies about the topic.

Methods mentioned in the literature generally depend on the PM machine phase diagram presented in Figure 3.5. The figure is similar to Figure 2.4 in CHAPTER 2. The angle between motor phase voltage V_t and back EMF E_o is motor load angle "δ". When talking about d-q axes parameters (E_o, L_d, L_q, X_d, X_q, I_d, I_q), this phase diagram should be considered.
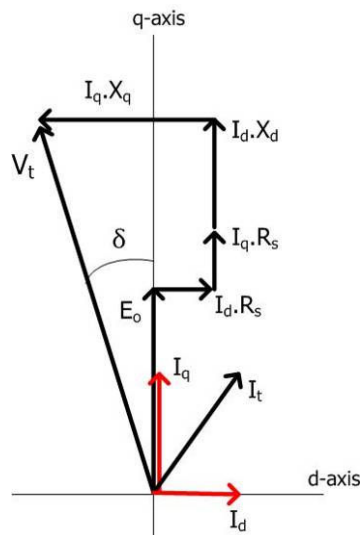
Figure 3.5: Phase diagram of PMSM at normal operation

Note: Vectors in the figure are exaggerated for clarity.

Having investigated many of the studies, a number of common features of the proposed methods are determined which can be listed as follows:

i. What is the aim of the study?
ii. What kind of machine is tested?
iii. What method is used to drive the tested machine?
iv. What is the measurement method?
v. Is load angle measured? How?
vi. Is frequency dependence of inductance investigated?
vii. Is current (or equivalently load) dependence of inductance investigated?
viii. Is cross-coupling between d-q axes components investigated?
ix. Does E_o vary with current (or equivalently load)?
x. What is the comment of authors about the results?
xi. Is the offered method suitable to apply on the test motor in this thesis work?

Selected papers from respected authors will be analyzed in terms of the determined features and presented in following sections in chronological order. Results and interpretations will be discussed in each section. At the end, inferences will be tabulated to have an overall view.

Study.1

Author: TJE Miller [13], 1981

The study by Miller is one of the first attempts to measure d-q reactances of a 1.5 kW internal magnet PM machine. Two different measurements are proposed; load test at running conditions and static (standstill) inductance measurement.

In standstill tests, the degree of interaction between d-q axes quantities is tried to be measured with a special double bridge circuit which is illustrated in Figure 3.6. Motor windings are connected in d-connection (phase B-C terminals are short circuited) and excited with dc while rotor is fixed at 0° (rotor is aligned with phase A magnetic axis). In the circuit, secondary voltage source V2 biases the windings with q-axis current without disturbing the balance of main bridge circuit. This second dc bias does not contribute to d-axis flux because d-axis MMFs of phase B and C cancel each other. Static flux linkage measurements were done to determine reactance variations while controlling d-q axes currents independently.
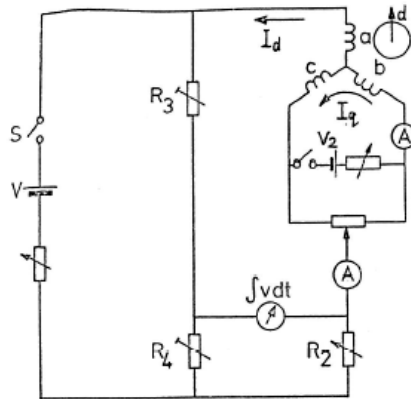
Figure 3.6: Double bridge circuit for measuring the interaction between d-q axis parameters [13]

In the load tests, the tested motor is driven directly from the line with an adjustable load coupled to the shaft. Line current is varied by adjusting the load. Voltage, current, power factor and torque angle are recorded to define the phase diagram. Load test measurements are conducted only in 50Hz by driving tested motor directly from line, so frequency dependence is not investigated. Back EMF voltage E_o is assumed to be constant at the value determined at rated motor speed. Variation of reactances X_q and X_d are investigated with respect to line current (Figure 3.7). The method of determining the load angle is not specifically defined but two methods have been proposed; stroboscopic illumination of a graduated disc attached to shaft, or clamping a collar to the shaft with a magnetic projection which produces a pulse to trigger line voltage waveform on oscilloscope. Results of this study are presented in Figure 3.7 and Figure 3.8.
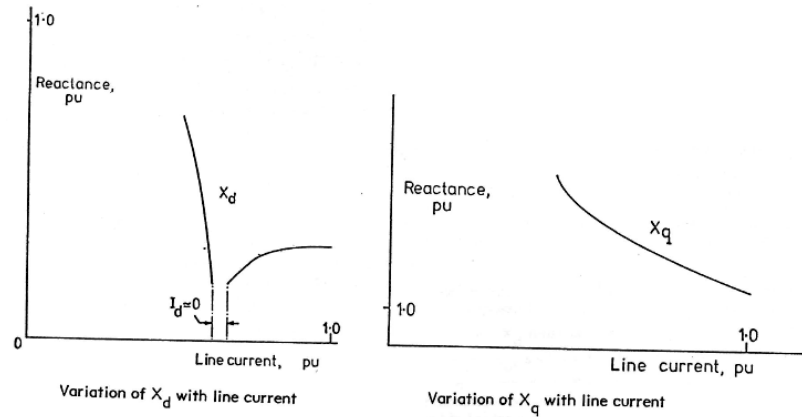
Figure 3.7: Results of X_d and X_q measurement from load tests by Miller [13]
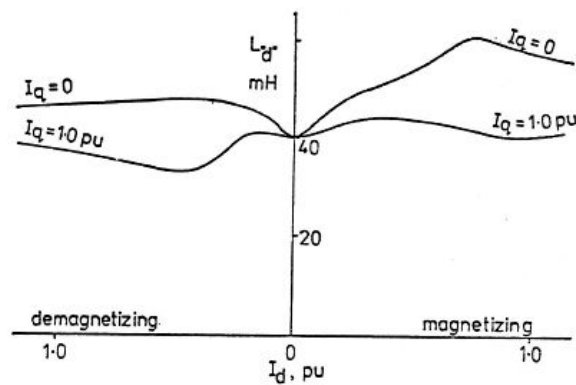
Figure 3.8: L_d variation with I_d and its interaction with I_q from standstill test [13]

From presented curves by Miller, it can be concluded that;

- X_d is not measurable at a specific line current where I_d equals zero. This is an expected result since the measured current and load angle quantities become very small and calculations are susceptible to measurement errors. Beyond this point, X_d dramatically rises with negative I_d whereas X_d doubles with positive I_d at rated line current (Figure 3.7).

- X_q measurements are available for 0.5 - 1.0 p.u. line current. In this range, X_q decreases to 25% of initial value (Figure 3.7).

- L_d increases by 50% up to 0.8 p.u. magnetizing I_d while I_q=0. Increase in L_d is suppressed in I_q=1 p.u. case where L_d value is same for I_d=0 and I_d=1 p.u.

33

(Figure 3.8). The increase of L_d with I_d is unexpected result. Common sense is a constant inductance value or decrease with current due to saturation.

- L_d increases by 10% with demagnetizing I_d while I_q=0. In presence of I_q=1 p.u., L_d decreases by 25% with 0.5 p.u. demagnetizing I_d then this value restores to initial L_d value with I_d=1 p.u. (Figure 3.8).

- L_d - X_d variations of standstill and load tests do not agree with each other in demagnetizing condition. The dramatic increase in X_d in load tests is not observed in standstill tests where Ld is constant for a wide range of I_d current. This is probably due to cross coupling between d-q axes components and constant E_o assumption in load tests. X_d is plotted against line current for load tests which may not be comparable with L_d - I_d variation where only I_d is present

- Miller concludes that "saturation characteristics of PM motors make it impossible to specify E_o and X_d uniquely because there exists only one equation for two unknowns; Any value quoted for Xd must be associated with a specified (arbitrary) value of E_o, such as the true open circuit". This statement refers to a need for constant E_o assumption because as seen in Figure 3.19-a, it is not possible to separate E_o and X_d with one d-axis voltage equation. One of them must be assigned with a value. Also it is stated that bridge method does not produce results of highest precision, but may be used to enhance the level of confidence in X_d and X_q values determined from load tests.

The other conclusions from this study can be summarized as follows:

- The load tests offered by Miller depend on extraction of load angle.

- Neglecting resistance of the windings as in the study is not acceptable in case of voltage drop on resistance is comparable to back EMF voltage E_o and must be inserted in the phase diagram.

- The inductance bridge method is not practical since stability of resistances in the circuit may not be controlled due to thermal changes with high currents ($17A_{rms}$ rated for this thesis work).

- Hysteresis effects may produce scatter in calculated reactance results which is also mentioned by the author of this study.

Study.2

Author: B.J. Chalmers [14], 1985

Chalmers et al [14] tried to determine reactances of the tested 275W, 100V, internal magnet PM machine based on two-axis machine theory. In the study, identification method of parameter estimation offered by Eykhoff [11] is applied and a new method which searches for I_d=0 condition to measure specifically X_q is proposed. The tested motor is driven with scalar control at different frequencies between 7.5Hz and 50Hz for the full 360° range of load angles at various supply frequencies. Voltage, current and power is measured at motor terminals for each operating condition. The load angle was measured using a stroboscope that is triggered by the sinusoidal motor phase voltage. Applied methods require measuring input current and power at a particular supply voltage, for a range of load angles in the range 0-90°. From these measurements, with the knowledge of load angle, I_d and I_q are evaluated with respect to Figure 3.5. Curves of I_d and I_q against load angle are then constructed and the point where $I_d = 0$ is found. X_q is calculated at that point. In this study, $X_q - I_q$ relation is identified (Figure 3.9). Results of frequency dependence of reactances are not illustrated as a figure, but explained in words instead.

(a) *Parameter values by identification method*   (b) *Variation of X_{q0} with I_q by the new method*
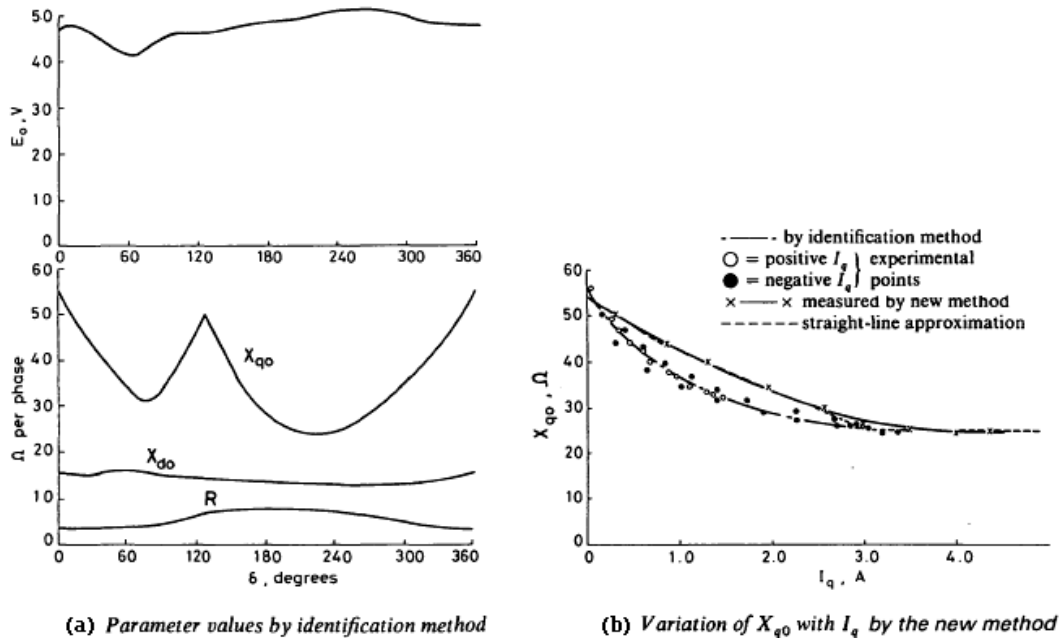
Figure 3.9: Results of the study by Chalmers et al. [14]

35

Chalmers et al concludes that;

- Excitation EMF E_o and d-axis reactance X_d are substantially constant under varying load, which is due to high coercive magnets on d-axis.

- Phase resistance R varies from its cold value, in regions of small load angle ($0 < \delta < 90°$), to about double that value at high currents ($120° < \delta < 300°$, see Figure 3.9-a). This variation is mainly attributed to temperature rise during the tests. This result

- A cyclic variation of X_{q0} with load angle is observed. This variation was clarified when X_{q0} was plotted against I_q (Figure 3.9-b), showing that X_{q0} followed the same curve for both positive and negative values of Iq.

- The only statement about frequency dependence is as follows; at rated torque, I_d is negative and its magnitude decreases as frequency is decreased. At the same torque, I_q increases as frequency is decreased. This causes L_{q0} to decrease owing to saturation, as in Figure 3.9-b. This relation, which says that Lq decreases with decreasing frequency, is not illustrated but interpreted depending on I_d - Torque and I_q - Torque curves.

Besides these conclusions, it is evident that the offered method to measure X_q by seeking $I_d=0$ condition through measurements is useful but primitive in presence of a vector control drive since $I_d=0$ condition, which is sought through measurements, can be easily satisfied. However the interpretations of the author on the results are important.

Study.3

Author: S.F. Gorman et.al. [42], 1988

In this work, authors try to determine synchronous reactance of an internal PM motor (0.55kW, 380V, 1.10A). The tested motor is driven as a generator by an auxiliary DC motor. A balanced three-phase load is placed across the terminals of the tested machine. The load angle is determined with a stroboscopic pointer system. X_d and X_q are determined by solving d-q axis voltage equations for each particular set of data (phase voltage and current, power factor angle, load angle, back EMF voltage). Back EMF voltage E_o is assumed to be constant at the value that is measured at motor terminals at no load at rated speed. DC value of phase resistance is inserted into d-q axes equations. The test is conducted for a single current value (for a single load condition) which does not give

variation of parameters with current and cross relation between d-q axes. Also frequency dependence is not studied.

Although this is not a comprehensive study, operating the PM machine as a generator is a different approach regarding other presented studies. If a variable three phase balanced load is available, which is fully characterized before the test in terms of resistance and inductance, one can determine the internal reactance of the motor by loading the motor at constant speed. At first step, the motor is driven by auxiliary machine and emf at motor terminals is observed. The observation must be done by triggering the measurement by means of a pulse generator attached to the rotor shaft which outputs a pulse per revolution. The observed waveform at motor terminals at this condition is internal emf voltage of the tested motor which is also zero load angle. Depending on loading, the observed voltage waveform will shift in terms of amplitude and angle because the current in the windings will result a voltage drop on internal resistance and inductance. For each specific loading case, defined set of data (phase voltage and current, power factor angle, load angle, back EMF voltage) must be recorded. By resolving the current into d-q components, X_d and X_q can be determined for that case from the phase diagram related to the operating condition.

There may be cross coupling between d-q axes components since I_d and I_q are present at the same time. However, at low current, cross coupling between axes may be assumed to be negligible and unsaturated d-q axes can be determined.

The weakness of this method is that d-q axis currents can not be controlled independently. For example, a pure q-axis current can not be drawn from the machine because it will not be in-phase with back EMF voltage E_o due to introduced phase by reactance of the windings and load. The same situation is valid for d-axis case.

Study.4

Author: P.H. Mellor et al. [16], 1991

Mellor et al [16] pointed out the difficulty of load angle measurement and tried to avoid dealing with load angle by an iterative solution of the two axis theory. A static inductance bridge test, no-load and load tests are conducted to determine X_d, X_q and E_o and their variation with current (or equivalently load). The tested motor (4-pole, internal magnet, $8A_{rms}$ rated, D60 frame motor with damper bars in the rotor) is driven by terminal voltage control. The equations to determine parameters from measurement data are based on the PMSM phase diagram (Figure 3.5) and two-axis motor model (Figure 2.3).

By running the machine at no load, the permanent-magnet excitation E_o at zero armature reaction and the core loss resistance R_c are identified.

$$E_0 = V_t - I_a R_s \tag{3-2}$$

$$R_c = \frac{E_0}{I_a} \tag{3-3}$$

The direct-axis synchronous reactance X_d is measured by performing the no-load test over a range of terminal voltages to vary the terminal current. At each load current, X_d is calculated from internal voltage E_i and current I_d using equations (3-4), (3-5) and (3-6). In the equations V_t is phase voltage, I_a is phase current, $\cos\phi$ is power factor.

$$X_d = \frac{|E_i - E_0|}{I_d} \tag{3-4}$$

$$E_i = V_t - I_a R_s \cos\phi \tag{3-5}$$

$$I_d = \left(I_a^2 - \frac{E_i^2}{R_c^2} \right)^{1/2} \tag{3-6}$$
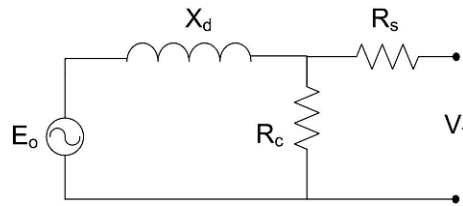
Figure 3.10: Equivalent circuit diagram of PM machine at no load

To determine X_q from a load test, a rotor sensor is used to index the direct axis alignment of one winding and adjusting the motor load and voltage until the terminal current is in-phase with back EMF E_o (I_d=0 condition). This is also the vector control condition. The phase diagram for this particular case is shown in Figure 3.11 and X_q is calculated by equation (3-7).
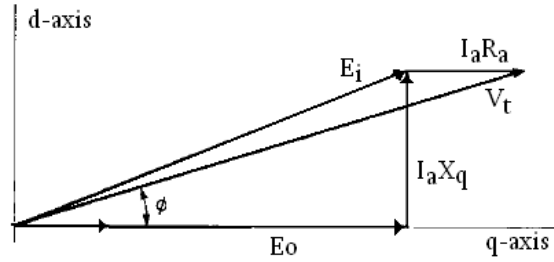
Figure 3.11: Phase diagram when I_a is on q-axis

(I_c neglected)

$$X_q = \frac{V_t \sin \phi}{I_a} \qquad (3\text{-}7)$$

Frequency dependence of parameters is not investigated since running tests are conducted at single speed (only 50Hz).

Besides running tests, an inductance bridge method is conducted at standstill to determine reactance variation which is similar to Miller's method. To obtain correct level of saturation, a DC current corresponding to peak value of current at running condition is supplied to the bridge. Measurement results of this work at 50Hz are presented in Figure 3.12.
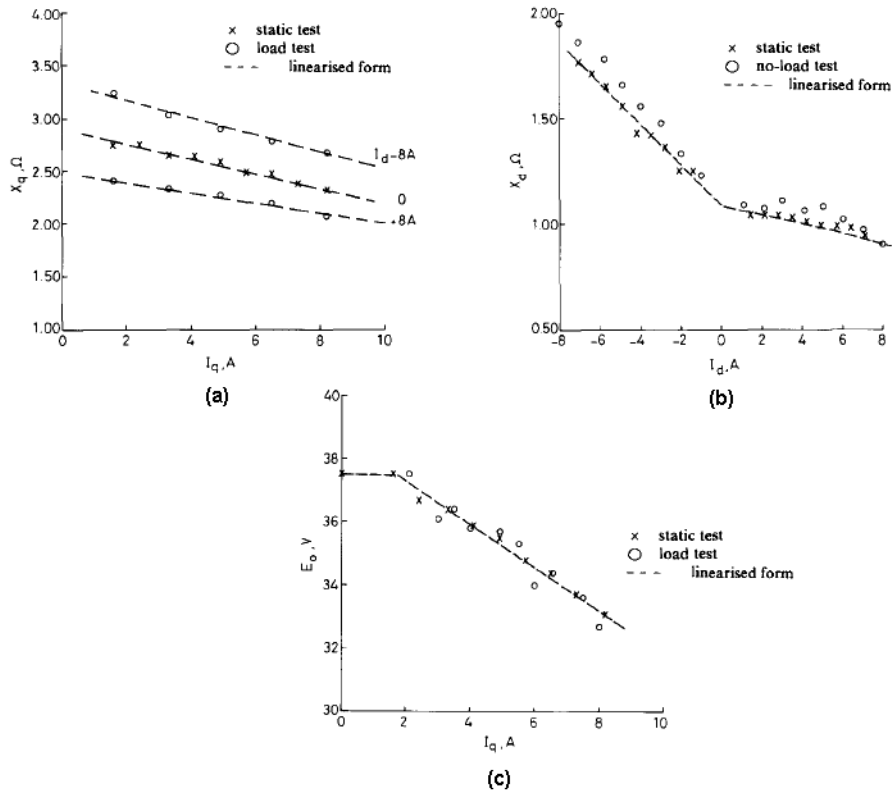
Figure 3.12: Variation of X_q, X_d and E_o by Mellor et al [16]

In Figure 3.12-a, it is shown that there is a cross coupling between I_d and X_q where a rated current in direct axis will cause approximately a 10% change in X_q. About 100% increase of X_d in negative I_d region in Figure 3.12-b is explained by a fall of the excitation field as a result of increase in the leakage around the magnet during demagnetization. On the other hand, a rated magnetizing current decreases X_d by 10%. E_o decreases by 15% with increasing I_q which is explained by higher level of saturation in the rotor poles with increasing I_q. Another fact is that results of standstill and running tests agree with each other.

The offered no load and load tests are easily applicable in presence of vector controlled drive since d-q axes current can be controlled independently. The inductance bridge method by the author may not be practical to apply since it is hard to maintain the stability of the bridge circuit under excessive currents if the motor has high current ratings.

Study.5

Author: M.A. Rahman, Ping Zhou [39], 1994

Rahman and Zhou [39] tried to determine saturated X_d, X_q and Eo parameters of a PM motor and variation of Eo with load. The tests are conducted on a 1 hp, 4 pole, interior PM motor which is driven from a 60Hz line with voltage control method. A variable load coupled to the shaft is used to alter load angle.

Load angle was detected by with a micro-processor based digital setup. As the authors stated; for motoring operation, when the zero crossing of any one of the three phase terminal voltages as the reference to initiate a pulse and the zero crossing of the magnet excitation voltage in the same phase winding to terminate the pulse are used, the resulting pulse width will then represent the instantaneous torque angle. For generating mode, the reverse will happen.

This study is based on the fact that d-q phase diagram of PM machine includes both three unknown parameters E_o, X_q and X_d but only two voltage equations (equations (2-5) and (2-6)) can be formed. This problem is solved by obtaining a third equation with a slight change of the load where it is assumed that back EMF and inductance does not change under this condition or the change can be ignored.. It is not defined how much the load is changed however Stumberger et al [17], who repeated Rahman's work with a different setup, defined this change as varying the load so that 0.1° change in phase angle between terminal voltage and current occurs. The derived third equation together with the other two equations related to d-q axes are as follows.

$$E_i \sin \delta_i = I \sin \delta X_q \qquad (3\text{-}8)$$

$$E_i \cos \delta_i = E_o + I \cos \beta X_d \qquad (3\text{-}9)$$

$$E_i' \cos \delta_i' = E_o + I' \cos \beta' X_d \qquad (3\text{-}10)$$

In the equations, E_i is motor phase voltage, I is phase current, δ is load angle, and β is motor current phase angle with respect to stator magnetic field d-axis. X_d and E_o are separately determined with equations (3-16) and (3-25). The result of the offered method is presented in Figure 3.13.
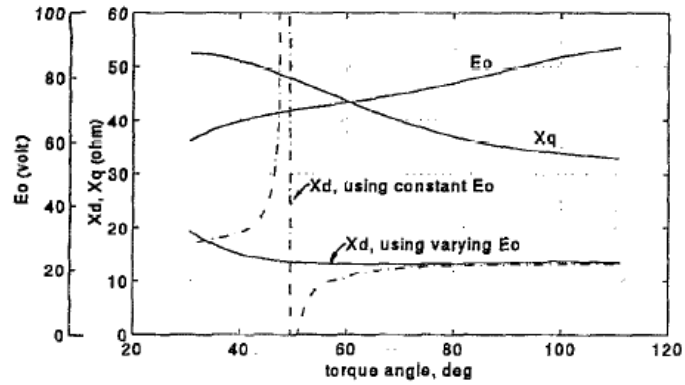
Figure 3.13: Variation of X_d, X_q and E_o by Rahman et al. [39]

The results of Stumberger's [17] similar work to Rahman's is presented in Figure 3.14. Stumberger conducted the tests on a 0.67kW, 380V, 1.49A 4-pole internal PM machine. In the figure, variation of X_d and X_q is investigated against motor load angle which is equivalent to investigating by motor terminal current and also variation of induced voltage due to magnets in dependency on internal load angle at line to line voltages 210V. 230V and 270V are presented.
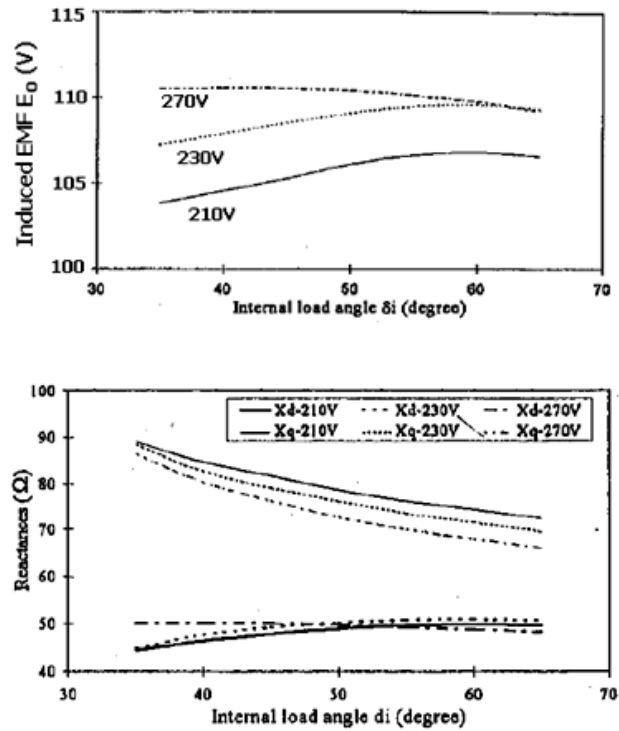
Figure 3.14: Variation of E$_o$, X$_d$ and X$_q$ at different terminal voltages by Stumberger et al [38]

Results of both Rahman's and Stumberger's work show that X$_d$ does not vary much with load. On the other hand X$_q$ considerable decreases (40% decrease in Rahman's work, 25% decrease in Stumberger's work) with increasing load. The increase in E$_o$ in Rahman's solutions is not expected to be the real case, because E$_o$ should be decreasing due to saturation of steel core with high load. It is probably due to flux enhancing with I$_d$ current injection since vector control is not applied during the defined tests.

The offered method to alter the load angle by 0.1^o is very problematic because a very precise test setup and measurement is needed which may be unrealizable in most laboratory environment. Also this very little change may not be determined even completely digital setup is used to detect load angle (instead of analog measurements like stroboscope) due to measurement errors. In conclude, this method does not seem to be practical to apply.

Study.6

Author: Fidel et al. [18], 2001

In this study variation of inductances with currents are investigated based on two-axis model. The tested motor is 220V 7A 2000rpm PM machine and it is driven by vector controlled inverter drive. The current, voltage and power are feedback to inverter through a current controller. The measured quantities are transformed to d-q rotating frame to do calculations. The tested motor is loaded with an induction motor which is controlled with an inverter. The tested motor is driven successively under $I_d=0$ and $I_q=0$ conditions. At each case the other non-zero axis current is varied up to rated value. Then L_d and L_q are calculated with equations (3-11) and (3-12) respectively which are extracted from equivalent electric circuit model (Figure 2.3).

$$I_q = 0; \qquad L_d = \frac{v_q - \omega \cdot \psi_a}{\omega \cdot I_d} \qquad (3\text{-}11)$$

$$I_d = 0; \qquad L_q = \frac{v_d}{\omega \cdot I_q - \dfrac{\omega^2 \cdot \psi_a}{R_c}} \qquad (3\text{-}12)$$

Inductance results of this study is presented in Figure 3.15.
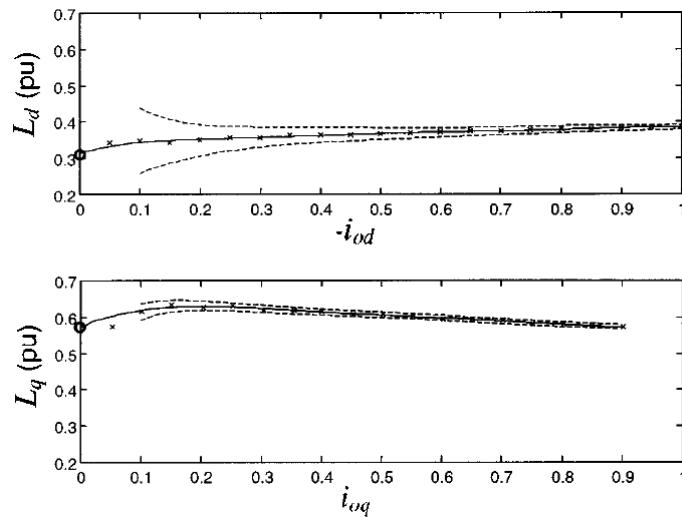
Figure 3.15: Experimental values of L_d and L_q respectively by Fidel [18]

(Dashed lines show measurement uncertainty)

44

Frequency dependence of inductances is studied by repeating the experiment at rated frequency (60Hz) and one-third (20Hz), but no significant difference due to frequency is reported. On the other hand, a 15% increase in L_d with I_d and 10% decrease in L_q with I_q are observed respectively (Figure 3.15). At very low currents, the authors recommend using an electronic bridge at standstill to determine d-q inductances and result is presented in Figure 3.15 using symbol "o" on the left axis.

Any comment on the results ox L_d and L_q variation is not presented by the authors. As seen in Figure 3.15, L_q decreases with increasing I_q which is probably due to increase in saturation level of q-axis flux path. L_d has an increasing trend with negative Id which can also be related to saturation level of associated d-axis flux path. Also in the results, uncertainty in the estimation of parameters rapidly increases as current decreases with the offered method.

Variation of E_o is not studied in this study. However determination of core loss (or equivalently iron loss) resistance R_c is stated to be very important. R_c is measured at no load with low current to reduce copper losses which can be achieved by setting $I_d=0$ and I_q sufficiently big to compensate mechanical losses at the operating speed. At this condition, current component I_{oq} in Figure 2.3 is zero and Rc can be calculated by;

$$R_c = \frac{V_q^2}{P_{in}}$$

(3-13)

where V_q is motor terminal voltage and P_{in} is measured input power. The phase resistance Rs is ignored in equation (3-13) since Rc has about 50-100 times higher value than Rs.

The offered test method by the authors is applicable to our machine since the same test setup is available and vector control drive is also present. The procedure is also straight forward and easy to follow.

Study.7

Author: R. Dutta, M.F. Rahman [44], 2006

In this work, authors compare the results of FE analysis, AC standstill and vector current control tests by applying them to a prototype IPM machine (rated as 550W, 14A, 20.2V) at same current levels. The obtained values from the tests are compared and differences are analyzed. The inductances were also computed from the finite-element (FE) model of the same machine to verify the findings.

FFT algorithm is applied to the measured voltages and currents to extract the fundamental components and then the rotor frame d-q transformation is applied to obtain d-q axis voltages and currents since d-q axes voltage equations (2-14) and (2-15) related to equivalent phase diagram of the motor PM motor is valid only for fundamental harmonic. In running tests, load angle is not measured because I_d and I_q currents are controlled by vector control and load angle is determined with respect to power factor and motor terminals (see Figure 3.19).

Frequency dependence is not studied by the authors. The influence of cross coupling currents over the flux linkages is investigated through standstill tests. Phase resistance Rs is taken into account in both tests. The obtained inductance measurements with respect to current together with FE results are presented in Figure 3.16.
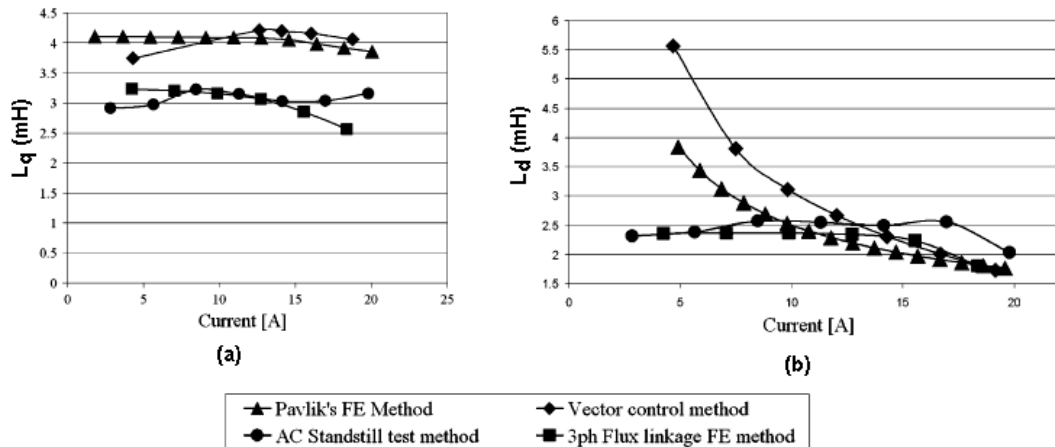
Figure 3.16: Variation of d-q inductances with current obtained from standstill and vector control tests by Dutta et al. [44]

In Figure 3.16, variation of L_q and L_d with current obtained from two test methods and FE calculations are compared respectively. AC standstill and flux linkage FE results agree for L_q, but vector control test gives out 33% larger L_q value (Figure 3.16-a). This result is explained by authors as cross coupling saturation of q-axis flux path by d-axis flux which includes both magnet flux and flux due to I_q current since they share the same flux path.

The ac standstill test and three-phase flux linkage FE method also give almost constant L_d values throughout the whole current range, whereas in the other two methods, L_d rises steeply when current is low (Figure 3.16-b). Authors explain this result with the saturation level of iron bridges in the rotor structure. In some motor structures, influence of current

46

over d-axis flux is minimal if iron bridges are fully saturated by the leakage flux between two adjacent magnet poles. However, in some of the rotor structures, the iron bridges may not be fully saturated by the magnet leakage flux alone and neither small I_d current can saturate them. In this type of situation, d-axis flux linkage is relatively higher, which results in a larger L_d for low current.

The effect of q-axis current on d-axis magnet flux linkage (cross coupling) is also studied. The effect of 10% error in magnet flux linkage on the calculated L_d is shown in Figure 3.17. It can be concluded from the result that constant back EMF voltage assumption under varying load is not truly correct and the change in magnet flux linkage due to the temperature rise should be included.

Change of L_d with error in magnet flux linkage.

With +10% error   With -10%error   Without error

Variation of magnet flux linkage with q-axis current.
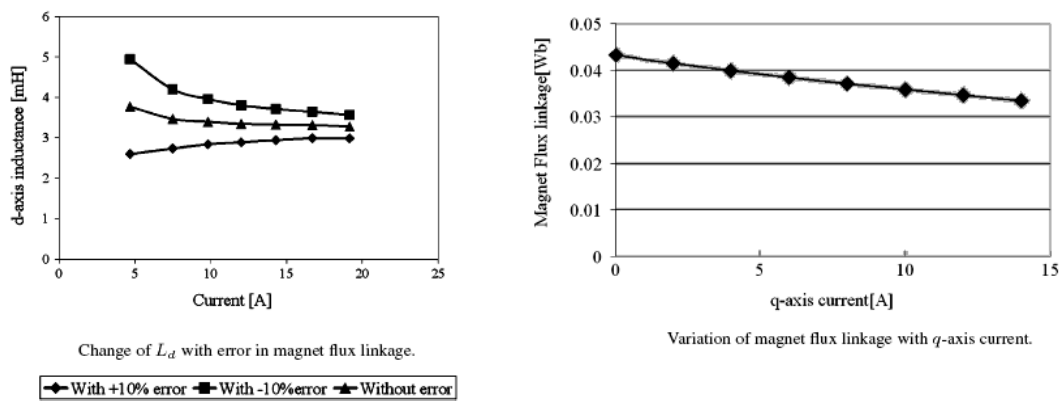
Figure 3.17: Variation of magnet flux linkage with I_q and change of L_d with different magnet flux linkage assumptions by Dutta et al. [44]

This study is an example of good approach to inductance measurement where different methods are applied and results are compared. The offered AC standstill, FE and load tests are easy to conduct.

Conclusion to Literature Review

Up to now, details of selected studies are summarized. Each of them is analyzed in terms of the features that are defined at the beginning of this section. To have an overall view of studies and to compare with each other easily, methods and results of these studies are tabulated in Table 3.4.

It can be observed in presented methods in the literature that most effort is on measurement of inductance of PM motors because it is most problematic topic. Other

motor characterization tests such as resistance measurement or torque-speed determination has straight forward procedures which are standardized for many motor types. However, very recent studies can be found on inductance measurement of PM machines which shows that methods for measurement of inductance are not mature yet to be standardized.

The presented various methods can be classified with respect to methodologies as in Figure 3.18. In the figure, proposed tests are grouped into two at first stage; Standstill Tests (where motor is not operated and the shaft is not rotating) and Running Tests (measurements are made online while the motor is rotating). Each group is divided into subgroups where load angle measurement is distinctive for running tests and excitation scheme is decisive for standstill tests.

The proposed load and no-load tests are realized either by connecting the tested motor directly to AC line or with a vector controlled drive. Since all presented methods can be realized with a vector control drive, this approach seems to be the most proper method to conduct running tests. In the running tests, half of the studies determine load angle of the tested motor at each operating condition, whereas the others accept that since axis currents can be independently controlled, power factor (PF) angle Ø can be used directly to determine the load angle. It is evident that load angle measurement is a must without a field oriented drive because there is no other way to decompose measurement quantities into d-q components. However, if there is a vector control, where d-q axes components are independently controlled, load angle can be determined from PF angle. For example, if $I_d=0$ condition is valid then load angle δ equals to PF angle Ø (Figure 3.19-a), and if Iq=0 condition is valid then load angle δ equals to "90- Ø" (Figure 3.19-b).

Table 3.4: Comparison of inductance measurement methods

Author of Study	Motor Type	Measurement Method	Drive method	Load angle	q-axis measurement	d-axis measurement	Cross-coupling	Frequency dependence	Eo
TJE Miller	Internal PM with damper bars	1) Load test	Voltage control	measured by stroboscope	Xq decreases by 75% while line current increases from 0.5 pu to 1 pu	dramatically rises with negative Id and Xd doubles with positive Id at rated line current	not investigated	only 50Hz	Constant Eo assumption
		2) Inductance bridge	DC excitation	-	-	decreases with Id	Ld decreases with increasing Iq		
Chalmers	Internal PM with damper bars	1) Load test (Parameter Identification)	Voltage control	measured by stroboscope	Xq reduces to 66% of its unsaturated value at rated current	substantially constant	not investigated	Lq decreases with decreasing frequency	substantially constant
		2) Load test (Id=0 search)	Voltage control	measured by stroboscope	Same founding as in method.1 but 10% larger values	not investigated	not investigated	not investigated	not investigated
Mellor	Internal PM with damper bars	1) No-Load Test	Voltage control	not measured	not measured	decreases by 10% with positive Id and increases by 100% with negative Id	-	Presented only 50Hz results	Eo at zero armature current is measured and used.
		2) Load Test	Voltage control	measured	Xq linearly decreases by 20% with rated Iq	-	Xq increases by 10% with negative Id and 10% decrease by positive Id	-	Linearly decreases by 15% with rated Iq
		3) Inductance bridge	DC excitation	-	Xq linearly decreases with Iq. Same trend and amplitude are measured as in load test.	Trend and amplitude of Xd variation agree with no-load test results.	Xq increases with negative Id and vice versa	-	-

Table 3.4 contd. - Comparison of inductance measurement methods

Author of Study	Motor Type	Measurement Method	Drive method	Load angle	q-axis measurement	d-axis measurement	Cross-coupling	Frequency dependence	Eo
1) Rahman 2)Stumberger	Internal PM	Load test	Voltage control	measured	30% decrease in Rahman with 80° load angle and 25% decrease in Stumberger with 30° load angle	Almost constant	Both Id and Iq exist, no controlled variation is applied	not investigated	Measured for each load angle
Matsuse	Internal PM with damper winding	DC Decay	DC excitation	-	single value at 50Hz	single value at 50Hz			
Fidel	Internal PM	1) No-Load Test 2) Load Test	Vector control	equals to PF angle	Lq decreases by 10% with rated Iq	Ld increases by 15% with negative rated Id	not investigated	no significant difference with frequency is reported	Constant Eo assumption
Dutta	Internal PM	1) AC Standstill	AC excitation	-	No significant variation of Lq with current	No significant variation of Ld with current	d-axis flux linkage decreases with Iq and q-axis flux linkage increases with negative Id	not investigated	Eo decreases with Iq
		2) Load Test	Vector control	equals to PF angle	Rises slightly by 10% then stays constant	Decreases steeply by 70% with rated Iq	-	-	-
		3) FE Analysis: a)Pavlik's method b)3ph flux linkage	-	-	Two different results from two FE analyses. Both does not vary with current	Two different results from two FE analyses. Both does not vary with current	3ph flux linkage method agrees with AC standstill	-	-

From Table 3.4, following observations can be made:

- Majority of the studies are performed on an internal magnet PM motor where magnets are placed inside the rotor steel. This shows that there is lack of attention about inset (for surface also) magnet PM machines.

- Proposed tests can be grouped in two; Standstill Tests (where motor is not operated and the shaft is not rotating) and Running Tests.

- Load angle measurement is distinctive for running tests and excitation scheme is decisive for standstill tests.

- Early works used stroboscope to determine load angle. Recent works used an encoder coupled to motor shaft for load angle extraction. Also vector control scheme is used in some recent works where load angle equals to power factor angle at motor terminals.

- Authors who use Load Test method (Miller, Chalmers, Mellor, Rahman, Stumberger, and Fidel) agree that either X_q decreases with I_q. Only Dutta states that no significant variation of X_q occurs with I_q.

- For X_d measurement; Miller, Mellor states that X_d decreases with positive I_d and increases with negative I_d. Fidel agrees with these authors for negative I_d case. On the other hand Chalmers, Rahman and Stumberger states X_d remains constant with Id. Dutta reports two different results where X_d remains constant in AC standstill test and decreases steeply with I_d in Load Test.

- Back EMF E_o may decrease with I_q (or equivalently) depending on the saturation of flux paths which is totally dependent on motor structure. Miller, Chalmers, Mellor and Fidel assume E_o to be constant in no-load tests. However Mellor and Dutta reports E_o decreases with I_q as observed in load tests.

- Frequency dependence of the inductance is studied by Chalmers, Mellor and Fidel. Only Chalmers report that L_q decreases with frequency. Others state that inductances do not vary much with frequency.

- Miller, Mellor and Dutta studied cross coupling between axes. Common statement is that inductances may decrease by cross axis current due to increased saturation.

- The proposed load and no-load tests are realized either by connecting the tested motor directly to AC line or with a vector controlled drive. Since all presented methods can be realized with a vector control drive, it seems to be the most proper method to conduct running tests.

51

- All authors except Dutta agree that X_q (or equivalently L_q) decreases with line current. Dutta states that the variation is insignificant. This is probable since the decrease in X_q may arise in case of saturation in q-axis flux path. If there is no saturation then a constant value may be determined from the test.

- For X_d measurements, all authors except Fidel reports that X_d (or equivalently L_d) stays constant or decreases in some extent with line current. Fidel states an increase in X_d value with negative I_d (about 12% difference between full load and no load) which is probably due to demagnetizing effect of negative I_d on saturation level of the d-axis flux path.
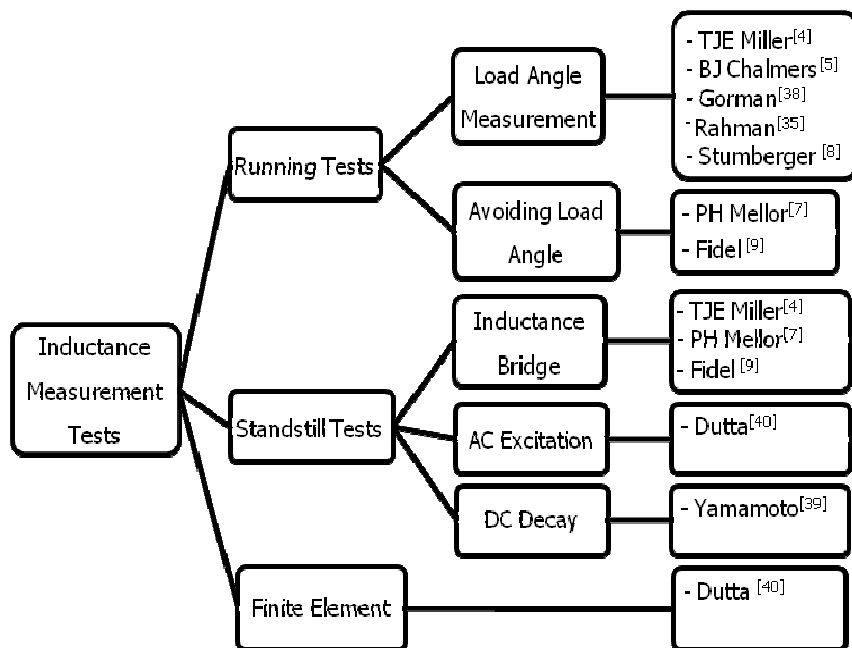
Figure 3.18: Proposed inductance measurement methods
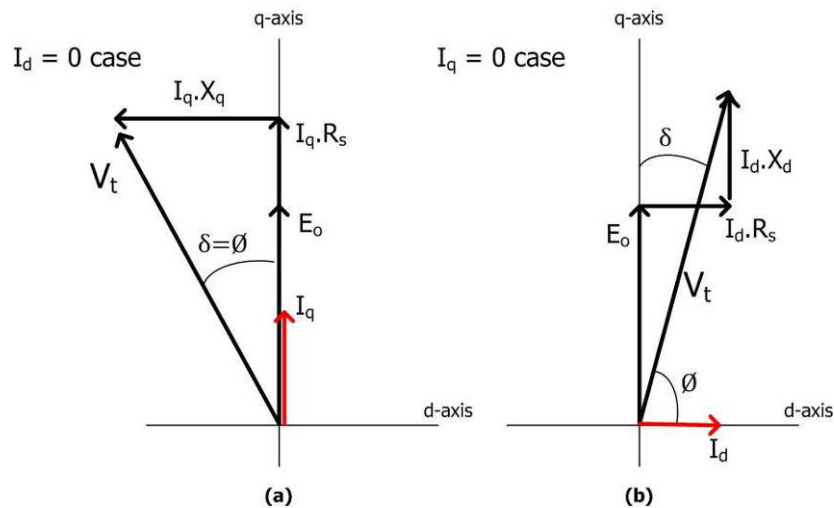
Figure 3.19: Phase diagrams related to $I_d=0$ and $I_q=0$ cases

- The studies depending on load angle measurement requires detecting the load angle of the tested motor both at no-load and under load to determine load angle deviation. There is a need for a stroboscope system which may be triggered with an external pulse generator per rotor revolution or a position encoder.

- The inductance bridge method seems to give satisfactory results however it is very difficult to construct a stable bridge circuit at high current levels. In this thesis work, the rated current of the tested motor is 17 A_{rms} which may result dissipation of considerable amount of energy on circuit elements. On the other hand, standstill AC excitation is simple to conduct in a laboratory environment, but monitoring of the winding temperature during the measurements and correction of the winding 20°C (cold) resistance values for operating temperatures is a very important issue [40].

- DC decay tests are simple but interpretation of the results is important. It is evident that an exponential decay waveform has at least two time constants; sub-transient and transient. Although standstill tests give out some inductance values, they do not simulate the real phenomena in the motor under normal operating conditions. DC decay test results can be relied on solely. In fact they should be conducted in conjunction with running tests to compare measurement results.

In conclude, since different methods give different results even on the same PM machine, any parameter measurement should be performed under the same conditions of normal

operating. If vector control is used to drive the motor in normal conditions, then parameter measurement should be also performed with vector control to be able to define two-axis model of the tested PM machine. However, it is wise to conduct all the proposed tests (standstill DC decay, standstill AC, no load and load tests, FE analysis) on a tested PM machine to completely characterize the inductance variation of a PM machine. The results of all measurements should interpreted together to determine inductance variation phenomena for the tested motor. While conducting tests, current and frequency dependency of measured quantities should be analyzed to have a full understanding.

3.2.3 Measurement of Back EMF Voltage

The back EMF is the voltage generated at stator windings due to time variation of linkage between rotating magnet flux and stationary stator windings.

There are no methods in [3] to be applied for emf voltage measurement. However the method for "Open-circuit saturation curve" defined in Section 4.2.5 in [3] can be modified. This method states that open circuit saturation curve is obtained by driving the tested machine at rated speed, open-circuited, and recording its armature terminal voltage.

Since field can not be adjusted in PM machines, speed can be varied instead of field current. This will give armature terminal voltage variation with respect to speed which is emf voltage variation with speed also. It is shown in Chapter.2 that amplitude of the terminal voltage is linearly dependent to rotational speed of the rotor as seen in equation (3-14). Since field excitation is constant and k_e is a function of flux linkage, the linear relation between open circuit terminal voltage and shaft speed is expected.

$$E_o = k_e \times w_{mech}$$
(3-14)

3.2.4 Measurement of No-Load Loss

There is no sense to imagine a system that converts energy from one form to another with 100% efficiency. Inevitably there is always an amount of lost energy that is not utilized. In PMSM (whether generating or motoring) some electromechanical work is lost and radiated as heat. Those losses can be listed as;

1. Copper losses
2. Friction and Windage losses
3. Core losses

54

Copper losses are modelled with a resistance in electrical model of the PMSM. Friction and windage losses are measured and taken into consideration as a reduction in output torque of the motor. Beside these losses, core losses arise in lamination (core) due to time variation of flux.

Procedure of friction-windage and core loss measurements of a synchronous motor is defined in "Section 4.2.7: Core loss and friction and windage loss" of reference [3].

In this case, the machine under test is usually driven by a motor, directly or through a belt or gear. It is stated that the friction and windage loss is obtained as the power input to the machine being tested, through auxiliary drive, with zero excitation. The tested machine should be fully demagnetized. The core loss at each value of armature voltage is determined by subtracting the friction and windage loss from the total power input to the machine being tested while the tested machine is excited with rated field current.

For PM machines, zero excitation is not realizable since magnets act as a permanent excitation source. In this case, friction-windage and core loss can not be separated from each other. The two torque components cannot be separated unless magnets are removed from the rotor. This is not feasible for most motors and disassembling a motor may result in performance drop.

The mechanical power input to the tested PM machine (with open terminals) driven by an auxiliary motor has to be measured by some means (most applicably with a torque transducer) and the measurement value has to be accepted as total of friction-windage and core loss.

3.2.5 Measurement of Motor Thermal Constant

In this test, motor is loaded with specific load at a constant speed. The test is carried on until the motor reaches a thermal equilibrium with the ambient. The test speed and load is totally subjective, but it must be noted that the load must not be too high to avoid reaching a thermal equilibrium.

During the test, motor temperature must be sampled. In this work, a thermistor placed in stator end-winding of the test motor is used to monitor temperature variation in every 5 minute. It is assumed that, all points of the test motor reaches nearly same temperature value in the thermal balance. This is acceptable as there is no forced cooling for this motor.

When the thermal balance is reached, temperature difference between the motor and ambient is accepted as the temperature rise due to losses in the motor. Motor losses are

55

calculated by subtracting output power from total input power to motor. By dividing power loss of the motor to temperature rise, thermal constant of the motor can be derived.

3.2.6 Measurement of Torque-Speed Characteristic

Methods for determining speed-torque curves of a synchronous motor are defined under Section 7.3 in reference [3]. Among proposed methods, "Method.4: Direct Measurement" method defined in section 7.3.5 is most applicable. This methods states that output torque can be measured by loading the tested machine at various speeds with a dynamometer or prony brake. This requires the maintenance of constant speed for each reading. Sufficient test points should be recorded to ensure that reliable curves, including irregularities, can be drawn in the regions of interest from the test data. Two different torque-speed characteristic may be determined which include rated and maximum current conditions.

3.2.7 Measurement of Efficiency

Efficiency measurement procedure is defined in "Section 4.6.2, Method 2: Input-output" of reference [3]. The efficiency from the input-output method is determined as ratio of output power to input power. The electric inputs (voltage, current, phase angle) to motor are measured with instruments. The output of the motor is measured with a dynamometer preferably.

3.2.8 Measurement of Cogging Torque

Cogging torque results from attraction of rotor magnets with stator teeth. Rotor tends to align itself with minimum reluctance. If the rotor is rotated, this alignment torque can be detected at rotor shaft as a ripple. In low speed and sensitive applications (i.e. drive-by-wire systems where automobile steering is done with an electric motor), minimum cogging torque is desirable.

It is proposed by Boldea [40] that an auxiliary motor with a very low torque ripple can be used to turn slowly (2-4 rpm) the rotor of the motor under test. An additional inertia may be placed on the shaft to increase the accuracy of the measurement. The accuracy of cogging torque measurement depends on preservation of shaft speed at a fixed speed. Fluctuation of the speed during cogging measurement will result in sideband torques around expected frequencies.

3.2.9 Conclusion to Measurement Methods Section

In the following chapters selected methods will be applied to the sample motor that this thesis work deals with. The aim of this section is to determine the variation of inductance with different test methods so that a comparison of offered methods may be done with respect to accuracy and dependency.

3.3   Applied Test Methods and Approach and Measurement Results

In the previous section, available standards and test methods for measurement of PM machine parameters are determined. In this section, the selected methods are to be applied to the tested motor and the results are presented.

The tested motor which is specified in Section 3.1 is a PM motor with inset mounted magnets. There is a saliency between adjacent magnets on the rotor to enhance the rotor mechanical structure which makes quadrature and direct axis parameters differ from each other. It can be observed in the presented studies in Section 3.2, there is no much effort on surface and inset magnet motors.

There is a vector controlled driver available for this thesis work which enables independent control of d-q axis excitation of the motor. There are parameter measurement studies with vector control drive ([18], [44]) however the tested motors are internal magnet motors. From this point of view, this thesis work explores application of offered methods to inset magnet motors (also applicable to surface magnets).

An overview of the tests to be conducted for PMSM parameter determination can be summarized as in Figure 3.20.
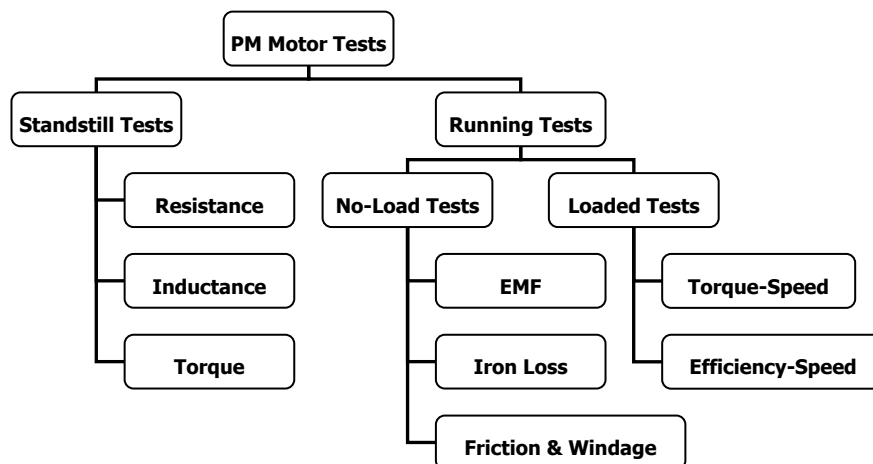
Figure 3.20: Overview of the Measurement Procedures for PMSM

3.3.1 Result of Resistance Measurement

In this work, four wired measurement method defined in Section 3.2.1 is applied where "Agilent 34420A Micro Ohm Meter" device is used and 0.140Ω is measured at terminals of the PM motor (line-line) at 20°C room temperature. To get per phase resistance, the measured value is divided by two, resulting 0.070Ω.

3.3.2 Results of Inductance Tests at Standstill

These studies focus on standstill tests to measure inductance because it is problematic to extract load angle when the motor is operating. Many modern motor drives have pulse width modulated (PWM) voltage output. Measuring the fundamental harmonic of terminal voltage of the motor may require special treatment. Beside exciting the motor terminals by PWM waveform, excitation with AC-source with variable voltage and frequency [13], [31], [36] or using a DC current decay setup [31], [37] may be used also to extract inductances. Frequency dependence and current dependence of inductance is studied to fully characterize inductance variation for different motor operation conditions.

i. Results of Inductance Measurement with AC sinusoidal excitation

The test bench for this method can be setup by connecting the PM motor with a variable AC source through voltage-current measurement device. In this work, a signal generator connected to an amplifier is used for the AC source. The signal with variable frequency is properly amplified to supply motor terminals. In serial with amplifier-motor connection, a harmonic tester is used for voltage, current and power measurement (Figure 3.21).
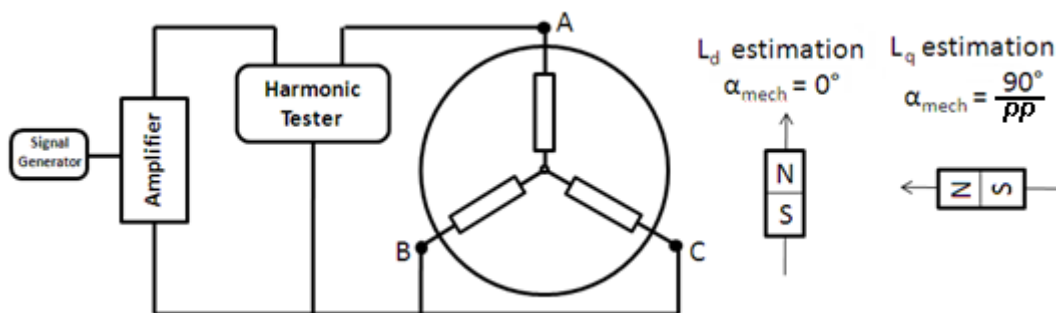
Figure 3.21: Test setup for standstill AC inductance measurement

When the motor terminals are excited as in Figure 3.21 with a sinusoidal voltage, a sinusoidal current will flow with a lagging phase (equation (3-15)).

$$\vec{I} = \frac{\vec{V}}{R + jw_e L} = \frac{|V|}{\sqrt{R^2 + w_e^2 L^2}} \times e^{-j\frac{w_e L}{R}}$$

(3-15)

The equation (3-15) shows that the phase of excitation current in the windings is defined by the ratio of reactance ($X=w_eL$) to resistance (R) seen at terminals. If the resistance of the windings is already determined, the inductance can also be calculated easily from the measured phase difference between voltage and current waveforms. This test is to be repeated for two different positions of rotor; d-axis aligned and q-axis aligned. If the terminals are excited with varying sinusoidal voltages, inductance variation with current can be determined.

Rotor can be aligned to d-axis by exciting windings when motor terminals connected as in Figure 3.21. Exciting the motor from terminal-A with terminals B and C short-circuited, will create a flux oriented exactly in magnetic axis of phase-A (Figure 3.22). Magnets eventually move to the direction of this flux created by stator windings, thus aligning the rotor to d-axis of phase-A. Throughout the test, the rotor must be fixed at this position in some manner. An electro-magnetic brake integrated in the machine is used in this study.

To repeat the test for q-axis, the rotor must be aligned 90°$_{elec}$ (90°$_{mech}$/*pole pair*) away from d-axis by some means. A simpler way to position the rotor to q-axis is exciting the stator windings by exciting motor terminals B and C (leaving terminal-A open). Excitation of B-C terminals will create a resultant magnetic field oriented at exactly q-axis; 90° electrical degrees away from d-axis (see Figure 3.23). In this study, the rotor is aligned to q-axis by exciting B-C terminals, which is simpler than aligning with a position sensor.
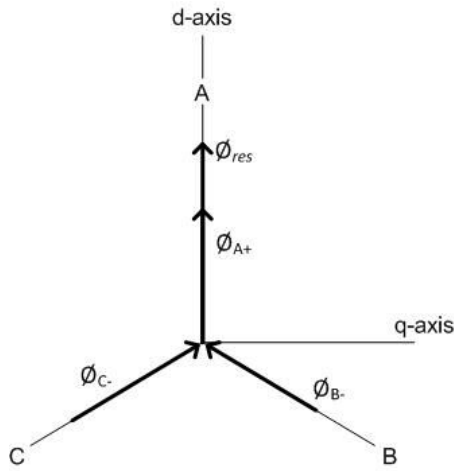
Figure 3.22: Phase diagram for d-axis excitation
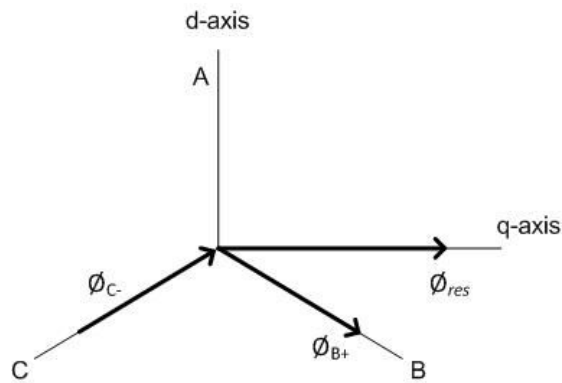
Figure 3.23: Phase diagram for q-axis excitation

In the figure, $\emptyset_{B+}$ and $\emptyset_{C-}$ are flux vectors created by phase currents and $\emptyset_{res}$ is resultant flux of those two vectors which is exactly at q-axis. Inductance seen at motor terminals can be calculated by observing amplitudes of voltage and current, with phase difference. The phase diagram of the electrical circuit is as in Figure 3.24.
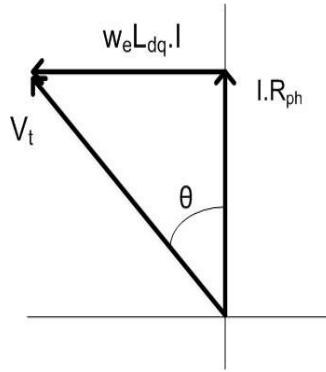
Figure 3.24: Phase diagram of standstill AC inductance test

In Figure 3.24, "w_e" is 2π times electrical frequency f_e, "L_{dq}" is axis inductance (d or q), "I_{dq}" is axis current (d or q), "θ" is phase difference between applied voltage and observed current. The calculation of inductance with respect to the presented phase diagram can be formulated by equation (3-16).

$$L_{dq} = \frac{V_t \sin \theta_{ph}}{I \times 2\pi f_e}$$

(3-16)

A complete view of inductance variation is formed by repeating the measurement for different current amplitudes and frequencies. The results of measurements for "d" and "q" axes are presented in Figure 3.25 and Figure 3.26. The results of the inductance measurements are also verified by a FE analysis. The same measurement method is used for a transient magnetic solution.

61
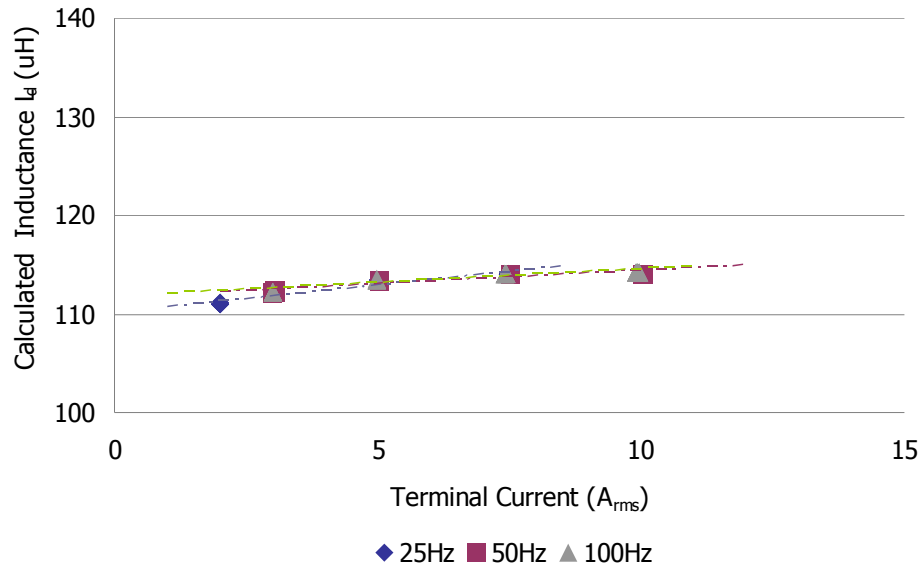
Figure 3.25: L$_d$ results for standstill AC test with sinusoidal voltage excitation
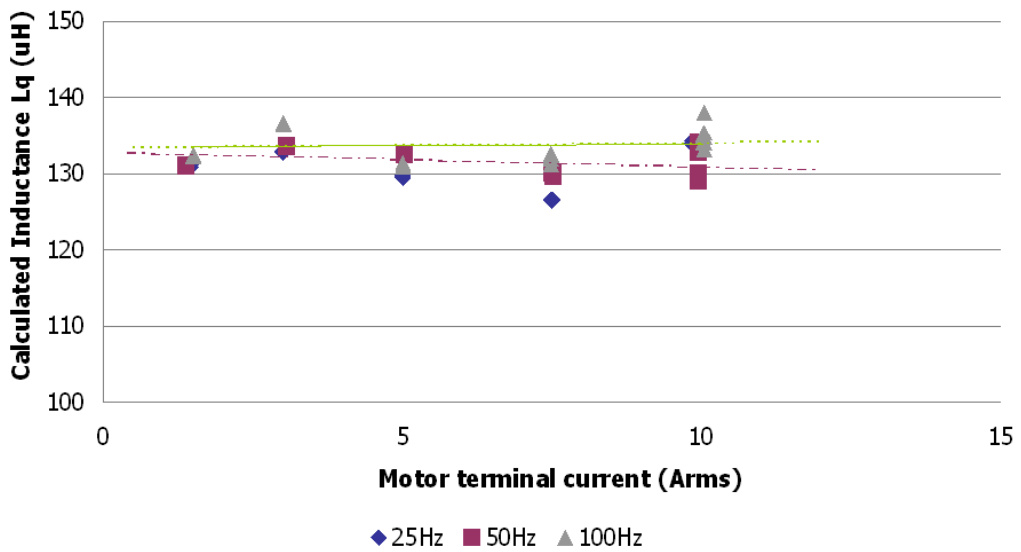
Figure 3.26: L$_q$ results for standstill AC test with sinusoidal voltage excitation

ii. *Results of Inductance Measurement with PWM excitation*

To investigate effect of PWM excitation and to determine the accuracy and reliability of measurement setup for distorted waveforms, standstill inductance measurements are repeated with PWM voltage excitation at motor terminals. The resultant current in motor

windings is again sinusoidal but the observed voltage waveform is a PWM signal. This is very similar with normal motor operation where motor is driven with an inverter with PWM output.

The measurement setup defined in Section 3.1.2. All the calculations are done for first order harmonic because as stated before the defined phase diagram of PM motor operation is valid for fundamental harmonic. So the observed PWM signal has to be filtered to get the first order harmonic. This is done autonomously by measurement device (HIOKI) in the test setup.

Table 3.5: Measurement data for L_d standstill test with PWM excitation

f (Hz)	Fundamental of measured Terminal voltage (V_{rms})	Measured winding current (A_{rms})	Measured power (W)	Measured phase angle for first harmonic (degree)	Calculated phase resistance (Ω)	Calculated Lq (mH)
25	0,555	5,08	2,73	14,32	0,071	0,115
25	1,107	10,00	10,75	14,02	0,072	0,114
25	1,68	15,01	24,5	13,82	0,072	0,113
50	0,599	5,03	2,69	26,87	0,071	0,114
50	1,2	10,02	10,76	26,57	0,071	0,114
50	1,833	15,08	24,84	26,01	0,073	0,113
100	0,763	5,04	2,71	45,17	0,071	0,114
100	1,529	10,07	10,87	45,09	0,071	0,114
100	2,137	14,00	21,27	44,63	0,072	0,114

Table 3.6: Measurement data for L_q standstill test with PWM excitation

f (Hz)	Fundamental of measured Terminal voltage (V_{rms})	Measured winding current (A_{rms})	Measured power (W)	Measured phase angle for first harmonic (degree)	Calculated phase resistance (Ω)	Calculated Lq (mH)
25	0,563	5,06	2,74	16,09	0,071	0,131
25	1,136	10,09	11,01	16,13	0,072	0,133
25	1,720	15,10	24,94	16,17	0,073	0,135
50	0,628	5,04	2,75	29,69	0,072	0,132
50	1,258	10,04	10,96	29,85	0,072	0,133
50	1,893	14,99	24,64	29,71	0,073	0,134
99	0,836	5,08	2,80	48,75	0,072	0,132
99	1,668	10,08	11,07	48,82	0,073	0,133
99	2,500	15,04	24,84	48,64	0,073	0,133
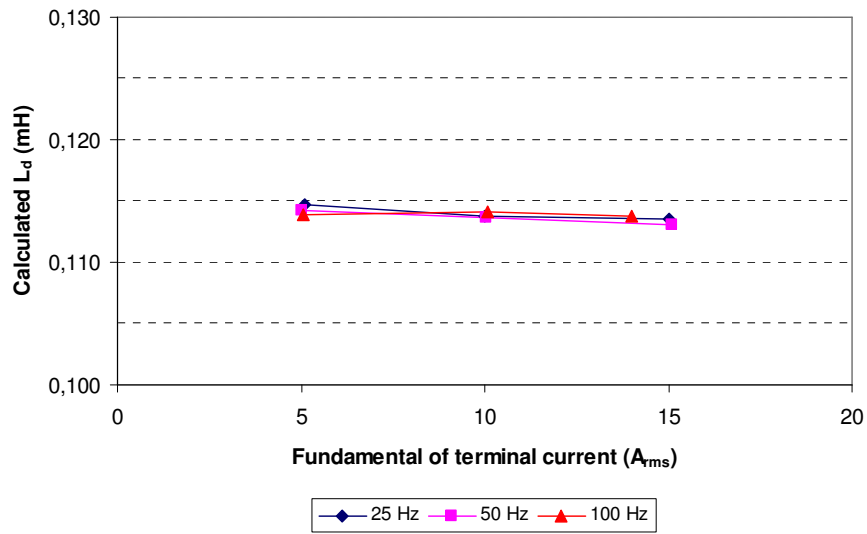
Figure 3.27: Variation of calculated L_d for standstill test with PWM voltage excitation
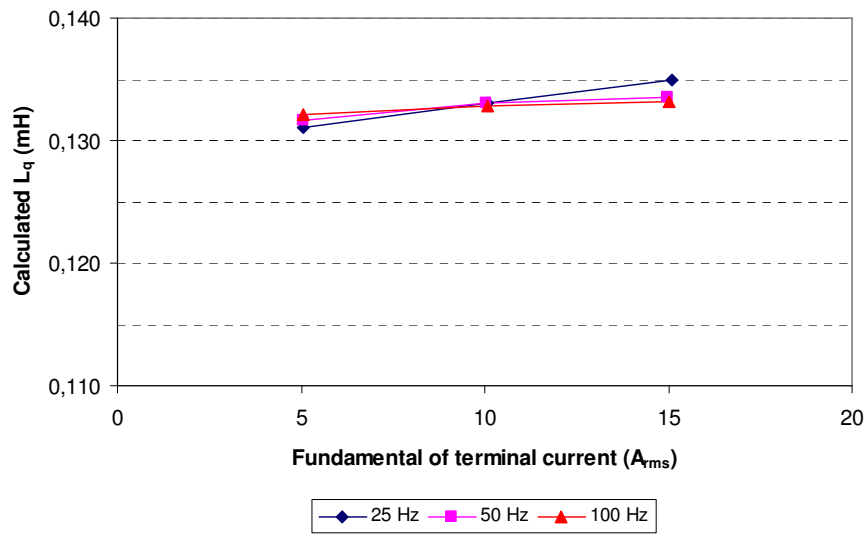
Figure 3.28: Variation of calculated L_q for standstill test with PWM voltage excitation

Comparing Figure 3.28 and Figure 3.27, it can be observed that results of standstill PWM excitation measurements results for 25 Hz, 50 Hz and 100 Hz agree within 1% accuracy for d-axis and q-axis.

3.3.3 Results of Inductance Tests under Running Condition

Although standstill tests for inductance determination are simple to carry out and easy to evaluate, they do not simulate the real magnetic phenomena occurring in the motor during operation. Studies like [13], [20], [39] also show that there are irregularities both for inductances and EMF voltage and they are dependent to each other in some extent. To account those, running tests should be performed.

In the Figure 3.5, phase model of a PM machine at vector operation is illustrated. In the figure, L_d and L_q are synchronous inductances, w_e is electrical speed in rad/s (2*pi*fe), V_{emf} is generated EMF voltage due to magnet flux and V_t is motor terminal voltage.

Since there are two axes in diagrams, two related equations can be constructed.

$$V_t \cos \delta = E_o + \left(I_d w_e L_d\right) + \left(I_q R_s\right) \tag{3-17}$$

$$V_t \sin \delta = E_o + \left(I_q w_e L_q\right) + \left(I_d R_s\right) \tag{3-18}$$

If there is no current in d-axis, which is a constraint for vector control of PMSM drives, the phase diagram can be simplified as in Figure 3.29 ("I_d=0" constraint is ensured by vector control drive). It should be noted that these phase diagrams are valid for only fundamental harmonics of voltage and current.
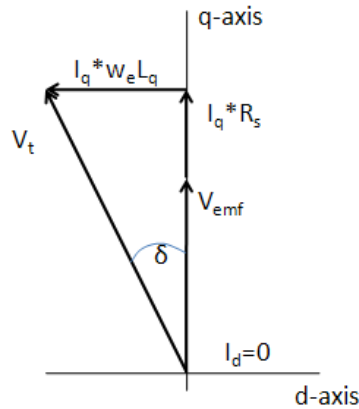
Figure 3.29: Phase diagram of PMSM for vector control

It is noted that although two equations can be derived, there are three unknown parameters (L_d, L_q and V_{emf}) which makes the equations unsolvable. The expressions for axes inductances obtained from phase diagram are functions of the load angle. To solve the equations, the load angle must be determined or dealing with load angle may be avoided by means of mathematical efforts. There are quite many methods in the literature

related to this problem which are presented in Section 3.2.2. Some of the proposed methods are going to be investigated with their applicability and effectiveness.

i. No-Load Tests

No-load tests are performed to minimize torque current (q-axis current). It is assumed that when the shaft of the motor is rotating freely, only load is counter torque created by friction, windage and core losses. The sum of these losses assumed to be very low with respect to rated torque of the motor (<3%). So that at no load, quadrature axis current is negligible in comparison to d-axis current

At this no-load condition, current is injected to the PMSM by applying field enhancing (positive d-axis current) or field weakening (negative d-axis current) with vector control drive. The variation of d-axis inductance with d-axis current can be revealed by measurements at different current levels (Figure 3.30).
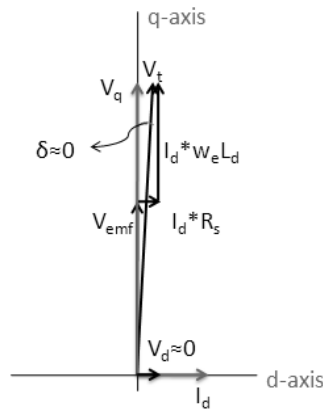
Figure 3.30: Phase diagram for no-load operation

The electrical relation between current and voltage is represented by following equation.

$$V_q = v_t \cos\phi = E_o + I_d w_e L_d \tag{3-19}$$

Assuming induced EMF voltage is fixed with constant shaft speed, the voltage difference between q-axis component of terminal voltage and calculated EMF voltage at that speed can be resolved to inductance (Equation (3-20)).

$$L_d = \frac{V_q - E_o}{(I_d - I_c)w_e}$$

(3-20)

The no-load current (equivalently core loss branch current) is subtracted from the terminal current. The result of no load L_d inductance measurements for different frequencies is given in Figure 3.31.
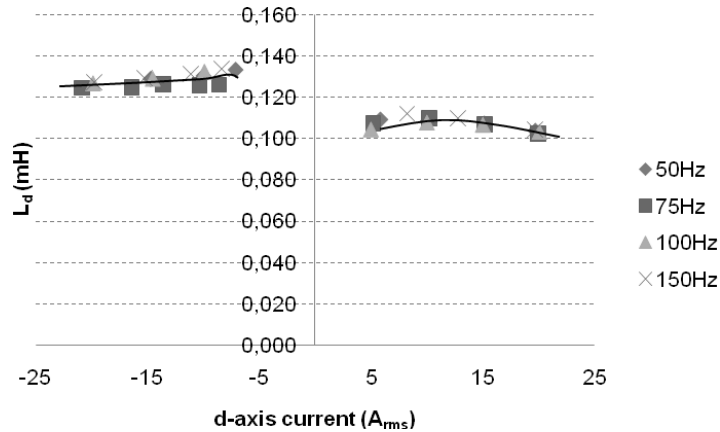
Figure 3.31: Result of no-load L_d inductance measurement

In Figure 3.31, it is observed that different measurements for four different frequencies result similar values for L_d. For positive I_d current inductance slightly decrease with increasing current due to saturation. On the other hand for negative I_d, calculated inductance is larger than the value for positive Id. This outcome is interpreted as follows.

Rare earth permanent magnets (also present in the tested motor) have a very large coercive force to oppose any demagnetizing flux. The magnet resists any flux that is flowing reversely through its magnetization direction. The demagnetizing flux created by negative I_d current in stator windings are forced to flow aside of the magnet instead of passing directly through it. This path has slightly lower reluctance due to saliency in the rotor core, so a larger inductance is measured.

ii. *Loaded Tests*

Loaded tests are performed to extract quadrature axis parameters. In the vector control operation of PM motors, no current flows in d-axis so that any measurement is related to

q-axis parameters. The aim of these tests is to establish q-axis currents so that related parameter L_q can be investigated.

In this test, motor is driven under normal vector control where only q-axis current is injected to the motor. The phase diagram related to this operation is presented in Figure 3.33. In the figure, w_e is operating electrical frequency, V_{emf} is back-EMF voltage, V_t is motor phase voltage.
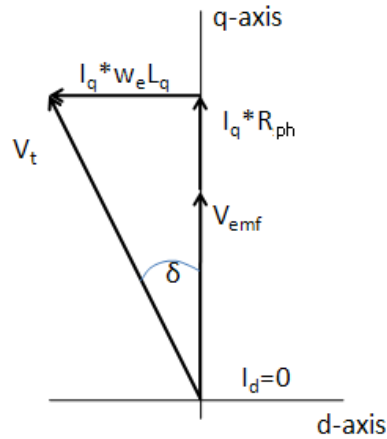
Figure 3.32: Phase diagram for L_q loaded test

Assuming induced EMF voltage is fixed with constant shaft speed, the voltage difference between q-axis component of terminal voltage and calculated EMF voltage at that speed can be resolved to inductance (Equation (3-21)).

$$L_q = \frac{V_q \sin \delta}{\left(I_q - I_c\right)w_e}$$

(3-21)

The no-load current (equivalently core loss branch current) is subtracted from the terminal current. The result of no load L_q inductance measurements for different frequencies are given in Figure 3.33.
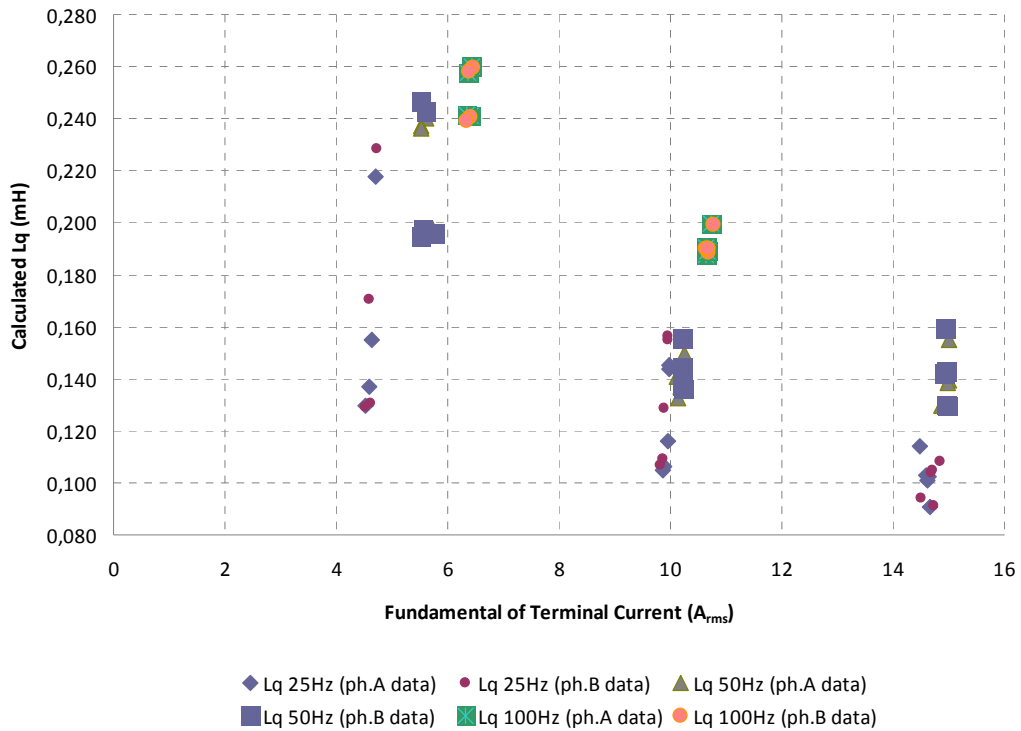
Figure 3.33: Result of loaded L$_q$ inductance measurement for loaded running test

As observed from Figure 3.33, there is not a unique L$_q$ value to determine from the loaded test results. It is observed that for each frequency calculated inductance increases with current. Toward twice of the rated current measured value stabilizes.

The expectation from the loaded test was to get a curve of Lq variation that is decreasing monotonously by motor terminal current (due to possible saturation with increasing current). However different trends for L$_q$ variation are observed for different frequencies. Discussions and probable reasons for these unexpected results will be presented in Section 3.4.

3.3.4 Result of Back EMF Voltage Measurement

The measurement was done while running the machine as a generator with open circuited terminals. The line-to-line voltage signal was recorded using a digital oscilloscope. The variation of back EMF voltage amplitude with speed is visualized in Figure 3.34 and one sample of recorded waveforms is presented in Figure 3.35. The gradient of linear approximation (slope of linear trend line) to recorded data points gives EMF voltage constant for the motor.
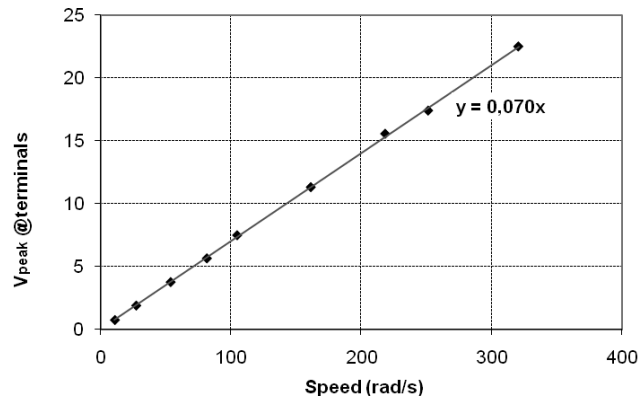
Figure 3.34: Measured EMF voltages for different speeds

As observed in Figure 3.34, EMF voltage constant is measured as 0.070 V_{peak}.s/rad at line which is equivalent to 0.029 V_{rms}.s/rad per phase. A sample measured voltage waveform showing sinusoidal back EMF at line is presented in Figure 3.35.
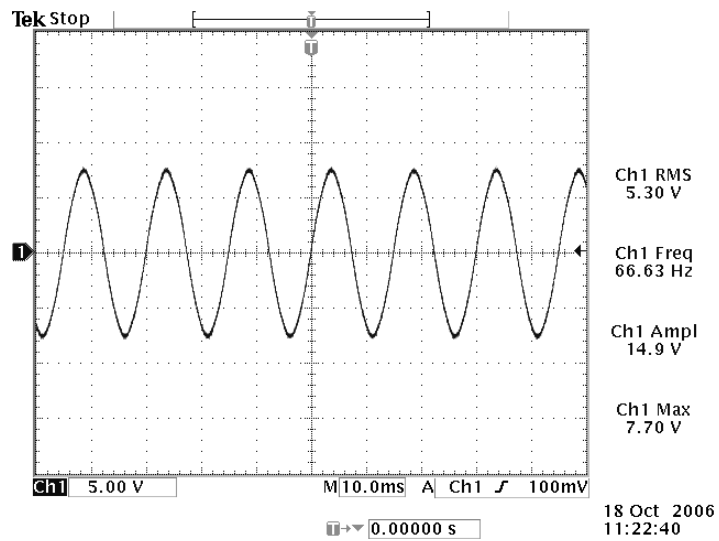
Figure 3.35: Measured EMF waveform at motor terminals at 1000rpm

3.3.5 Results of No-Load Loss Measurement

In this thesis work, two different loss measurement tests are performed. In one case, motor is driven by an auxiliary motor and torque at shaft is measured as power input to the tested motor. In the other case, the tested motor is operated at no load and power input at terminal is measured.

Method.1 – Test motor driven by an auxiliary motor

In the test, the PMSM is externally coupled to a driving motor which can be operated in variable speeds. There is a torque transducer between the driving motor and the PMSM. When the driving motor is operated, the measured torque corresponds to total of mechanical losses; friction and windage losses. The measurement results for the sample motor are tabulated in Table 3.7.

Table 3.7: Measurement results for Losses by Method.1

Shaft Speed (rpm)	Operating Electrical Frequency (Hz)	Measured Torque (Nm)	Measured Power Input (W)
172	11	0,010	0,18
325	22	0,017	0,58
630	42	0,021	1,39
745	50	0,023	1,79
974	65	0,024	2,45
1300	87	0,028	3,81

Method.2 – Test motor driven at no load by an inverter

For this test, motor is run with no-load at various speeds. The rms terminal voltage, rms current and input power are recorded. In this operation, it is assumed that a negligible electromagnetic torque is produced (only for friction-windage) for any speed so that measured power input to the motor can be treated as total of friction-windage losses and core loss. In this test, the test setup in Figure 3.2 is used without any load coupled to PM motor. Copper losses are ignored in this test since current is very small. The measurement results at motor terminals and calculations are presented in Table 3.8.

Table 3.8: Measurement results for Losses by Method.2

Shaft Speed (rpm)	Operating Electrical Frequency (Hz)	Motor Terminal Current (A_{rms})	Motor Terminal Voltage (V_{rms})	Measured Input power (W)
750	50	0,31	3,95	2,12
1125	75	0,33	5,89	3,37
1500	100	0,36	7,71	4,81
2250	150	0,44	11,15	8,50

The variation of the losses by both methods is clearer in Figure 3.36 where a second order approximation is done for calculated loss data points.
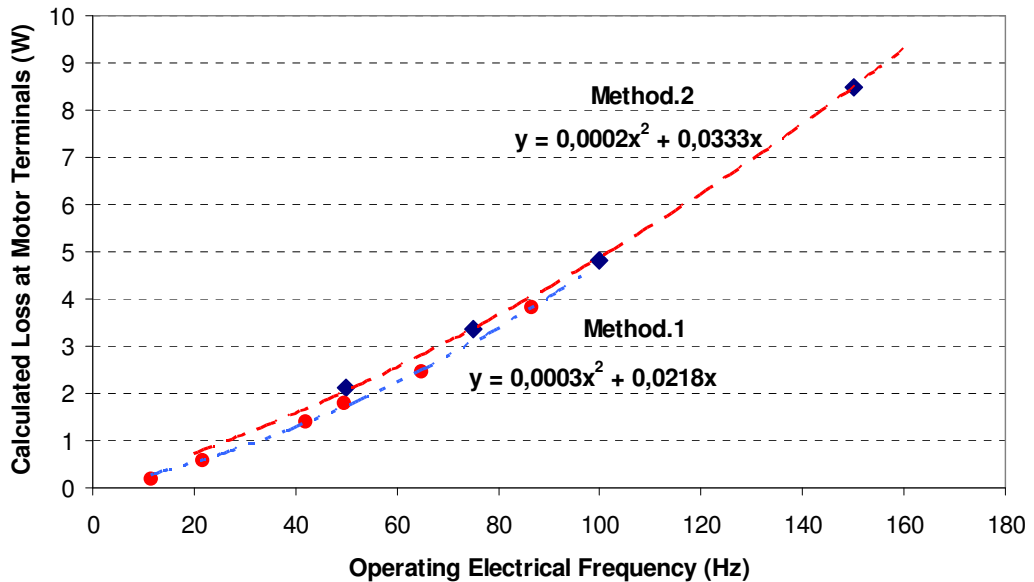
Figure 3.36: Variation of no-load losses with frequency by two methods

It is observed that 0.2W larger loss is measured by Method.2 at low frequencies but Method.1 measurements have steeper trend line which means that losses will be higher at higher frequencies. Either of them may be selected to include in analytical calculations. In this thesis work, results of no-load loss tests by Method.2 are selected to be used in analytical calculations.

3.3.6 Results of Inductance Test by DC Current Decay

The DC decay method is presented in Section 3.2.2-iii which is proposed by Boldea [40]. The idea behind this test is that rate of current flow in a conducting medium cannot be altered discretely in a conducting medium. Instead, the change happens in an exponential trend with time constant. The time constant is solely dependent on total impedance of the path.

Exciting the motor windings with DC will result in a constant current flow. Opening the switch, blocking the current from source, induced currents in motor windings will flow through the diode and diminish rapidly with a time-constant. If the oscilloscope is triggered to track the decaying current, inductance can be calculated determined from the recorded waveform.

The test bench for DC current decay can be setup by connecting the PM motor, in parallel with a diode, to a DC source through a switch. In serial with switch-motor connection, an oscilloscope is used for recording the terminal current.
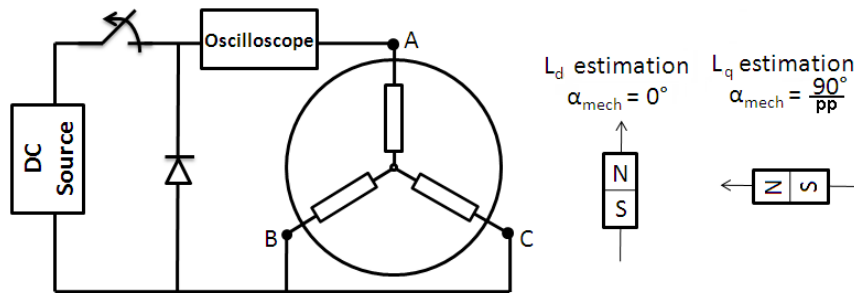
Figure 3.37: Test setup for standstill DC current decay test

Calculation of inductance may be done in terms of preservation of energy rule. The initial energy stored in the inductor at the time of switching will be dissipated on resistance of the system. If resistance of the system is known then equivalent inductance of the system may be calculated by energy balance equation.

$$E_{\text{ stored in inductor}} = E_{\text{ dissipated on resistance}} \qquad\qquad (3\text{-}22)$$

Equation (3-22) can be explicitly written as follows.

$$\frac{1}{2}LI_o^2 = \int_0^\infty I^2(t) \cdot R \cdot dt \qquad (3\text{-}23)$$

For discrete time data, the expression in equation (3-23) can be rewritten as follows.

$$\frac{1}{2}LI_o^2 = \sum_{k=0}^{N} I_k^2 \cdot h \cdot R \qquad (3\text{-}24)$$

The sampling time "h", resistance "R", initial value of the direct current "I_o" and the current samples "I_k" during the decay period are known.

Inductance variation by DC current is identified by repeating the measurement for different current amplitudes and for both d-axis and q-axis. Alignment is done as proposed in standstill AC test.

A sample DC decay current from recorded waveforms is presented in Figure 3.38. The oscilloscope is triggered with opening of switch at time t=0.
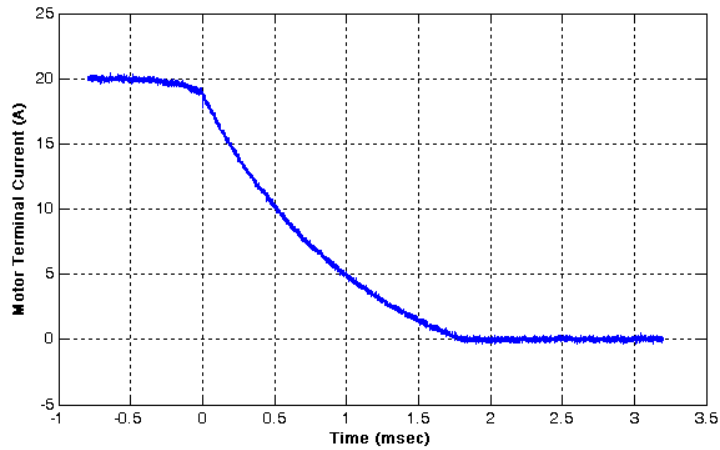
Figure 3.38: Recorded DC decay current in d-axis DC current decay test at 20A

Inductance can be calculated by recorded data if equation (3-24) is rewritten with known parameters.

$$L = \frac{2 \cdot R \cdot h \cdot \sum_{k=0}^{N} I_k^2}{I_o^2} \qquad (3\text{-}25)$$

Calculated inductances by equation (3-25) from DC decay measurements are tabulated in Table 3.9.

Table 3.9: Results of DC current decay

	Initial current I_o (A)	Sampling time h (μsec)	Calculated Inductance (μH)
q-axis	4,48	0,2	33
	9,24	0,4	52
	14,10	0,4	63
	19,68	0,4	67
d-axis	4,32	0,2	29
	9,44	0,2	42
	13,95	0,4	50
	18,56	0,4	53
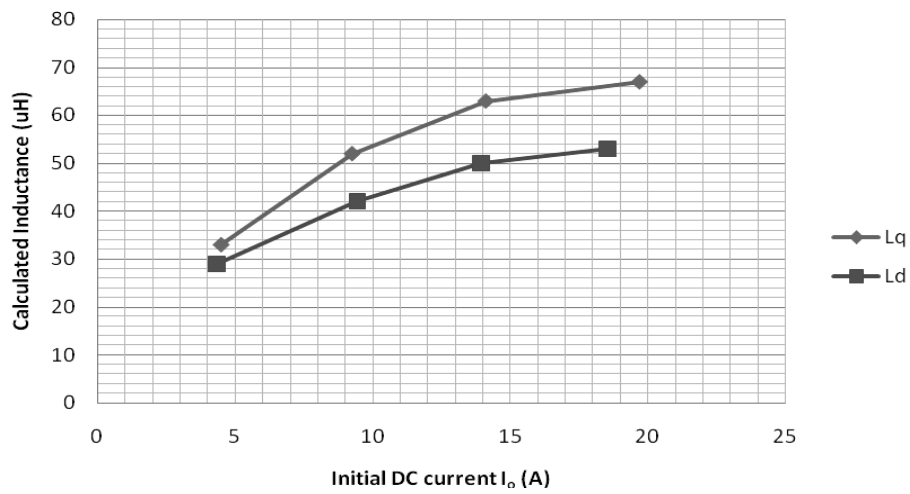
Figure 3.39: DC current decay test results

3.3.7 Result of Motor Thermal Constant Measurement

The test motor is loaded with 1 Nm at 1400 rpm. Thermal equilibrium is observed after 90 minutes of operation. The temperature rise of the motor with respect to time is illustrated in Figure 3.40.

At the defined operating condition, measurements and thermal constant calculations are as follows:

Output power	: 147 W	(1 Nm @ 1400 rpm)
Input power	: 187 W	
Total loss	: 40 W	
Efficiency	: 78%	
Ambient temperature	: 20 °C	
Temperature rise	: 80 °C	
Thermal constant	: 2 °C/W	(80°C / 40W)
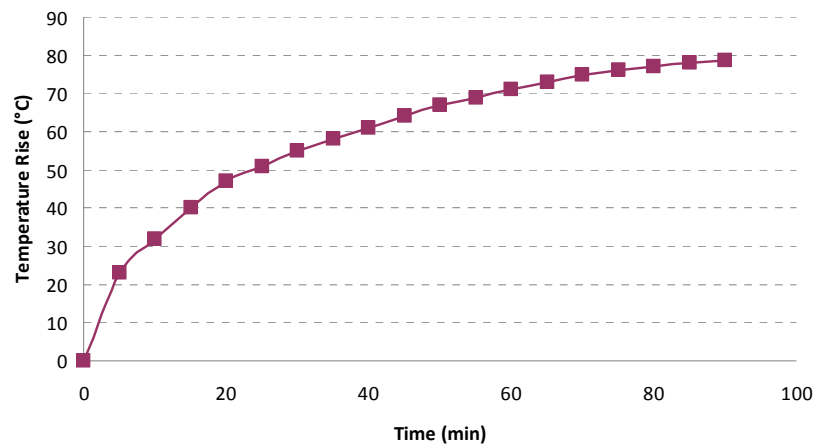
Figure 3.40: Temperature rise of tested motor under 1 Nm load at 1400 rpm

3.3.8 Result of Torque – Speed Measurement

During this test, the motor is driven at selected frequencies. At a specific frequency (equivalently speed), the load is gradually increased until the permissible peak current (35 A_{rms}) is reached. The value of torque recorded at that point is taken as pull-out torque at that speed. The result is presented in Figure 3.41.

Table 3.10: Measured data for torque-speed test

Speed (rpm)	Measured torque (Nm)
500	2.9
1000	2.9
1500	2.9
1800	2.9
2000	2.6
2200	2.0
2500	1.1
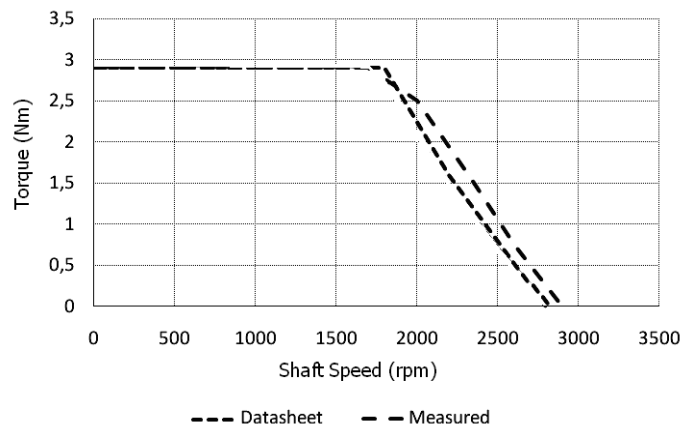
Figure 3.41: Measured Pull-out Torque vs. Shaft Speed for sample motor

The flat torque characteristic up to 1800 rpm is due to current limitation of the driver. This region is called as "constant torque region". The width of this region is limited by the bus voltage of the driver (inverter). The driver is able to excite the motor with the maximum current unless the bus voltage is not enough At higher speeds, driver current is limited by the back-EMF of motor unless a method is used to overcome excessive back-EMF voltage (i.e. field weakening).

3.3.9 Results of Efficiency Measurements

This test is done by varying load at a constant speed. The test setup is illustrated in Figure 3.2. To have complete view measurements are done in three different speeds. Recorded data are tabulated in Table 3.11 and variation of efficiency is presented in Figure 3.42.
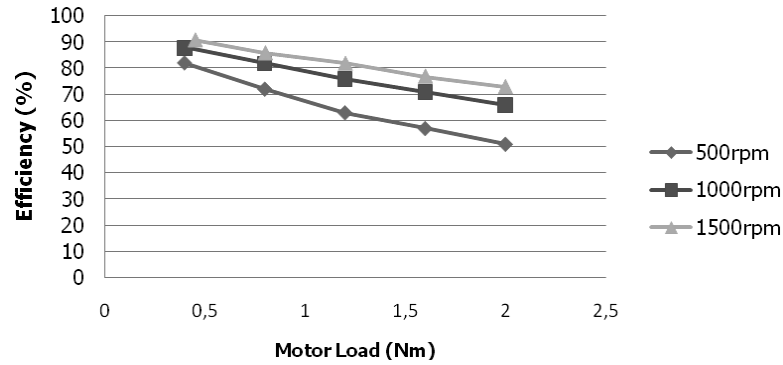
Figure 3.42: Sample motor efficiency vs. shaft load at constant speed

Table 3.11: Measured efficiency test data

Speed (rpm)	Terminal Current (Arms)	Input Power (W)	Input Power Factor	Motor Output Power (W)	Efficiency (%)
500	5,70	33,26	1,00	25,6	77
	11,04	78,01	0,99	49,7	64
	16,00	132,08	0,98	72,0	55
	20,77	198,4	0,98	93,5	47
	25,36	277,38	0,98	114,2	41
1000	5,78	60,88	1,00	52,1	86
	11,10	129,61	0,99	99,9	77
	15,84	201,10	0,99	142,6	71
	20,72	290,40	0,98	186,6	64
	25,76	402,92	0,97	232,0	58
1500	5,25	79,83	1,00	70,9	89
	11,09	180,47	0,99	149,8	83
	16,00	281,38	0,99	216,2	77
	20,97	397,20	0,98	283,5	71
	26,12	515,98	0,97	352,9	68

It is an expected result that efficiency is better for higher speeds. The major loss in PM machines is copper loss. Since the machine gives same torque output at same current levels for different speeds, copper losses stays same as the output power increases. So losses become less dominant and efficiency is calculated to be higher.

3.3.10 Results of Cogging Torque Measurement

The frequency of this torque depends on number of poles on rotor and number of teeth in stator. It is expected to see cogging torque at multiples of pole number, stator number and minimum common multiple of them [7]. For the tested sample motor which has 8 poles and 27 slots, cogging torque is expected at 8, 27 and 8*27 multiples of shaft rotational frequency.

In this thesis work, a 90L frame 1.1kW induction motor was used to drive the test motor assuming that the inertia will be enough to keep the speed constant.
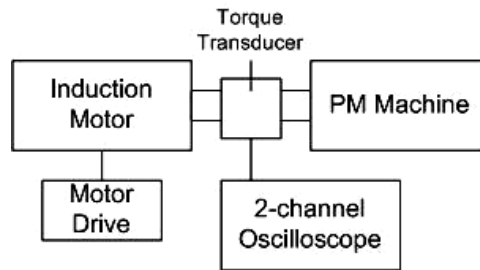
Figure 3.43: Cogging torque measurement test setup

Torque on the shaft is measured at different speeds ranging from 60 rpm to 563 rpm to observe the effect of shaft speed to cogging torque measurements. Shaft speed and torque is measured by transducer and displayed on a two-channel oscilloscope which records this waveform also. FFT analysis applied to measured torque waveform to investigate different harmonic components of torque. At each measurement, harmonic components with amplitude less than 1% of highest component are ignored.

From the measurements, following interpretations can be done:

i. The DC torque component in the measurements about 4.5 Ncm is interpreted as friction.

ii. It was expected to observe torque components at 8, 27 and 8*27 times shaft frequency but it is not possible to identify those from the measurements. Measured torque values at sub-frequencies are all lower than 0.002 Nm.

iii. As the speed increases, torque harmonics at supply frequency diminish.

Table 3.12: Measured torque data for cogging torque test

Speed: 60 rpm, f_m = 1 Hz, Speed fluctuation: 1.2rpm (±0.02Hz)						
Frequency Component	DC		f_m	$6f_m$	$7,5f_m$	
Measured Moment (Ncm)	4,77		0,1	0,2	0,1	
Speed: 141.6rpm, f_m = 2.36Hz, Speed fluctuation: 1.8rpm (±0.03Hz)						
Frequency Component	DC		f_m	6_{fm}	$7,5f_m$	
Measured Moment (Ncm)	4,7					
Speed: 282rpm, f_m = 4.7Hz, Speed fluctuation: 1.8rpm (±0.03Hz)						
Frequency Component	DC		f_m	$2f_m$	$7,5f_m$	
Measured Moment (Ncm)	4,59		0,05	0,16		
Speed: 420rpm, f_m = 7Hz, Speed fluctuation: 0rpm						
Frequency Component	DC	f_m-1	f_m	f_m+1	$2f_m$-1	$2f_m$	$2f_m$+1
Measured Moment (Ncm)	4	0,06	-	0,15	0,04	0,125	0,08
Speed: 564rpm, f_m: 9.4Hz, Speed fluctuation: 0rpm						
Frequency Component	DC	f_m-1	f_m	f_m+1	$2f_m$-1	$2f_m$	$2f_m$+1
Measured Moment (Ncm)	4,14		0,088			0,122	

The cogging torque of sample motor is also analyzed by FE analysis with Maxwell and Flux2D. In Maxwell, cogging torque is determined as 0.002 Nm peak whereas in Flux2D as 0.0018 Nm peak. Resultant waveforms are presented in Figure 3.44, Figure 3.45.
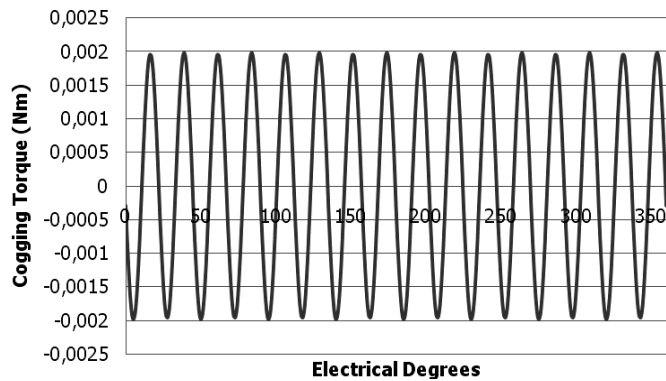
Figure 3.44: Cogging torque analysis results by Maxwell
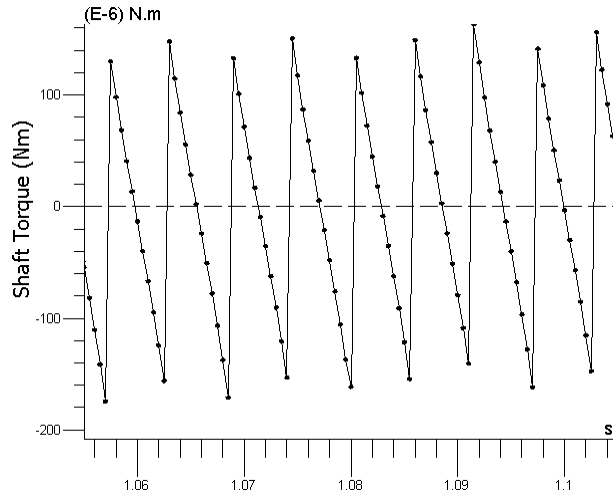
Figure 3.45: Cogging torque analysis results by Flux2D

3.4 Comparison of Inductance Measurements and Discussions

In this section results of different inductance measurements tests are discussed. The purpose is to investigate and compare results of the proposed methods and conclude which ones are most applicable.

3.4.1 Direct-Axis Inductance L_d Measurements

a.)   Comparison of measurements at Standstill

The results of standstill tests are presented in Section 3.3.2. Following comments can be made regarding to results:

- Measured L_d from AC sinusoidal excitation tests is around 115 uH and has a decreasing trend with 1% slope up to rated current.

- Measured L_d from PWM excitation tests is around 115 uH and has an increasing trend with 1% slope up to rated current.

- Both standstill results are independent of test frequency (same L_d values for 25Hz, 50Hz, 100Hz).

- Measured L_d values from DC decay tests do not give comparable results with other tests. The measured value is around 29 uH at $5A_{dc}$. L_d variation has an increasing trend up to rated current where measured value reaches 50 uH.

81

b.)   ***Comparison of Running test results with standstill tests***

▪   Measured L_d from running no-load tests is within the bound 105 uH…110 uH up to rated current.

▪   Measured L_d values is within 3% for different test frequencies.

▪   Since standstill tests also give L_d value of 110 uH, it can be concluded that no-load running tests and standstill tests agree with each other.

c.)   ***Comparison under demagnetizing conditions***

▪ L_d tests under demagnetizing conditions are performed only in no-load running tests because in standstill tests, the magnets subjected to variable flux which realizes magnetizing and demagnetizing conditions at the same time.

▪   Measured L_d from running tests is larger than magnetizing conditions. This outcome is interpreted as follows. Weakening of magnet flux decreases flux level in stator steel so that any present saturations in flux paths diminishes. This results in increased inductance value.

3.4.2 Quadrature-Axis Inductance L_q Measurements

  a.) ***Comparison of measurements at Standstill***

▪   Measured L_q from AC sinusoidal excitation tests is around 130…133 uH and has a decreasing trend to 130 uH with 1% slope up to rated current.

▪   Measured L_q from PWM excitation tests is around 132 uH and has an increasing trend to 133 uH with 1% slope up to rated current.

▪   Measured L_q from DC decay tests do not give comparable results with standstill excitation tests. The measured value is around 33 uH at $5A_{dc}$. L_q variation has an increasing trend up to rated current where measured value reaches 67 uH.

  b.) ***Comparison of Running test results with standstill tests***

▪   It is observed in loaded q-axis inductance tests that measured L_q values are very diverse for different frequencies and currents. Measured L_q values from running tests spread over a wide range.

▪   It is not possible to comment on the exact value of inductance from measured results. A single L_q value can not be defined even for the same current and frequency for load test which questions the accuracy and reliability of the measurement.

- Scattering of L_q values decreases with higher current (equivalently load).

3.4.3 Result of Inductance Measurements

For each axis inductance (L_d, L_q), four different measurements (Standstill AC test, Standstill PWM test, DC current decay test, Running load test) are made and also each measurement is validated by FE analyses. A comparison of the inductances obtained by measurements proposed methods are tabulated in Table 3.13, Table 3.14 and Table 3.15. To be able to compare results of different measurements, all given data in the tables is for the same current level.

Table 3.13: Inductance measurement results for different methods at 5 A$_{rms}$

Fundamental of Terminal current: 5 A$_{rms}$		
Measurement Method	**d-axis Inductance** L_d **(mH)** *(25 Hz / 50 Hz / 100 Hz)*	**q-axis Inductance** L_q **(mH)** *(25 Hz / 50 Hz / 100 Hz)*
Manufacturer data	0.125	0.133
Standstill AC Test (Sinusoidal voltage excitation)	0.113 / 0.113 / 0.114	0.129 / 0.130 / 0.132
Standstill AC Test (PWM voltage excitation)	0.115 / 0.114 / 0.114	0.131 / 0.132 / 0.132
Running No-Load Test	0.104 / 0.108 / 0.110	-
Running Load Test	-	0.130~0.230 / 0.195~0.250 / 0.240~0.260
DC Decay	0.029	0.033

Both load tests and dc decay test results are not consistent with theory which states that inductance may decrease with increasing current due to saturation. It can be concluded that standstill tests give satisfactory and reliable results where as it is not possible to state this for running and dc decay tests. In the following sections, possible reasons for inaccuracy in load tests are tried to be defined.

Table 3.14: Inductance measurement results for different methods at 10 A$_{rms}$

Fundamental of Terminal current: 10 A$_{rms}$		
Measurement Method	**d-axis Inductance** **L$_d$ (mH)** *(25 Hz / 50 Hz / 100 Hz)*	**q-axis Inductance** **L$_q$ (mH)** *(25 Hz / 50 Hz / 100 Hz)*
Manufacturer data	0.125	0.133
Standstill AC Test (Sinusoidal voltage excitation)	0.114 / 0.114 / 0.114	0.129 / 0.130 / 0.135
Standstill AC Test (PWM voltage excitation)	0.114 / 0.114 / 0.114	0.133 / 0.133 / 0.133
Running No-Load Test	0.108 / 0.109 / 0.110	-
Running Load Test	-	0.106~0.155 / 0.132~0.156 / 0.189~0.200
DC Decay	0.042	0.052

Table 3.15: Inductance measurement results for different methods at 15 A$_{rms}$

Fundamental of Terminal current: 15 A$_{rms}$		
Measurement Method	**d-axis Inductance** **L$_d$ (mH)** *(25 Hz / 50 Hz / 100 Hz)*	**q-axis Inductance** **L$_q$ (mH)** *(25 Hz / 50 Hz / 100 Hz)*
Manufacturer data	0.125	0.133
Standstill AC Test (Sinusoidal voltage excitation)	0.119 *(only data for 50Hz)*	0.130 *(only data for 50Hz)*
Standstill AC Test (PWM voltage excitation)	0.113 / 0.113 / 0.114	0.135 / 0.134 / 0.133
Running No-Load Test	0.107 / 0.108 / 0.108	-
Running Load Test	-	0.091~0.114 / 0.130~0.160 / no data for 100Hz
DC Decay	0.050	0.063

Dependency of Inductance measurements to Load Angle

The determination of load angle is critical if running tests are performed for parameters measurements. To have a solvable equation set of motor model (equations (2-5) and (2-6)) either the load angle must be determined accurately in some manner or another set of equations based on some assumptions have to be developed.

The accuracy of the determined load angle with decreasing load (equivalently lower motor terminal current) since load angle is proportional to load. It may be very small at light

loads (around 5° electrical). In this situation any miscalculation may lead to large variation of load angle. To understand the dependence of measured load angle and calculated inductance, a fictitious derivation is made as follows:

Say that in a specific loading condition (which is probable where the PM machine is loaded below rated conditions) the machine operating with a load angle of 5 degrees electrical. Also assume that the load angle is measured exactly. In q-axis running tests, the amplitude of fundamental harmonic of terminal voltage is multiplied by sin δ to calculate voltage induced on q-axis inductance (Figure 3.29).

$$\sin(\delta = 5°) = 0.087 \tag{3-26}$$

If the determined load angle was measured within ±1° error:

$$\sin(\delta = 4°) = 0.070 \tag{3-27}$$

$$\sin(\delta = 6°) = 0.104 \tag{3-28}$$

It is obvious that a ±1° (20%) error in angle measurement (which is very probable in case of such small angles) dramatically affects inductance calculation. If studied load angle was larger (around 20° as in standstill test measurements, see presented results in Section 3.3.2), a measurement error would not be so effective. However as the load angle becomes smaller, a linear relation is observed with angle error and calculated inductance.

Some recorded phase angles during q-axis running test at 50 Hz is tabulated in Table 3.16 for three different terminal currents. Many measurements are done to specify the variation of the recorded angle.

Table 3.16: Measured phase angles at different currents

Motor Terminal Current (A$_{rms}$)	Measured Phase Angles	Variation of measured values
6.2	3,09 / 3 / 2,96 / 2,83 / 2 / 1,93 2,88 / 2,82 / 2,94 / 2,89 / 2,85 1,93 / 3,08 / 3,04 / 2,18 / 2,63 2,7 / 3,09 / 3,68 / 2,07 / 2,77	±30%
10.8	4,69 / 4,81 / 4,64 / 5,1 / 4,62 / 4,77 4,92 / 4,82 / 4,76 / 4,63 / 4,64 / 4,77 / 4,58 / 4,93 / 4,77 / 5,01 / 4,85 / 4,9 / 5 / 5,03 / 4,09	±5%
15	6,88 / 7,17 / 6,94 / 7,17 / 6,8 / 7,21 6,83 / 6,94 / 6,93 / 6,88 / 7,06	±3%

It is observed in Table 3.16 that as the measured phase angle gets smaller, scattering of measured phase angle becomes larger; or equivalently as the terminal current decreases the uncertainty in measured phase angle increases. Consequently, for this range of phase angle (equivalently load angle), calculations of inductance based on measurements become unreliable.

Sine value of load angle is plotted with respect to current for different frequencies in Figure 3.46. It is observed that, although frequency becomes 8 times larger, sine of load angle is only 2 times at maximum current.
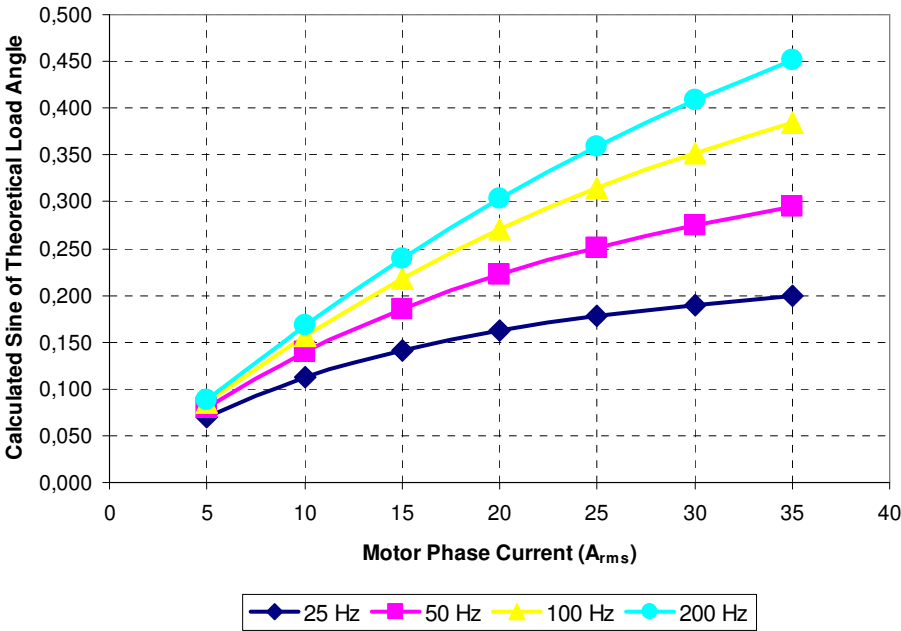
Figure 3.46: Value of sine of load angle for different frequencies and currents

Dependency of Measurements to Vector Control

As stated before, a vector controlled drive is used in the tests. It is assumed that vector control satisfies $I_d=0$ condition where I_q becomes completely in phase with back EFM voltage E_o (Figure 3.47).
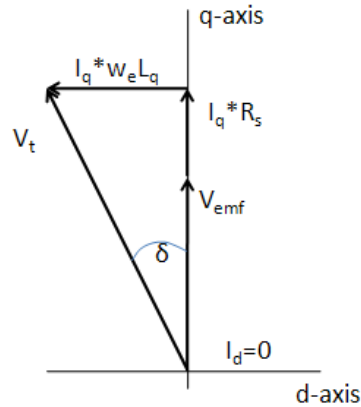
Figure 3.47: Phase diagram of PMSM for vector control

It is evident that exact real time control can not be achieved even for simple digital circuits. There is always a delay time between successive control steps due to process time. In today's drive applications generally 150 µsec passes to close a control loop (e.g. speed loop) and apply the vector excitation to motor terminals. This states that during 150 µsec time no feedback comes from motor and control is lost. $I_d=0$ case may be valid for the instant of applied excitation however for the next 150 µsec the applied excitation can not satisfy $I_d=0$ condition. The error in such a condition can be checked easily as follows.

Let's assume that motor is operated at 1500rpm. It must be noted that the tested motor has four pole pairs which results in four times 360 electrical degrees in one mechanical revolution. At this speed, rotor completes one mechanical revolution at 40 µsec. Four times 360 degrees is spanned in 40 µsec. We stated that one control loop lasts 150 µsec. The angular rotation of rotor in this period can be calculated as;

$$\frac{0.15}{40} x4x360° = 5.4° \tag{3-29}$$

It is clear that a vector control drive with 150 µsec control loop time has a maximum of 5.4° angle error in vector control. This means that terminal current vector I may be out of phase with back EMF voltage E_o by 5.4° where $I_d=0$ can not be satisfied.

Since all the calculations in running tests rely on $I_d=0$ condition to be satisfied, all inductance calculations are completely distributed over an error range. The observed distributed inductance values in load tests in Figure 3.33 results from this situation. Running tests has a fixed error range regarding to vector control loop time. It is shown in

previous section that such an angle error results in calculation errors by 100% which questions reliability and accuracy of inductance values measured by load tests.

Dependency of Measurements on Test Frequency

In presented results in section 3.3.3 that calculated inductance values vary by operating frequency. As stated before, this is completely contradictory with theory which states inductance is a function of flux created per unit of a current, no relation to frequency is present. This result may be an outcome of vector control error stated in section 0.

On the other hand, Senjyu et. al. [32] had a similar result which shows lower inductance for higher frequencies (Figure 3.48).
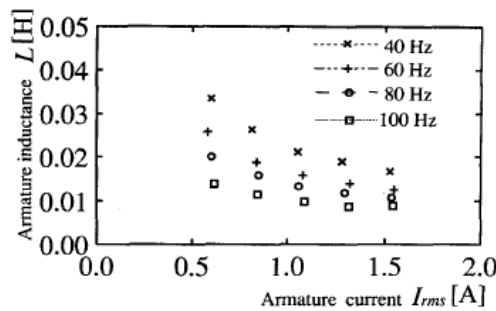
Figure 3.48: Result of inductance measurement by Senjyu [32]

This does not state that inductance may vary with frequency; however it is useful to show that variations with frequency may be observed due to possible load angle measurement errors.

Dependency of Measurements to Harmonic Elimination

Most of modern motor drive systems have a PWM output voltage to supply currents to motor terminals. The voltage waveform at motor terminals is highly distorted and far from sinusoidal shape. In inductance calculations, the fundamental harmonic components of voltages and currents are used since phase diagrams modelling the motor is constructed based on fundamental quantities.

For a PWM voltage waveform, the extraction of fundamental component both affects amplitude and phase which are two main parameters in inductance calculation. Inaccuracies in harmonic directly affect the calculated inductance. For example, a 5% error in amplitude of voltage fundamental will result in 5% error in calculated inductance. With other probable measurement inaccuracies, this error may establish a result far from reality.

The consistency between calculated inductance values for AC excitation and PWM shows that fundamental components of both voltage and current are correctly extracted with the harmonic analyzer used in the test setup. It can assumed that harmonic extraction can be performed reliably with a harmonic analyzer; so a PWM waveform can not be (or the last) a cause for unreliable distributed inductance values observed in load tests.

3.5   Discussions on Measurements

In section 3.3, selected test methods from the proposed tests in Section 3.2 are performed on the tested motor. Following conclusions can be made regarding to measurement results.

- Winding resistance can be measured precisely with four-wired setup as described in 3.2.1. The measured value at room temperature must be modified at higher temperatures. A 100°C can result in 35% increase in actual resistance as mathematically expressed in (3-1).

- Inductance measurement is a challenging issue, especially measurement of Lq. Standstill measurements with AC or PWM excitation give reliable results for both Ld and Lq measurements.

Running no-load test for L_d gives accurate results for different frequencies and current values. The reason for that is, load angle is small in this tests and cosine of load angle δ is used in calculations. This result in reliable measurements which are not very sensitive to load angle errors.

Running load test for L_q gives scattered inductance values on the current and frequency range. Since sine function of load angle is used in the calculations, calculated inductance value is very sensitive to load angle. Vector control loop also introduces a load angle error naturally due to control in discrete times (e.g. every 150 μsec).

The sensitivity of L_q measurement to load angle may be reduced by performing the test at specific conditions where load angle is big and angle errors introduced by vector control is low. This condition can be satisfied by performing the test at low

speed with high load where vector control loop is fast enough to realize $I_d=0$ condition and motor current is high enough to have a large "$I_q.X_q$" vector on the phase diagram. This comment can be validated by observing load angle variation with respect to frequency and load. The variation of sine value of load angle is plotted in Figure 3.46. It can be observed that load angle sine value at 200 Hz at maximum current becomes 2.5 times although frequency is increased 8 times from 25 Hz to 200 Hz.

- Back-emf voltage measurement of PM machine is easy to conduct. As long as the tested motor is driven by auxiliary means at a speed, generated can be observed at motor terminals. The emf – speed relation is expected to have a linear relation between. An extra but useful effort may be to perform emf test at different ambient temperatures to extract temperature dependence of back emf. This kind of test can be conducted in a temperature chamber.

- It is shown in Section 3.2.4 that friction-windage losses can not be separated from core loss in PM machines. Rotor magnets have to be removed to measure only friction-windage loss which requires disassembling of the motor.

- Torque-Speed measurement has a straight forward procedure which is described in 3.2.5. As observed in Figure 3.41, measurements are consistent with manufacturer data.

- Motor efficiency test can be performed as described in Section 3.2.7. During the test, it wise to record motor temperature also beside electrical measurements.

- It is better to perform cogging torque measurements at very low speed with high inertia. This is also suggested by Boldea [40]. Test at low speed enhances the torque accuracy and high inertia assists keeping the shaft speed constant while driving the test motor by auxiliary means.

CHAPTER 4

ANALYTICAL CALCULATION of
BRUSHLESS DC MOTOR PARAMETERS and PERFORMANCE

In this chapter, mathematical equations related to the parameters in the magnetic and electrical model of an inset-magnet PM motor is going to be derived in terms of motor dimensions and some other parameters. The ultimate goal is to develop a mathematical model which can be used to analytically estimate the performance of a radial flux inset-magnet electrical machine from its geometry and material properties.

Mechanical dimensions and material properties in the machine will be used as an input the model. The outcomes are values of the parameters in the machine model and performance characteristics like torque-speed, power-speed etc.

The equations will be derived in terms of designated names like "L" for axial length of steel core and "Br" for magnet remanent flux density to get a generalized view. At the end of this chapter, the verification of the derived mathematical model will be done with an available PM motor which is fully characterized by performance tests, parameter measurements and dimensional measurements on the disassembled mechanical body. The measurement results are presented in CHAPTER 3 and abbreviations for mechanical dimensions are illustrated in Figure 4.1.
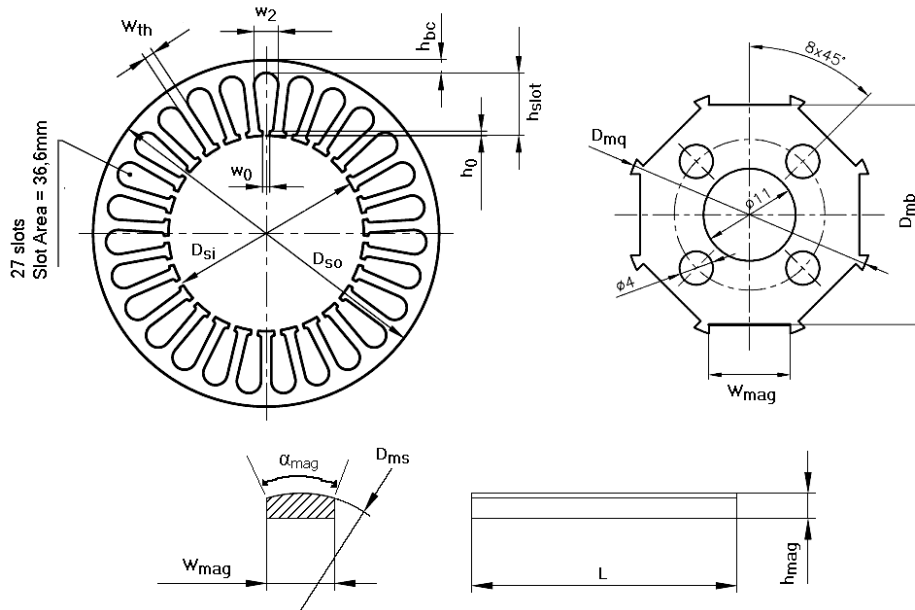
Figure 4.1: Abbreviations for stator, rotor and magnet dimensions

4.1 Equivalent Magnetic Model Calculations

The magnetic equivalent circuit of PM machine was derived in Section 2.1. The circuit is also presented in Figure 4.2 . Each parameter in the given circuit should be expressed analytically to calculate the motor performance.
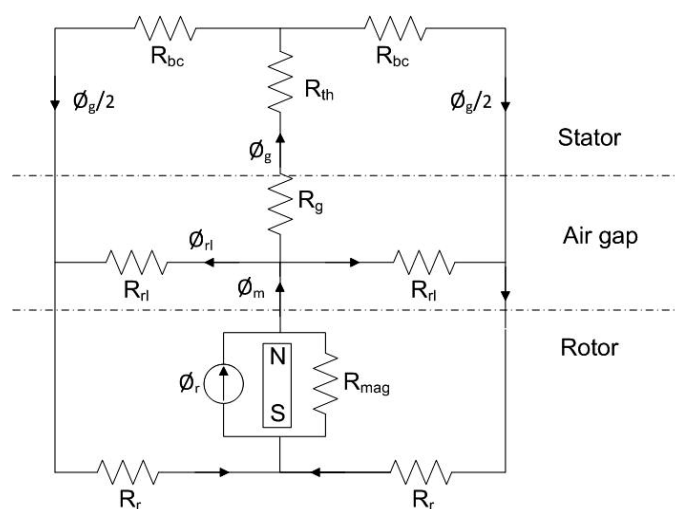
Figure 4.2: Equivalent magnetic circuit model of PM motor

The parameters in the equivalent circuit are defined as follows. Definitions of the variables may be found in Chapter 2.

- $\emptyset_r$: Flux generated by magnet
- $\emptyset_m$: Flux leaving magnet and passing to airgap
- $\emptyset_{rl}$: Rotor leakage flux between poles (through R_{rl})
- $\emptyset_g$: Flux at airgap passing from rotor to stator side
- R_{mag} : Magnet internal leakage path reluctance
- R_{rl} : Reluctance of leakage path between magnets
- R_g : Equivalent airgap magnetic reluctance
- R_{th} : Equivalent tooth magnetic reluctance
- R_{bc} : Equivalent back core magnetic reluctance
- Rr : Reluctance of rotor yoke

4.1.1 Magnet Flux and Reluctances

The process of obtaining analytical expressions of the parameters is started with modelling the magnet. In the magnetic equivalent model, the magnet is modelled with a flux source $\emptyset_r$ in parallel with leakage reluctance R_{mag} which is Norton equivalent model. This method is also used in electrical circuit analysis for voltage sources. Norton equivalent of the magnet can be expressed as follows.

$$\phi_0 = B_r A_{mag} \tag{4-1}$$

$$R_{mag} = \frac{h_{mag}}{\mu_r \mu_0 A_{mag}} \tag{4-2}$$

In the equations (4-1) and (4-2), B_r is remanent flux density of the magnet which is defined by the magnet manufacturer and it is temperature dependent, A_{mag} is cross sectional area of the magnet in normal direction to magnetization direction, h_{mag} is magnet length in magnetization direction, μ_r and μ_o are magnet relative recoil and free space permeabilities respectively. Magnet cross sectional area "A_{mag}" is calculated by multiplying magnet width "W_{mag}" with axial length L (Figure 4.3).

$$A_{mag} = W_{mag} L \tag{4-3}$$
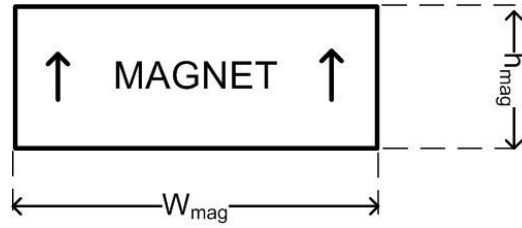
Figure 4.3: Defined dimensions of a cubic magnet

(Arrows show magnetization direction)

For simple shaped magnets like in Figure 4.3, reluctance expression given in equation (4-2) is useful. However for most machine designs, magnets have special shapes to get a sinusoidal flux distribution in the air gap. In such case, it is wise to split the magnet along the magnetization direction into smaller pieces, calculate reluctance for each piece and then treat them as in parallel to get total reluctance. In this work, the magnet is shaped as shown in Fig. 4.4 It is split into five pieces as seen in Figure 4.4.
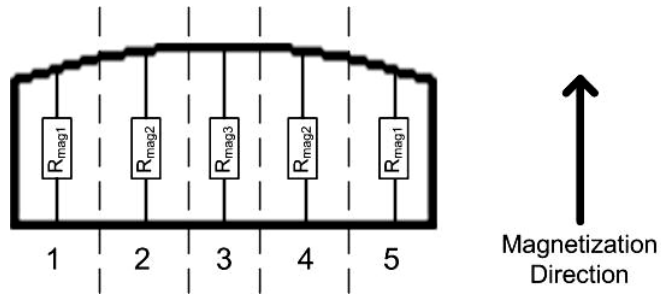
Figure 4.4: Illustration of magnet reluctance derivation

In the above figure, reluctances are assigned for each magnet piece. However it should be noted that since pieces 2 & 4 and 1 & 5 are identical due to symmetry, same reluctances are assigned for them in pairs. The total reluctance of the magnet can be obtained from equation (4-4).

$$R_{mag} = \left(\frac{2}{R_{mag1}} + \frac{2}{R_{mag2}} + \frac{1}{R_{mag3}} \right)^{-1} \tag{4-4}$$

Since magnet is sliced into 5 equal width pieces, cross sectional area in equation (4-1) must be taken as $A_{mag}/5$ to calculate reluctance for each. Also it must be noted that h_{mag} is different for each piece. To calculate height of each magnet piece, some geometrical derivation must be faced.

$$R_{mag} = \left(\frac{2}{R_{mag1}} + \frac{2}{R_{mag2}} + \frac{1}{R_{mag3}} \right)^{-1}$$

(4-5)

$$= \left(\frac{2}{\dfrac{h_{mag1}}{\mu_r \mu_0 \dfrac{W_{mag}}{5} L}} + \frac{2}{\dfrac{h_{mag2}}{\mu_r \mu_0 \dfrac{W_{mag}}{5} L}} + \frac{1}{\dfrac{h_{mag3}}{\mu_r \mu_0 \dfrac{W_{mag}}{5} L}} \right)^{-1}$$

$$= \frac{1}{\mu_r \mu_0 \dfrac{W_{mag}}{5} L} \left(\frac{2}{h_{mag1}} + \frac{2}{h_{mag2}} + \frac{1}{h_{mag3}} \right)^{-1}$$

$$h_{mag1} = 0.5 \times \left[D_{ms} \cos\left(\frac{2}{5} \alpha_{mag} \right) - D_{mb} \right]$$

(4-6)

$$h_{mag2} = 0.5 \times \left[D_{ms} \cos\left(\frac{1}{5} \alpha_{mag} \right) - D_{mb} \right]$$

(4-7)

$$h_{mag3} = 0.5 \times \left[D_{ms} \cos\left(\frac{0}{5} \alpha_{mag} \right) - D_{mb} \right] = 0.5 \times \left(D_{ms} - D_{mb} \right)$$

(4-8)

$$\alpha_{mag} = 2 \times \sin^{-1}\left(\frac{W_{mag}}{D_{ms}} \right)$$

(4-9)

In the equations (4-5)-(4-9), $h_{mag1-2-3}$ are height of each magnet region as defined in Figure 4.4, D_{ms}, D_{mb}, W_{mag} are illustrated in Figure 4.1, θ_{mag} is angle span of magnet surface in mechanical degrees. To be more clear, a magnet having a 2/3 pole pitch in 8 pole motor has 30° angle span (equation (4-10)).

$$\theta_{mag} = \frac{2}{3} \times \frac{360}{8} = 30°$$

(4-10)

4.1.2 Rotor Leakage Reluctance

This parameter represents the path for flux which does not pass from magnet to stator but instead leak from one magnet to adjacent one. As Miller [6] stated, it is hard to define leakage paths but instead they can be assigned a value as a portion of magnet reluctance

and R_{rl} is expected to be 5-20% of magnet reluctance R_{mag}. The effect of leakage reluctance on airgap magnetic flux density results in 0,005Nm torque calculation error. Considering the rated torque of the sample motor (1,47Nm), this error is acceptable. In conclude, R_{rl} is going to be defined as "10*R_{mag}".

$$R_{rl} = 10 \times R_{mag}$$
(4-11)

4.1.3 Airgap Reluctance

The airgap reluctance is perhaps the most important parameter in the equivalent magnetic circuit, since to determine airgap flux, airgap reluctance must be defined. Also this parameter determines the magnetizing inductance of a motor. The general expression for airgap reluctance is given by

$$R_g = \frac{g'}{\mu_0 A_{gap}}$$
(4-12)

where A_{gap} is the pole pitch area midway along flux direction between stator inner surface and magnet surface. "g'' is modified airgap g with Carter's coefficient k_c to include effect of stator slotting on airgap flux density. Airgap is modified as in equation (4-13).

$$g' = g \cdot k_c$$
(4-13)

Derivation of Carter Coefficient is presented by F.W. Carter [41] as in equation (4-14).

$$k_{c0/00} = \frac{\lambda_{0/00}}{\lambda_{0/1} - \dfrac{\omega_{0/00}^{2}}{\omega_{0/00} + 5g}}$$
(4-14)

In the equation, the subscript "0" refers to stator side whereas "00" refers to rotor side. Respective dimensions should be selected to calculate Carter's coefficient for stator or rotor side. Dimensions of stator and rotor surface structure are defined as in Figure 4.5 for the tested sample motor.
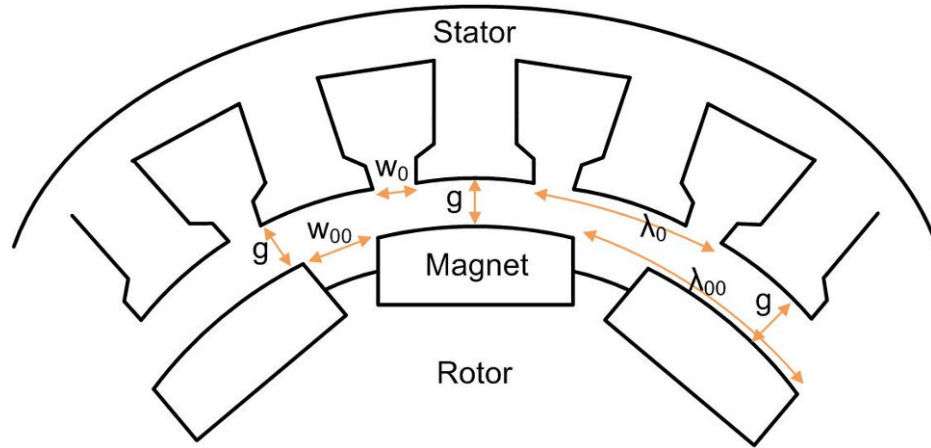
Figure 4.5: Abbreviations for stator and rotor surface dimensions for Carter's coefficient calculation

In the figure; "g" is airgap, "w_0" is stator slot opening width, "w_{00}" displacement between rotor magnets, "λ_0" is stator slot pitch, "λ_{00}" is rotor pole pitch calculated at radius tangential to magnet surface tip. Carter coefficient for stator side "k_{c0}" can be calculated as in equation (4-15).

$$k_{c0} = \frac{\pi D_{si} / N_{slot}}{\pi D_{si} / N_{slot} - \dfrac{\omega_0^2}{\omega_0 + 5g}}$$

(4-15)

The airgap area (Figure 4.6) is defined as the cross sectional area of the path that the flux follows while passing from magnet to stator (or vice versa). The flux path in the airgap is dominantly set up by the magnetization direction of the magnet. However some fringing flux inevitably exists in the airgap. The area seen by the flux increases with the fringing flux. Exact area may not be defined easily but an acceptable approximation can be made.

In Figure 4.6, flux passing from magnet to stator is shown by arrows. The shaded areas at two sides of the magnet point to fringing flux. The width of each fringing area is approximated as equal to airgap depth "g" [6], so area of total region seen by flux can be evaluated as in equation (4-16) by adding two times airgap to magnet surface width.

$$A_{gap} = \left(\frac{1}{2} D_{ms} \alpha_{mag} + 2g \right) \times L$$

(4-16)

In the equation "D_{ms}" is diameter of roundness of magnet surface and "α_{mag}" is angular span of magnet defined in Figure 4.1.
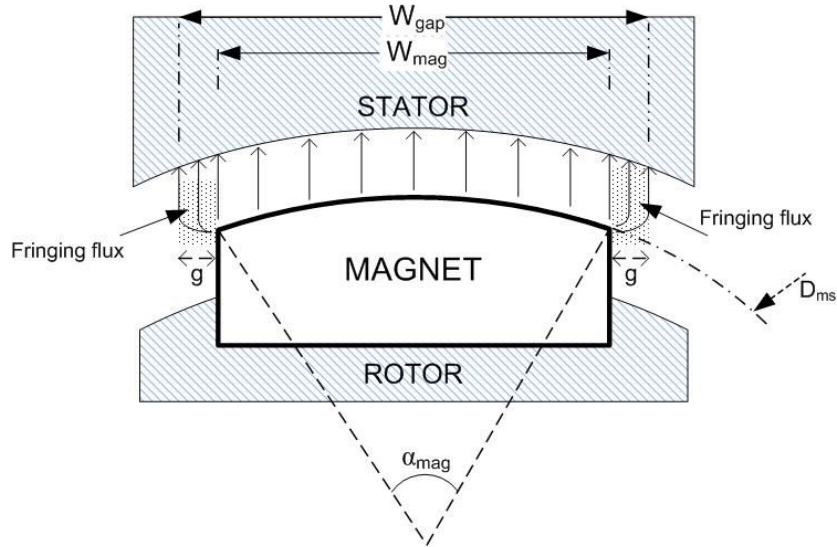
Figure 4.6: Fringing flux in the airgap

(Arrows show flux direction)

To calculate total airgap reluctance equation (4-12) may be used with modified flux region width.

$$R_g = \frac{g \cdot k_c}{\mu_0 \left(\dfrac{1}{2} D_{ms} \alpha_{mag} + 2g \right) \cdot L}$$

(4-17)

4.1.4 Stator Tooth and Back-core Reluctance

The stator teeth and back core can be often assumed to be infinitely permeable and their reluctance may be neglected. However, for high field density motors such as servo applications, motor volume is forced to be minimized by pushing flux densities to saturation level. In such cases there can be considerable amount of mmf drop on tooth and back core path, so reluctances for these paths should be included in magnetic field calculations. Equation (4-12) can be modified to calculate teeth and back core path reluctances.

$$R = \frac{flux\,path\,length}{\mu_{steel} \cdot \mu_0 \cdot flux\,path\,cross\,sec\,tional\,area}$$

(4-18)

$$R_{th} = \frac{(h_0 + h_1 + h_2)}{\mu_{steel}\,\mu_0\,(w_{th}L)} / S_{pitch}$$

(4-19)

$$R_{bc} = \frac{\pi \cdot (D_{so} - h_{bc})/p}{\mu_{steel} \, \mu_0 \, (h_{bc} \, L)}$$

(4-20)

In the above equations, "$h_0+h_1+h_2$" defines length of path from tooth tip to slot dip, Ns/p is number of slots per pole, L is axial length of steel core. The path for back core reluctance is chosen to be in the middle of back core depth. Therefore the diameter of the path at is defined as (D_{so}-h_{bc}).
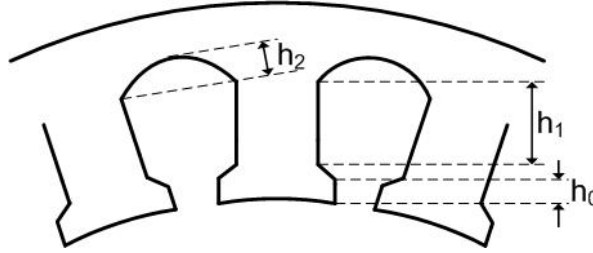
Figure 4.7: Abbreviations for slot dimensions

4.1.5 Solving Magnetic Circuit

In previous sections, parameters in the magnetic equivalent circuit have been derived. Flux densities in the magnetic circuit can be determined now by solving the magnetic circuit. Magneto motive force (MMF) created by the magnet equals to total MMF drop in the magnetic circuit. It is going to be assumed that the MMF drop in the steel core is insignificant with respect to MMF drop in airgap. The validation of this assumption is shown mathematically in section 4.4.1 by equations (4-92), (4-93) and (4-94) such that airgap reluctance is 1000 times of stator rotor and back core reluctances. MMF equation related to magnetic circuit can be written as in equation (4-21).

$$F_m = (\phi_r - \phi_g) \times (R_{mag} + R_{rl})$$

(4-21)

$$(\phi_r - \phi_g) \times (R_{mag} + R_{rl}) = \phi_g \cdot R_g$$

(4-22)

$$\phi_g = \frac{\phi_r}{1 + R_g / R_{mag}}$$

(4-23)

Considering rotor leakage path, magnet operating flux density can be calculated as follows.

$$B_m = \frac{1 + R_g / R_{rl}}{1 + R_g / R_{mag}} B_r \tag{4-24}$$

Airgap flux density can be calculated as follows.

$$B_g A_g = \frac{B_r A_{mag}}{1 + R_g / R_{mag}} \tag{4-25}$$

$$B_g = \frac{A_{mag} / A_g}{1 + R_g / R_{mag}} B_r \tag{4-26}$$

Calculated flux density B_g is present only in "$D_{ms}*\alpha_{mag}+2g$" pole region as presented in Figure 4.6. Airgap mean flux density is calculated as follows:

$$\overline{B}_g = \frac{\left(\frac{1}{2} D_{ms} \alpha_{mag} + 2g\right)}{\pi(D_{si} - g)/ p} \times B_g \tag{4-27}$$

Tooth flux density can be calculated assuming that all airgap flux passes to stator teeth. It is assumed that all flux in one slot pitch links one tooth so that peak flux density in airgap can be scaled to determine peak tooth flux density. Peak flux density can be calculated as in equation (4-28).

$$\hat{B}_g = \frac{h_{mag}}{h_{mag} + g\mu_r} B_r \tag{4-28}$$

Maximum tooth flux density occurs when this calculated peak flux in one slot pitch λ_{th} links one slot.

$$B_{th} = \hat{B}_g \frac{\lambda_{th}}{w_{th}} = \frac{h_{mag}}{h_{mag} + g\mu_r} \frac{\pi D_{si} / N_s}{w_{th}} B_r \tag{4-29}$$

Back core flux density can be calculated assuming that half of total pole flux passes through back core.

$$B_{bc} A_{bc} = \frac{1}{2} B_g A_g \tag{4-30}$$

$$B_{bc} = \frac{\frac{1}{2} B_g A_g}{h_{bc} L} \tag{4-31}$$

At this point, every parameter and flux density in magnetic equivalent circuit is expressed analytically in terms of magnetic circuit dimensions. The next step is obtaining expression for the electrical circuit parameters.

4.2 Equivalent Electrical Model Calculations

The magnetic equivalent circuit of PM machine was derived in Chapter 2.2. To be a reminder, the equivalent electrical model circuit is also presented in Figure 4.8. Each parameter in the given circuit should be derived analytically to build the complete analytical model.
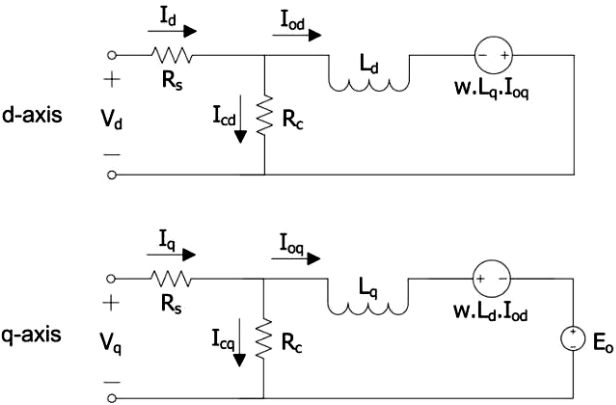
Figure 4.8: Two axes electrical model of PM motor

The given electrical circuit will be solved for vector control operation. The phase diagram for this specific condition is given in Figure 3.29. That phase diagram shows that no Id current is present in the motor that means only q-axis circuit is active.

4.2.1 Stator Winding Phase Resistance

The resistance of a conductor is calculated with following equation;

$$R = \rho \frac{L_c}{A_c}$$

(4-32)

where "ρ" is conductor resistivity in ohm.m units, "L_c" is total conductor length in meters and "A_c" is cross sectional area of the conductor in m^2. The conductor cross sectional area A is dependent on slot fill factor and winding scheme; single layer or double layer.

i. Wire cross-sectional area

Assuming that the wire conductor is selected with diameter D_{wire}, wire cross sectional area can be calculated as;

$$A_{wire} = \pi D_{wire}^2 / 4 \qquad (4\text{-}33)$$

If coil wire is not known, it can be calculated by slot area A_{slot}, copper fill factor k_{fill} and turns per coil N_t by equation (4-34).

$$A_{wire} = \frac{0.5 \cdot A_{slot} \cdot k_{fill}}{N_t} \qquad (4\text{-}34)$$

ii. Conductor length in one coil

The conductor length in one coil can be approximately calculated with steel core dimensions.

$$L_{wire} = 2 N_t \left(L + L_{ext} + \left[S_{pitch} / N_{slot} \cdot (D_{si} + h_{slot}) \cdot \pi \right] \right) \qquad (4\text{-}35)$$

N_t : Turns per coil
L : Steel core axial length
L_{ext} : Extension of end winding from stator
S_{pitch} : Number of slots between two conductors of a coil
N_{slot} : Total number of slots
D_{si} : Diameter at stator inner surface
h_{slot} : Total depth of a slot

In equation (4-35), "L_{ext}" defines end winding height from the stator steel. The extension is visualized in Figure 4.12 in section 4.2.2. Its value is totally up to winding workmanship. Similar motors have been investigated to define this length as 15mm. The expression in parenthesis in equation (4-35) is related to one conductor side of a coil. To calculate total length, there is a multiplication by 2.

iii. Length of conductor for connecting phase coils in series

There is also a wire connection between coils in a phase. Their resistance has to be included in resistance calculation also. In this work, length of connection between two adjacent coils is assumed to be equal to the length of coil end winding w_{c1} (Figure 4.12).
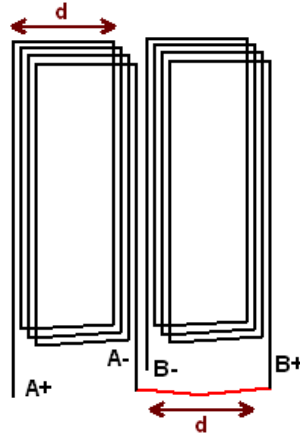
Figure 4.9: Connection between two adjacent coils

As shown in Figure 4.9, coil.A and coil.B are electrically connected as an example. The length of connection wire between A- and B+ terminals of two coils is assumed to be equal to length between two conductors of same coil ("w_{c1}" in Figure 4.12). The length of connection wires can vary in a single phase, but it is observed in the sample motor that total length of connections can be approximated by multiplying coil number with single coil end winding. With this assumption, total length of coil connections can be calculated with equation (4-36).

$$L_{con} = \frac{N_{coil} S_{pitch}}{N_{slot}} \left(D_{so} - h_{slot} \right) \pi \qquad (4\text{-}36)$$

where Ncoil is found by dividing slot number by number of phase.

$$N_{coil} = \frac{N_{slot}}{3} \qquad (4\text{-}37)$$

Total phase resistance can be calculating by rewriting equation (4-32).

$$R = 1.68 \cdot 10^{-8} \frac{\left(N_{coil} L_{wire} + L_{con} \right)}{A_{wire}} \quad (\Omega) \qquad (4\text{-}38)$$

It must be remembered that this calculated resistance is valid for room temperatures (25°C). The calculated value must be modified to include temperature effect by

$$R' = R \times \frac{234.5 + T}{234.5 + 25} \quad (\Omega) \qquad (4\text{-}39)$$

where R is calculated value at room temperature and R' is resistance at temperature T .

103

4.2.2 Inductance Calculation

In this section, expressions for d-q axes inductances L_d and L_q are going to be obtained in terms of motor dimensions. In the derivation, magnetic saturation is ignored.

Total inductance of a winding has following sub-components [9].

    i.   Slot leakage inductance

    ii.   End-winding leakage inductance

    iii.   Magnetizing inductance

In the following sub-sections, those leakage parameters are derived.

i.   *Slot Leakage Inductance*

Slot leakage is the due to the flux crossing the slot opening and linking the conductors in that slot (Figure 4.10).In case the motor has a double layer winding, there are two components of slot leakage.

-     Self leakage of each coil conductor
-     Mutual leakage between coils

Slot leakage inductance can be calculated by adding L_{sls} - Slot leakages due to each coil in a slot and L_{slm} - Mutual leakage inductance between coils. It is assumed that all coils in a phase are serially connected.

$$L_{slot} = L_{sls} + L_{slm}$$
(4-40)

The sample motor in this thesis work is 8-pole motor and has 27 slots for 3 phase winding. Since total number of slots per pole per phase is 1.125, there has to be double layer winding which must be considered in leakage calculations. The leakage terms for each coil conductor in one slot have to be calculated separately. Obviously the leakage of the conductor in slot dip is not equal to leakage of conductor located near to slot opening. Considering all these facts, the slot leakage terms Lsls and Lslm for a double-layer winding can be calculated with slot dimensions by following equations [9].

$$L_{sls} = \frac{3N^2 L}{N_{slot}}\left(pT + pB + 2 \cdot pTB \cdot \left(3C_{pitch} - 2\right)\right)$$
(4-41)

$$L_{slm} = \frac{3N^2 L}{N_{slot}} pTB \cdot 3\left(1 - C_{pitch}\right)$$
(4-42)

N : Total number of turns per phase
L : Steel core axial length
Nslot : Total number of slots
pT, pB, pTB : Specific Slot Permeance Coefficients
C_{pitch} : Coil pitch – Ratio of angular span of a coil to one pole.

Specific slot permeances defined in (4-41) and (4-42) are related to magnetic structure on leakage flux paths. The leakage flux due to top layer conductor travels a different path than leakage flux due to bottom layer conductor. Also there is a mutual flux path due to interaction of top and bottom layer winding (Figure 4.10).
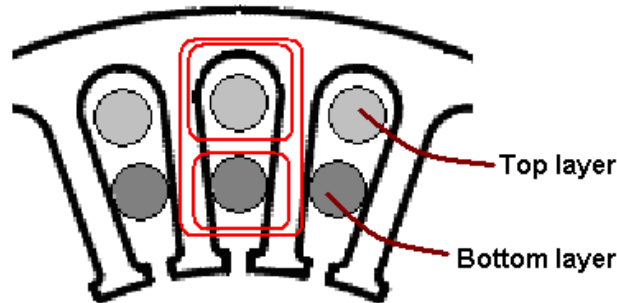
Figure 4.10: Contours showing slot leakage paths

In Figure 4.10, double layer winding is shown by two conductors and there are three contours of leakage flux path. Each path has its own inductance which are called pT for top layer, pB for bottom layer and pTB for mutual inductance path (outer contour).

The depth and width of leakage path defines these reluctances. In the derivation of slot leakage permeances, it is assumed that each layer has same cross sectional area.

$$\text{Area of top-layer = Area of bottom-layer} = \frac{A_{slot}}{2} \qquad (4\text{-}43)$$

$$A_{slot} = \frac{1}{2}\left(w_1 + w_2\right)\cdot h_1 + \frac{1}{2}\pi h_2 \qquad (4\text{-}44)$$

The dimensional abbreviations are illustrated in Figure 4.11. In the figure, area of top layer is equal to area of bottom layer.
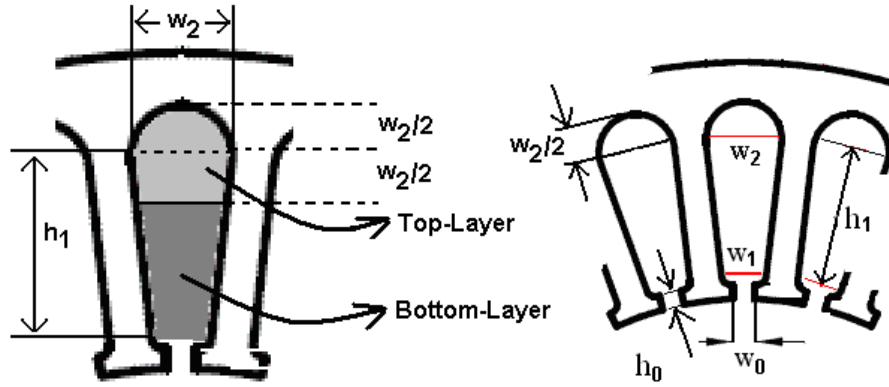
Figure 4.11: Illustration of top and bottom coil sides in a slot and abbreviations related to dimensions of stator

Specific slot leakage permeances can be calculated with following equations.

pT: Leakage permeance for top coil

: Leakage for half circle with height h_2 + leakage in rectangular are with height h_2

$$pT = \frac{1}{2}\mu_0\left(0.623 + \frac{h_0}{w_0}\right) + \frac{1}{3}\mu_0\frac{w_2/2}{w_2} \tag{4-45}$$

pB : Leakage permeance for bottom coil

$$pB = \mu_0\left(\frac{h_0}{w_0} + 2\frac{h_1 - \frac{w_2}{2}}{w_1 + w_2}\right) \tag{4-46}$$

pTB : Mutual leakage permeance between top and bottom coil

$$pTB = \mu_0\left(\frac{h_0}{w_0} + \frac{h_1 - \frac{w_2}{2}}{w_1 + w_2}\right) \tag{4-47}$$

Once the specific leakage permeances are calculated, slot leakage inductance L_{slot} can be calculated by inserting pT, pB and pTB to equations (4-41) and (4-42).

ii. *End Winding Leakage Inductance*

Exact leakage paths of end-winding can not be determined unless 3D finite element solution is performed. However an analytical expression for end winding leakage L_{end} is given by Gieras [7] for double layer windings.

$$L_{end} = 4\mu_0 \frac{N_s^2}{p} L_{1e} \lambda_{end}$$ (4-48)

μ₀ : Free space permeability
Ns : Total number of turns per phase
p : Pole number of motor
L_{1e} : Total end winding length
λ_{end} : Leakage permeance for end winding

In Figure 4.12, a sample stator with winding is illustrated to show end winding connections. As seen in the figure, there has to be a clearance for end winding connections to bend a bunch of coil conductors to form a coil. This clearance L_{ext} is assumed to be 15mm in this thesis work owing to observations on electric machines at same power levels (0.33kW). However, this value may be modified for different power level designs. Also the displacement between two sides of a coil is shown with "w_{c1}".

$$w_{c1} = \pi (D_{so} - h_{bc} - h_{slot}) \frac{S_{pitch}}{N_{slot}}$$ (4-49)

D_{so} : Stator outside diameter
h_{bc} : Stator back core depth
h_{slot} : Total slot depth
S_{pitch} : Coil pitch in number of slots
N_{slot} : Total number of slots
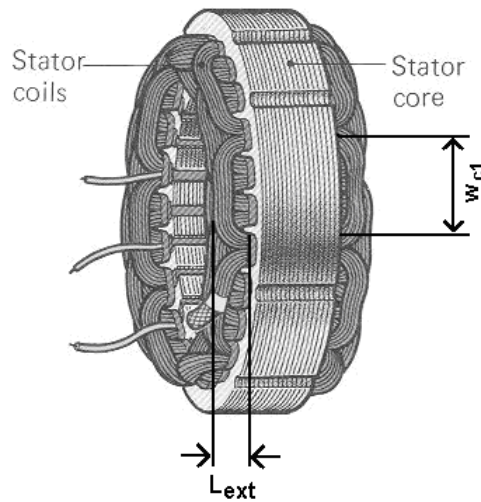
Figure 4.12: Illustration for stator end-winding connections

The leakage permeance λ_{end} is a function of displacement between two sides of a coil w_{c1}, number of slots per pole per phase q and length of end winding for a single coil [7].

$$\lambda_{end} = 0.34 \cdot q \cdot \left(1 - \frac{2}{\pi} \frac{w_{c1}}{L_{1e}}\right) \quad (4\text{-}50)$$

The length of end winding for a single coil is approximately calculated by adding 15mm of end winding clearance ().

$$L_{1e} = 2 \times L_{ext} + w_{c1} \quad (4\text{-}51)$$

iii.   Magnetizing Inductance

Magnetizing inductance is related to the flux created by phase coils that crosses motor air gap from stator to rotor and then from rotor to stator, linking the phase coils. Phase diagram of equivalent motor model is formed for fundamental harmonic, inductance calculations must be done for fundamental harmonic also.

Basically, magnetizing inductance of a coil with N turns in a magnetic circuit with air gap (see Figure 4.13) can be calculated with equation (4-52).

$$L_m = N^2 / R \quad (4\text{-}52)$$

N   : Coil turns
R   : Reluctance of magnetic path
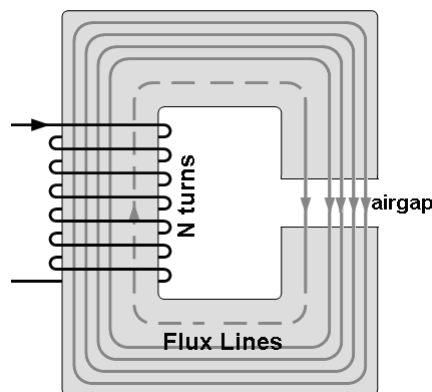
Figure 4.13: Simplest magnetic circuit with air gap

Since motor phase windings consist of coils connected in series, equation (4-52) can be used in calculation of magnetizing inductance of phase windings also. A modification has to be made to equation (4-52) since stator-rotor structure of the motor can not be overviewed as a simple magnetic circuit. The turns per phase parameter N must be

replaced with effective number of turns N_{eff} because flux in the air gap is not fully utilized due to winding scheme. N_{eff} is simply equal to N times winding factor k_w.

$$N_{eff} = N \cdot k_w \qquad (4\text{-}53)$$

The MMF created in the air gap for concentrated stator windings (which is the case in sample motor) can be illustrated as in Figure 4.14.
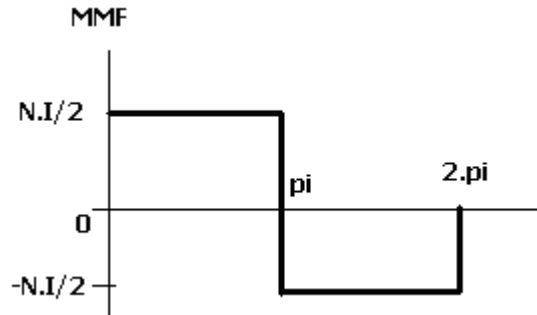
Figure 4.14: MMF distribution in air gap with concentrated winding

The amplitude of fundamental component "F_1" of the MMF distribution in Figure 4.14 for 3-phase excitation can be derived as in equation (4-54).

$$F_1 = \frac{3}{2}\frac{4}{\pi} N_{eff} I \qquad (4\text{-}54)$$

N_{eff} : Effective number of turns per phase
I   : Excitation current

Rewriting equation (4-52) with expressions equations (4-53) and (4-54), equation (4-55) is derived.

$$L_m = \frac{3}{2} \cdot \frac{4}{\pi} \cdot N_{eff}^{\;2} / R \qquad (4\text{-}55)$$

For equivalent reluctance R, there has to be two analytical equations due to saliency of PM machine rotor. Two reluctances have to be derived related to d-axis and q-axis alignment of the rotor.
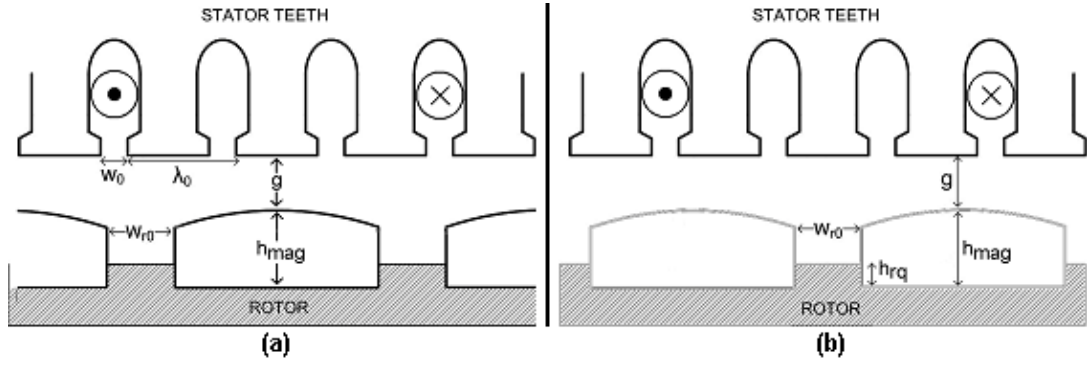
Figure 4.15: d-q positions for reluctance calculations

In Figure 4.15, d-axis alignment of rotor for coil in stator is shown in (a) and q-axis alignment in (b). As presented before in section 3.1.1, each coil has a coil pitch of 8/9 (or equivalently 3 slots for 27 slots and 8 poles) which is the same case in sample motor. For case (a), equivalent airgap for reluctance derivation will be calculated by modifying g with carter's coefficients for stator surface and rotor surface treating magnets as teeth. This is because; magnets act as teeth guiding flux lines through themselves. For case (b), airgap calculation will be made as if there were no magnets. The saliency between magnets will be treated as a tooth and carter's coefficient for rotor surface will be used to modify the gap between stator surface and top of the saliency. Calling equivalent airgap for d-axis as g_d' and for q-axis as g_q', they can be calculated as in equations (4-56) and (4-57).

$$g_d^{'} = g \cdot k_c + \frac{h_{mag}}{\mu_r} \tag{4-56}$$

$$g_q^{'} = \left(D_{si} - D_{mq}\right)/2 \times k_c \times k_{cr} \tag{4-57}$$

k_{c0} : Carter's coefficient for stator surface
k_{c00} : Carter's coefficient for rotor surface with no magnets

Carter coefficient for stator surface "k_{c0}" has been previously derived in equation (4-15). "k_{c00}" is crater coefficient for rotor surface as if there were no magnets.

$$k_{cr} = \frac{\lambda_{00}}{\lambda_{00} - \dfrac{W_{mag}^{2}}{W_{mag} + 5 \cdot (g + \dfrac{D_{mq} - D_{mb}}{2})}} \tag{4-58}$$

Having defined equivalent airgap and carter coefficients, equivalent magnetizing inductance equations for d-axis and q-axis alignments can be derived as in equations (4-59) and (4-60).

$$L_{md} = \frac{3}{2} \cdot \frac{4}{\pi} \cdot (N \cdot k_w)^2 \cdot \frac{\mu_0 . A_{pole}}{g_d'} \tag{4-59}$$

$$L_{mq} = \frac{3}{2} \cdot \frac{4}{\pi} \cdot (N \cdot k_w)^2 \cdot \frac{\mu_0 . A_{pole}}{g_q'} \tag{4-60}$$

Up to now, all sub-components of inductance have been calculated. Total equivalent d-q axes inductances can be derived by summing all three sub-component values.

$$L_d = L_{slot} + L_{end} + L_{md} \tag{4-61}$$

$$L_q = L_{slot} + L_{end} + L_{mq} \tag{4-62}$$

4.2.3 Calculation of Losses

Beside equivalent circuit parameter calculations, prediction of losses is also a major requirement, especially if optimization is involved. For PM machines, targets such as high efficiency and high torque density are in fact contradictory to each other. For example, high torque density requires reduced machine size with high flux densities. However higher core losses and lower efficiency arises with high flux densities. To find a good balance between contradictory requirements, machine loses have to be accurately predicted also. The main types of losses in PM motors are copper loss, core loss, magnet loss and mechanical losses due to windage and friction.

Copper Loss

Copper loss of an armature winding can be calculated if resistance of the winding and armature rms current are known. The resistance of the winding is calculated in Section 4.2.1. The total winding loss is calculated according to

$$P_{cu} = 3 \times I^2 \times R \tag{4-63}$$

where I is the rms value of the armature current and R is per phase resistance. It must be noted that per phase resistance value has to be modified by equation (4-39) if copper loss is to be calculated at high or low temperatures different than room temperature.

111

Core Loss

A good estimate of core loss power in steel core of a PM motor can be calculated by FE numerical computations. However an approximate calculation can be made by equation (4-64). This analytical equation [45] divides core loss into two components, eddy and hysteresis loss, and approximates the total loss by loss coefficients.

$$P_{loss} = \left(k_h f \hat{B}^2 + k_e f^2 \hat{B}^2 \right) \times M \quad Watts \tag{4-64}$$

In the above equation, k_h and k_e are hysteresis and eddy loss coefficients respectively, f is operating electrical frequency, $\hat{B}$ is peak of flux density and M is total weight of the medium where loss is calculated.

In the tested motor, core loss variation with frequency has been measured and results are presented in section 3.2.4. Core loss variation with respect to operating frequency is measured as in equation (4-65).

$$P_{loss} = 0.0002 f^2 + 0.0333 f \tag{4-65}$$

This expression is related to measured total loss. It is assumed in this study that friction-windage losses are very small and do not contribute to total loss expression. It is also assumed that negligible loss appear in the rotor steel since presence of magnets on the rotor avoids variation of flux densities in time by creating a constant magnetic field. Only losses appear in stator tooth and back core steel. Equation (4-64) should be solved for tooth and back-core regions separately as follows.

$$P_{loss} = P_{teeth} + P_{back-core} \tag{4-66}$$

The total mass of teeth and back-core area can be calculated by equations (4-67) and (4-68).

$$
\begin{aligned}
W_{th} &= N_s \times \left(h_0 + h_1 + h_2 \right) \times w_t \times L \times m_o \\
&= 27 \times 10.75mm \times 1.82mm \times 38mm \times 7.7 kg / dm^3 \\
&= 0.15 kg
\end{aligned}
\tag{4-67}
$$

$$
\begin{aligned}
W_{bc} &= \left(D_{so} - h_{bc} \right) \cdot \pi \cdot h_{bc} \cdot L \cdot m_o \\
&= (62mm - 2.25mm) \times \pi \times 2.25mm \times 38mm \times 7.7 kg / dm^3 \\
&= 0.12 kg
\end{aligned}
\tag{4-68}
$$

In the equations h_0, h_1 and h_2 are slot dimensions illustrated in Figure 4.11, w_t is tooth width, D_{so} is stator outer diameter, h_{bc} is stator back core depth behind slot dip, L is axial length, p is pole number and m_0 is weight density of steel core which is 7.7 kg/dm3

approximately as given in JFE Steel Catalog No.F1E-001-003 [59]. Reviewing equation (4-66), equation for total core loss can be derived as in equation (4-69) which includes losses in teeth and back core of stator.

$$P_{core} = \left(k_h f \hat{B}_{th}{}^2 + k_e f^2 \hat{B}_{th}{}^2 \right) \cdot W_{th} + \left(k_h f \hat{B}_{bc}{}^2 + k_e f^2 \hat{B}_{bc}{}^2 \right) \cdot W_{bc} \tag{4-69}$$

In the above equation B_{th} and B_{bc} are tooth and back core peak flux densities calculated as 1.9T and 1.8T respectively. W_{th} and W_{bc} are total mass of teeth and back core material. At this point, all unknowns in equation (4-69) are defined except k_e and k_h.

The values of k_h and k_e can be determined by equating the expression in (4-70) to equation (4-65).

$$\begin{aligned} P_{core} &= \left(k_h \times f \times (1.9)^2 + k_e \times f^2 (1.9)^2 \right) \times 0.15 \\ &\quad + \left(k_h \times f \times (1.8)^2 + k_e \times f^2 \times (1.8)^2 \right) \times 0.12 \\ &= k_e \times 0.93 \times f^2 + k_h \times 0.93 \times f \end{aligned} \tag{4-70}$$

$$k_e = \frac{0.0333}{0.93} = 0.0358 \tag{4-71}$$

$$k_h = \frac{0.0002}{0.93} = 0.000215 \tag{4-72}$$

It is determined that k_e can be taken as 0.0358 for and k_h as 0.000215 in equation (4-69). It is assumed here that iron loss of any motor of at 0.33 kW rated power as the sample motor can be calculated by substituting these kh and ke values into equation (4-69). This approach is used for the calculation of core loss in the optimization stage.

Core loss resistance can be derived by assigning the calculated core loss into the equivalent electrical circuit in Figure 4.8. The power loss on a resistor can be calculated by equation (4-73).

$$P = \frac{V^2}{R} \rightarrow R = \frac{V^2}{P} \tag{4-73}$$

The core loss resistance can be calculated by the same relation in equation (4-73).

$$R_c = \frac{\left(V_q - I_q R_s \right)^2}{P_{core}} \tag{4-74}$$

Magnet Losses, Friction and Windage Losses

No detailed analysis has been carried out to determine accurate expressions for magnet, friction and windage losses. It has been assumed that since magnets have very high coercivity and resistivity, space harmonics in the armature winding MMF does not induce eddy currents in the magnets. Friction and windage losses are also neglected regarding to small dimension of rotor due to low power PM machine (0.33kW rated). However a simple equation is available, to predict friction and windage losses, which is presented by Gieras [7]. That formula can be used to include these losses in a future study.

4.2.4 Back EMF Voltage

Probably the easiest way of identifying a PM motor is to measure back EMF voltage waveform because by identifying the generated back-EMF, many property of the tested motor like EMF and torque constants, pole number, speed range, torque-speed characteristic can be derived. Also the waveform of the back-EMF tells a lot about the motor drive requirements like bus voltage and current waveform (sinusoidal or trapezoidal). So, if the back EMF of a PM motor can be analytically represented, analytical modelling of the PM motor is completed.

The mathematical expression relating EMF to a square wave shaped magnetic flux distribution is derived in Chapter 2.3. The derived equation (2-11) must be revised for a sinusoidal distribution of flux. Also a stacking factor k_{st} and winding factor k_w should be inserted to include effects of laminated stator package and stator winding scheme. The modified expression is given in equation (4-75).

$$\hat{E}_o = \frac{p}{2}\omega_m N \phi_g k_w k_{st} \quad (\text{V}_{\text{peak}})$$ (4-75)

The flux per pole ϕ_g equals to integration of airgap flux over one pole pitch. Also airgap mean flux density $\overline{B}_g$ can be multiplied by pole area A_{pole} to calculate ϕ_g. In the equation (4-75), p is motor pole number, ω_m is shaft speed in rad/s, N is total number of turns per phase. In equation (4-75), it is clear that motor EMF voltage is linearly proportional to shaft speed ω_m so there can be stated an EMF voltage constant which simplifies the calculation of EMF voltage at motor terminals at a given shaft speed (equation (4-76)).

$$k_e = \sqrt{3}\frac{p}{2} N \overline{B}_g A_{pole} k_w k_{st} \quad (\text{V}_{\text{peak}}.\text{s/rad})$$ (4-76)

4.2.5 Developed Electromagnetic Torque

The torque output of a motor can be calculated by deriving electromagnetic power in the motor which is simply as in equation (4-77).

$$P_{em} = 3 \cdot E_o \bullet I \quad \text{(Watt)} \tag{4-77}$$

In the above equation, per phase EMF rms voltage E_o is multiplied with phase rms current I to obtain the power output of the motor. This expression is valid under vector control drive of the motor which states that only q-axis current is excited in motor windings not to alter flux in the airgap created by magnets.

Also it is known that power at the shaft of a motor can be calculated by multiplying torque with shaft speed in rad/s. Equation (4-77) can be rewritten to form developed electromagnetic torque equation.

$$T_{em} = \frac{3 \cdot E_o I_q}{\omega_m} \quad \text{(Watt)} \tag{4-78}$$

The above equation can be written more explicitly by inserting equation (4-75). It must be noted that the expression in equation (4-75) must be divided by $\sqrt{2}$ to get rms values instead of peak.

$$T_{em} = 3 \frac{1}{\sqrt{2}} \frac{p}{2} N \overline{B}_g A_{pole} k_w k_{st} I_q \quad \text{(Nm)} \tag{4-79}$$

In the above equation, it is observed that developed torque is linearly proportional to I_q which states that unless the motor field excitation is changed the motor has a constant torque constant. The magnetic saturation is ignored in this statement.

$$k_t = 3 \frac{1}{\sqrt{2}} \frac{p}{2} N \overline{B}_g A_{pole} k_w k_{st} \quad \text{(Nm /A}_{rms}) \tag{4-80}$$

4.3 Thermal Model

A simplified the thermal model is used in the optimization to reduce complexity of the optimization and save computation time. The temperature rise per watt loss is calculated with a thermal constant. The thermal constant "R_{th}" of the sample motor is measured in Section 3.3.7 as 2 °K/W. The simplified thermal model to be used in analytical temperature rise calculations is presented in Figure 4.16.
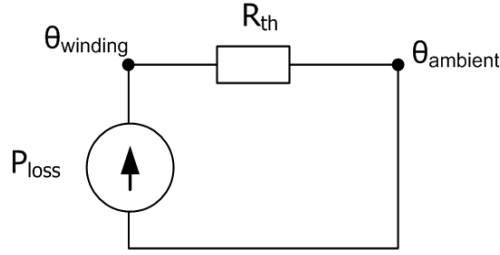
Figure 4.16: Simplified thermal model for analytical calculations

The measured motor temperature is the potential at node $\theta_{winding}$ and the ambient temperature is the potential at $\theta_{ambient}$. The power losses are modelled as a current source.

It is assumed that all the generated heat is dissipated from motor surface, so this constant can be modified with motor dimensions for the new design. This value is modified for every new design by equation (4-81) where motor outer diameter and axial length are considered.

$$R_{th}^{'} = R_{th} \frac{Outer\ surface\ of\ new\ design}{Outer\ surface\ of\ sample\ motor} = R_{th} \frac{\pi D'_{so} L'}{\pi D_{so} L} \tag{4-81}$$

In the above equation, R'_{th} is the modified thermal constant for new design, D'_{so} and L' are outer diameter and axial length of new design respectively. Temperature rise is calculated by dividing total loss power to thermal constant.

4.4 Calculations on Analytical Model

In this section, verification of the derived mathematical model will be performed in terms of an available PM motor which is fully characterized by manufacturer datasheet and measurements. Electrical data of the motor is given in Table 3.2, torque-speed characteristic is given in Figure 3.1, measured dimensions of stator, rotor and magnet is illustrated in Figure 4.17. Derived equations in previous sections will be assigned with values to calculate sample motor parameters and performance.
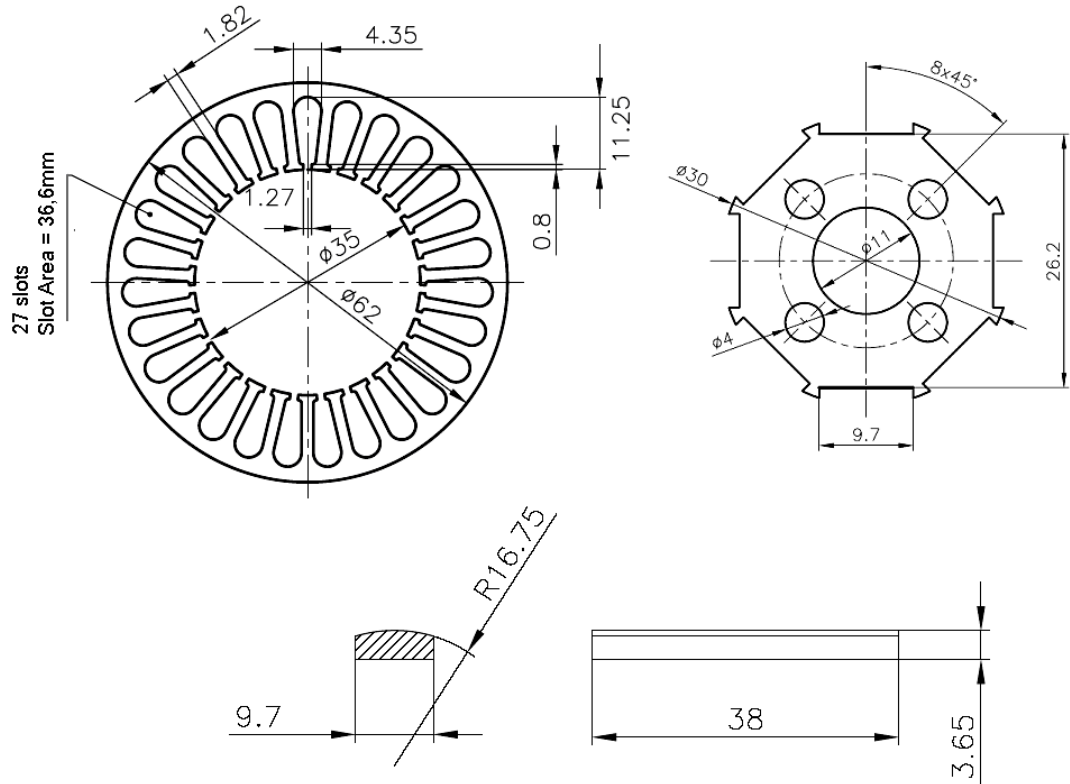
Figure 4.17: Measured dimensions for stator, rotor and magnet of sample motor

4.4.1 Calculation of Flux Densities

Although motor parameter measurements are performed and results are presented in CHAPTER 3, note that magnet Br value is not indicated yet. The only way to determine Br is expressing motor EMF or torque constant which include Br expression inside so that Br can be extracted. Equations with Br expressions are to be calculated after magnet Br value is calculated from EMF constant derivation.

Magnet cross sectional area by equation (4-3):

$$A_{mag} = 9.7 \cdot 10^{-3} \times 38 \cdot 10^{-3} = 369 \cdot 10^{-6} m^2 \qquad (4-82)$$

Magnet flux source by equation (4-1):

$$\phi_0 = B_r \times 369 \cdot 10^{-6} Wb \qquad (4-83)$$

Magnet angle span by equation (4-9):

$$\alpha_{mag} = 2 \times \sin^{-1}\left(\frac{9.7mm}{33.5mm}\right) = 33.66° = 0.5875 rad \qquad (4-84)$$

117

Magnet height in each magnet partition by equations (4-6), (4-7) and (4-8):

$$h_{mag1} = 0.5 \times \left[33.5mm \times \cos\left(\frac{2}{5}33.66\right) - 26.2mm \right] = 3.2mm \tag{4-85}$$

$$h_{mag2} = 0.5 \times \left[D_{ms} \cos\left(\frac{1}{5}\theta_{mag}\right) - D_{mb} \right] = 3.53mm \tag{4-86}$$

$$h_{mag3} = 0.5 \times (D_{ms} - D_{mb}) = 3.65mm \tag{4-87}$$

Magnet internal reluctance and leakage reluctances by equations (4-5) and (4-11) :

$$R_{mag} = \frac{1}{1.05 \times 4\pi \cdot 10^{-7} \dfrac{9.7 \cdot 10^{-3}}{5} 38 \cdot 10^{-3}} \left(\frac{2}{3.2 \cdot 10^{-3}} + \frac{2}{3.53 \cdot 10^{-3}} + \frac{1}{3.65 \cdot 10^{-3}} \right)^{-1} \tag{4-88}$$
$$= 7.015 \cdot 10^6 \quad (A - t / Wb)$$

$$R_{rl} = 10 \cdot R_{mag} = 70.15 \cdot 10^6 \quad (A.t / Wb) \tag{4-89}$$

Carter's coefficient for stator surface by equation (4-15):

$$k_c = \frac{\pi \cdot 35 \cdot 10^{-3} / 27}{\pi \cdot 35 \cdot 10^{-3} / 27 - \dfrac{1.27^2}{1.27 + 5 \cdot 0.75} 10^{-3}} = 1.086 \tag{4-90}$$

Airgap area by equation (4-16):

$$A_{gap} = \left(\frac{1}{2} 33.5 \cdot 10^{-3} \times 0.5875 + 2 \times 0.75 \cdot 10^{-3} \right) \times 38 \cdot 10^{-3} = 431 \cdot 10^{-6} \, m^2 \tag{4-91}$$

Airgap reluctance by equation (4-17):

$$R_g = \frac{0.75 \cdot 10^{-3} \times 1.086}{4\pi \cdot 10^{-7} \left(\dfrac{1}{2} 33.5 \cdot 10^{-3} \times 0.5875 + 2 \times 0.75 \cdot 10^{-3} \right) \times 38 \cdot 10^{-3}} \tag{4-92}$$
$$= 1.5 \cdot 10^6 \quad (A.t / Wb)$$

Stator tooth and back-core reluctances by equations (4-19) and (4-20):

$$R_{th} = \frac{11.25 \cdot 10^{-3}}{40000 \times 4\pi \cdot 10^{-7} \left(1.82 \cdot 10^{-3} \times 38 \cdot 10^{-3} \right)} / 3 = 1078 \, A.t / Wb \tag{4-93}$$

$$R_{bc} = \frac{\pi \cdot \left(62 \cdot 10^{-3} - 2.25 \cdot 10^{-3} \right) / 8}{40000 \times 4\pi \cdot 10^{-7} \left(2.25 \cdot 10^{-3} \times 38 \cdot 10^{-3} \right)} = 5460 \, A.t / Wb \tag{4-94}$$

Magnet operating flux density by equation (4-24):

$$B_m = \frac{1+1.5/70.15}{1+1.5/7.015} B_r = 0.84 \cdot B_r \tag{4-95}$$

Airgap mean flux density by equation (4-26):

$$B_g = \frac{369 \cdot 10^{-6}/431 \cdot 10^{-6}}{1+1.5 \cdot 10^6/7.015 \cdot 10^6} B_r = 0.705 \cdot B_r \tag{4-96}$$

$$\overline{B}_g = \frac{(33.5/2 \times 0.5875 + 2 \times 0.75)}{\pi(35-0.75)/8} \times 0.705 \cdot B_r = 0.59 \cdot B_r \tag{4-97}$$

Peak airgap flux density by equation (4-28):

$$\hat{B}_g = \frac{3.65}{3.65+0.75 \times 1.05} B_r = 0.82 \cdot B_r \tag{4-98}$$

Maximum tooth flux density by equation (4-29):

$$B_{th} = 0.82 \times \frac{\pi \cdot 35 \cdot 10^{-3}/27}{1.82 \cdot 10^{-3}} B_r = 1.83 \cdot B_r \tag{4-99}$$

Back core flux density by equation (4-31):

$$B_{bc} = \frac{0.5 \cdot 0.705 \cdot B_r \times 426 \cdot 10^{-6}}{2.25 \cdot 10^{-3} \times 38 \cdot 10^{-3}} = 1.77 \cdot B_r \tag{4-100}$$

Calculated reluctances and flux densities can be summarized in Table 4.1.

Table 4.1: Calculated reluctances and flux densities for sample motor

Reluctance	Calculated Value (A-t/Wb)	Flux Density	Calculated Value (Tesla)
R_{mag}	7.015×10^6	B_g	$0.705 \times B_r$ (0.74)
R_{rl}	70.15×10^6	$\overline{B}_g$	$0.59 \times B_r$ (0.62)
R_g	1.5×10^6	B_m	$0.84 \times B_r$ (0.88)
R_{th}	1078	B_{th}	$1.83 \times B_r$ (1.92)
R_{bc}	5460	B_{bc}	$1.77 \times B_r$ (1.85)

In next section 4.4.2, it is derived from measurements that Br value of tested sample motor is around 1.05 T. Flux densities in Table 4.1 can be derived by inserting this Br value into related equations. The calculation results are given in parenthesis in last column of Table 4.1.

4.4.2 Calculation of Electrical Parameters

Phase resistance:

Slot area by equation (4-44):

$$A_{slot} = \frac{1}{2}\left(2.55 \cdot 10^{-3} + 4.35 \cdot 10^{-3}\right) \cdot 7.78 \cdot 10^{-3} + \frac{1}{2}\pi\left(\frac{4.35 \cdot 10^{-3}}{2}\right)^2 \tag{4-101}$$

$$= 34.27 \cdot 10^{-6}\ m^2$$

Wire cross section area by equation (4-34):

$$A_{wire} = \frac{0.5 \cdot 34.27 \cdot 10^{-6} \cdot 0.339}{4} = 1.45 \cdot 10^{-6}\ m^2 \tag{4-102}$$

Conductor length in one coil by equation (4-35):

$$L_{wire} = 2 \times 4 \cdot \left(0.038 + 0.015 + \left[\frac{3}{27}(0.035 + 0.011) \cdot \pi\right]\right) = 0.55\,m \tag{4-103}$$

Length conductor for connecting coils in series by equation (4-36):

$$L_{con} = \frac{9 \times 3}{27}(0.062 - 0.011)\pi + 2 \times 9 \times 0.015 = 0.43\,m \tag{4-104}$$

Total phase resistance by equation (4-38):

$$R = 1.68 \cdot 10^{-8}\frac{(9 \times 0.55 + 0.43)}{1.45 \cdot 10^{-6}} = 0.062\ \Omega \tag{4-105}$$

d-q axes Inductances:

Slot leakage permeance coefficients by equations (4-45), (4-46) and (4-47):

$$pT = \frac{1}{2}\mu_0\left(0.623 + \frac{0.8}{1.27}\right) + \frac{1}{3}\mu_0\frac{4.35/2}{4.35} = 1 \cdot 10^{-6} \tag{4-106}$$

$$pB = \mu_0\left(\frac{0.8}{1.27} + 2\frac{8.275 - \frac{4.35}{2}}{2.55 + 4.35}\right) = 2.83 \cdot 10^{-6} \tag{4-107}$$

$$pTB = \mu_0\left(\frac{0.8}{1.27} + \frac{7.78 - \frac{4.35}{2}}{2.55 + 4.35}\right) = 1.81 \cdot 10^{-6} \tag{4-108}$$

Slot leakage inductance by equations (4-40), (4-41) and (4-42):

$$L_{sls} = \frac{3 \times 36^2 \times 0.038}{27} \left(10^{-6} + 2.83 \cdot 10^{-6} + 2 \cdot 1.81 \cdot 10^{-6} \cdot (3 \times 0.86 - 2) \right) \tag{4-109}$$
$$= 0.032\,mH$$

$$L_{slm} = \frac{3 \times 36^2 \times 0.038}{27} 1.81 \cdot 10^{-6} \times 3 \cdot (1 - 0.86) = 4.16 \cdot 10^{-6}\,H \tag{4-110}$$

$$L_{slot} = 32.45 \cdot 10^{-6} + 4.16 \cdot 10^{-6} = 0.037\,mH \tag{4-111}$$

End-winding inductance by equations (4-48), (4-50), (4-51) and (4-49):

$$w_{c1} = \pi \left(0.062 - 2.25 \cdot 10^{-6} - 0.011 \right) \frac{3}{27} = 0.017\,m \tag{4-112}$$

$$L_{1e} = 2 \cdot 0.015 + 0.017 = 0.047\,m \tag{4-113}$$

$$\lambda_{end} = 0.34 \cdot \frac{27}{3 \cdot 8} \cdot \left(1 - \frac{2}{\pi} \frac{0.017}{0.047} \right) = 0.3 \tag{4-114}$$

$$L_{end} = 4\mu_0 \frac{36^2}{8} 0.047 \times 0.3 = 0.011\,mH \tag{4-115}$$

Magnetizing inductance calculation by equations (4-56)−(4-60):

$$k_{cr} = \frac{11.78}{11.78 - \dfrac{9.7^2}{9.7 + 5 \cdot (35 - 30)/2}} = 1.56 \tag{4-116}$$

$$g_d{}' = 0.75 \cdot 10^{-3} \times 1.086 + \frac{3.65}{1.05} = 4.29 \cdot 10^{-3}\,m \tag{4-117}$$

$$g_q{}' = \left(35 \cdot 10^{-3} - 30 \cdot 10^{-3} \right)/2 \times 1.086 \times 1.56 = 4.23 \cdot 10^{-3}\,m \tag{4-118}$$

$$L_{md} = \frac{3}{2} \cdot \frac{4}{\pi} \cdot \frac{1}{8} \cdot (36 \times 0.94)^2 \cdot \frac{\mu_0 .511 \cdot 10^{-6}}{4.29 \cdot 10^{-3}} = 0.041\,mH \tag{4-119}$$

$$L_{mq} = \frac{3}{2} \cdot \frac{4}{\pi} \cdot \frac{1}{8} \cdot (36 \times 0.94)^2 \cdot \frac{\mu_0 .511 \cdot 10^{-6}}{4.23 \cdot 10^{-3}} = 0.042\,mH \tag{4-120}$$

Total inductance by equations (4-61) and (4-62):

$$L_d = 0.037 + 0.011 + 0.041 = 0.089\,mH \tag{4-121}$$

$$L_q = 0.037 + 0.011 + 0.042 = 0.090\,mH \tag{4-122}$$

EMF and Torque Constants:

EMF and Torque constants by equations (4-76) and (4-80):

$$k_e = \sqrt{3}\frac{8}{2}\times 36\times\left(0.59\cdot B_r\right)\times 511\cdot 10^{-6}\times 0.94\times 0.95 = 0.067\times B_r \quad (\text{V}_{\text{peak}}.\text{s/rad}) \quad (4\text{-}123)$$

$$k_t = 3\frac{1}{\sqrt{2}}\frac{8}{2}36\times\left(0.59\cdot B_r\right)\times 511\cdot 10^{-6}\times 0.94\times 0.95 = 0.082\times B_r \quad (\text{Nm}/\text{A}_{\text{rms}}) \quad (4\text{-}124)$$

In manufacturer's datasheet, it is stated that k_e is 0.071 V_{peak}.s/rad and k_t is 0.086 Nm/A_{rms}. Inserting these given values to equations (4-123) and (4-124) magnet Br is calculated as 1.05 T by equations (4-125) and (4-126).

$$0.071 = 0.067\times B_r \rightarrow B_r = 1.05\,T \quad (4\text{-}125)$$

$$0.086 = 0.082\times B_r \rightarrow B_r = 1.05\,T \quad (4\text{-}126)$$

It can be concluded that the magnets in the sample motor have Br value of at least 1.05T. NdFeB magnets are classified with respect to operating temperature and Br values by manufacturers. The sample motor has H class insulation which is to be operated up to 150°C. At this operating temperature, NdFeB magnets have a Br value of around 1.05T are 28SH, 30SH, 28UH, 30UH [57]. The most probable candidate is 30UH with temperature rating 180°C and minimum Br value of 1.08T (see Table 4.2) because the presented values by the manufacturer is theoretical values for simple shaped magnets which do not include coating. Final product from the manufacturer will have slightly lower Br value due to coating and shaping of the magnets.

A slightly higher Br value for the magnet should be selected for prototyping because demagnetization may occur in manufacturing the motor.

Table 4.2: Magnetic Characteristics and Physical Properties of Sintered NdFeB [57]

Magnet Grade	Remanence Br (T)	Coercive Force Hcb (kA/m)	Intrinsic Coercive Force Hcj (kA/m)	Max Energy Product BH$_{max}$ (kJ/m^3)	Max Working Temperature (°C)
30UH	1.08-1.13	≥ 812	≥ 1990	223 - 247	≤180

4.4.3 Calculation of Torque-Speed Characteristic

Having defined all equivalent circuit parameters, performance characteristics of the PM machine such as torque-speed and power-speed can be analytically determined. To do this, equivalent electrical circuit should be solved at some speed steps to determine current and then torque and power output can be calculated easily by multiplying torque constant k_t with the current value.

In this thesis work, for each 100rpm speed step starting from 1rpm and up to 5001rpm, equivalent electrical circuit is solved and motor terminal current is determined. The related equations and assumptions are presented in Chapter 2.2. Bus voltage is 21V_{DC} and maximum current limit is 35A_{rms} as in sample motor manufacturer datasheet.
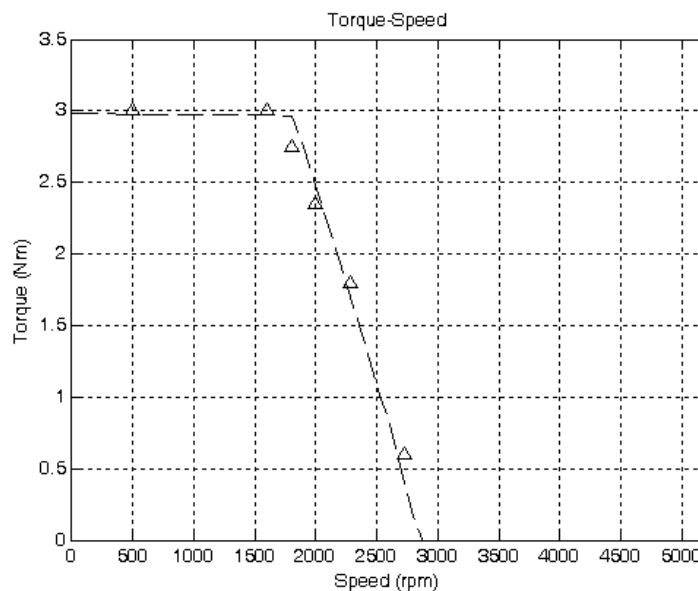
Figure 4.18: Measured and analytically calculated Torque-Speed characteristic of sample PM motor

In Figure 4.18, measured torque values are marked with "Δ" whereas analytically calculated maximum torque curve is plotted with dashed line. As observed in the figure, analytical and measurement values agree well with each other.

4.5 Magnetic FE Analysis

In this section, the purpose is to perform a no-load magnetic FE analysis and observe magnetic parameters such as EMF and flux densities. The sample motor is modelled in Maxwell[ii] and in Flux2D[iii] for this purpose. Modelling of the motor is quite easy in Maxwell which only asks for motor dimensions whereas a 2D cad program is used to model the sample motor magnetic structure which is then exported to Flux2D.

4.5.1 Maxwell RMxprt Model:

In Maxwell, a FE analysis is started by choosing a motor model from predefined library. There are many options such as 3-phase induction motor, permanent magnet dc, universal motor etc (see Figure 4.19)). The most appropriate for this thesis work is "Adjust-Speed Synchronous Machine". This model has permanent magnets on the rotor and a three-phase winding on the stator.
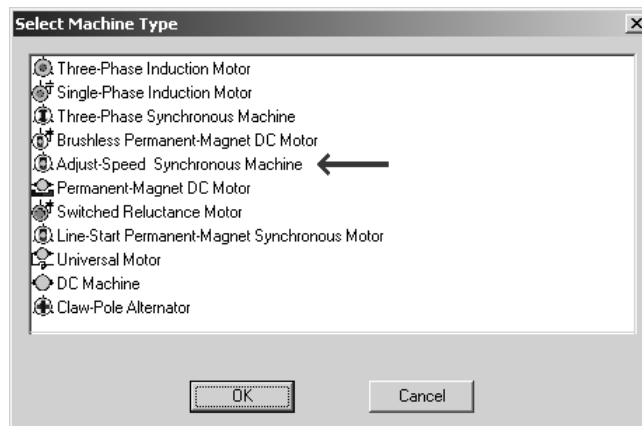
Figure 4.19: Machine model selection in RMxprt

After the selection, the motor model is inserted to main program window (Figure 4.20). There are sub menus under the model which contain many parameters to be assigned with a value such as stator slot number, winding scheme etc. The parameter tree in the program to be filled is illustrated in Figure 4.20 and values of the parameters are tabulated in Table 4.3.

[ii] Maxwell v11.1 with RMxprt toolbox by ANSOFT (www.ansoft.com)

[iii] Flux 2D v8.1 by CEDRAT (www.cedrat.com)
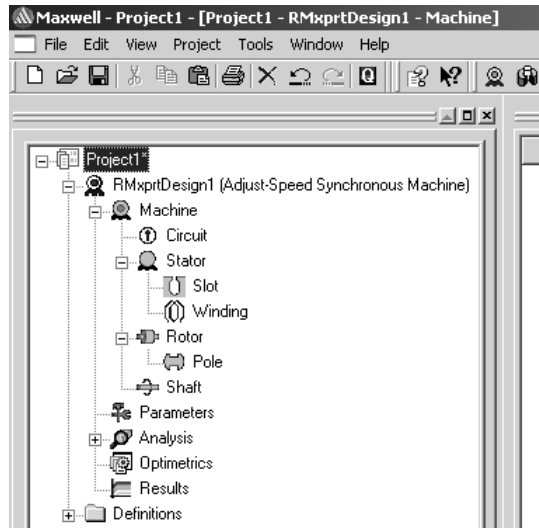
Figure 4.20: Model details to be filled in RMxprt

Table 4.3: Maxwell RMxprt parameter values to model sample PM machine

Menu	Parameters	Values
Machine	Number of Poles Rotor Position Frictional Loss Wind Loss Reference Speed Control Type Circuit Type	8 Inner rotor 0 0 2200rpm PWM Y3
Circuit	Transistor Drop Diode Drop Modulation Index Carrier Frequency	0 0 0.99 60
Stator	Outer Diameter Inner Diameter Length Stacking Factor Steel Type Number of Slots Slot Type Skew Width	62 35 38 0.95 steel_RM23 27 1 0

Table 4.3: Maxwell RMxprt parameter values to model sample PM machine, contd.

Slot	Auto Design	False
	Parallel Tooth	True
	Tooth width	1.82
	Hs0	0.8
	Hs2	7.78
	Bs0	1.27
Winding	Winding Layers	2
	Winding Type	Whole Coiled
	Parallel Branches	1
	Conductors per Slot	8
	Coil Pitch	3
	Number of Strands	1
	Wire Wrap	0
	Wire Size	0
End/Insulation	Input Half-turn Length	False
	End Adjustment	15
	Base Inner Radius	1
	Tip Inner Diameter	1
	End Clearance	0.25
	Slot Liner	0.5
	Wedge Thickness	0.25
	Layer Insulation	0.25
	Limited Fill Factor	0.4
Rotor	Outer Diameter	33.5
	Inner Diameter	11
	Length	38
	Steel Type	steel_RM23
	Stacking Factor	0.95
	Pole Type	3
Pole (Magnet Properties)	Embrace	0.748
	Offset	0
	Magnet Type	NdFe30
	Magnet Thickness	3.65
Shaft	Magnetic Shaft	False

BH Curve of the electrical steel (defined as steel_RM23 in Table 4.3) is presented in Figure 4.21. It can be observed that the electrical steel begins to saturate at around 1.8T and fully saturates at 2.1T.

126
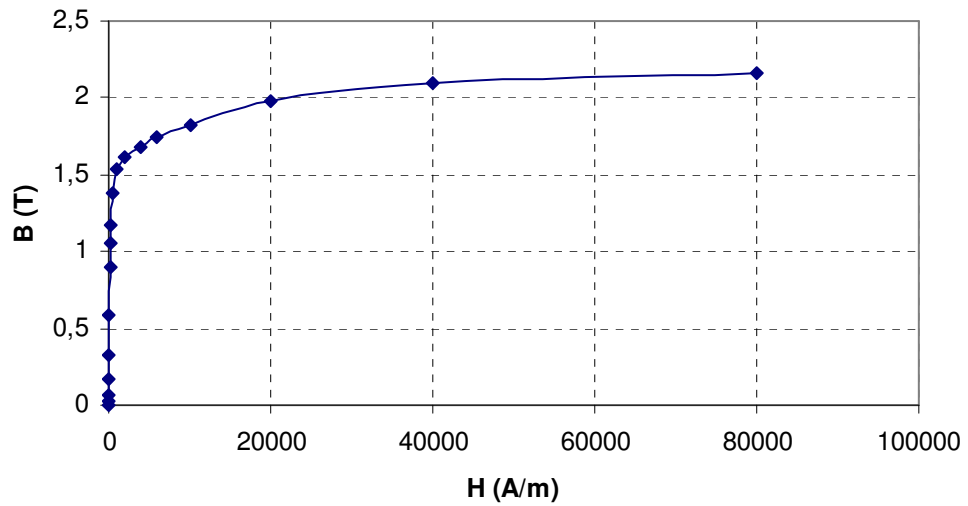
Figure 4.21: B-H curve for electrical steel

In Figure 4.22, induced EMF voltage waveforms in motor windings calculated by Maxwell are presented. It can be observed in the figure that at 1000rpm, peak of EMF voltage at motor terminals is 7.20V which states that EMF constant k_e is $0.069V_{peak}.s/rad$. If one inserts the presented parameter values in Table 4.3 into RMxprt, same results as presented in Table 4.4 can be expected.
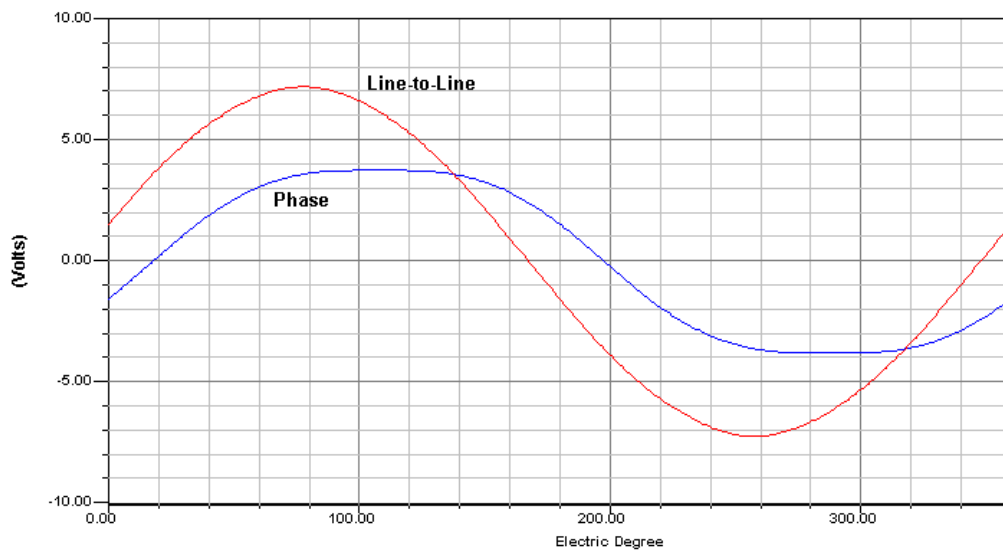
Figure 4.22: Induced voltage waveforms at 1000rpm for sample motor in Maxwell

4.5.2 Flux2D Model:

The magnetic structure of the sample motor is created in a CAD program with respect to mechanical dimensions presented in Figure 4.17. The created 2D model is then exported to Flux2D program. Proper meshing is applied to the model as presented in Appendix. Magnets are assigned from program library as NdFe30. A sample view of the Flux2D model is illustrated in Figure 4.23.
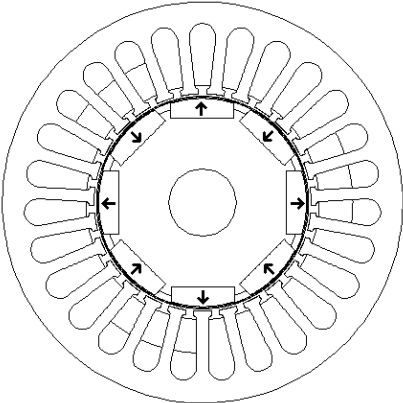
Figure 4.23: 2D cad model used in Flux2D for FE analysis

Note: Arrows in the figure show magnetization direction of magnets
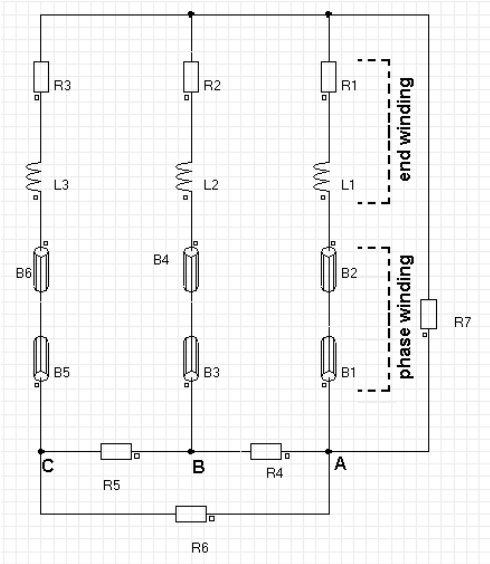
Figure 4.24: Motor equivalent circuit model in Flux2D for FE analysis

128

Transient magnetic solution is performed to determine EMF at motor terminals. Motor electrical equivalent circuit is modelled as in Figure 4.24. In the circuit "R4, R5, R6, R7" are inserted to sense voltage across terminals and phase. Their resistance is infinite with respect to phase resistances so that it can be assumed no current passes through. Motor terminals are presented in the figure as "A, B, C". The end winding resistance is assigned so that total phase resistance is 0.068 ohm. Flux2D calculated phase resistances as 0.032 ohm, so end winding resistance is assigned as 0.036ohm. The value of end winding inductance is assigned as calculated with equation (4-115) in Chapter 0.

The transient FE analysis is performed with such time steps that in one electrical period there are 50 data points. A sample waveform of back EMF voltage for sample motor at 750rpm is presented in Figure 4.25. Peak value of fundamental harmonic of presented EMF voltage waveform at motor terminals is 5.39V which states that EMF constant k_e is 0.069 V_{peak}.s/rad.
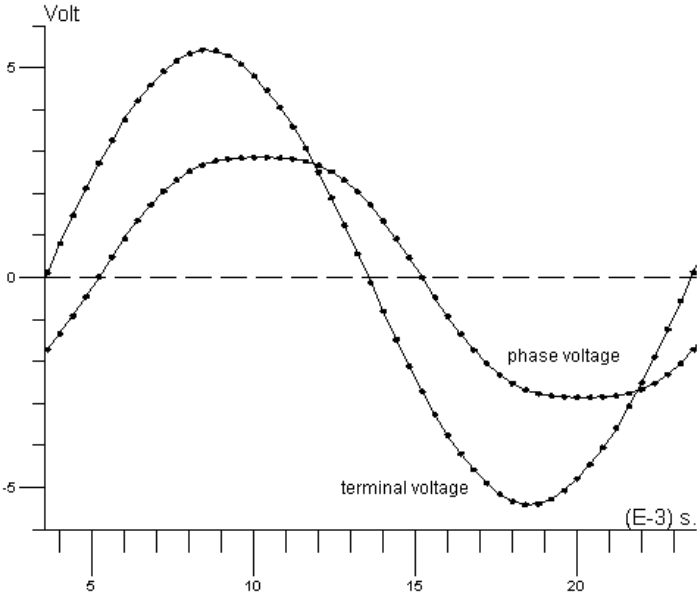
Figure 4.25: Induced voltage waveforms at 750rpm for sample motor in Flux2D

Summary of the results of FE analysis from both Maxwell and Flux2D programs are tabulated in Table 4.4.

4.6 Comparison of Analytical Results with Measurements and FE Analysis

In this section, analytical calculations of equivalent electrical circuit parameters (Figure 2.3) of PM motor and magnetic FE results are compared.

4.6.1 Comparison of Motor Magnetic Parameters

Characteristic parameters of the sample PM machine which are calculated by analytical equations are summarized in Table 4.4. The values from sample motor manufacturer datasheet are also presented to show accuracy of analytical results.

Table 4.4: Comparison of calculated and measured results for some PM motor parameters

Parameter	Manufacturer Data	Measurement Result	Analytical Result	Maxwell RMxprt	Flux 2D
Phase resistance (Ω)	0.068	0.068	0.067	0.069	0.068
Ld / Lq (mH)	0.125 / 0.133	0.110 / 0.130	0.095 / 0.138	0.093 / 0.096	-
EMF constant (V_{peak}.s/rad)	0.071	0.070	0.071*	0.069	0.069
Torque constant (Nm/A_{rms})	0.086	0.085	0.086*	0.83	0.087
Airgap per pole mean flux density (T)	-	-	0.62	0.57	0.61
Max Tooth flux density (T)	-	-	1.76	1.85**	1.69
Max stator back core flux density (T)	-	-	1.56	1.89**	1.74
Magnet operating point (T)	-	-	0.92	0.85	0.88

These results are calculated with Br value 1.05T which is extracted from measurement results. More explicitly; Br value is selected to meet the measurement results.

** These values are reported by Maxwell and they may correspond to local extremes such as tooth tip. It is not available to look for flux density in every region in Maxwell.

Presented values in Table 4.4 show that analytical torque and emf constants are consistent with measurements, FE analysis results and manufacturers datasheet. Torque-speed curve agrees well with measurement data. Airgap and stator flux densities are also accurately predicted. It can be concluded that the analytical model is sufficient to utilize it in an optimization based design and a new PM motor can be designed which is similar to the sample motor in terms of electromagnetic performance (such as torque-speed).

4.6.2 Analytical Determination of Torque-Speed Characteristic

In previous sections, an electrical equivalent PM motor model is formed and parameters in the model are measured. The model can be verified by inserting parameter values in the equivalent circuit and solving it to determine terminal current.

In laboratory, the tested PM machine is driven by vector control where only q-axis current is present in the motor windings.
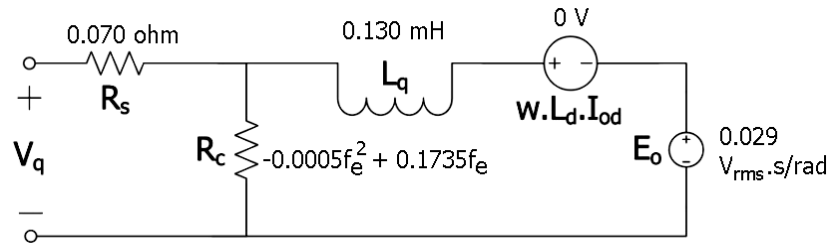
Figure 4.26: Sample motor q-axis electrical equivalent with parameter values

Since it is assumed that there is no d-axis current, the parameter "$w.L_d.I_d$" is assigned with zero volt in the above figure.

Table 4.5: Calculated torque values with equivalent PM motor model

Shaft Speed (rpm)	Measured Terminal Voltage (V_{rms} line)	Calculated EMF Voltage (V_{rms} line)	Calculated Core Loss Resistance (ohm)	Calculated X_q (ohm)	Calculated Line Current (A_{rms})	Calculated Torque (Nm)
500	5,99	2,59	5,23	0,027	35	2,94
1000	9,54	5,18	9,34	0,054	35	2,94
1500	13,08	7,78	12,35	0,082	35	2,93
1700	14,50	8,81	13,24	0,093	35	2,92
1800	14,85	9,33	13,62	0,098	32,8	2,74
2000	14,85	10,37	14,24	0,109	25,1	2,07
2200	14,85	11,40	14,69	0,120	18,2	1,48
2500	14,85	12,96	15,03	0,136	9,2	0,71
2800	14,85	14,51	14,96	0,152	1,5	0,04
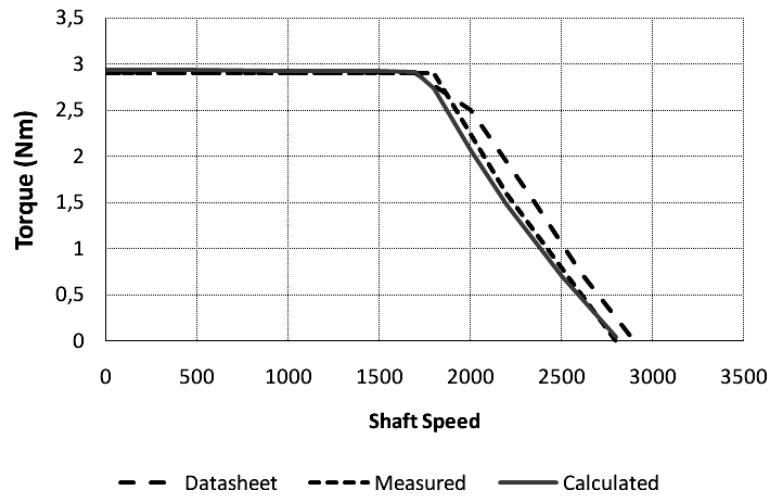
Figure 4.27: Comparison of sample PM motor torque-speed characteristics from manufacturer datasheet, measurements and calculations

It is observed in Figure 4.27 that all three torque-speed characteristics agree by 1% 'n constant torque region whereas a 5% disparity occurs in constant power region. The consistency of calculated characteristic with measured and datasheet shows that the equivalent motor model is correct and measured parameter values are sufficiently accurate.

CHAPTER 5

OPTIMUM DESIGN of a PM MOTOR

In this chapter, a mathematical design optimization strategy will be developed with the analytical model presented in CHAPTER 4. The aim of optimized design is to find an optimum balance between expected performance requirements and volume of the designed machine.

A multi-objective optimization problem consists of objectives associated with inequality and equality constraints. The optimisation problem as a constrained minimization problem can be defined in n-dimensional calculation space where n is equal to the number of optimized parameters. Mathematically, the problem can be expressed as follows:

$$\text{Minimize / Maximize} \qquad f_i(\overline{X}) \qquad i = 1, 2, \dots N$$

$$\text{Subject to;} \qquad g_j(\overline{X}) \le 0 \quad j = 1, 2, \dots J$$

$$h_k(\overline{X}) = 0 \quad k = 1, 2, \dots K$$

It is stated with this expression that an optimization problem consists of an objective function $f_i()$ and constraint functions $g_j()$, $h_k(\overline{X})$ which are a function of design vector $\overline{X}$. The $\overline{X}$ is a p dimensional vector with n design or decision variables (equivalently n dimensions). The design vector $\overline{X}$ consists of independent design variables which are to be varied to find the optimum design vector $\overline{X}_m$. Therefore there is a need for a model from which the performance of the motor can be calculated. The parameters of the model need to be calculated in terms of design vector members which are generally selected from motor dimensions.

In this thesis work, the analytical model developed in CHAPTER 4 is preferred. As shown in Section 4.6, this model is capable of predicting the motor performance with good accuracy. Employing FE analysis for motor optimum design is not a practical proposition. During optimum design, repetitive performance calculations are required. Due to numerous parameters affecting motor performance, the solution time becomes unacceptably long. FE analysis can be used later to assess the optimal solution.

5.1 Definition of the Optimization Problem

5.1.1 Specifications

The designed motor is expected to satisfy some performance requirements within defined system boundaries. Calculated performance parameters are output torque, input power, efficiency in entire current and speed range. Parameters in equivalent electrical and magnetic circuit of the motor are calculated for each new design and inserted into performance calculations. These are per phase resistance, d-q axis inductances, core loss current, back EMF voltage, flux densities (airgap, tooth, back core).

The designed motor shall be capable of delivering minimum of 330 W at 2000 rpm. Reference calculations (such as torque and power output, efficiency, temperature rise) are going to be performed at 2000 rpm. Motor shall be capable of delivering up required performance up to 150°C temperature for stator winding.

The motor is going to be driven by vector controlled 3 phase inverter assuming that the bus voltage is necessary to supply 21 V_{peak} line-line voltage at motor terminals. The motor is driven with vector control method and no field weakening is to be applied during operation. The phase diagram of this drive method is presented in Figure 3.19-a. The inverter has 3-phase sinusoidal current outputs with a maximum current of 35A_{rms}.

The motor must have 8 poles as required by the motor drive system. The back EMF voltage is also expected to have a sinusoidal waveform. For this reason, different slot number combinations (such as 9, 15, 18, 21, 24, 27, 30, 36) are inspected where maximum EMF voltage with minimum harmonic distortion is aimed. As presented in the book by Hanselman [8], the most suitable slot number for 8 poles is 27 in terms of minimum harmonic winding coefficients. For this reason, the motor slot/pole ratio is fixed as 27/8 for the design.

It must be noted that 27 slot – 8 pole combination results slot/pole/phase number as 1.125 which is fractional. This number is an integer every 8 coils which states that winding scheme repeats it self every 8 poles. Since there can be only 9 coils in 27 slots for three phase, all coils have to be connected in serial inevitably. If the slot number is selected as 30, slot/pole/phase number is 1.25 and winding can be constructed of 8 coils where 4 coils are in parallel with other 4 coil group.

The outer diameter of the motor can be 65 mm at maximum due to packaging issues. The housing has a hollow body with 65 mm inner diameter. Also rotor is going to be mounted on 11 mm shaft which limits rotor inner diameter.

The airgap of the motor is first selected as 0.5mm assuming that this space is sufficient to allow free run of rotor with a bandage over magnets. In first prototypes heat-shrink tubes were used and it is observed that the width of the tubes after heating may vary much. It is decided that 0.5mm is not sufficient for safe operation so that the minimum airgap was presumed to be larger than 0.75mm and it should be defined in the optimization in this way. On the other hand, theoretically, it is evident that the optimum airgap is the minimum allowable so it is wise to fix the airgap width rather than search for optimum value. For this reason, the airgap width is fixed as 0.75mm in the optimization after considering manufacturing issues.

No mechanical requirements are defined such as mass and inertia. The optimization aims to reach the minimum volume within the defined criteria, so it is also assumed that the optimum design has the minimum feasible mass and inertia.

Steady state torque - speed curve of the motor is calculated by the analytical equations in CHAPTER 4. In these calculations there are many motor parameters such as dimensions and electrical parameters. Some of them are chosen to be a member of design vector. Others can be expressed in terms of selected design vector variables and some constant parameter values. The design vector elements are defined in Section 5.1.4 as independent variables.

The proposed simple thermal model in Section 4.3 will be used to predict the thermal behaviour of the new design. Calculated power loss will be inserted into the thermal model to determine temperature rise under specific loading condition.

Table 5.1: Specifications table for the new motor design

Specification	Sample Motor Value	Design Specification	Remark
Number of poles	8	8	Pre-defined to be compatible with available motor driver
Slot number	27	27	Selected by harmonic investigation from the book by Hanselman [8]
Motor Terminal voltage	21 V_{peak} line-line	21 V_{peak} line-line	Maximum value of motor terminal voltage. Assuming DC bus voltage is enough to allow drive to generate this voltage.
Airgap	0.75 mm	0.75 mm	Pre-defined for all designs
Outer Diameter	62 mm	65 mm	Maximum feasible value
Peak torque	3 Nm	3 Nm	Minimum peak torque at 1500 rpm. This also defines peak stall torque to be at least 3Nm.
Rated power	330 W	330 W	Minimum delivered mechanical power at 2000 rpm
Max Speed	2820 rpm	-	No maximum speed specification is defined.
Winding connection	Serial	Serial	All coils in each phase are connected in series
EMF constant	0.071 V_{peak}.s/Rad	-	No EMF constant specification is defined.
Torque constant	0.086 Nm/A_{rms}	-	No torque constant specification is defined.
Temperature rise at rated speed and load	100°C	100°C	Motor is hanging in the air.
Resistance	0.067 Ω	-	Per phase resistance
Inductance	0.237 mH	-	Terminal to terminal inductance
Mass	2.3 kg		No specification for mass is defined.
Inertia	0.6 kg.cm^2		No specification for inertia is defined.

5.1.2 Objective Function

The aim of this study is to have most efficient electromagnetic energy conversion in the smallest volume. For this purpose, two main parameters of the optimized motor design are:

1. Maximize efficiency
2. Minimize volume

On the other hand, to minimize torque rippler, a constraint is placed on the airgap flux density harmonics as discussed in Section 5.1.3.

These two objectives are in fact contradictory to each other since high efficiency comes with larger volume which has more space for copper, lower flux density in the core, larger flux linkage per pole. The two objective functions are weighted to define a single cost function because two functions have incomparable values. Effect of efficiency variation will dominate variation in volume. For this purpose, sample motor efficiency at selected reference speed (2000 rpm) and volume are used to normalize two objectives and define a single cost function as in equation (5-2).

$$f_{\cos t} = k_1 f_{\min vol} + k_2 f_{\max eff} \tag{5-1}$$

The defined weights k_1 and k_2 sum up to 1 which states $k_2 = 1-k_1$. Optimization can be performed in terms of trade off between efficiency and minimized volume by adjusting the weights of k_1 and k_2. By defining a single cost function, the optimization is no longer a multi-objective, but a scalar objective optimization.

Normalized values for efficiency and volume will be very useful in terms of deciding whether the new design is better than the sample motor according to defined weights. Normalization of the calculated volume and efficiency for new design can be done by dividing each term to sample motor values as in equation (5-2).

$$f_{\cos t} = k_1 \frac{V_{new design}}{V_{sample motor}} + k_2 \frac{Eff_{sample motor}}{Eff_{new design}} \tag{5-2}$$

Considering the sample motor volume and efficiency at selected operating point (2000rpm, 21 V_{peak} line-line voltage), equation (5-2) can be explicitly written as in equation (5-3).

$$f_{\cos t} = 0.50 \frac{V_{new design}}{114.8 \times 10^{-6}} + 0.50 \frac{0.73}{Eff_{new design}} \tag{5-3}$$

The defined cost function outputs "1" for same volume and efficiency as sample motor. A new design with objective function value smaller than 1 means a better design than sample motor with the defined cost function. This cost function is to be minimized with the optimization.

5.1.3 Constraints

A constraint can be defined as a boundary which must be satisfied by the optimized system. Constraints may be due to various reasons such as;

- Performance constraints: Max torque, Max speed, No load current etc…

- Manufacturing difficulties or realization limits: Minimum airgap, Minimum tooth width, Outer diameter etc…

- Material properties: Saturation level of electrical steel etc…

The outer diameter is selected to be 65mm at maximum because the designed stator is going to be fit into an available motor housing and the maximum allowable inner diameter is 65 mm due to workmanship.

Maximum flux densities in teeth and back core are limited as 1.89T and 1.77T respectively which are the calculated densities in the sample motor.

Motor peak stall torque is defined as a specification by the manufacturer of the sample motor. However in this study, instead of defining a stall torque, peak torque at 1500rpm is defined as a specification. PM machines torque characteristic consists of two regions; constant torque region and constant power region where torque is monotonically decreasing (see Figure 3.1). So, if output torque at a speed is defined than it can be concluded that stall torque is at least that value due to monotonically decreasing torque characteristic. In this work, by defining output torque of 3Nm at 1500rpm, stall torque is defined indirectly which states that peak stall torque is also at least 3Nm.

Rated torque and speed are also given as a performance specification by the manufacturer. In this work, no torque or EMF constant is defined as a specification, but instead torque output at 1500rpm and 2000rpm are defined as electromagnetic output performance specification which defines EMF and torque constants indirectly as well.

Constraints for slot width, back core depth, tooth width and magnet displacements are all to ensure feasibility of realization of the design. For example, a design with 0.1mm tooth width is not realizable with the machinery available to be used for this thesis work.

The available motor drive is capable of supplying 35-40Arms peak and 15-20Arms to a motor. For this reason, the rated current of the designed motor is defined to be lower or equal to $20A_{rms}$ to be compatible with the drive. The current density is also defined to be lower or equal to $12A_{rms}$ which is the calculated value for the sample motor.

In the specifications, it is stated that the designed motor is expected to develop minimum 3Nm at 1500rpm, deliver 330W at 2000rpm and the temperature rise must be maximum of 100°C at 2000rpm which defines the rated speed of the motor. All these three specifications are introduced as constraints in the optimization.

The defined design constraints for the optimization are tabulated in Table 5.2. The BH curve for the electrical steel to be used for lamination is presented in Figure 5.1.

Table 5.2: Design constraints for optimization

Constraint Vector element	Constraint name	Limit	Remark
g_1	Stator outer diameter "D_{so}"	≤ 65mm	Motor housing does not allow larger outer diameter
g_2	Peak Tooth flux density "B_{th}"	≤ 1.89T	Calculated flux density in sample motor
g_3	Peak Stator yoke flux density "B_{bc}"	≤ 1.77T	Calculated flux density in sample motor
g_4	Slot width at lower side "w_1"	≥ 1mm	This ensures that final design does not have a closed slot bottom
g_5	Back-core depth "h_{bc}"	≥ 1mm	Minimum width from manufacturing limitations
g_7	Tooth width "W_{th}"	≥ 1mm	Thinner tooth width may be unrealizable
g_8	Displacement between two magnet tips (rotortest)	≥ 1mm	This ensures that two successive magnets on the rotor do not interfere with each other (Figure 5.2).
g_6	THD of airgap flux density due to magnets	≤ 8%	A sinusoidal flux distribution is aimed
g_9	Rated current "I_{rated}"	≤ 20A_{rms}	This ensures that final design is compatible with available motor drive.
g_{10}	Rated current density "J_{rated}"	≤ 12A_{rms}/mm^2	This value is selected based on a thermal model.
g_{11}	Maximum torque output at 1500 rpm "$maxTe_{ref}$"	≥ 3 Nm	The operating range of the system is aimed to be 0-1500rpm where 3Nm peak torque is demanded
g_{12}	Rated power output at reference speed (2000rpm) "P_{ref}"	≥ 330 W	The designed motor should be capable of delivering 330W at 2000rpm.
g_{13}	Temperature rise at reference speed (2000rpm) "$Temp_{ref}$"	≤ 100 °C	Temperature rise at reference speed at reference power must not exceed 100°C
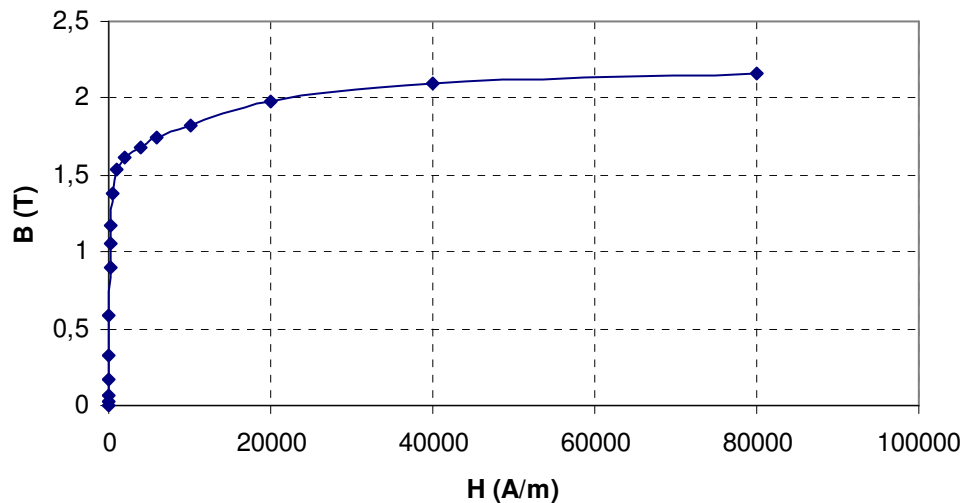
Figure 5.1: B-H curve for electrical steel used in design

139

There are geometrical constraints also such as minimum tooth width and displacement between two magnet tips to ensure mechanical realization (rotortest variable in Figure 5.2). Too small dimensions may not be realizable in manufacturing. In this thesis work, minimum mechanical dimension is chosen to be 1mm such that there is no part in lamination (i.e. tooth width, tooth tip, back core) that is thinner than 1mm.

Torque ripple is not calculated analytically in the developed analytical model. However the amplitude of ripple is a very important criterion for PM machines and minimum torque ripple is always preferred for highest performance. To consider this issue, harmonic distortion of airgap flux distribution is included in the constraints. Theoretically, in PM machines, the torque is developed by interaction of airgap flux with current in stator windings. So, if there is no harmonic in airgap flux or stator, no harmonic torque resulting ripple can be developed. For this reason, THD of airgap flux distribution is included in the constraints to have the minimum torque ripple in the design. It must be noted that cogging torque is different than torque ripple which results from interaction of rotor magnets with stator inner surface structure.
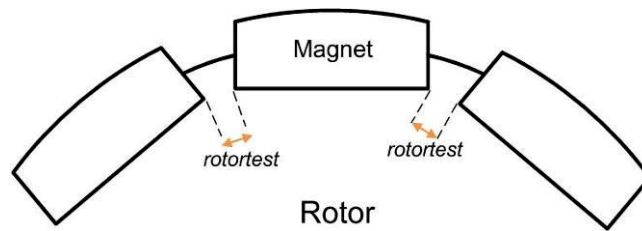
Figure 5.2: Rotortest constraint to check rotor structure feasibility

The defined constraints are defined in modeFrontier as "less than" (<) or "greater than" (>) since there is no option to define as "equal or less/greater than" (≤, ≥). Also all parameter magnitudes are represented by 20 digit numbers in the program. For example an outer diameter magnitude of "62mm" is defined as "0.062000000000000000". The handicap of this magnitude representation is that even unfeasible variations in real life such as 1 nm are taken into consideration which decreases the efficiency of the optimization.

The effect of magtnitude representation to optimization convergence is studied in Section 5.5 by running the optimization with variation steps defined for each design variable.

5.1.4 Independent Variables

The independent design variables are the machine parameters which constitute design vector X and vary during optimized design process. Independent variables have to be selected so that all other dimensions can be expressed of these variables. For example, if stator inner diameter D_{si} and rotor outer diameter (diameter at magnet surface) D_{ms} are design variables, then airgap g should be discarded as a variable because it has already been defined by these two diameters.

$$g = \frac{1}{2}\left(D_{si} - D_{ms}\right)$$
(5-4)

The selected independent design variables with their limits for this thesis work are listed in Table 5.3. As observed, some of them discrete variables because it has no sense to define continuous variable space. The axial length is dependent on steel lamination which has 0.5mm thickness, so the length in axial direction can be in 0.5 steps. Also winding coil turns is in discrete steps of one ranging from 1 to 6. This limit is set to avoid unnecessary search of coil turns in wide range. Slot depth defines the slot area where the upper limit is set based on geometrical observations based on the defined 65 mm outer diameter limit. Minimum tooth width is set as 1 mm as narrower geometry may not be realizable and the upper limit is set also with respect to geometrical observations based on 65 mm outer diameter. The same situation is valid also for stator yoke (back-core) height.

Magnet Br value range is defined with respect to product list magnets from a magnet manufacturer [Appendix A.5]. On the other hand, magnet height is set free on the continuous range (1…5 mm) by interpretation of geometrical limitations.

Table 5.3: Independent variables in optimized design of a PM machine

Independent variable Vector element	Independent Variable Name	Abbreviation (Figure 5.3)	Variable Type	Limits
x_1	Axial length	L	discrete by 0.5mm steps	30mm < L < 50mm
x_2	Slot depth	h_1	continuous	5mm < h_1 < 12mm
x_3	Stator yoke height	h_{bc}	continuous	1mm < h_{bc} < 4.5mm
x_4	Tooth width	W_{th}	continuous	1mm w_{th} < 3.5mm
x_5	Diameter at magnet base	D_{mb}	continuous	20mm < D_{mb} < 40mm
x_6	Magnet height	h_{mag}	continuous	1mm < h_{mag} < 5mm
x_7	Magnet arc span in one pole pitch	alfa	continuous	0.6 ≤ alfa ≤ 0.9
x_8	Turns per coil	N_{turn}	discrete by 1 steps	1 ≤ N_{turn} ≤ 6

x_9	Magnet Br	Br	discrete by 0.02T steps	$1.15 \leq Br \leq 1.25$

The defined variable "alfa" which relates magnet pitch to one pole pitch is illustrated in Figure 5.4. Multiplication of "alfa" with one pole pitch gives magnet pitch.
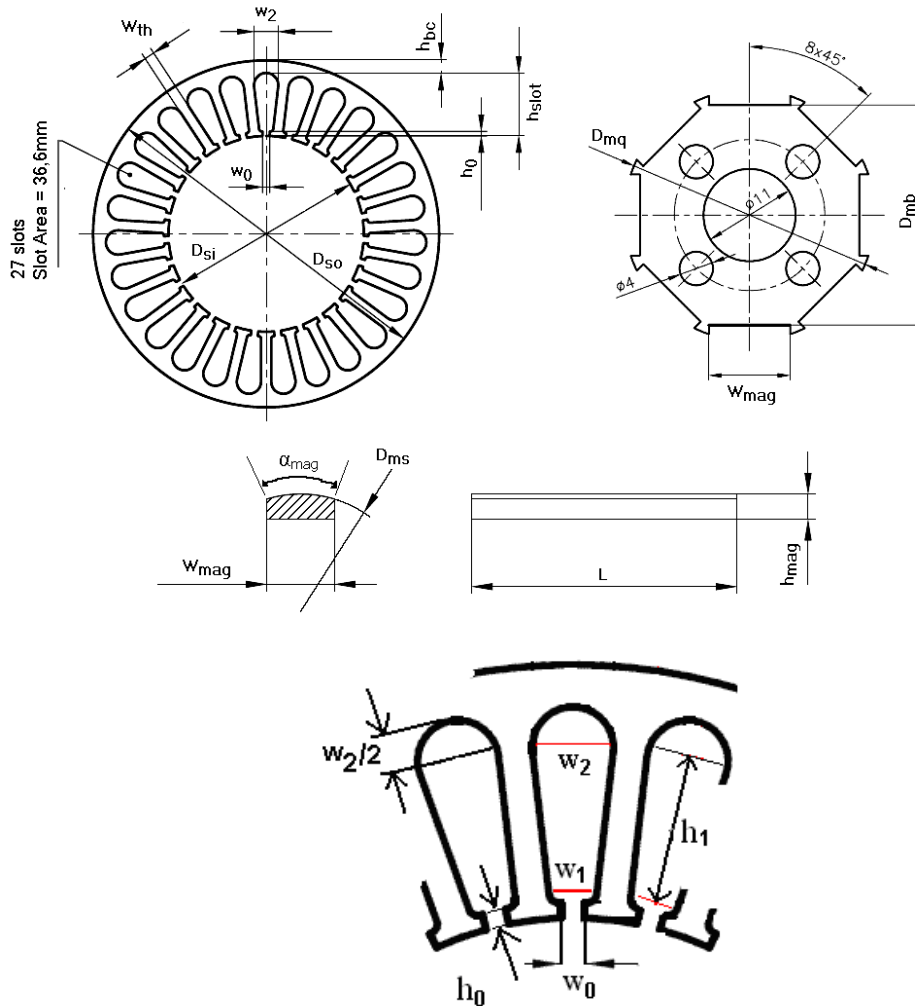
Figure 5.3: Corresponding dimensions for geometric abbreviations of design variables
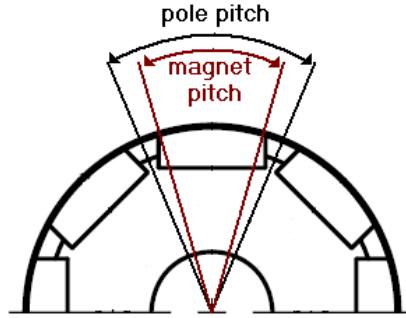
Figure 5.4: Figure showing one pole pitch and magnet pitch

5.1.5 Dependent Variables

Dependent variables are defined as motor dimensions which can be calculated with evaluation of independent variables together with constant parameters. The dependent variables are listed in Table 5.4.

Table 5.4: Dependent variables in optimized design of a PM machine

Dependent Variable	Abbreviation (Figure 5.3)	Value
Diameter at magnet surface	D_{ms}	$D_{mb} + 2.h_{mag}$
Diameter at stator inner surface	D_{si}	$D_{ms} + 2.g$
Slot width at narrow side	w_1	$\left(D_{si} + 2(h_0 + 0.5mm)\right)\dfrac{\pi}{N_{slot}} - w_{th}$
Slot width at wider side	w_2	$\left(D_{si} + 2(h_0 + 0.5mm + h1)\right)\dfrac{\pi}{N_{slot}} - w_{th}$
Slot bottom radius	h_2	$w_2 / 2$
Diameter at stator outer surface	D_{so}	$D_{si} + 2(h_0 + 0.5mm + h1 + h_2)$
Magnet width	w_{mag}	$D_{ms} \sin\left(\dfrac{1}{2}alfa \cdot \dfrac{360}{p}\right)$

In Table 5.4, calculations of dependent variables are also illustrated in the last column. The 0.5mm clearance defined in w1, w2 and D_{so} expressions is corresponding to slot liner thickness which is used to close the slot opening to avoid windings to slip out (see Figure 5.5).
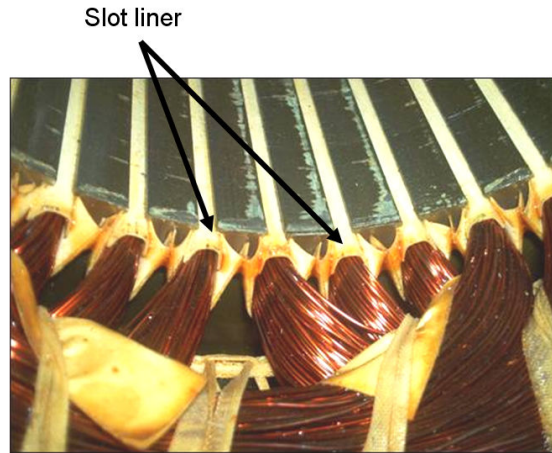
Slot liner

Figure 5.5: Illustration for slot liner

5.1.6 Constants and Pre-Defined Parameters

Besides, some parameters can be fixed prior to the design to simplify calculations and to avoid complex iterative process in the optimization. These parameters are listed in Table 5.5. Note that some of these parameters are defined by the design specifications that are presented in Section 5.1.1.

Table 5.5: Constant parameters in optimized design of a PM machine

Constant Parameter	Abbreviation in calculations	Value
Airgap	g	0.75 mm
Pole number	p	8
Slot number	N_{slot}	27
Magnet remanence	Br	1.05T
Coil per phase	N_{coil}	9
Coil pitch	C_{pitch}	3 slots (equivalently 16/18 with respect to one pole pitch)
Width of the slot opening	w_o (see Figure 5.3)	1.25 mm
Depth of the slot opening	h_o (see Figure 5.3)	0.8 mm
Slot fill factor	k_{fill}	0.34 (34% equivalent)
Magnet magnetic relative permeability	μ_R	1.05
Winding factor	k_w	0.94

The defined airgap height 0.75 mm is minimum feasible value because a fiber glass bandage is present over magnets on the rotor which requires approximately 0.3-0.4 mm clearance. Taking mechanical issues (rotor bending etc.) into account also, 0.75 mm is

144

chosen as airgap height. Since the designed motor is to be integrated to the available driver on a system, the pole number is restricted as 8. Number of slots

5.1.7 Performance Calculations

During the design process, the performance (torque, power, current etc.) of the motor is going to be calculated for each new design vector $\overline{X}$ according to the model presented in CHAPTER 2. The equivalent circuit of the motor for performance calculations under vector control is given in Figure 2.3. It must be noted that since it is assumed that the motor is driven by vector control, no d-axis excitation is present and only the q-axis equivalent circuit (Figure 5.6) is going to be considered.
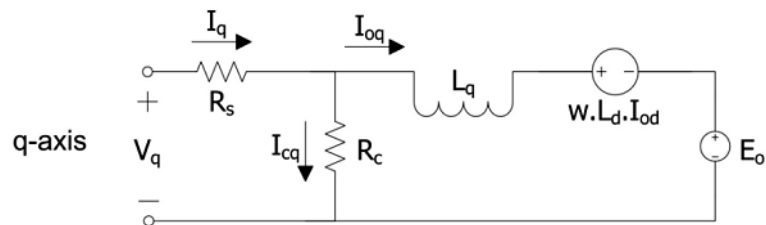
Figure 5.6: q-axis equivalent electrical circuit of PM machine under vector control

It has been shown in Section 4.6 of CHAPTER 4 that calculated performance using this model is consistent with measurements within 5% accuracy which ensures the accuracy of the model. From the model, it can be observed that phase resistance, core loss resistance, q-axis inductance and back EMF voltage constant are the parameters involved. To be able to perform optimization with this model, each parameter has to be defined in terms of the independent variables; i.e. design vector $\overline{X}$. This is done in CHAPTER 4 by expressing equivalent electrical circuit parameters and magnetic parameters (flux densities, torque/EMF constant etc.) in terms of motor dimensions. The calculations of desired motor performance, such as torque at a given speed, are explained in Section 4.3.

Up to now in sections 5.1.1 - 5.1.7, the optimization problem is defined with its objective function, requirements, constraints and performance calculation model. The next step is to decide on how to perform the optimization. There are plenty of studies in the literature on optimum design of PM machines. A review of selected studies is presented in section 5.2.

5.2 Literature Review

There are many optimization techniques available for motor design; some require an initial design and some can search the entire design space for global optimum. Many authors presented different approaches to optimized design [46] - [52].

In this section, selected studies from the literature are presented in terms of;

     i.   Purpose of the study
    ii.   Design objectives
   iii.   Design variables
   iv.   Optimization method
    v.   Results and comments of the author

5.2.1 Review of Selected Studies for Optimum Design

Boules [47] (1990) presents an analytical model for the design optimization of inner rotor, brush contact, surface magnet, PM DC motor is presented. The analytical model combines electric and magnetic circuit equations with the motor design equations. The design objectives are defined as minimum weight, minimum volume, maximum efficiency at a specific operating condition (12V, 3250rpm, 154W). The design variables are selected as back EMF amplitude, magnet height and width, axial length, tooth width, airgap diameter, stator frame thickness, slot number and pole number. The author use an indirect method for constrained optimization; "sequential unconstrained minimization technique". The validation of the optimization is examined by comparing an optimum motor design by for maximum efficiency to an existing motor subject to the same space and thermal constraints. The author concludes that analytical model combines accuracy and high computing speed which makes it most suitable for optimization purposes. Normalization of the design variables overcomes difficulty to guess reasonable initial values for design variables. On the other hand, an analytical optimization based merely on efficiency may be more costly (in terms of production) than the existing motor. However, cost factors can be easily introduced to the objective function to take machine cost into account.

Bolognani [49] (1997) combined a fully analytical procedure for the design, including thermal constraints, with a genetic algorithms procedure on a surface magnet PM motor. The motor material cost is chosen as objective function. The independent variables are selected as slot width, slot pitch, stack length, tooth flux density, back iron flux density, rotor iron flux density, slot per pole per phase and pole pairs. In the optimization, a control of geometrical feasibility is introduced to avoid with geometrical discrepancies. A comparison between climbing-hill direct-search method and GA has also been carried out.

The author concluded that even if the genetic algorithms generally required a higher number of iterations, they are not affected by goodness of starting point and the presence of local partial optima.

Boldea et al [48] (2007) presents an optimal design method, via Hooke Jeeves method of 6/4 brushless DC (BLDC) motor. The purpose is to have the minimum cost in terms of material consumption and price, and motor losses. Ten geometrical parameters are chosen as optimization parameters; inner stator diameter, outer stator diameter, stator pole width, stator yoke width, stator pole span angle, the heights of stator slots closure, stator core stack length, air-gap length, permanent magnet height. The optimization is implemented in MATLAB using the modified Hooke-Jeeves algorithm and validation of the final design is made by finite element method. The analytically optimal design was then validated by FEM also.

Mellor [52] (2004) studied genetic algorithm in the design optimization of a surface magnet brushless DC machine. The research is being applied to the design synthesis of electro-hydraulic actuation systems. Compact size and highest efficiency are major requirements for this study. The objective function is based on maximizing torque for a given volume of permanent magnet, assuming the electrical loading of the machine remains unchanged. For this purpose, average value of the EMF over the 120' electrical commutation period of the brushless DC operation is maximized. The variables set includes geometrical parameters related to magnets, magnetization direction assuming that the rotor is constructed from discrete blocks of permanent magnets mounted to the surface of a soft iron hub. The offered method combines a two-dimensional magneto static finite element model (FEM) with a genetic algorithm (GA) to investigate the influence of the shape of the permanent magnets and their direction of magnetization. A parametric FE analysis is used to solve the magnet field distribution. The optimization algorithms have been implemented in MATLAB and combined with the parameterized FEM model. The study resulted with optimal magnet numbers and shapes. Authors state that although GA is characterized by the high probability of finding the global optimum, convergence of the optimization process requires a significant number of iterations. Also it is stated that the convergence depends strongly on the number of variables in the optimization and is slower for higher number of variables. A good starting point (a good feasible design) is suggested to improve the calculation efficiency of the algorithm.

Duan et al [50] (2009) studied a multi-objective design method for comparison of the traditional distributed winding (DW) and the more popular concentrated winding (CW) configuration for SPM machines. The objectives of the optimization are selected as volume, weight, efficiency, weight of the magnets and torque per ampere at the rated

condition. Stator diameter in the airgap side, motor axial length and magnet thickness are chosen as design variables. The stator slot fill factor, stator winding current density, output power and rated voltage are the design constraints. Particle Swarm Optimization (PSO) method is applied to optimize the motor design with the analytical design model. PSO is run for two types of winding configurations; distributed (DW) and concentrated (CW). Verification of the analytical design is done by FE analysis. Authors conclude that CW designs have superior performance in terms of weight and volume. In addition, it is stated that, "the lower phase resistance helps to diminish the negative impact of the relatively low winding factor". Authors claim that "PSO optimization results agree with the physics reasoning behind the analytical equations" and they also propose that "particle swarm intelligence is able to correctly understand the underlying physical behaviour of the objective system in the searching process and find the best solution".

Kim et al [46] (2009) performed a multi-objective optimal design of an internal PM machine. Purpose of the study is to reach an optimum rotor design with V-shaped magnets in terms of back emf constant, maximum torque, cogging torque, torque ripple at maximum torque point, and total harmonic distortion (THD) of back emf. Five multi-objective functions are adopted where of back emf constant, maximum torque are maximized while other three objective functions are tried to be minimized. Three design variables for the V-shaped permanent magnet rotor are suggested; angle of one pole magnet, depth of rotor yoke, ratio of magnet length to barrier length. For each design, optimization is done in two steps; first basic design of IPMSM is performed by equivalent magnetic circuit theory which gives an outline of dimensions and windings, second FE analysis is performed to arrange and shape permanent magnets and barriers in the rotor so the rotor design is optimized. Verification of the final design is done by measurements on the realized prototype motor. A multiobjective optimal design is performed by Taguchi method. The author states that the resultant rotor design has low THD of back emf, high back emf value, and low cogging torque which was the aim of this study.

5.2.2 Conclusion to Literature Review of Optimum Design Studies

The specific properties of selected studies are tabulated in Table 5.6. Two more studies which are not summarized in previous section are also included in the table. It is presented that both analytical and FE based designs are applicable in optimization. A common way is to use analytical model in optimization for a draft design than perform a FE analysis for detailed analysis on the optimized design. Evolution strategy based optimization methods (Genetic Algorithm, Differential Evolution) are more common.

Table 5.6: Optimization studies for PM machine design in literature

Author	Motor type	Optimization Method	Design Model	Number of design variables	Verification
Boules [47]	Surface PM	Sequential unconstrained minimization with penalty	Analytical	8	Numerical comparison
Bolognani [49]	Surface PM	GA, Direct Search	Analytical	8	*not defined*
Boldea [48]	Surface PM	Hooke-Jeeves	Analytical	10	FE
Mellor [52]	Surface PM	GA	FE	6	*not defined*
Zarko [51]	Internal PM	Monte Carlo, Differential Evolution	FE	11	Measurements
Duan [50]	Surface PM	Particle Swarm Optimization	Analytical	3	FE
Kim [46]	Internal PM	Taguchi	Analytical and FE combined	3 for magnet	Measurements

In case of designing a new motor for a specific purpose, finding a feasible starting point may be very difficult. Optimization techniques which do not require a feasible starting point may offer a more flexible approach. Evolutionary algorithms do not require a starting design but instead a carefully selected design space with respect design variables must be introduced. These algorithms are capable of solving global multi-objective optimization problems subject to constraints very fast in case of carefully selected design space and objectives.

In this thesis work, a Genetic Algorithm (GA) based optimization will be employed to look for the best design in the entire design space which is formed by motor design variables. No initial design is defined so that a global optimum result can be searched in terms of the defined cost function, instead a randomly generated initial population will be the starting point. The GA combines principles of survival of fittest with a randomized information exchange [7].

In the study here for the inset PM machine design optimization, analytical motor model developed in CHAPTER 4 is implemented in MATLAB and is used along with optimization software called modeFrontier. The following section describes genetic algorithm approach used for the optimization. This is followed by description of the model created in MATLAB and how the motor performance is calculated. Setting up the optimization problem in modeFrontier is described in Appendix A.4.

5.3   Definition of Genetic Algorithm

In this section theoretical background of genetic algorithm is going to be presented. The genetic algorithm defined as "a fast elitist non-dominated sorting genetic algorithm for multi-objective optimization" by the authors [54].

5.3.1 Implementation of Genetic Algorithm with Non-Dominating Sorting

Solutions to a multi-objective problem can be expressed mathematically in terms of non-dominated points. If a solution vector $x^{(1)}$ is partially less than $x^{(2)}$, it is defined as $x^{(1)}$ dominates $x^{(2)}$ (Tmaura and Miura 1979).

Theoretically, optimization may be ended if one solution on Pareto-optimal set is reached. However, there could a number of Pareto-optimal solutions which may not be all suitable for the application or designer's choice.

Non-dominated search is based on a ranking selection method which emphasizes good design points in solution space. The application of non-sorting method to genetic algorithm changes only the selection method of good solutions. The cross over and mutation operators remain same. Before a selection of design is performed, each member of the population is ranked according to individual's non-domination.

5.3.2 Definition of Ranking Attributes

The selection process of fronts is guided by "crowded comparison operator" ($\geq_n$) at various stages of algorithm to reach a uniformly spread out Pareto-optimal front. This operator utilizes two attributes of each individual "i" in the population; non-domination rank i_{rank} and local crowding distance $i_{distance}$. In order to sort N number of solutions according to non-domination rank, each solution must be compared with every other to find out if it is dominated.

The non-domination rank i_{rank} is a measure for each specific design which shows by how many other designs it is dominated. If a member of solution space x is not dominated by any other member, then it is called as non-dominated. The number of members dominating that member is domination rank value irank for that individual. The optimal solutions to a multi-objective optimization are non-dominated members which are called also as Pareto-optimal solutions.

The crowding distance $i_{distance}$ refers to density of solutions surrounding a particular point in the population. It serves as an estimate of the size of the largest cuboid enclosing the point /without including any other point in the population (crowding distance). To get an

estimate of the density of solutions surrounding a particular solution in the population, we calculate the average distance of two points on either side of this point along each of the objectives. This cuboid is illustrated in Figure 5.7.
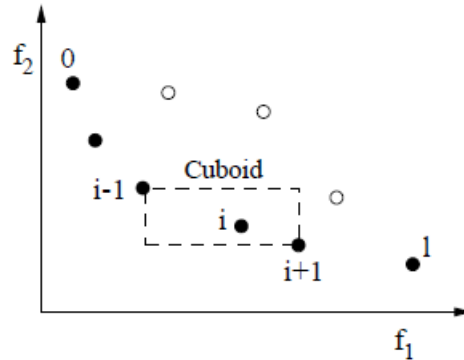
Figure 5.7: The crowding distance [54]

In Figure 1, f_1 and f_2 are two objectives of design. The crowding distance of the ith solution in its front (marked with solid circles) is the average length of two sides of the cuboid (shown with a dashed box).

The ranking operator "$<_n$" is defined by the presented two attributes; i_{rank} and $i_{distance}$. The ranking of each individual is performed according to following definition:

$$x1 <_n x2 \quad if(x1_{rank} < x2_{rank}) \text{ or } ((x1_{rank} = x2_{rank}) \text{ and } (x1_{distance} > x2_{distance}))$$

This definition formulates the described ranking of individuals x1 and x2 of population. It states that between two solutions x1 and x2 with differing non-domination ranks, the point with the lower rank (x1) is preferred or if two have same ranking than the solution which has the largest cuboid in objective function space is preferred.

5.3.3 Generation of populations and Selection

The genetic algorithm starts with a parent (initial) population P_0 of size N. This population may be generated randomly by the algorithm itself or presented by the user manually. The population is sorted based on non-domination ranking. Each solution is assigned a fitness equal to its non-domination rank (1 is the best level) and minimization of fitness is assumed. Binary tournament cross-over and mutation operators are used to create a child population Q_0 of same size N.

151

In the next step, a combined population $R_0 = P_0 \ U \ Q_0$ is generated with size 2N. This new population is again sorted according to non-domination ranking. The first N points (with highest ranking) are selected to form new parent population P_1. This new population is used to create a new population Q_1 of size N with crossovers and mutations. The procedure is same for all the next generation of populations. An illustration for the defined procedure is presented in Figure 5.8.
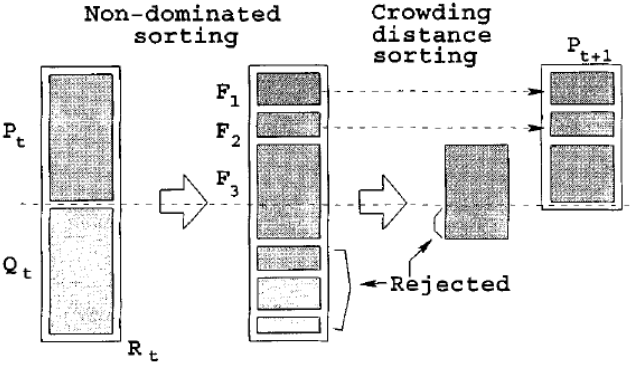
Figure 5.8: Sorting procedure [54]

5.4 Design Program in MATLAB

The analytical model developed in CHAPTER 4 is implemented in MATLAB in order to calculate characteristics of a motor (such as torque vs. speed and power vs. speed) with a design vector $\overline{X}$.

On the following sections, implementation of the developed analytical model is going to be presented in successive steps.
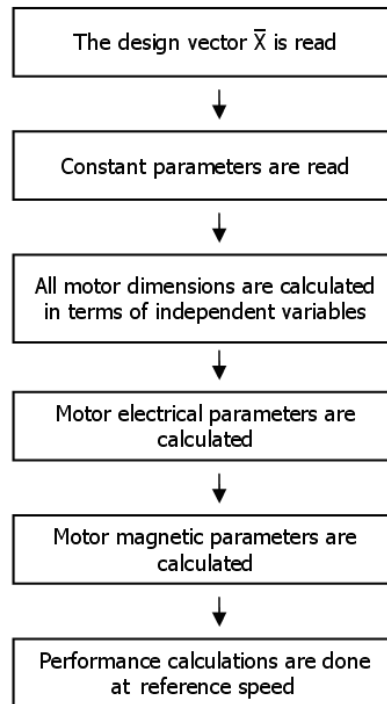
Figure 5.9: Calculation steps of design program in MATLAB

In this design program performance computations are going to be performed for the selected reference point; 2000 rpm. At this speed, motor parameters such as torque, power, efficiency, temperature rise will be calculated. The requirements for the design are defined in Section 5.1.1.

All of the motor electrical parameters are calculated with the developed analytical model equations in Section 4.2. These parameters include winding per phase resistance, d-q axis inductances. The related equations are also presented in Section 4.2.

All of the motor equivalent magnetic circuit parameters and flux densities are calculated with the developed analytical model equations in Section 4.1. These parameters include reluctances, emf voltage constant, torque constant, airgap peak and mean flux density, tooth peak flux density, back core peak flux density. The related equations are also presented in Section 4.1.

Developed electromagnetic torque is calculated by multiplying calculated torque constant with the motor terminal current. The phase diagram of PM machine under vector control operation is presented in Figure 5.10. The only unknown is I_q because E_o is calculated

153

from frequency by emf constant, per phase resistance is calculated from geometrical dimensions, terminal voltage is fixed at 21Vpeak as defined in specifications. The maximum allowable current is 35 Arms at this condition. Once Iq is determined from the phase diagram, then torque is calculated by multiplying motor current with motor torque constant k_{torq} which is calculated in previous step under magnetic parameters calculation.
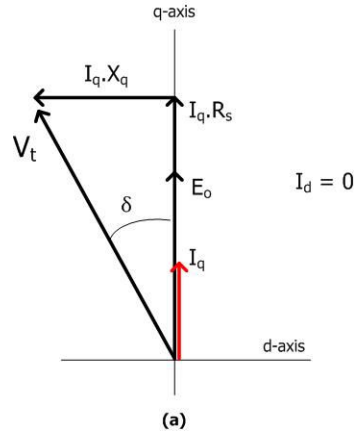
Figure 5.10: Electrical phase diagram of PM machine in vector control

Loss Calculation

As discussed in Section 3.3.5, no-load losses are dominated by friction-windage. Since the new design will have similar dimensions and structure, friction-windage plus core loss in the motor is represented by the same function determined for sample motor.

The analytical equation predicting no-load losses was derived in Section 4.2.3. The derived equation (4-69) will be used to predict core losses and it is also presented in (5-4).

$$P_{loss} = \left(0.035 \times f.\hat{B}_{th}^{2} + 0.0002 \times f^{2}\hat{B}_{th}^{2}\right) \cdot W_{th}$$
$$+ \left(0.035 \times f.\hat{B}_{bc}^{2} + 0.0002 \times f^{2}\hat{B}_{bc}^{2}\right) \cdot W_{bc}$$

(5-5)

Calculated flux densities in and motor volume in previous steps is inserted in this equation to calculate core loss.

In the design program, equations are solved for all valid operating points at the same time by matrix multiplications and all required matrices such as power, torque, and current are formed. At that point any characteristic graph can be plotted such as max power vs. speed by selecting maximum values in each column of power and torque matrices respectively. It

must be remembered that columns in matrices refer to selected speed steps. The code of the developed design program in MATLAB is presented in Appendix A.1.

In this thesis work, the optimized solution is selected with respect to objective function values of resultant feasible designs. The results are sorted and the design with minimum objective function value is selected.

5.5   Optimization Results

In this study, different optimization runs are performed to determine effect of defined design constraints on the search for an optimum design. It is assumed that the sample motor presented in detail in Section 3.1.1 is an optimized design in terms of some performance criteria. Based on the available manufacturer data, some performance criteria are derived which are presented in Section 5.1.1. Also based on the analytical calculations of the sample motor, constraints for the optimization are derived which are presented in Section 5.1.3.

As seen in Table 5.3 in Section 5.1.4, the design vector for the optimization is nine dimensional. The effect of number of parameters in the design vector is studied by fixing one of them and letting the others to be free within the same constraints set. For this purpose following optimization runs are performed and the objective function in these runs is as defined by equation (5-3):

- **Case.A1:** Fixed outer diameter:
  Outer diameter D_{so} is fixed at 62mm which is outer diameter of sample motor. By defining that outer diameter, rest of the dimensions in radial direction are diameter at magnet bottom, magnet height, slot depth and stator back core height which are free to vary as well as rest of the design variables (tooth width, magnet Br etc.) within the constraints imposed.

- **Case.A2:** Repeating fixed outer diameter run with different initial population:
  Outer diameter D_{so} is again fixed at 62mm. The initial population for GA is regenerated by "Random" method as described in Appendix A.4 with a total of 100 members. Rest of design variables are set free within defined limits in Section 5.1.

- **Case.B:** Fixed magnet type:
  Magnet Br value is fixed at 1.05T which is Br value for sample motor. Extraction of magnet Br value from design variables results a design vector consisting of only geometric parameters. All other design variables are set free.

- **Case.C1:** All variables are free:

  All parameters are set free in the design space where Br and D_{so} values are selected among defined boundaries.

- **Case.C2:** All variables are free with step sizes defined for variations:

  In this design, a step size is defined for all design variables so that each of them is expressed with 6 digit numbers at most to observe variation of evaluation time of optimization. By default, the optimization expresses each variable value with a 20 digit number which considerable affects evaluation time.

  Discrete steps defined for design variables are presented in Table 5.7. Axial length has a step of 0.5 mm due to lamination thickness. Slot depth, Stator yoke height, diameter at magnet base, and magnet height are assigned 0.05mm steps since a smaller step size is not critical and higher accuracy representations are not used mechanical drawings. On the other hand, discrete step for tooth width is assigned as 0.02mm equivalent to 1% of sample motor tooth width (1.82mm) for being more accurate in design under defined flux density constraints.

Table 5.7: Discretisation steps for design variables for Case.C2-C3

Independent Variable Name	Abbreviation (Figure 5.3)	Sample motor value	Discretisation steps	Variation wrt. Sample Motor	Range
Axial length	L	38 mm	0.5 mm	1.3 %	30mm < L < 50mm
Slot depth	h_1	7.7 mm	0.05 mm	1%	5mm < h_1 < 12mm
Stator yoke height	h_{bc}	2.25 mm	0.05 mm	2%	1mm < h_{bc} < 4.5mm
Tooth width	W_{th}	1.82 mm	0.02 mm	1%	1mm w_{th} < 3.5mm
Diameter at magnet base	D_{mb}	26.2 mm	0.05 mm	0.2%	20mm < D_{mb} < 40mm
Magnet height	h_{mag}	3.65 mm	0.05 mm	1.4%	1mm < h_{mag} < 5mm
Magnet arc span in one pole pitch	alfa	0.739	0.0555 (equivalent to 1° electrical)	7.5% (equivalent to 1° electrical)	0.6 ≤ alfa ≤ 0.9
Turns per coil	N_{turn}	4	1 steps	25%	1 ≤ N_{turn} ≤ 6
Magnet Br	Br	1.05	0.02T	2%	1.15 ≤ Br ≤ 1.25

- **Case.C3:** All variables except number of turns are free with step sizes defined for variations:

  Having investigated Case.C2 results, it is decided to fix the number of turns to 4 to observe algorithm behaviour. Discretisation steps for design variables are as presented in Table 5.7.

Three of the optimization runs (case A1, B and C1) are repeated for two sets of flux density constraints; calculated flux densities of sample motor (1.89T and 1.77T respectively) and lowered flux densities of 1.85T and 1.70T. The aim of performing the optimization with new flux densities is to see effect of flux density constraints on optimization result.

The optimizations are terminated automatically after 1000 generations which results in 100.000 designs in total in the entire design space. Except for discrete step optimization (Case.C1-C2-C3), the process takes about 20 hours.

Results of optimizations with high (with sample motor values) and low (with newly defined values) are presented in tables from Table 5.8 to Table 5.11.

5.5.1 Results for Optimization with Fixed Outer Diameter (Case.A1)

Table 5.8 presents the results of optimization carried out by fixing the outer diameter to sample motor outer dimension 62mm. The optimization lasts around 20 hours.

Following observations can be made:

- Efficiency is increased by 10% in both designs in return for increased volume by over 15%. That is why cost functions appear larger than sample motor's.

- Flux densities are pushed to defined constraint limits in both designs.

- Power and torque constraints are satisfied at their limits.

- Rated current and rated current densities are not pushed to limit which is probably because efficiency is part of the objective function.

- Two different magnets are preferred in the final designs.

- Magnet volume is decreased in both designs. Higher Br value leads to more magnet volume reduction as seen in high flux design.

- Higher flux density constraint did not lead to a lower motor volume.

Table 5.8: Results of optimization with outer diameter fixed with high and low flux constraints

	Sample Motor	**Low Flux Density Design** (Bth≤1.85T, Bbc≤1.70T)	**Variation %**	**High Flux Density Design** (Bth≤1.89T, Bbc≤1.77T)	**Variation %**
Objective function: Normalized Volume and Efficiency values are equally weighted					
Outer diameter D$_{so}$: Fixed at 62mm					
Magnet Br value: Free between 1.15T and 1.25T with 0.02T steps					
Objective function value	1	1.06	+6	1.06	+6
Total Volume (cm^3)	115	134	+16.5	138	+20
Efficiency (%)	73	80.4	+10	80.7	+10.5
Magnet Br	1.05	1.17	+11.4	1.21	+15.2
Magnet volume (cm^3)	1.25	1.15	-8	0.97	-22
Number of turns	4	4	-	4	-
Torque at 1500rpm (3Nm)	3	3	-	3	-
Power output at 2000rpm (W)	330	330	-	330	-
Tooth Flux Density (T)	1.89	1.85	-2.1	1.89	-
Back Core Flux Density (T)	1.77	1.70	-4.0	1.77	-
Current Density (A$_{rms}$/mm^2) (constraint ≤12)	11.5	9.39	-18.3	9.2	-20
Rated Current (A$_{rms}$) (constraint ≤20)	18.5	16.5	-10.8	16.4	-11.4

5.5.2 Results for Optimization with Fixed Outer Diameter with new population (Case.A2)

Table 5.9 presents the results of optimization carried out by fixing the outer diameter to sample motor value 62mm and running the optimization with a new initial population generated by Random algorithm in modeFrontier (see Appendix A.4). Only high-flux design optimization is repeated. Results are compared with previous high-flux design. The optimization lasts around 20 hours.

Following observations can be made from Table 5.9:

- Final designs have 6% higher value than sample motor as in previous optimization run presented in Case.A1 results.

158

- Increase in volume is larger in low-flux design contrary to what was found for Case.A1. This may be pointing out a need for further iteration or trying optimization with more initial population.

- Power constraint is satisfied as in limits but output torque at 1500rpm is 15% higher than 3Nm constraint. The optimization could proceed to lower torque output to 3Nm because of power constraint. This result is most likely due to number of turns.

- Increase in efficiency is almost same for both populations whereas the volume is increased from 20% to 23% for the new population.

- Flux densities are again pushed to limits for the new population.

- Although similar rated current is reached in new design, rated current density is pushed to the limit which may be due to effort to decrease the volume.

- A magnet with lower Br value is selected. This may be a result of effort to reduce torque output to constraint limit.

- A dramatic increase by 61% in magnet volume is observed which may be due to effort to develop same power with reduced magnet Br and lower number of turns.

Table 5.9: Results of optimization with outer diameter fixed with high and low flux constraints

Objective function: Normalized Volume and Efficiency values are equally weighted
Outer diameter D$_{so}$: Fixed at 62mm
Magnet Br value: Free between 1.15T and 1.25T with 0.02T steps
New initial population of 100 members generated by Random method in modeFrontier.

	Sample Motor	New population		Old population	
		High Flux Density Design (Bth≤1.89T, Bbc≤1.77T)	**Variation** %	**High Flux Density Design** (Bth≤1.89T, Bbc≤1.77T)	**Variation** %
Objective function value	1	1.06	+6	1.06	+6
Volume (cm^3)	115	142	+23	138	+20
Efficiency (%)	73	81	+11	80.7	+10.5
Magnet Br (T)	1.05	1.17	+11	1.21	+15.2
Magnet volume (cm^3)	1.25	2.01	+61	0.97	-22
Number of turns	4	3	-	4	-25
Torque at 1500rpm (3Nm)	3	3.44	+15	3	-
Power output at 2000rpm (W)	330	333	+1	330	-
Tooth Flux Density (T)	1.89	1.89	-	1.89	-
Back Core Flux Density (T)	1.77	1.77	-	1.77	-
Current Density (A$_{rms}$/mm^2) (constraint ≤12)	11.5	11.7	+1.7	9.2	-20
Rated Current (A$_{rms}$) (constraint ≤20)	18.5	16	-14	16.4	-11.4

5.5.3 Results for Optimization with Fixed Magnet Type (Case.B)

Table 5.10 presents the results of optimization carried out by fixing the magnet type as used in the sample motor. The optimization lasts around 20 hours.

Table 5.10: Results of optimization with magnet Br value fixed

Objective function: Normalized Volume and Efficiency values are equally weighted					
Outer diameter D_{so}: Free, constrained with lower or equal to 65mm.					
Magnet Br value: Fixed at 1.05T					
	Sample Motor	**Low Flux Density Design** (Bth≤1.85T, Bbc≤1.70T)	**Variation** (%)	**High Flux Density Design** (Bth≤1.89T, Bbc≤1.77T)	**Variation** (%)
Objective function value	1	1.02	+2	1.01	+1
Volume (cm³)	115	124.3	+8.1	123	+7
Magnet Volume (cm³)	1.25	1.38	+10	1.41	+12.8
Efficiency (%)	73	78	+6.8	77	+5.5
D_{so} (mm)	62	63	+1.6	63	+1.6
Number of turns	4	4	-	4	-
Torque at 1500rpm (>3Nm)	3	3	-	3	-
Power output at 2000rpm (>330W)	330	330	-	330	-
Tooth Flux Density (T)	1.89	1.85	-2.1	1.89	-
Back Core Flux Density (T)	1.77	1.70	-4	1.77	-
Current Density (A_{rms}/mm^2) (constraint ≤12)	11.5	11.2	-2.6	12	+4.3
Rated Current (A_{rms}) (constraint ≤20)	18.5	17.5	-5.4	18.2	-1.6

Following observations can be made from Table 5.10:

- Efficiency is increased by about 6% in both designs in return for increased volume by over than 7%. The effect of larger volume on cost function is compensated by increased efficiency. That is why cost functions appear similar with sample motor's.

- Better designs than optimizations by fixing D_{so} (Table 5.8) are reached.

- Flux densities are pushed to defined constraint limits in both designs.

- Rated current and rated current densities are not pushed to limit. Note that current densities are higher here as compared to Case.A.

- Higher flux densities resulted in better design in terms of cost function.

- In this case, as compared to fixed D_{so} designs, volume and efficiency improvements are smaller. However still the efficiency is 7-8% higher than sample motor.

5.5.4 Results for Optimization with All Design Variables Free (Case.C1)

Table 5.11 presents the results of optimization carried out by setting all design variables free. The optimization lasts around 20 hours.

Table 5.11: Results of optimization with all variables free

Objective function: Normalized Volume and Efficiency values are equally weighted

Outer diameter D_{so}: Free, constrained with lower or equal to 65mm.

Magnet Br value: Free between 1.15T and 1.25T with 0.02T steps

Duration: 20 hours

	Sample Motor	Low Flux Density Design (Bth≤1.85T, Bbc≤1.70T)	Variation (%)	High Flux Density Design (Bth≤1.89T, Bbc≤1.77T)	Variation (%)
Objective function value	1	1.0	-1.7	0.96	-4
Volume (cm³)	115	118.3	+2.9	113	-1.7
Efficiency (%)	73	77.6	+6.3	77.5	+6.2
Br	1.05	1.21	+15.2	1.25	+19
Magnet volume (cm³)	1.25	1.36	+8.8	1.25	-
Number of turns	4	4	-	4	-
Dso (mm) (constraint ≤65)	62	63	+1.6	65	+5
Torque at 1500rpm (3Nm)	3	3	-	3	-
Power output at 2000rpm (W)	330	330	-	330	-
Tooth Flux Density (T)	1.89	1.82	-4.2	1.89	-
Back Core Flux Density (T)	1.77	1.70	-4	1.77	-
Current Density (A$_{rms}$/mm²) (constraint ≤12)	11.5	11.8	+2.6	12	+4.3

Following observations can be made from Table 5.11:

- Final designs here have same or smaller objective function values than sample motor.

- Efficiency is increased by about 6% in both designs. In return for increased efficiency, the volumes of the designs are larger than sample motor by 2.9% in low-flux design and by 1.7% in high-flux design.

- Better designs are achieved than previous optimizations where D_{so} and Br (Table 5.8, Table 5.9 and Table 5.10) are fixed.

- Flux densities are pushed to defined constraint limits in both designs.

- Magnet Br value is pushed to upper limit in the high flux design.

- About 9% higher magnet volume is reached in low-flux design whereas same magnet volume is utilized in high-flux design.

- Rated current value and rated current densities are not pushed to limits.

- Higher flux densities resulted in better design in terms of cost function.

5.5.5 Results for Optimization where All Variables are Free and Discrete (Case.C2)

In this case, effect of discretisation of design variable variations are studied. It is observed in Case.C1 that a 1000 generation optimization run lasts around 20 hours. To observe any improvement in optimization time is studied by defining variation steps for design variables.

At the end of first optimization run with 1000 generations resulting 100.000 designs, no feasible designs are present. So a further iteration is performed with additional 2000 generations. The design with minimum outer diameter is selected in first 1000 generations to compare with the feasible design with minimum cost among 3000 generations as well as sample motor. Maximum allowable number of generations is 5000 in modeFrontier.

Table 5.12 presents the results of optimization carried out by setting all design variables free but also defining discrete steps for variation. Duration time for both runs are 3:36 hours for 1000 generations and 6:46 hours for 3000 generations.

Table 5.12: Results of optimization with all variables free and discrete

Objective function: Normalized Volume and Efficiency values are equally weighted

Outer diameter D_{so}: Free, constrained with lower or equal to 65mm.

Magnet Br value: Free between 1.15T and 1.25T with 0.02T steps

		1000 generations Duration: 3:36 hours		3000 generations Duration: 6:46 hours	
	Sample Motor	**High Flux Density Design** (Bth≤1.89T, Bbc≤1.77T)	**Variation** (%)	**High Flux Density Design** (Bth≤1.89T, Bbc≤1.77T)	**Variation** (%)
Objective function value	1	1.15	+15	1.10	+10
D_{so} (mm) (constraint <65mm)	62	66.9 *(65mm constraint is not satisfied in first 1000 generations)*	+7.9	63.6	+2.5
Volume (cm³)	115	161	+40	149	+30
Magnet volume	1.25	1.24	-1	1.21	-3
Efficiency (%)	73	81.1	+11	81.1	+11
Br	1.05	1.25	+19	1.25	+19
Number of turns	4	3	-25	3	-25
Torque at 1500rpm (constraint >3Nm)	3	3.48	+16	3.37	+12
Power output at 2000rpm (W) (const. >330W)	330	330	-	330	-
Tooth Flux Density (T)	1.89	1.36	-28	1.60	-15
Back Core Flux Density (T)	1.77	1.77	-	1.74	-2
Current Density (A_{rms}/mm^2) (constraint ≤12)	11.5	11.8	+2.6	11.75	+2
Rated Current (A_{rms}) (constraint ≤20)	18.5	17.1	-7.5	15.9	-14

Following observations can be made from Table 5.12:

- Optimization time is considerably reduced from 20 hours to 3:36 hours for 1000 generatios. Even 3000 generations are faster about 300% than previous free design (Case.D).

- The cost function is larger than sample motor and previous run for both designs but it is observed a better solution is reached with more generations.

- The final design has 40% larger volume after 1000 generations whereas volume increase is reduced to 30% after 3000 generations.

164

- Both designs have 11% higher efficiency than sample motor at 2000rpm.

- Number of turns is 3 for both designs. This leads to oversized design to satisfy power constraint because of reduced torque constant due to lowered number of turns.

- Magnet Br value is pushed to upper limit for both designs which is theoretically expected for minimum volume design.

- Power constraint is satisfied for both designs.

- Torque output at 1500rpm is 16% higher than constraint limit at 1000 generations. This over qualified torque output is decreased to 12% which is an outcome of reduced total volume.

- Tooth flux density is 28% lower than constraint limit after 1000 generations. It is pushed more towards limit value after 3000 generations where it is still 15% lower.

- Current density is pushed to its limit for both designs and rated current density is selected around 16-17 A_{rms} as in previous designs.

The dramatical decrease in convergence time is studied and following results are derived:

- When a new population is generated by modeFrontier, each member (design vector) is compared with previous evaluated members. If that member (or design) is evaluated before then it is skipped.

- By defining variation steps, design space for each independent variable are considerably reduced with respect to unsized step variations (6 digit expression instead of 20 digit). More explicitly; since each value of design parameter are selected from a smaller design space, it is more likely to pick a parameter set which is also evaluated before.

- Since repeated designs are skipped, required time for evaluating all members of a generation are reduced due to possible repeated designs.

- When the optimization is run in its new form, it is observed that; at the end of first 2000 generations, out of 200.000 members generated, 519 are feasible with cost function values between 1.087 and 1.042. Further iterations are performed to create 2000 more generations to find out whether a smaller cost function value can be obtained.

- Total number of members evaluated is around 33.500 in 3000 generations which states nearly 11% of generated members are unique and rest consists of repeated designs.

- The low diversity (11%) of generated populations is due to conservatively selected control parameters of GA (see Appendix A.4)

5.5.6 Results for Optimization where All Variables but Number of Turns are Free and Discrete (Case.C3)

It is observed from Case.C2 results that optimization is probably stuck into local minima because the objective function remains 15% larger as compared to the optimal design found when all variables are set free (0.96 vs. 1.10). When inspected closely it is found that the number of turns is set at 3 resulting in a designs capable of producing much more torque than necessary in the constant torque region as observed in Table 5.12 For example torque output at 1500rpm is 12% higher than defined 3Nm constraint. This results in oversizing of the motor to fit power constraint.

It is interpreted that non-optimum value for number of turns dominantly affects motor volume so it is decided to experiment with the optimization algorithm by fixing Nturn=4 and reducing the number of free variables to 8. All other parameters are set free with discrete variation steps. Tooth and back-core flux densities are set to higher limits; 1.89T and 1.77T respectively.

When the optimization is run in its new form, it is observed that; at the end of first 2000 generations, out of 200.000 members generated, 519 are feasible with cost function values between 1.087 and 1.042. Further iterations are performed to create 2000 more generations to find out whether a smaller cost function value can be obtained.

Optimization durations for the discrete variable optimization runs are 3:50 hours for 2000 generations and 6:45 hours for 4000 generations. Note that, as expected, this is a considerable reduction in computation time. Outcome of these two successive optimization runs is given in Table 5.13.

Table 5.13: Results of optimization with all variables but number of turns are free and discrete

Objective function: Normalized Volume and Efficiency values are equally weighted					
Outer diameter D_{so}: Free, constrained with lower or equal to 65mm.					
Magnet Br value: Free between 1.15T and 1.25T with 0.02T steps					

		2000 generations Duration: 3:50 hours		4000 generations Duration: 6:45 hours	
	Sample Motor	**High Flux Density Design** (Bth≤1.89T, Bbc≤1.77T)	**Variation (%)**	**aHigh Flux Density Design** (Bth≤1.89T, Bbc≤1.77T)	**Variation (%)**
Objective function value	1	1.04	+4%	1.02	+2%
D_{so} (mm) (constraint <65mm)	62	63.3	+2%	62	-
Volume (cm³)	115	132	+15%	127	+10%
Magnet volume	1.25	0.82	-34%	0.87	-30%
Efficiency (%)	73	78.3	+7.3%	77.5	+6.2%
Br	1.05	1.21	+15%	1.21	+15%
Number of turns	4	4	fixed	4	fixed
Torque at 1500rpm (constraint >3Nm)	3	3	-	3	-
Power output at 2000rpm (W) (const. >330W)	330	332	-	340	+3%
Tooth Flux Density (T)	1.89	1.80	-3%	1.73	-8.5%
Back Core Flux Density (T)	1.77	1.51	-15%	1.77	-
Current Density (A_{rms}/mm^2) (constraint ≤12)	11.5	11	-4%	11.4	-
Rated Current (A_{rms}) (constraint ≤20)	18.5	17	-8%	17.6	-5%

Following observations can be made from Table 5.12:

- Optimization finishes faster than continuous variable cases A1, A2, B, C1. Only 6:45 hours is enough for 4000 generations whereas it took about 20 hours for 1000 generations in continuous cases.

- Algortihm is also faster than Case.C2 where design variables also discrete. In Case.C2, 3000 generations took 6:36 hours while 4000 generations could be computed in the same time for Case.C3.

- Fixing number of turns avoided to go to local minima as observed in Case.C2 and better designs are reached. An objective function 1.02 is reached where it is 1.10 in Case.C2.

- The objective function could be reduced by a further 2% with 2000 more generations.

- The final design has 15% larger volume after 2000 generations whereas volume increase is reduced to 10% at the end of 4000 generations.

- In first run, optimum design efficiency is 7.3% higher than sample motor. Efficiency decreases in further iterations and is only 6.2% higher after 4000 generations. Note that after this second run volume of the motor is reduced by 5%.

- Magnet Br value is pushed to 1.21 T and magnet volume is considerably lower.

- Power constraint at 2000 rpm and torque constraint at 1500 rpm are satisfied for both designs.

- Tooth flux density is not pushed to limits; it was 3% lower in the first run and 8.5% lower after 4000 generations. This may be a sign for a need for further iterations.

- Current density is pushed to towards limit for both designs and rated current density is selected around 17-18 A_{rms} similar to results of previous cases.

5.6   Convergence Behavior of Optimization Algorithm

To see evolution of the optimized results, design outputs at selected generations of GA is tabulated in Table 5.14. Number of feasible designs as well as values of minimum and maximum cost function values are listed for selected generations. The cost function range is also plotted as shown in Figure 5.11.

The initial population for GA algorithm consist of 100 designs all of which are generated by modeFrontier as described in Appendix A.4. No feasible designs exist in initial population. The cost function value diverges between 1.47 at max -2.3 at minimum. The negative cost function is due to negative efficiency calculated for that design. For some designs, negative power output values are calculated which results in negative efficiencies. Of course these designs are marked as unfeasible and next generations are improved to fit into constraints.

Table 5.14: Evolution of designs for high-flux optimization with all design parameters set free

Number of generation	Number of feasible designs	Minimum cost function value for unfeasible designs	Maximum cost function value for unfeasible designs	Feasible minimum cost	Feasible maximum cost	Variation of feasible designs
Initial population	0	-2,3	1,47	-	-	
100	0	0,55	1,23	-	-	
200	0	0,48	1,24	-	-	
400	0	0,48	1,10	-	-	
600	5	0,50	1,10	0,971	0,972	±0.5%
700	23	0,42	1,19	0,968	0,969	±0.5%
800	6	-4,43	1,13	0,968	0,968	0
900	11	0,41	1,74	0,967	0,967	0
1000	25	0,42	1,20	0,967	0,971	±2%
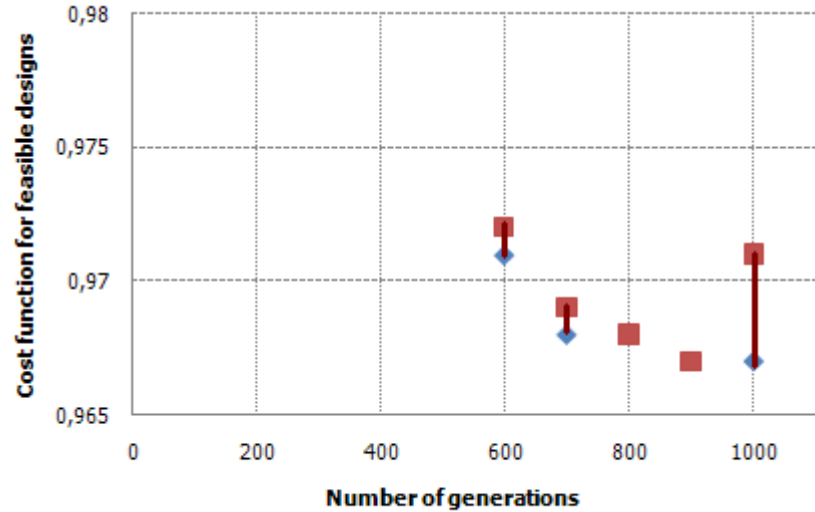
Figure 5.11: Evolution of feasible designs high-flux optimization with maximum ordered design vector

Following observations can be made from the presented figure Figure 5.11:

- First feasible designs appear at 600th generation and more feasible designs are reached in next generations.

- Once a generation with feasible solutions is reached, the variation between maximum and minimum objective function value for feasible designs is 0.5% which tells that diversity of feasible designs is very limited. This shows that optimization algorithm sticks to observed feasible designs very much and new designs with distinct cost function values are not created.

- Furthermore it can be argued that the the process can be stopped say after about 600 generations to reduce computer time consumption without sacrificing much accuracy

- Limited diversity of feasible designs may be due to algorithm parameters which are set at the beginning of the run. These parameters include cross-over probability and distribution index for cross-over which are presented in Appendix A.4 in detail. It may be concluded that values for these control parameters for GA are conservative and limits diversity of generated population for feasible designs.

5.7 Conclusions on Optimization Results

Based on the presented observations on optimization results, following commons conclusions can be made about the optimization:

- Flux densities are mostly pushed to the constraint limits in the designs even it is low or high. It can be stated that the flux density limits in a design must be chosen carefully. Preferably maximum feasible flux densities must be set to have the best design in terms of volume and efficiency.

- Efficiency objective appears to be more dominant than volume objective although they are equally weighted. This may be because of more parameters and calculations affecting these objectives. Volume is dependant on geometrical dimensions, but efficiency depends on geometrical dimensions as well as magnetic calculations which means that more variables exist in efficiency calculations.

- Better designs in terms of cost function are obtained when no design variable is fixed. This states that more efficient optimization is performed when the

optimization algorithm is set free to assign values of design parameters. Also it can be avoided to stick in a local minimum by setting all parameters free.

- Control parameter values for GA are very effective on the diversity of generated feasible designs. Conservative parameter tuning leads to limited variation of feasible designs. On the other hand, too much randomness in the algorithm by setting control parameters liberally may come with need for more generations to reach designs with cost functions as reached by conservative parameters. This issue needs further investigation.

- Number of turns for stator winding is selected as 4 in three of the designs (Case.A1-B-C1) whereas it is selected as 3 in optimization runs with new population (Case.A2) and discrete variation steps (Case.C2). Investigating the results with 3 number of turns show that 4 is optimum value. Although 330W power constraint at 2000rpm is satisfied at defined limit, torque output at 1500rpm is achieved much higher than 3 Nm constraint. The number of turns affects torque-speed profile at constant power region very much. A design with 3 turns can output 330W output 2000rpm but leads to over-sized torque output at 1500rpm. This is not the case as observed in Case.A-C-D where optimizations lead to 4 turns. This shows that if power and/or torque outputs are not pushed to the constraint limits, than most probably, number of turns or another parameter with high degree of effect (Number of turns is directly present in torque and emf equations) in performance calculations is improperly selected.

- Although discrete optimizations perform faster, there is a possibility of converging to local minima if algorithm control variables (mutation and cross-over probability etc.) are not properly set.

CHAPTER 6

CONCLUSION

The objective of this thesis work can be summarized as follows:

1. To develop an accurate PM machine model for performance calculations

2. To investigate measurement methods in the literature for PM motor parameters and performance

3. To conduct selected test methods on the PM motor and determine model parameters

4. To study reliability of the presented model by performing performance analysis (e.g. torque-speed) on the model with the measured parameters and compare calculated performance

5. To propose a set of test methods to fully characterize a PM machine. Any test method has not been standardized yet.

6. To develop an analytical set of equations to relate motor performance and parameters to machine dimensions and material properties for optimization purpose.

7. To study accuracy of developed analytical model by comparing calculated parameters and performance with measurements

8. To perform optimum design with the developed analytical model

These objectives have been greatly achieved in this work.

In CHAPTER 2, the conventional two-axis electrical model for brushless DC machines is employed for performance calculations of the sample motor. This model is reviewed in this chapter. The lumped magnetic circuit model given in the literature is also reviewed. Calculation of the steady-state motor performance using this equivalent circuit is discussed.

Accuracy of the model must be studied first by comparing calculated sample motor performance by utilizing measured parameters; with the measured performance. To

achieve a reliable comparison, accurate measurement of the parameters and the motor performance is necessary. For this reason, a section in CHAPTER 3 is devoted to literature survey mainly among IEEE Standards and IEEE published papers on measurement of PM brushless DC motor performance characteristics and two-axis model equivalent circuit parameters.

It is observed that although many studies are present for internal magnet type PM machines, there is not much work on surface PM type motors. A group of parameter and performance test methods has been selected for further investigation.

It is observed that most of the equivalent circuit parameters are simple to measure except inductance measurement. The measurement of d-q axis inductances of a PM motor is a challenging issue. Many studies on inductance measurement of PM machines are published covering various methods. Selected methods from the literature for inductance measurement are applied on a test motor and results are compared which include:

- Inductance measurement at running conditions
- Inductance measurement at standstill
- Inductance measurement by DC decay tests

Measurements are repeated at different current levels and frequencies, to find out whether these factors affect inductance.

For d-axis, it is shown that standstill and running tests results agree by 5% and they agree with manufacturer data for the sample motor by 10%. Results at different frequencies agree within 3%. Also inductance is almost constant within 5% dispersion with increasing current. The effect of demagnetizing current on d-axis inductance is also investigated. It is found that measured inductance is 10% higher than what is found with armature current in magnetizing direction. This result shows general agreement with the literature.

For q-axis, running and standstill tests results do not agree with manufacturer data. On the other hand the standstill test result agrees with the manufacturer data.

When investigated it is found that inductance measurements from running tests (load test) show considerable variation under changing frequency and current. It is observed that q-axis inductance measurements are largely dependent on accurate load angle measurement. This is because inductance calculation during running test involves sine of load angle. Electrical load angle of sample PM motor is about 20-25° at full load, calculated inductance values become very diverse with even 1° measurement error. On the other hand, calculated inductances from standstill tests are almost same (only 1% dispersion) at different currents and frequencies.

On the other hand, DC decay tests did not give similar results with both running and standstill tests for d-q inductances. Also dc decay test results for d-q axes do not agree with manufacturer data either. Inductance variation trend with current' for this test, is also contrary to expectation where a decrease with increasing current was expected due to possible saturation in magnetic paths.

Standstill tests are concluded to be most proper method for d-q inductance measurements, because results are reliable, test rig is easy to setup and inductance calculation from measurement data is simple. Standstill tests are performed by aligning the rotor to magnetic "d" and "q" axes and exciting the motor terminals. It is also shown that the excitation scheme (AC sinusoidal or PWM) do not affect results unless fundamental harmonic of both excitation voltage and induced motor current are used in calculations.

The most valuable contribution of this work is that not much study is available on measurement of d-q inductances of a surface PM motor. Furthermore, no previous work is found which covers all test methods at once on the same motor.

Also cogging torque measurement is performed on the sample motor, by driving the motor by external means, at different speeds. Measured cogging torque values are compared with FE solution results. It is found that measured cogging torque is 0.2Nm is at most, that is about 1% of rated torque. On the other hand FE solutions predicted much smaller cogging torque (0.02). This is possibly because some of the cogging torque is due to manufacturing problems and because of the test set up irregularities. It is concluded that cogging torque measurements should be performed at very low speed with high inertia especially if measured magnitudes are very low. Test at low speed with high inertia on the shaft enhances the measurement accuracy.

CHAPTER 4 concentrates on the calculation of motor equivalent circuit parameters from motor dimensions. Once this is done, for a given set of dimensions, the motor performance can also be calculated. The approach used for parameter calculations is based on what is available in the literature.

The accuracy of the analytical model is validated by inserting measured parameters to the model and comparing calculated performance with measured performance. Following performance calculations are done for performance determination:

- Torque-Speed
- Power-Speed
- Current-Speed

No-load losses (friction-windage and core loss) are not calculated in the model, but instead no-load losses of the sample motor is measured and its variation with speed is obtained. It is assumed that since the designed motor is similar to sample motor in size and power, similar no-load loss will exist in the new design. The equation representing no-load loss variation with speed is used in the new torque output calculations. The equivalent losses at an operating speed are represented as a decrease in the developed electromagnetic torque.

Although this approach gave satisfactory results for this thesis work, it may not work for larger machines where core-losses are more effective in no-load losses. Friction-Windage losses are dominant because electrical steel body is very small in 0.33kW sample motor. When larger machines (30-40 kW) are to be designed, core losses may rise to 10% of rated power and these losses must be accurately calculated for reliable performance validations. More accurate analytical equations shall be developed based on electrical steel loss characteristic rather than interpretation of measurements.

A comparison of torque-speed curves are performed based on calculated and measured characteristic as well as manufacturer data. It is shown that steady state torque can be calculated within 1% accuracy in constant torque region and with 5% accuracy in constant power region as shown in Figure 4.27. Having validated the developed analytical model, it is employed fin the software developed for optimum design of a Surface Mount PM Machine.

In CHAPTER 5, the software developed for optimum motor design of surface mount PM motors is described. The application is developed on a commercially available software platform; modeFrontier. The program includes many optimization algorithms which can be linked to auxiliary programs such as MATLAB, Excel and Ansys. In this work, no original optimization algorithm is developed but modeFrontier is linked to the developed MATLAB script which includes all the set of derived analytical equations developed in CHAPTER 4.

Genetic algorithm (GA) is selected as the optimization algorithm because it needs no initial feasible designs. The ability of GA for searching optimum design in the entire design space for variables is also preferred.

The design vector consists of 9 design parameters including Axial length, Slot depth, Stator yoke height, Tooth width, Diameter at magnet base, Magnet height, magnet arc span in one pole pitch, turns per coil, magnet Br. It is shown in CHAPTER 4 that all motor parameters and performance curves can be analytically calculated by these 9 variables.

Optimization study is repeated under following conditions to examine their effects on finding an optimum solution:

- Effect of flux density constraints
- Importance of initial population on the solution
- Assigning discrete variation steps for design variables
- Fixing a parameter to reduce the number of independent variables

This study led to the following conclusions:

1. In most of the final designs, flux densities are pushed to defined limits. When designs with high and low flux density constraints are compared, it can be stated that volume and efficiency of the final designs are dependent on the flux density constraints because designs with higher flux densities have lower volume. Preferably, maximum feasible flux densities must be set to have the best design in terms of minimum volume with maximum efficiency.

2. Results showed that convergence behaviour of GA algorithm is dependent on initial population. Different optimum designs were reached with two different initial populations. It can be recommended that any optimization should be repeated with different initial designs to determine better of the local minima.

3. It is observed that introducing step changes for design variables (see Section 5.5.5), wherever possible, greatly reduces convergence time. In the study here, 1000 generations in GA was executed in 3:36 hours when discrete variables were used instead of 20 hours needed with continuous variables. On the other hand, best designs are reached when all design parameters were continuously varied.

4. Effect of reducing design variables is studied by fixing magnet type, motor outer diameter and umber of turns per phase one at a time. Results showed that fixing number of turns may increase the possibility of reaching feasible designs in earlier generations which leads to smaller objective functions in final design. On the other hand, fixing outer diameter resulted in worse designs than optimization with all variables free.

5. Almost the same magnitude of objective function could be reached in final designs when magnet type was fixed. When magnet type is extracted from design variables, only geometrical parameters are left as independent variables. It is interpreted that if the design vector for an optimization consists of similar types of parameters, better designs can be reached.

6. Having investigated final designs of different optimization studies, it can be concluded that global optimum is not always guaranteed for GA. Control parameters (such as mutation and cross-over probabilities) are very effective on ability of the algorithm to converge to a global optimum design. Conservatively selected control parameters may lead to convergence to local minima. Different optimization runs may be performed to search for best control parameters for a specific optimization.

In addition to studied and presented work in this thesis, following topics can be studied further as a future work:

- A more intense core loss calculation can be developed and integrated into motor design script in MATLAB. It is evident that for larger machines where core-loss is a major part of losses, the already available equations will not give accurate results.

- Magnets are assumed to be parallel magnetized for all designs. Effect of magnetization direction variation to magnet shaping is not studied. This can be included in the developed analytical equations.

- Cogging torque calculation is not included in the analytical model.

- Torque ripple calculation is not included in the in the developed model. Instead a constraint is placed on the total harmonic distortion of the air gap flux density variation. The validity of this approach needs to be investigated.

- Different objective functions can be studied to observe optimization algorithm behaviour. The inclusion of efficiency in the objective function is found to increase the volume of the final design. It may be worthwhile to investigate what happens when volume is defined as the sole objective function.

- Finite element analysis is not employed in the optimization here. FE can be included in optimum design process in some manner to increase accuracy of the magnetic model or to calculate cogging torque.

- Only genetic algorithm (GA) is employed in optimization. There are also many other algorithms such as Simplex, Levenberg-Marquardt and Game theory. Those can be studied to observe their effect in terms of converge time, constraint satisfaction, converging to global optimum.

REFERENCES

STANDARDS

[1]   IEC Pub. 34-4: Methods for determining synchronous machine quantities from tests, 1985.

[2]   IEEE Standard 115A: IEEE Standard procedures for obtaining synchronous machine parameters by standstill response testing, 1987.

[3]   IEEE Standard 115-1995, IEEE Guide: Test Procedures for Synchronous Machines, IEEE Std. 115 ISBN 1-55 937-710-0, 1995.

[4]   IEEE Standard 118-1978, "IEEE Standard Test Code for Resistance Measurement"

[5]   IEEE Standard 100-2000, "The Authoritative Dictionary of IEEE Standards Terms", Seventh Edition, 2000.

BOOKS

[6]   T.J.E. Miller, "Brushless Permanent-Magnet and Reluctance Motor Drives", Claredon Press, Oxford University Press, 1989.

[7]   J.F. Gieras, M.Wing, "Permanent Magnet Motor Technology – Design and Applications", 2nd Ed., Marcel Dekker Inc., New York, ISBN: 0-8247-0739-7, 2002.

[8]   D. Hanselman, "Brushless Permanent Magnet Motor Design", 2nd Ed., The Writers' Collective, ISBN:1-932133-63-1, 2003.

[9]   T.A. Lipo, "Introduction to AC Machine Design", Vol.1, Wisconsin Power Electronics Research Center, University of Wisconsin, 1996.

[10]   G. Henneberger, Lecture Notes on "Electrical Machines II - Dynamic Behavior, Converter Supply and Control", Aachen University, Rev.2, July 2003.

[11]   P Eykhoff, "System identification, parameters and state estimation", Wiley, 1974.

PUBLISHED PAPERS

[12]   F. W. Merrill, "Permanent-Magnet Excited Synchronous Motors", Transactions of the AIEE Power Apparatus and Systems, Vol. 73, Issue 2, Part III-B, Jan 1954.

[13]   T.J.E. Miller, "Methods for Testing Permanent Magnel Polyphase AC Motors", IEEE IAS Conference Record, pp.494-499, 1981.

[14] B.J. Chalmers, S.A. Hamed, G.D. Baines, "Parameters and performance of a high-field permanent-magnet synchronous motor for variable-frequency", IEE Proceedings, Vol.132, Pt. B, No.3, pp.117-124, May 1985.

[15] A. Consoli, A. Raciti, "Parameter Analysis of Permanent Magnet Synchronous Machines", IEEE Trans. on Industry Applications, Vol.2, Issue.2, pp.350-354, Mar/Apr 1991.

[16] P. H. Mellor, F. B. Chaaban, K. J. Binns, "Estimation of parameters and performance of rare-earth permanent-magnet motors avoiding measurement of load angle", IEE Proceedings-b, Vol.138, Issue.6, pp.322-330, Nov 1991.

[17] B. Stumberger, B. Kreca, B. Hribernik, "Determination of Parameters of Synchronous Motor with Permanent Magnets from Measurement of Load Conditions", IEEE Transactions on Energy Conversion, Vol.14, No.4, pp.1413-1416, Dec 1999.

[18] Fidel FB, Aurelio GC, R. Faure, "Determination of Parameters in Interior Permanent-Magnet Synchronous Motors with Iron Losses without Torque Measurement", IEEE Transactions On Industry Applications, Vol. 37, No. 5, pp.1265-1272, Sep/Oct 2001.

[19] J.F. Gieras, E. Santini, M. Wing, "Calculation of synchronous reactances of small permanent-magnet alternating-current motors: comparison of analytical approach and finite element method with measurements", IEEE Transactions on Magnetics, Volume 34, Issue.5, Part.2, pp.3712-3720, Sep 1998.

[20] M. A. Rahman, M. A. Jabbar, P. Zhou, "Field Circuit Analysis of Permanent Magnet Synchronous Motors", IEEE Transactions On Magnetics, Vol. 30, No. 4, pp.1350-1359, Jul 1994.

[21] P. Pillay, R. Krishnan, "Application Characteristics of Permanent Magnet Synchronous and Brushless dc Motors for Servo Drives", IEEE Transactions on Industry Applications, Vol. 21, No. 5, pp.986-996, Sep 1991.

[22] P. Pillay, P. Freere, "Literature Survey of Permanent Magnet AC Motors and Drives", IEEE Conference Record of the Industry Applications Society Annual Meeting, pp.74-84, 1989.

[23] A. Binder, T. Schneider, "Permanent magnet synchronous generators for regenerative energy conversion - A Survey", European Conference on Power Electronics and Applications, pp.10, Sep 2005.

[24] R.S. Colby, "Classification of Inverter Driven Permanent Magnet Synchronous Motors", Industry Applications Society Annual Meeting, Vol.1, pp.1-6, 1988.

[25]   R. Mizutani, T. Takeshita, N. Matsui, "Current model-based sensorless drives of salient-pole PMSM at low speed and standstill", IEEE Transactions on Industry Applications, Vol.34, Issue.4, pp.841-846, July 1998.

[26]   S. Bolognani, R. Oboe, M. Zigliotto, "Sensorless full-digital PMSM drive with EKF estimation of speed and rotor position", IEEE Transactions on Industrial Electronics, Vol.46, Issue.1, pp.184-191, Feb 1999.

[27]   S. Morimoto, K. Kawamoto, M. Sanada, Y. Takeda, "Sensorless Control Strategy for Salient-Pole PMSM Based on Extended EMF in Rotating Reference Frame", IEEE Transactions On Industry Applications, Vol. 38, No. 4, pp.2637-2644, July/Aug 2002.

[28]   A.H. Wijenayake, P. Schmidt, "Modeling and Analysis of Permanent Magnet Synchronous Motor by Taking Saturation and Core Loss into Account", Proc. of Int. Conf. on Power Electronics and Drive Systems, Vol.2, pp.530-534, May 1997.

[29]   T. Kenjo, S. Nagamori, "Permanent Magnet and Brushless DC Motors", Claredon Press, Oxford University Press, 1985.

[30]   K.J. Overshott, "Magnetism: it is permanent", IEE Proceedings-A, Vol. 138, No.1, pp.22-30, Jan 1991.

[31]   N. Urasaki, T. Senjyu, K. Uezato, "Automatic Parameter Measurement for Permanent Magnet Synchronous Motors Compensating Dead Time Effect", Proc. of the 2002 IEEE Int Symposium on Industrial Electronics, Vol.3, pp.717-722, 2002.

[32]   T. Senjyu, Y. Kuwae, N. Urasaki, K. Uezato, "Accurate parameter measurement for high speed permanent magnet synchronous motors", IEEE 32nd Annual Power Electronics Specialists Conference, Vol.2, pp.772-777, 2001.

[33]   J. P. Wang, D. K. Lieu, W. L. Lorimer, and A. Hartman, "Comparison of Lumped Parameter and Finite Element Magnetic Modeling in a Brushless DC Motor", IEEE Transactions On Magnetics, Vol. 33, No. 5, Part.2, pp.4092-4094, Sep 1997.

[34]   Qu Ronghai, M. Aydin, T.A. Lipo, "Performance comparison of dual-rotor radial-flux and axial-flux permanent-magnet BLDC machines", IEEE International Electric Machines and Drives Conference, Vol.3, pp.1948-1954, 2003.

[35]   K.J. Strnat, "Modern Permanent Magnets for Applications in Electro-Technology", Proc. of the IEEE, Vol.78, No.6, pp.923-946, June 1990.

[36]   M.A. Jabbar, J. Dong, Z. Liu, "Determination of Parameters for Internal Permanent Magnet Synchronous Motors", IEEE Int. Conf. on Electric Mach and Drives, pp.149-156, 2005.

[37] V.Z. Groza, M. Biriescu, G. Liuba, "Measurement of reactance of synchronous machines at standstill", IEEE Int. Conf. on Elec. Mach. and Drives (IEMD, pp.171-173), May 1999.

[38] B. Stumberger, B. Kreca, B. Hribernik, "Determination of Parameters of Synchronous Motor with Permanent Magnets from Measurement of Load Conditions", IEEE Transactions on Energy Conversion, Vol. 14, No. 4, pp.1413-1416, Dec 1999.

[39] M. A. Rahman, P. Zhou, "Accurate determination of PM motor parameters by digital torque angle measurement", Journal of Appl. Physics, Vol.76, No.10, pp.6868-6870, 1994.

[40] D. Iles-Klumpner, I. Boldea, "Comprehensive Experimental Analysis of the IPMSM for Automotive Applications", 12th International Power Electronics and Motion Control Conference, pp.1776-1783, 2006.

[41] F.W. Carter, "Note on air gap and interpolar induction", Journal of Proceedings of the Institution of Electrical Engineers, Part 146, Vol.29, pp.925-933, 1900.

[42] S.F.Gorman, C.Chen, J.J. Cathey, "Determination of Permanent Magnet Synchronous Motor Parameters for Use in Brushless DC Motor Drive Analysis", IEEE Transactions on Energy Conversion, Vol.3, No.3, pp.674-681, Sep 1988.

[43] S. Yamamoto, T. Ara, S. Oda, K. Matsuse, "Prediction of starting performance of PM motors by DC decay testing method", IEEE Transactions on Industry Applications, Vol.36, Issue.4, pp.1053-1060, July/Aug 2000.

[44] R. Dutta, M.F. Rahman, "A Comparative Analysis of Two Test Methods of Measuring d-q Axes Inductances of Interior Permanent-Magnet Machine", IEEE Transactions on Magnetics, Vol.42, Issue.11, pp.3712-3718, Nov 2006.

[45] F. Deng, "An improved iron loss estimation for permanent magnet brushless machines", IEEE Transaction on Energy Conversion, Vol.14, Issue.4, pp.1391-1395, Dec 1999.

[46] KC Kim, J. Lee, HJ Kim, DH Koo, "Multiobjective Optimal Design for Interior Permanent Magnet Synchronous Motor", IEEE Transactions On Magnetics, Vol. 45, No. 3, pp.1780-1783, March 2009.

[47] N. Boules, "Design Optimization of Permanent Magnet DC Motors", IEEE Transactions on Industry Applications, Vol. 26, No. 4, pp.786-792, July/Aug 1990.

[48] L. Tutelea, I. Boldea, "Optimal Design of Residential Brushless d.c. Permanent Magnet Motors with FEM Validation", ACEMP 2007, pp.435-439, 2007.

181

[49]   N. Bianchi, S. Bolognani, "Brushless Dc Motor Design: An Optimisation Procedure Based on Genetic Algorithms", EMD Conference Publication, No. 444, pp.16-20, 1997.

[50]   Y. Duan, R.G. Harley, T.G. Habetler, "Method for Multi-objective Optimized Designs of Surface Mount Permanent Magnet Motors with Concentrated or Distributed Stator Windings", Proceedings of IEMDC 2009, pp.323-328, 2009.

[51]   W. Ouyang, D. Zarko, T.A.Lipo, "Permanent Magnet Machine Design Practice and Optimization", Industry Applications Conference, IAS 2006, pp.1905-1911, 2006.

[52]   R. Wrobel, P. H. Mellor, "The use of a genetic algorithm in the design optimisation of a brushless DC permanent magnet machine rotor", PEMD 2004, No.498, pp.823-827, 2004.

[53]   T. J. Vyncke, F. M. De Belie, R. K. Boel, J. A. Melkebeek, Y. Cheng, P. Lataire, "Identification of PM Synchronous Machines in the Frequency Domain by Broadband Excitation", International Symposium on Power Electronics, Electrical Drives, Automation and Motion (SPEEDAM), pp.1253-1258, 2008.

[54]   K. Deb, A. Pratap, S. Agarwal, T. Meyarivan, " A Fast and Elitist Multiobjective Genetic Algorithm: NSGA-II", IEEE Transactions on Evolutionary Computation, Vol.6, No.2, April 2002.

INTERNET WEB-SITES

[55]   Wikipedia, Magnet, "http://en.wikipedia.org/wiki/Four_Great_Inventions_of_Ancient_China", Last visited on Nov 27, 2008.

[56]   IBS Magnet, "Permanent Magnets – Materials and Magnet Systems", "http://www.ibsmagnet.de", Last visited on Dec 14, 2007.

[57]   Ningbo Ketian Magnet Co Magnet, "http://www.kt-magnet.com", Last visited on June 20, 2009.

[58]   ESTECO, "http://www.esteco.com", Last visited on July 10, 2009.

[59]   JFE Steel Corporation, "http://www.jfe-steel.co.jp/en/", Last visited on Aug 15, 2008.

MANUALS

[60]   modeFrontier[®] 4 User Manual, ESTECO

APPENDIX

A.1 MATLAB Code of Analytical Calculation Program

Main Program

```
eval('p1_IndependentVariables') %take independent variables   % in optimization program, these variables are assigned by the modeFrontier
                                        % itself. You have to remove this line to call for independet variables.
eval('p2_Assumptions_Definitions') %define assumptions
eval('p3_Dimensions')      %calculate stator and rotor dimensions
eval('p4_Electrical_Parameters')  %calculate electrical parameters such as "Rs, Lq"
eval('p5_Magnetic_Circuit_Calculations') %calculate magnetic parameters such as "kemf, ktorq"
eval('p6_reference_calculations') %calculations at reference speed
eval('p7_matrix_form') %matrix form
%% GRAPH PLOTINGS
% experiment torque-speed data [500 1600 1800 2000 2280 2730],[3 3 2.55 2.35 1.8 0.6]
%subplot(2,1,1),plot(w,maxTe,'m--',w,ratedTe,'b'),grid,ylabel('Torque (Nm)'),xlabel('Speed (rpm)'),title('Torque-Speed'),%axis([0 3500 0 4])
%subplot(2,1,2),plot(w,maxIt,'m--',w,ratedIt,'b-'),xlabel('speed (rpm)'),ylabel('Current (Arms)'),grid,%axis([0 3500 0 40])
```

"p1_IndependentVariables" Module

```
Br   = 1.05;        %magnet remanent flux density
Lsta  = 38e-3;       %axial length of magnetic circuit
h1    = 8.275e-3;    %slot depth (check drawings)
hbc   = 2.25e-3;     %back-core depth (check drawings)
g    = 0.75e-3;     %airgap (check drawings)
Wth   = 1.82e-3;     %Tooth width (check drawings)
Dmb   = 26.2e-3;      %diameter at magnet base. Draw a circle touching the magnet bottom
                %which is centered in the center of the rotor. This is the diameter of that circle.
alfa  = 0.748;      %magnet pitch / pole pitch
                %angular span of magnet with respect to total pole pitch. The angle that
                %mnagnet covers.
hmag  = 3.65e-3;     %magnet maximum height in the middle
Nturn = 4;          %turns per coil.
```

"p2_Assumptions_Definitions" Module

```
w = 1:20:3501;          %Speed step in rpm for calculations
Imax = 35;                %Current Limit in Arms. already defined by inverter
Vline = 21;               %bus voltage of inverter
pole = 8;          %Motor pole number
Nslot = 27;             %slot number of stator
phase = 3;            %number of phase
Kstack = 0.985;        %"Stacking factor"
kfill = 0.339;        %Slot fill factor
Cu_rho = 59.6e-6;     %Copper conductivity (Siemens/m)
muR = 1.05;              %Magnet muR
magnet_muR =1.05;      %ignore it for this time
prl = 0.1;            %Rotor leakage factor between adjacent magnets
w0 = 1.27e-3;          %Slot opening width (meters) - check drawings
h0 = 0.8e-3;           %Slot opening depth (meters) - check drawings
mu0 = 4e-07*pi;         %"space air permeability" - Henry /m
Ncoil = 9;             %Coils per phase, this is fixed for a defined slot number
Coilpitch = 16/18;     %Coil pitch of the winding. We have concentrated winding.
kw = 0.94;             %winding factor- precalculated from the distribution.
```

"p3_Dimensions" Module

```
%Airgap calculations (above magnet)
%magnet is divided into five pieces. Check ilker's thesis for details.
```

```
g1= g;                          %airgap at magnet surface tip. at max magnet height
g2= g / cos(1*alfa/4);          %airgap at magnet second region
g3= g / cos(2*alfa/4);          %airgap at magnet side

%Stator dimensions
Dms = Dmb+2*hmag;               %Diameter at magnet surface (meters)
Dmq = Dmb+2*hmag-2*1e-3;        %Diameter at surafece of saliency between magnets (meters)
Dsi = Dmb+2*(hmag+g);           %Diameter at stator inner surface (meters)

%Magnet dimensions
teta = alfa*360/pole;           %Angle span of magnet at magnet surface
Wmag = Dms*sind(teta/2);        %Width of magnet dip (meters)
hm2= hmag-0.5*(Dms-Dms*cosd(teta/4));       %mean magnet height at region 2
hm3= hmag-0.5*(Dms-Dms*cosd(teta/2));       %mean magnet height at regions 3
hmagmean = hm3+(hmag-hm3)*2/pi;       %overall mean magnet height
Apole = pi*(Dsi-g)*Lsta/pole;   %Total pole area (m^2)
Amag = Wmag*Lsta;               %Magnet cross sectional area at magnetization direction (m^2)
Ag = (Wmag+2*g)*(Lsta+2*g);     %Airgap area including fringing flux (m^2)

%Stator dimensions (Refer to drawings)
w1 = (Dsi+2*h0)*pi/Nslot-Wth;       %slot width near to slot opening (meters)
w2 = (Dsi+2*h0+2*h1)*pi/Nslot-Wth;  %slot width at slot dip (meters)
h2 = w2/2;                      %tooth height (meters)
hslot = h0+h1+h2;               %Total slot height (meters)
Aslot = (w1+w2)/2*h1 + pi*0.5*h2^2;   %Total slot area (m^2)
Abc = hbc*Lsta;                 %back core cros sectional area (m^2)
Ath = Wth*Lsta;                 %Tooth cross sectional area (m^2)
Dso = Dsi + 2*hslot+2*hbc;      %Stator outer diameter (meters)
Vol = pi*(0.5*Dso)^2*Lsta;      %total volume stator+rotor (m^3)
Surface = 4*Dso*Lsta + 2*Dso^2;       %Total surface area for heat transfer (m^2)
Rth = 1/(58.229*Surface);       %Thermal resistance (oC/Watt) - from MOOG datasheet
Dwire = 2*sqrt(Aslot/2*kfill/Nturn/pi);   %winding wire diameter
rotortest = 0.5*((Dmb-Wmag)/sqrt(2)-Wmag); %Distance between bottom tip of two adjacent magnets
                        %to check interference

Mdens = 7.65e3;                 %density of lamination kg/m3
Mth = Nslot*hslot*Wth*Lsta;     %Total mass of tooth lamination
Mbc = hbc*Lsta*pi*(Dso-hbc);    %Total mass of back-core lamination
Mrot = (0.5*Dmb)*(tan(2*pi/pole/2)*0.5*Dmb);  %Total mass of rotor roke
Mtot = Mdens*(Mth+Mbc+Mrot);    %Total mass of stator yoke
```

"p4_Electrical_Parameters" Module

```
%Electrical parameters
slotMatrix = [0 0 0 0 0 0; 9 15 18 21 24 0; 0 0 0 0 0 0; 18 21 27 30 33 36];
%matrix for available slot numbers for 4 and 8 pole motors with sinusoidal back EMF
slotpitchMatrix =[0 0 0 0 0 0; 2 3 4 5 6 0; 0 0 0 0 0 0; 2 2 3 3 4 4];
% matrix for available slot pitches for defined slot numbers

Spitch = (slotMatrix(pole/2,:)==Nslot)*(slotpitchMatrix(pole/2,:))';    %selected slot pitch
Cpitch = Spitch/(Nslot/pole);   %selected coil pitch

Ncoil = Nslot/phase;            %Number of coils
q1 = Nslot/pole/phase;          %Slots per pole per phase


% Carter coef. calculation (refer to drawings)
bo2 = w0;           %slot opening width
To2 = pi*Di/Nslot;  %one slot pitch
carter2 =To2/(To2 -bo2^2/(bo2+5*g3)); %carter coeffcent

%Winding resistance calculation
Awire = pi*(0.5*Dwire)^2;               %winding wire cross sectional area
Lwire = 2*Ncoil*(Lsta+0.01+(Spitch/Nslot*(Dsi+hslot)*pi));   %Total wire length 0.01 is assumption for end
winding height.
Lcon = (Dsi+hslot)*pi + 2*Ncoil*0.01; %total length of connections between coils
Rs = Nturn*(Lwire+Lcon)/Cu_rho/Awire; %Total phase resistance at 25oC
Rs = 1.44*Rs;                   %Total phase resistance at 150oC

pT1 =0.5*mu0*(0.623+h0/w0);             %Calculated leakage permeances
pT2 =mu0/3*h2/w2;                       %to be cited after
```

```
pT =pT1+pT2;
pB =mu0*(h0/w0 +2*(h1-h2)/(w1+w2));
pTB =mu0*(h0/w0 +(h1-h2)/(w1+w2));

Llm =3*(Ncoil*Nturn)^2*Lsta/Nslot*pTB;
Lsls =3*(Ncoil*Nturn)^2*Lsta/Nslot*(pT +pB +2*pTB*(3*Cpitch-2));
Lslm =-Llm*3*(1-Cpitch);
Lslot =Lsls -Lslm;          %calculated slot leakage inductance

wc1 = 3/Nslot*(Dsi+11.25e-3)*pi;      %length of end-winding
p_end = 0.34*q1*(1-2/pi*wc1/(2*0.01+wc1));
Lew =2*mu0*(Ncoil*Nturn*kw)^2/(pole/2*q1)*p_end*(2*0.01+wc1); %end winding inductance
%calculated from Jack F. Gieras book. Apoendix.A  pg.545

Nse =kw*Ncoil*Nturn;              %per phase effective coil turn, winding factor included
ged = g*carter2+hm3/muR;        %total airgap at d-axis (magnet height is included)
geq =(Dsi-Dmq)/2*carter2;        %total airgap at q-axis

Agapd =0.5*(Dsi-g)*(5*alfa/4)*Lsta;      %d-axis equivalent airgap area -m2
Agapq =(Dsi-g)*pi*Lsta/pole -Agapd;      %q-axis equivalent airgap area -m2
Apole =pi*(Dsi-g)/pole*Lsta;             %total pole area -m2

Lmsd =phase/2 *4/pi/pole *Nse^2 /(ged /(Apole*mu0)); %d-axis magnetizing inductance
Lmsq =phase/2 *4/pi/pole *Nse^2 /(geq /(Apole*mu0)); %q-axis magnetizing inductance

Ld =Lslot+Lew+Lmsd;          %Total d-axis inductance
Lq =Lslot+Lew+Lmsq;          %Total q-axis inductance
```

"p5_Magnetic_Circuit_Calculations" Module

```
%Check Miller-Brushless Permanent Magnet and Reluctance Motor Drives book.
%pg.61 - (The red cover book)
Pm0 = mu0*muR*Amag/(hmagmean);   %"Magnet internal leakage permeance"
Pr1 = 1/10*Pm0;                %"Rotor leakage permeance."
Pm = Pm0 + Pr1;                %"Magnet internal permance, leakage included"
Rg = g*carter2/(mu0*Ag);              %"Airgap reluctance"
PC = muR*(1+Pr1*Rg)/(Pm0*Rg);        %"Permeance coefficient"

Bm = (1+Pr1*Rg)/ (1+Pm*Rg)*Br;       %Magnet operating point
Bg = (Amag/Ag) / (1+Pm*Rg)*Br;       %Flux density in airgap
Bgpeak = hmag/(hmag+g*muR)*Br;      %peak flux density in airgap
Bgmean = Bg * (Wmag+2*g)/((Dsi-g)*pi/pole);   %mean flux density in airgap

Bth = Bgpeak * (pi*(Dsi-g)/Nslot)/Wth; %max peak tooth flux density
Bbc = Bgmean*pi*(Dsi-g)/pole/2/hbc;         %peak back-core flux density

Qm = sqrt(2)*(Ncoil*Nturn*kw)*Bgmean*Apole; %Flux linkage in one phase due to magnets

Bg1peak = 1/1 * 4/pi * Bg * sind(1* 0.5 *(Wmag+2*g)/((Dsi-g)*pi/ pole)*180 );
%peak of fundamental component of flux density

%Airgap flux harmonics (3,5,7 and 9th) peak values:
Bg3peak = 1/9 * 4/pi * Bg * sind(3* 0.5 *(Wmag+2*g)/((Dsi-g)*pi/ pole)*180 ); %3rd
Bg5peak = 1/25* 4/pi * Bg * sind(5* 0.5 *(Wmag+2*g)/((Dsi-g)*pi/ pole)*180 ); %5th
Bg7peak = 1/49* 4/pi * Bg * sind(7* 0.5 *(Wmag+2*g)/((Dsi-g)*pi/ pole)*180 ); %7th
Bg9peak = 1/81* 4/pi * Bg * sind(9* 0.5 *(Wmag+2*g)/((Dsi-g)*pi/ pole)*180 ); %9th

%Total Harmonic Distortion of airgao flux density distribution:
THD = 100* sqrt(Bg3peak^2+Bg5peak^2+Bg7peak^2+Bg9peak^2)/Bg1peak;

%Torque constant (Nm/Arms)
ktorq   = 3/sqrt(2)*pole/2*(Nturn*Ncoil*kw)*Bgmean*Apole;
% Back-emf constant per phase - (Vrms)
kemf    = 1/sqrt(2)*pole/2*(Nturn*Ncoil*kw)*Bgmean*Apole;
```

"p6_reference_calculations" Module

```
%These calculations are for optimization program. Calculated values are
%checked for constraints. With respect to these calculations independent
%variables are varied to search for optimum design.
wref = 2001;                    %Defined reference speed for calculations - RPM
```

185

```
wrad = wref/60*2*pi;     %Reference speed in rad/s
fe = wref/60*(pole/2); %Electrical operating frequency at reference speed
Xq = Lq*2*pi*fe;                  %Xq reactance at reference speed to be used in electrical equivalent
%circuit. Current is to be calculated.

emfrpm = wrad*kemf;            %Induced EMF voltage per phase in Vrms
Vtrpm_ = zeros(1,500); %Dummy matrix filled with zeros
for i=1:500
   Vtrpm_(i)= sqrt( (emfrpm+ i/10*Rs)^2 + (i/10*Xq)^2 );
   %At selected speed, current is increased by steps and we calculate
   %required terminal voltage for that condition.
end

% Limiter
Vtrpm_( Vtrpm_ > (Vline/sqrt(3)/sqrt(2)) ) = 0;    %Eliminating cells above limited bus voltage at reference speed
Irpm = length(Vtrpm_(Vtrpm_~=0))/10; %Max current at reference speed after elimination
Jcurref = Irpm*Nturn/(Aslot/2*kfill)*10^(-6); %Current density - Arms/mm2
Irated=Irpm; %Rated current is equal to the max current at reference speed

%Core-loss calculations
%Ref: Fang Deng,"An Improved Iron Loss Estýmatýon For Permanent Magnet Brushless Machines"
%IEEE Transactions on Energy Conversion, Vol. 14, No. 4, December 1999
%refer to the reference paper for defined constants in equations

ke = 0.2; kh = 0.5; kexc = 0.25; rhot = 0;
alfatt = 2*pi*pole/2 /Nslot;
Betam = pi*(1-alfa);
Pironref = ( kh*fe*Bth^2 + ke*fe^2*Bth)*Mth + ( kh*fe*Bbc^2 + ke*fe^2*Bbc^2)*Mbc;
                      %At this step we have calculated iron loss for every operating frequency
                      %or equivalently for every speed.

Pcuref = 3*Irpm^2*Rs; %Copper loss at reference speed for the maximum current available
Plossref = Pironref+Pwindref+Pcuref;            %Total loss at ref. speed
                                 %iron loss + windage loss + copper loss
```

"p7_matrix_form" Module

```
% Calculations in matrix form
f = w./(60*2/pole);         %Conversion of speed steps to electrical operating frequency for calculations
Xq = Lq*2*pi*f;    %q-axis reactance Xq at every operating frequency
%
emf = (w/60*2*pi)*kemf;%Induced emf per phase in Vrms
Vt_=zeros(Imax*20,length(w)); %Dummy voltage matrix filled with zeros. x-axis is speed, y-axis is current
It_=zeros(20*Imax,length(w));   %Dummy current matrix filled with zeros. x-axis is speed, y-axis is current
for rw=1:(20*Imax)        %for every current step of 0.05Arms
   for clmn=1:length(w)  %for every speed step of 0.06rad/s
     Vt_(rw,clmn)= sqrt( (emf(clmn)+ rw/20*Rs)^2 + (rw/20*Xq(clmn))^2 ); %required bus voltage is calculated
   end
   It_(rw,1:length(w)) = rw/20; %assign current value to current matrix
end

% Limitations
Vlim = (Vt_>=0).*(Vt_<=(Vline/sqrt(3)/sqrt(2))); %Eliminate points in votage and current matrix refering to voltage
values over fixed bus voltage Vline
Vmatrix = Vlim.*Vt_; %limited voltage matrix. Over voltage values are replaced with zeros.
maxVt = max(Vmatrix,[],1); %Terminal voltage at each speed step for max current
Imatrix = Vlim.*It_; %terminal current at each speed step
Iratedlim = (It_>0).*(It_<=Irpm).*Vlim; %Rated current level limit
ratedIt = max((It_.*Iratedlim),[],1);  %Rated current level
%
% Losses
Twind = (0.0025*(w/60).^2 + 0.0889*(w/60))./(w/60*2*pi);
%"windage+friction" loss for entire speed range

maxIt = max(Imatrix,[],1);      %Max current at each speed step
maxTe = maxIt*ktorq -Twind;     %Net torque output at each speed step
ratedTe = ratedIt*ktorq -Twind; %Rated torque at each speed step
```

A.2 Matrix Operations in Design Program in MATLAB

At every 100rpm step in full speed range and every $0.5A_{rms}$ step in current range, the motor model will be solved to determine motor performance data such as torque, power, loss, efficiency etc. The defined step in speed range results in 36 operating speeds and current step results in 70 steps in entire current range.

A.2.1 Voltage and Current Matrices

Considering the specified calculation points in previous section, we have 2520 operating conditions (36 speed steps x 70 current steps) to solve previously discussed equations. One approach may be solving electrical and magnetic equivalent circuit for one operating point and look for the result. However, since we have a powerful calculation tool like MATLAB, we can solve all equations related to motor performance in once for the entire operation range. MATLAB has the capability of performing matrix operations very fast. If proper matrices can be formed, MATLAB can solve the whole problem in a few seconds.

As stated we have 36 operating speed points and 70 current steps. To represent all operating points, we can use 70x36 matrices in all equations. Using matrices will allow us to compute all equations at the same time.

In this section, matrices representing induced emf voltage due to magnets and terminal currents to drive motor are formed. Throughout the whole simulation program calculations are performed as matrix manipulations since MATLAB responds much faster with matrices.

A.2.2 EMF Matrix

The emf matrix $|E_t|$ is formed by calculating generated EMF in the motor for each speed step. For each speed step, emf constant k_e is multiplied by the operating speed. In fact EMF matrix is an array rather than a matrix because it has one dimension referring to speed steps. However, to perform matrix operations, we need also second dimension which corresponds to current steps. For this purpose, the EMF array is cloned 70 times to form a 70 x 36 array. The resultant emf matrix (Figure A.1) consists of 70 identical rows which has emf voltage values for each speed step.

$$
\begin{vmatrix}
e_{1\text{-}1} & e_{1\text{-}2} & \dots & e_{1\text{-}36} \\
e_{2\text{-}1} & . & . & . \\
. & . & . & . \\
e_{70\text{-}1} & . & . & e_{70\text{-}36}
\end{vmatrix}
$$

Figure A.1: EMF matrix $|E_t|$ for MATLAB calculation

For example, in "e1-1" is the back emf magnitude when speed is 1rpm and "e1n" is emf at 3501rpm. As stated the values in the same column is identical such that e1-1,e2-1 and e70-1 are all same which is emf calculated at 1rpm. Equivalently $e_{1\text{-}36}$ and are $e_{70\text{-}36}$ emf calculated at 3501rpm with equation (a-1).

$$
e_{1-36} = e_{70-36} = k_e \times \frac{3501}{60} 2\pi \tag{a-1}
$$

A.2.3 Current Matrix

Similar to voltage matrix, current matrix $|I_t|$ is formed by 36 similar columns which consist of 70 cells representing terminal current step.

$$
\begin{vmatrix}
0.5A_{rms} & 0.5A_{rms} & \dots & 0.5A_{rms} \\
1.0A_{rms} & . & . & . \\
1.5A_{rms} & . & . & . \\
. & & & . \\
35.0A_{rms} & . & . & 35.0A_{rms}
\end{vmatrix}
$$

Figure A.2: Current matrix $|I_t|$ for MATLAB

A.2.4 Matrix Calculations

We now have formed voltage and current matrices that will be used in equation (a-2). This equation is based on the phase diagram of the motor operating under vector control which is presented in Figure 3.29 in Chapter 3.3.3. With this equation, terminal voltage matrix is

formed which will include the required bus voltage values for all operating conditions (36 speed steps, 70 current steps).

$$V_t = \left[\left(E_o + I_t R_{ph} \right)^2 + \left(I_t w_e L_q \right)^2 \right]^{\frac{1}{2}}$$ (a-2)

In the above equation, E_o is per phase back emf rms voltage at operating speed, I_t is phase rms current, R_{ph} is per phase resistance w_e is electrical operating speed in rad/s which can be calculated with equation (a-3);

$$w_e = \frac{N}{60} 2\pi \times \frac{p}{2}$$ (a-3)

where "N" is operating speed in rpm and "p" is motor pole number.

By equation (a-2), V_t is calculated for all operating points and a terminal voltage matrix $|V_t|$ is formed which is also a 36x70 matrix as voltage and current matrices. After that $|V_t|$ is checked for voltage limitation violation that is each cell value in the matrix is compared with bus voltage limit (21V_{peak} line-line or 8.57V_{rms} per phase in this thesis work) for terminal voltage.

To understand this better, consider the following example. Assume that motor is operating at speed 2000rpm with 30A_{rms} terminal current. The back emf voltage at this speed is;

$$E_e = \frac{0.070V_{peak}}{\sqrt{3}\sqrt{2}} \times \frac{2000rpm}{60} 2\pi = 6V_{rms} \ per \ phase$$ (a-4)

where 0.070 V_{peak}.s/rad is measured line emf voltage constant of tested motor is divided by √3 and √2 to get per phase rms voltage. Now let's solve equation (a-2) at this operating point.

$$V_t = \left[\left(6V_{rms} + 30A_{rms} \cdot 0.070ohm \right)^2 + \left(30A_{rms} \frac{2000rpm}{60} 2\pi \frac{8poles}{2} \times 0.133mH \right)^2 \right]^{\frac{1}{2}}$$
$$= 8.70V_{rms}$$ (a-5)

Remembering phase voltage limit as 21V_{peak} at motor terminals and 8.57V_{rms} per phase, the calculated terminal voltage 8.70V_{rms} is over the limitation that is available 21V bus voltage is not enough to operate the motor at 2000rpm with 30A_{rms} terminal current. So we can conclude that this operating point (2000rpm, 30A_{rms}) is unrealizable, no further calculation (torque,power, etc.) must be done, the value of this cell can be overwritten with zero not to include in calculations.

A.2.5 Matrix Operations

By solving equation (a-2) for all operating conditions, the terminal voltage matrix $|V_t|$ is formed. In this part we try to trim the formed matrices with respect to current and voltage limitations. As previously presented, there are invalid operating points where no performance calculations must be done. It should be checked that motor terminal voltage remains within limits for each step.

In the terminal voltage matrix, all cells having a value larger than $8.57V_{rms}$ are equated to zero. Also those cells also marked in current matrix, not to solve any torque, power or efficiency at that point. For example check following sample current and voltage matrices $|I_t|$ and $|V_t|$.

$$| I_t | =
\begin{array}{|c|c|c|c|c|}
\hline
1A_{rms} & 1A_{rms} & 1A_{rms} & 1A_{rms} & 1A_{rms} \\
\hline
2A_{rms} & 2A_{rms} & 2A_{rms} & 2A_{rms} & 2A_{rms} \\
\hline
3A_{rms} & 3A_{rms} & 3A_{rms} & 3A_{rms} & 3A_{rms} \\
\hline
4A_{rms} & 4A_{rms} & 4A_{rms} & 4A_{rms} & 4A_{rms} \\
\hline
5A_{rms} & 5A_{rms} & 5A_{rms} & 5A_{rms} & 5A_{rms} \\
\hline
\end{array}$$

$$| V_t | =
\begin{array}{|c|c|c|c|c|}
\hline
0.5V_{rms} & 1.0V_{rms} & 2.0V_{rms} & 3.5V_{rms} & 0.5A_{rms} \\
\hline
2.5V_{rms} & 2.8V_{rms} & 3.0V_{rms} & 5.5V_{rms} & 8.5V_{rms} \\
\hline
3.5V_{rms} & 4.0V_{rms} & 6.0V_{rms} & 8.0V_{rms} & 9.0V_{rms} \\
\hline
4.0V_{rms} & 5.5V_{rms} & 7.5V_{rms} & 8.5V_{rms} & 9.25V_{rms} \\
\hline
5.0V_{rms} & 6.5V_{rms} & 8.5V_{rms} & 9.0V_{rms} & 9.5V_{rms} \\
\hline
\end{array}$$

The values in the cells are arbitrarily assigned which are not based on calculations. If $8.57V_{rms}$ bus voltage limitation is applied to voltage matrix then the resultant will be as follows.

190

$0.5V_{rms}$	$1.0V_{rms}$	$2.0V_{rms}$	$3.5V_{rms}$	$0.5A_{rms}$
$2.5V_{rms}$	$2.8V_{rms}$	$3.0V_{rms}$	$5.5V_{rms}$	$8.5V_{rms}$
$3.5V_{rms}$	$4.0V_{rms}$	$6.0V_{rms}$	$8.0V_{rms}$	0
$4.0V_{rms}$	$5.5V_{rms}$	$7.5V_{rms}$	$8.5V_{rms}$	0
$5.0V_{rms}$	$6.5V_{rms}$	$8.5V_{rms}$	0	0

$$|V_t| =$$

As it can be noted, the cells with values larger than $8.57V_{rms}$ are overwritten with zeros. Exactly same cells in the current matrix must also be overwritten with zeros.

$$|I_t| =$$

$1A_{rms}$	$1A_{rms}$	$1A_{rms}$	$1A_{rms}$	$1A_{rms}$
$2A_{rms}$	$2A_{rms}$	$2A_{rms}$	$2A_{rms}$	$2A_{rms}$
$3A_{rms}$	$3A_{rms}$	$3A_{rms}$	$3A_{rms}$	0
$4A_{rms}$	$4A_{rms}$	$4A_{rms}$	$4A_{rms}$	0
$5A_{rms}$	$5A_{rms}$	$5A_{rms}$	0	0

After eliminating invalid cells, any calculation can be done with any considerations. For example we can look for pull-out torque of motor, or torque at a specific current. The torque is calculated by multiplying each cell in the current matrix $|I_t|$ with torque constant k_t. The resultant is torque matrix $|T_{torq}|$.

A.3 Voltage and Current Waveforms of Servo-Motors [10]

Permanent-field (PM = permanent-magnet, permanent-field) synchronous machines can be operated in different ways. In block-operation, the motor is supplied with rectangular block) currents and the distribution of the air-gap flux density is rectangular. If the motor is supplied with sinusoidal currents and the rectangular distribution of the air-gap flux density is retained, then we have mixed operation. In sinusoidal operation, the current and the distribution of the air-gap flux are sinusoidal. The figure shows the characteristics of flux density, current and voltage.

If a machine is operated in block-operation, then it is also called brushless or electrically commutated DC machine. If a machine is operated in sinusoidal operation, it is also called self-controlled synchronous machine. The operational performance of permanent-field synchronous machines with rotor position encoder generally corresponds to the operational performance of DC machines.

If the machine is supplied with sinusoidal currents, sinusoidal induced voltages are necessary. We can obtain a nearly sinusoidal air-gap field using parallel magnetized instead of radial magnetized permanent magnets and by designing a suitable stator winding (chording for example).

Another possibility is to supply the machine with rectangular (block) currents. The total supply current has a constant magnitude and is distributed cyclic to the three stator phases, which results in current blocks with an electrical length of 120° and dead times of 60°. If the induced voltage during the length of a current block is constant, then power of the phase is constant too. During the dead times the induced voltage has no influence on the torque generation. The trapezoidal characteristic of the induced voltage results from q>1 and because of the skewing of the stator slots of one slot pitch.

The advantages of the rectangular supply in comparison to the sinusoidal supply are a 15% higher utilization of the machine and the usage of simple position sensors (three photoelectric barriers) instead of expensive resolvers and an easier signal processing. The disadvantages of the rectangular supply in comparison to the sinusoidal supply are with increasing speed eddy-current losses arise in the conductive rare-earth permanent magnets (in comparison with non-conductive ferrite magnets) caused by the slot harmonics and the jumping rotating mmf because of the machine- inductances and the voltage limitation of the converter, there are heavy deviances from the rectangular current form at high speed. The results are a reduced torque and higher losses. because of the

non-ideal commutation of the phase currents at rectangular supply, angle dependent huntings occur at lower speed, which has to be compensated by the control.

In contrast the mixed operation has advantages. If the machine is supplied sinusoidal, if it has a rectangular flux-density distribution in the air-gap and if the stator winding is chorded, to achieve a sinusoidal induced voltage, then the best motor utilization is obtained. In this case the fundamental wave of the flux-density in the air-gap is increased and at the same time the losses are reduced. A 26% higher machine utilization can be achieved, compared to sinusoidal supply, respectively 10% higher compared to rectangular supply.

A summary of the presented information is illustrated in Figure A.3.

Block (B1), Block (I1) Trapezoidal (Ui)	Block (B1), Sinusoidal (I1), Sinusoidal (Ui)	Sinusoidal (B1), Sinusoidal (I1), Sinusoidal (Ui)
$U_{i\sqcap} = 2l(w\xi)BV_A$ $= \omega(w\xi)\frac{2}{\pi}\tau_p lB_{max}$ $= cB_{max}$	$U_{i\sim\sqcap}$ $= \omega(w\xi)\frac{2}{\pi}\tau_p lB_{max}\frac{\frac{4}{\pi}\sin(a_i\frac{\pi}{2})}{\sqrt{2}}$ $= \frac{cB_{max}}{\sqrt{2}}\frac{4}{\pi}\sin(a_i\frac{\pi}{2})$	$U_{i\sim}$ $= \omega(w\xi)\frac{\frac{2}{\pi}\tau_p lB_{max}}{\sqrt{2}}$ $= \frac{cB_{max}}{\sqrt{2}}$
$P_V = 2RI_{\sqcap}^2$ $I = \sqrt{\frac{3}{2}}I_\sim$	$P_V = 3RI_\sim^2$	$P_V = 3RI_\sim^2$
$P_\sqcap = 2U_{i\sqcap}I_\sqcap$	$P_{\sim\sqcap} = 3U_{i\sim\sqcap}I_\sim$	$P_\sim = 3U_{i\sim}I_\sim$
discrete position measurement (3 photoelectric barriers)	continuous position measurement (resolver or incremental encoder)	
$\frac{P_\sqcap}{P_\sim} = \frac{2}{\sqrt{3}} = 1,15$		
$\frac{P_\sqcap}{P_{\sim\sqcap}} = \frac{2}{\sqrt{3}}\frac{1}{\frac{4}{\pi}\sin(a_i\frac{\pi}{2})} = 0,91$ für $a_i = 1$		
$\frac{P_{\sim\sqcap}}{P_\sim} = \frac{P_{\sim\sqcap}}{P_\sqcap}\frac{P_\sqcap}{P_\sim} = \frac{1}{0,91}1,15 = 1,26$ for $a_i = 1$		

Figure A.3: Comparison of different excitation methods of PM machines

A.4 Optimization Toolbox: modeFrontier

In optimized design of the PM machine, a commercial program called modeFrontier® is used as the optimization tool. It is a multi-objective optimization environment software which features most recent optimization techniques available today in literature ranging from Design of Experiments to Direct Optimizers [58].

It applies a selected optimization method to the design program in design space to look for optimized solution regarding defined constraints. An optimization problem can be prepared in modeFrontier as presented in Section 0.

The main window of modeFrontier is called "workflow". In this page all main design measures are defined; inputs (or parameters) with boundary limitations, resource code that should be used to compute the outputs (or measures), goals of the process.
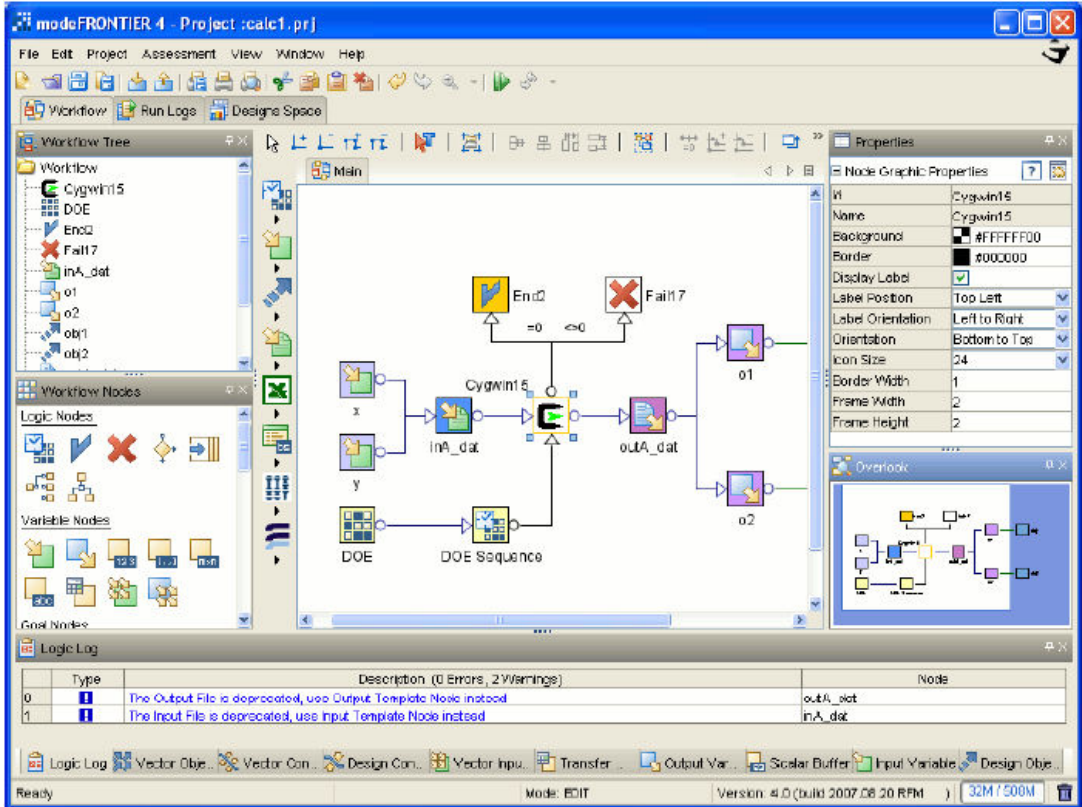
Figure A.4: Workflow window of modeFrontier

A.4.1   Blocks in Workflow

When a new project is started in modeFrontier, an empty workflow is initiated. Required elements which are represented by blocks have to be placed into this empty workflow. The required blocks can be listed as follows:

- **Input Variable block**: Defines the input variable to be inserted in design program. Its value can be constant or variable. The defined value is assigned to modeFrontier workspace through this block.

- **Output Variable block:** Defines the output variable of the design program. Its value is assigned by design program used in optimization. An output varliable is calculated inside the design program and assigned to modeFrontier workspace through this block.

- **Script Block:** This is the main design program to be used in optimization. The modeFrontier accepts many types such as Excel, Mathcad, Matlab, spreadsheets. In this thesis work, a Matlab script is assigned to this block.

- **Scheduler block:** This block defines optimization method to be performed. Many methods are available such as Simplex, Genetic Algorithm, Game Theory, Particle Swarm. In this thesis "Non-dominated Sorting Genetic Algorithm" is used which is a version of Genetic algorithm by prof. K. Deb et al [54].

- **Design of Experiments block:** This block is used to define the initial set of designs to be evaluated. Accordingly, one, and only one, such node must exists in any legal Workflow. This node always appears in conjunction with the scheduler node, which actually determines which DOE designs will be evaluated.

A.4.2   Implementation of Optimization in modeFrontier

The optimization process can be outlined in three steps.

1. Create initial population
2. Run optimization
3. Select best solution from optimization pareto set

In the following sections, details of these steps are presented.

Step 1: Define initial population

There have to be an initial population for the GA to start searching the design space. This population may consist of feasible designs for the design objectives or random inputs. In

this thesis work, no initial feasible design has been defined in the initial population; instead a population of 100 designs has been randomly created by the help of optimization tool modeFrontier®.

In the program, there are two options in modeFrontier® which help to create random populations without an initial feasible design; option "Random" fills the design space randomly without any consideration whereas other option "Sobol" fills the design space with uniformly distributed elements based on random Sobol sequence.

In this thesis work, both options "Random" and "Sobol" are used to create an initial population of 100 elements (50 designs from each). Details of sequence generations are presented as follows:

Random: It is defined in [60] that the random sequence spreads points uniformly in design space and it is based on the mathematical theory of random number generation. User interface of random sequence panel is illustrated in Figure A.5.

⊟ Random
Design of experiments based on a random sequence. It fills randomly, with a uniform distribution, the design space.
The sequence of points is determined by the value of the Seed.
Three parameters can be defined:
  1) Number of experiments to be generated;
  2) Reject or accept unfeasible designs;
  3) Random seed for sequence repeatability.

It can be used as initial design population for MOGA and Simplex algorithm. The number of generated designs is limited to 256000.
⊟ Parameters

Number of Designs	[1,256000]	10
Reject Unfeasible Samples		☑
Random Generator Seed	[0,999]	1

| Add DOE Sequence | Stop DOE Sequence |

Figure A.5: Random Sequence Dialog Panel

Three parameters must be defined in the panel:

- Number of Design
- Reject Unfeasible Samples
- Random Generator Seed

"Reject Unfeasible Samples" option automatically keeps or rejects values that do not respect the constraints. "Random generator seed" option is effective if two

random sequences are created. Generation of identical sequences of numbers with the same seed is avoided if the seed value is 0. The sequence is automatically seeded to a value based on the current time in this case.

Sobol: Sobol is defined as a deterministic algorithm that mimics the behaviour of the random sequence but with a more uniform sampling of the design space. User interface of sobol sequence panel is illustrated in Figure A.6.

□ Sobol

Design of experiments based on a pseudo random Sobol sequence. It works best with 2 to 20 variables. The experiments are uniformly distributed in the design space. It is recommended as initial design population for MOGA algorithm.

The max number of generated designs is limited to 256000.

□ Parameters

Number of Designs   [1,256000] 10

Add DOE Sequence   Stop DOE Sequence

Figure A.6: Sobol Sequence Dialog Panel

The sobol sequence is defined as "quasi-random" in [60] where the design space is filled in a uniform manner. In Figure A-7, 1000 points generated with a Random (left) and a Sobol (right) sequence are presented. It is observed that Sobol sequence fills more uniformly the Design space.
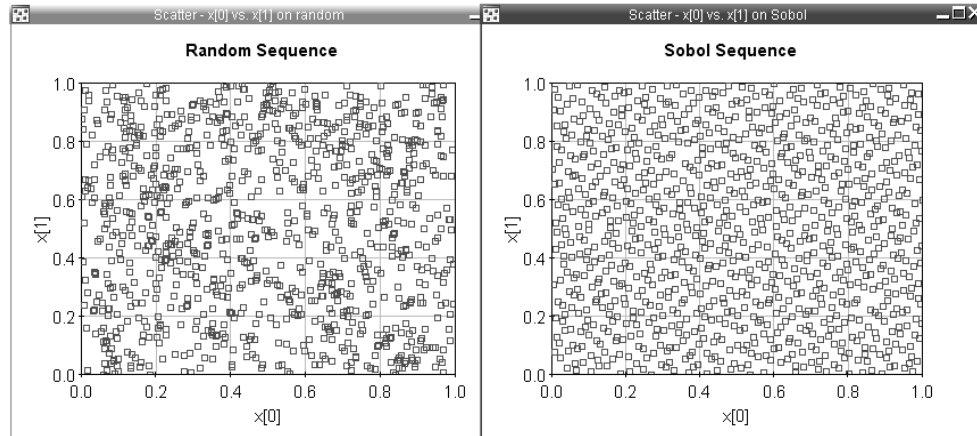
**Figure A-7: Comparison of design spaces created with Random and Sobol
sequences [60]**

Step 2: Run Optimization

"Non-dominated Sorting Genetic Algorithm II" (NSGA-II) is selected as the optimization method in modeFrontier. This method is developed by prof. K. Deb et al. [54] at Kanpur Genetic Algorithms Laboratory (KanGAL).

NSGA-II is defined as a fast and elitist multi-objective evolutionary algorithm. NSGA-II implements elitism for multiobjective search, using an elitism-preserving approach. Elitism is introduced storing all non-dominated solutions discovered so far, beginning from the initial population. Elitism enhances the convergence properties towards the true Pareto-optimal set. A parameter-less diversity preservation mechanism is adopted. Diversity and spread of solutions is guaranteed without use of sharing parameters, since NSGA-II adopts a suitable parameter-less niching approach. It is used the crowding distance, which estimates the density of solutions in the objective space, and the crowded comparison operator, which guides the selection process towards a uniformly spread Pareto frontier. The constraint handling method does not make use of penalty parameters. The algorithm implements a modified definition of dominance in order to solve constrained multi-objective problems efficiently. NSGA-II allows both continuous ("real-coded") and discrete ("binary-coded") design variables. The original feature is the application of a genetic algorithm in the field of continuous variables.

Before running the GA, some decisions have to be made to control optimization procedure.

Number of Generations	[1,5000]	2000
Crossover Probability	[0.0,1.0]	0.9
Mutation Probability for Real-Coded Vectors	[0.0,1.0]	1.0
Mutation Probability for Binary Strings	[0.0,1.0]	1.0
⊟ Advanced Parameters		
Distribution Index for Real-Coded Crossover	[0.5,100.0]	20.0
Distribution Index for Real-Coded Mutation	[0.5,500.0]	20.0
Crossover Type for Binary-Coded Variables		Simple ▾
Random Generator Seed	[0,999]	1

Figure A.8: Parameters to be set for Genetic Algoritm

Definitions of control parameters presented in Figure A.8 are as follows:

- **Number of Generations:** This value defines the maximum size of the run. It is set as 2000 in this work.

- **Crossover Probability:** This parameter specifies the occurrence probability of the Classical Cross-Over operator. The value range is 0-1. It is set as 0.9 which recommended by the program also.

The size of the initial population is usually related to the number of design variables. In most cases a good initial guess is to set the population size at 3-5 times larger than the number of design variables [51]. If the chosen population size chosen is too small, there will not be enough variety among the members of the population. This can lead to a premature convergence to some local minimum.

Alternatively, if the population size is too large, then it will take a lot more computational time to evaluate all the members of the population without significantly reducing the number of generations needed to reach the optimal solution. In the case of a surface PM motor design there are 9 independent variables as presented in Section 5.1.4. An initial population size of 50 seems (more than 5 times of independent variables) to be reasonable.

The maximum generations is limited as 2000 so that after 2000 iterations resulting in 100.000 designs, no more iteration will be performed to avoid excessive work. It is assumed that before 2000 generations, GE will result an optimized solution which can be no more improved. Certainly the iteration process can be continued in case of no optimum solution in 2000 generations.

Step 3: Select best solution from optimization pareto set

As for any optimized design problem, several alternative designs may be reached, which satisfy the defined constraints and requirements. The designs which fit into requirements are called feasible designs. However, optimum design is best among these feasible designs in some sense. This could be a minimum weight, size, cost, maximum efficiency, or a combination of them.

A.5 Magnet Data

NO	Materials	Remanence Br		Coercive Force Hcb		Intrinsic Coercive force Hci		Max Energy Product (BH) max		Square Degrees Hk/Hcj		Highest Work temperature
		KG	T	KOe	KA/m	KOe	KA/m	MGOe	KJ/m	Block	Cylinder	□
1	N-35	11.4-11.8	1.18-1.28	≥10.8	≥836	≥12	≥955	33-36	263-287	>=90%	>=86.8%	80
2	N-38	11.8-12.3	1.18-1.28	≥10.8	≥860	≥12	≥955	36-39	287-310	>=90%	>=86.8%	80
3	N-40	12.7-12.9	1.27-1.29	≥11.0	≥876	≥12	≥955	38-41	303-326	>=90%	>=86.8%	80
4	N-42	12.9-13.3	1.29-1.33	≥10.5	≥836	≥12	≥955	40-43	318-342	>=90%	>=86.8%	80
5	N-45	13.3-13.8	1.33-1.38	≥9.5	≥756	≥12	≥955	43-46	342-366	>=90%	>=86.8%	80
6	N-48	13.8-14.2	1.38-1.42	≥10.5	≥835	≥12	≥955	46-49	366-390	>=90%	>=86.8%	80
7	N-50	13.8-14.5	1.38-1.45	≥10.5	≥835	≥11	≥955	47-51	374-406	>=90%	>=86.8%	80
8	N-52	14.3-14.8	1.43-1.48	≥10.8	≥860	≥11	≥876	50-53	398-422	>=90%	>=86.8%	80
9	33M	11.4-11.8	1.14-1.18	≥10.3	≥820	≥14	≥1114	31-33	247-263	>=90%	>=86.8%	100
10	35M	11.8-12.3	1.18-1.23	≥10.8	≥860	≥14	≥1114	33-36	263-287	>=90%	>=86.8%	100
11	38M	12.3-12.7	1.23-1.27	≥11.0	≥876	≥14	≥1114	38-41	303-326	>=90%	>=86.8%	100
12	40M	12.7-12.9	1.27-1.29	≥11.4	≥907	≥14	≥1114	38-41	303-326	>=90%	>=86.8%	100
13	42M	12.8-13.2	1.28-1.32	≥11.6	≥923	≥14	≥1114	40-43	318-342	>=90%	>=86.8%	100
14	45M	13.2-13.8	1.32-1.38	≥11.8	≥939	≥14	≥1114	43-46	342-366	>=90%	>=86.8%	100
15	48M	13.6-14.0	1.36-1.40	≥11.8	≥939	≥14	≥1114	46-49	366-390	>=90%	>=86.8%	100
16	50M	14.0-14.5	1.40-1.45	≥13.0	≥1033	≥14	≥1114	48-51	382-406	>=90%	>=86.8%	100
17	30H	10.8-11.4	1.08-1.14	≥10.2	≥812	≥17	≥1353	28-31	223-247	>=90%	>=86.8%	120
18	33H	11.4-11.8	1.14-1.18	≥10.6	≥844	≥17	≥1353	31-33	247-263	>=90%	>=86.8%	120
19	35H	11.8-12.3	1.18-1.28	≥11.0	≥876	≥17	≥1353	33-36	263-287	>=90%	>=86.8%	120
20	38H	12.3-12.7	1.23-1.27	≥11.2	≥890	≥17	≥1353	36-39	287-310	>=90%	>=86.8%	120
21	40H	12.7-12.9	1.27-1.29	≥11.5	≥915	≥17	≥1353	38-41	303-326	>=90%	>=86.8%	120
22	42H	12.8-13.2	1.28-1.32	≥12.0	≥955	≥17	≥1353	40-43	318-342	>=90%	>=86.8%	120
23	45H	13.2-13.5	1.32-1.38	≥12.0	≥955	≥17	≥1353	42-46	335-366	>=90%	>=86.8%	120
24	46H	13.3-13.8	1.33-1.38	≥12.2	≥972	≥16	≥1274	44-47	350-374	>=90%	>=86.8%	120
25	48H	13.6-14.3	1.36-1.43	≥12.5	≥995	≥16	≥1274	46-49	366-390	>=90%	>=86.8%	120
26	30SH	10.8-11.4	1.08-1.14	≥10.0	≥796	≥20	≥1672	28-31	223-247	>=90%	>=86.8%	150
27	33SH	11.4-11.8	1.14-1.18	≥10.5	≥836	≥20	≥1672	31-34	247-276	>=90%	>=86.8%	150
28	35SH	11.8-12.3	1.18-1.23	≥11.0	≥876	≥20	≥1672	33-36	263-287	>=90%	>=86.8%	150
29	38SH	12.3-12.7	1.23-1.27	≥11.4	≥907	≥20	≥1972	36-39	287-310	>=90%	>=86.8%	150
30	40SH	12.5-12.8	1.25-1.28	≥11.8	≥939	≥20	≥1972	38-41	302-326	>=90%	>=86.8%	150
31	42SH	12.8-13.2	1.28-1.32	≥	≥	≥	≥	40-43	320-343	>=90%	>=86.8%	150

No.	Grade	Br	Br(T)	Hcb	Hcb	HcJ	HcJ	(BH)max	(BH)max			Temp
				11.8	939	20	1672					
32	45SH	13.2-13.8	1.32-1.38	≥12.6	≥1003	≥20	≥1592	43-46	342-366	>=90%	>=86.8%	150
33	30UH	10.8-11.4	1.08-1.14	≥10.2	≥812	≥25	≥1990	28-31	223-247	>=90%	>=86.8%	180
34	33UH	11.3-11.7	1.13-1.17	≥10.7	≥852	≥25	≥1990	31-33	247-263	>=90%	>=86.8%	180
35	35UH	11.7-12.1	1.17-1.21	≥10.7	≥852	≥25	≥1990	33-36	263-287	>=90%	>=86.8%	180
36	38UH	12.1-12.5	1.21-1.25	≥11.4	≥907	≥25	≥1990	36-39	287-310	>=90%	>=86.8%	180
37	40UH	12.5-12.8	1.25-1.28	≥11.4	≥907	≥25	≥1990	38-41	302-326	>=90%	>=86.8%	180
38	28EH	10.5-10.8	1.05-1.08	≥9.5	≥756	≥30	≥2388	26-29	207-231	>=90%	>=86.8%	200
39	30EH	10.8-11.4	1.08-1.14	≥9.5	≥756	≥30	≥2388	28-31	223-241	>=90%	>=86.8%	200
40	33EH	11.3-11.7	1.13-1.17	≥10.2	≥812	≥30	≥2388	31-33	247-263	>=90%	>=86.8%	200
41	35EH	11.7-12.1	1.17-1.21	≥10.2	≥812	≥30	≥2388	33-36	263-287	>=90%	>=86.8%	200
42	38EH	12.1-12.5	1.21-1.25	≥11.4	≥907	≥30	≥2388	36-39	287-310	>=90%	>=86.8%	200
43	30AH	10.8-11.3	1.08-1.13	≥10.2	≥812	≥35	≥2785	28-32	223-255	>=90%	>=86.8%	220
44	33AH	11.2-11.7	1.12-1.17	≥10.2	≥812	≥35	≥2785	31-34	247-271	>=90%	>=86.8%	220

Notes:

1. The above-mentioned data of magnetic parameters and physical properties are given at room temperature.
2. The maximun service temperature of magnet is changeable due to the ratio length and diameter and environmental factors.

Typical magnetic properties:

α(Br) = -0.12%/□ testing temperature range: 20～140□

α(HcJ) = -0.60%/□ testing temperature range : 20～140□ (Not include Tseries、L-Tseries)
μrec =1.05

Tc:	N series 312□	M series 320□	H series 330□	SH series 340□	UH、EH series 380□

T series	
α(Br) = -0.11%/□	testing temperature range 20～150□
α(HcJ) = -0.65～-0.50%/□	testing temperature range 20～150□

L-······T series (Low Co-efficient of Temperature)	
α(Br) （absolute value）＜-0.10%/□ testing temperature range 20～180□	
α(HcJ) （absolute value）＜ -0.50%/□ testing temperature range 20～180□	

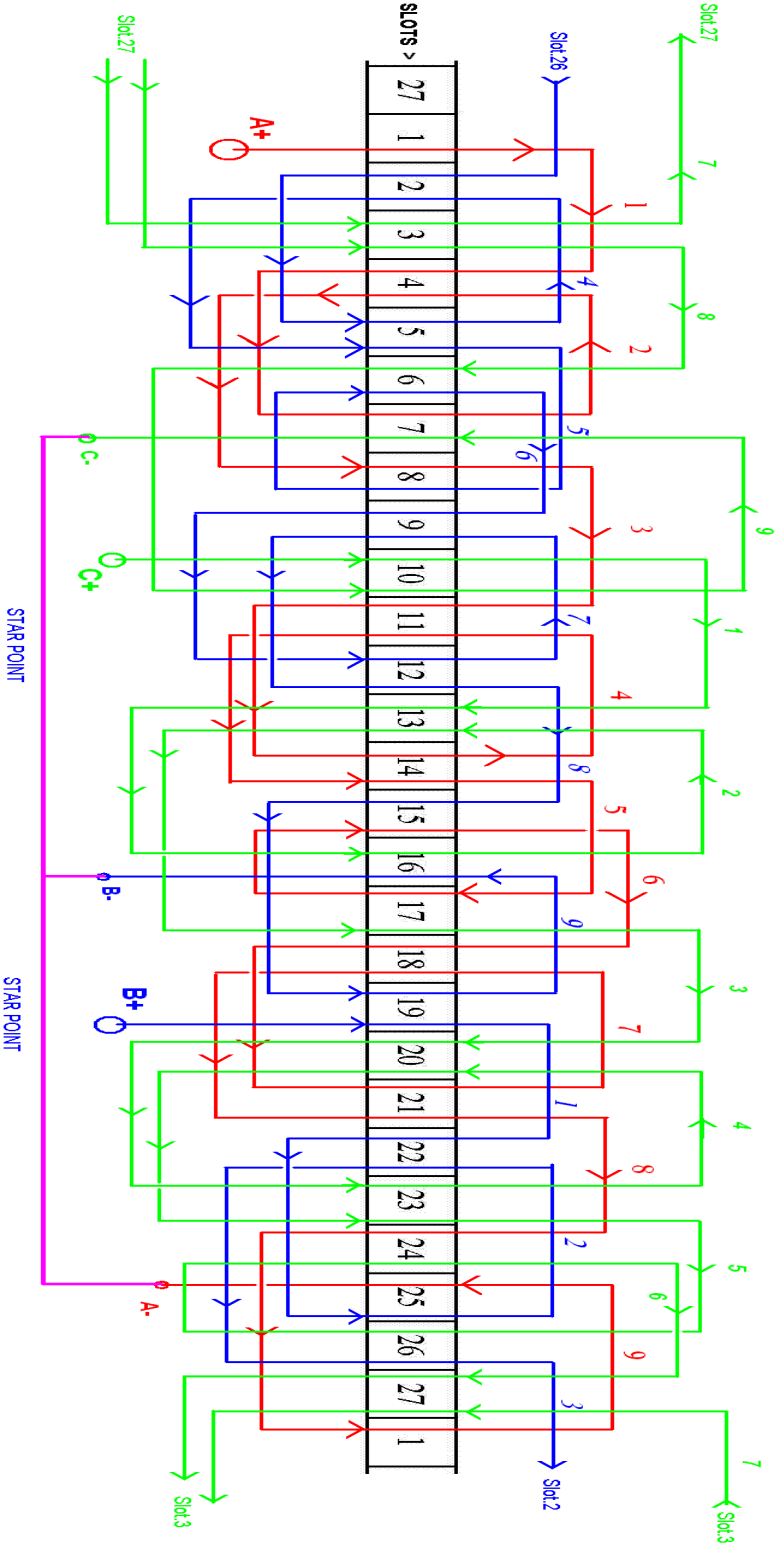| PS: 1T=10kGs	1kOe=79.6kA/m	1MGOe=7.96kJ/m3	1mT=10Gs
PS: 1T=10kGs	1kOe=79.6kA/m	1MGOe=7.96kJ/m3	1mT=10Gs

A.6 Winding Scheme

Figure A.9: Winding scheme of sample motor and new designs